THE UNIVERSITY OF CHICAGO

INVESTIGATING TISSUE-SPECIFIC IMMUNITY IN THE UPPER DIGESTIVE SYSTEM

A DISSERTATION SUBMITTED TO

THE FACULTY OF THE DIVISION OF THE BIOLOGICAL SCIENCES

AND THE PRITZKER SCHOOL OF MEDICINE

IN CANDIDACY FOR THE DEGREE OF

DOCTOR OF PHILOSOPHY

COMMITTEE ON IMMUNOLOGY

BY

YIXUAN DEAN ZHOU

CHICAGO, ILLINOIS

JUNE 2026

© 2026 by Yixuan Dean Zhou

All rights reserved

Abstract

The immune system must balance effective responses against pathogens and malignancies with tolerance towards self. The digestive system, comprising the liver, pancreas and intestine, represents a uniquely interconnected organ system: tissue specific characteristics such as epithelial barriers, food exposure and commensal microbes may impact the nearby organs through shared lymphatic drainage, ductal systems and vasculature. Despite their close anatomical and developmental relationships, how these tissues coordinate innate and adaptative immune responses while maintaining tissue specific needs remains incompletely understood. This thesis investigates how antigen source, inflammatory context and inter-tissue communication collectively shape tissue-specific immunity across the gut-pancreas-liver axis.

First, we examine how antigen source, dietary versus intestinal epithelial self-antigen, shapes $CD4^+$ T cell fate in gut-draining lymph nodes (gLNs). Using oral Ovalbumin (OVA) administration and transgenic mice expressing epithelial OVA in distinct subcellular compartments, we demonstrate that $ROR\gamma t^+MHC\text{-}II^+$ antigen-presenting cells (APCs), while essential for tolerance induction to dietary antigens, are dispensable for tolerance to self-antigens. Furthermore, the subcellular localization of self-antigens differentially governs their access to specific APC subsets, with direct consequences for susceptibility to T-cell-mediated immunopathology.

Secondly, leveraging these models in the context of shared lymphatic drainage, we define how the liver, pancreas and intestine employ distinct tolerance mechanisms—immunological ignorance, clonal deletion, or regulatory T (Treg) cell induction—at homeostasis. These outcomes are determined by both tissue origin and subcellular location of self-antigens. We further show that lymph node co-drainage selectively influences Treg cell differentiation without overriding

tissue-intrinsic tolerance programs, and that inflammatory perturbations in one tissue can unmask pathogenic T cell responses in another co-drained organ.

Finally, we investigate an additional axis of inter-organ immune communication between the pancreas and intestine by focusing on the *REG/Reg* gene family, a conserved group of antimicrobial and pancreatitis-associated proteins. We demonstrate that *REG/Reg* isoforms exhibit distinct baseline expression patterns and inducibility across tissues. A subset of *REG/Reg* members is inducible, microbiota-responsive, and IL-22-dependent, whereas other isoforms are constitutively expressed. Notably, intestinal perturbations selectively upregulate inducible *Reg* members in the pancreas, revealing coordinated regulation of innate immunity across organs.

Collectively, this thesis identifies antigen origin, whether dietary versus self or self-derived from distinct cellular compartments, as a key determinants of T cell fate. These factors shape adaptive immune outcomes by directing access to specialized APC subsets and distinct tolerance pathways. In parallel, this work highlights inter-organ communication, mediated through both shared lymphatic drainage and microbiota-responsive signals that likely use the blood route as a mechanism for coordinating immune responses across the upper digestive system. Together, these findings add new layers to how tissue specific immune homeostasis and disease are defined, potentially explaining pathologies with hitherto unknown etiologies and offering novel therapeutic strategies for combatting autoimmune disorders and cancer.

Table of Contents

List of Figures ix

List of Tables xii

Acknowledgements xiii

Chapter 1. Introduction 1

1.1 Determinants of T cell fate in peripheral tissues 1

1.1.1 T cell activation and differentiation 1

1.1.2 Distinct APC subsets specialize immune outcomes 2

1.1.3 Mechanisms of oral tolerance to dietary antigens 3

1.2 Tissue-specific immunity and the impact of shared lymphatic drainage 4

1.2.1 The liver, pancreas and intestine exhibit distinct immune landscape 4

1.2.2 The liver, pancreas and intestine share LNs 5

1.3 Additional routes of communications between gut and pancreas and their impact on tissue innate immunity 5

1.3.1 Routes of communications between gut and pancreas 5

1.3.2 REG/Reg isoforms and regulation 6

1.4 Summary 6

Chapter 2. T cell fate is dictated by different antigen presenting cells in response to dietary *versus* gut epithelial self-antigen 8

2.1 Summary 8

2.2 Introduction 9

2.3 Results 11

2.3.1 Intestinal epithelial self-antigens and oral antigen induce similar antigen-specific FOXP3^{+} T cell levels in an antigen dose-dependent manner 11

2.3.2 Antigen presentation by RORγt^{+}MHC-II^{+} APCs is dispensable for pTreg cell induction and systemic tolerance to gut self-antigens 16

2.3.3 BATF3-dependent APCs are required for pTreg cell induction to gut self-antigens 18

2.3.4 Intestinal viral infection similarly alters epithelial self- and oral antigen-specific T cell fate 19

2.3.5 Intestinal viral infection drives pro-inflammatory T cell infiltration of the gut and comparable tissue damage upon oral and self-antigen recognition 20

2.3.6 Secreted but not cytosolic self-antigen induces Th2 cells in response to helminth infection in a cDC2-dependent manner 21

2.3.7 Helminth infection triggers breakdown of tolerance and anaphylaxis in response to secreted but not cytosolic gut-self antigen or dietary antigen 23

2.4 Discussion 24

2.5 Limitations of the study 28

2.6 Figures and figure legends 29

2.7 Material and methods 43

Chapter 3. Tissue-specific tolerance mechanisms and lymph node co-drainage shape T cell immunity in the upper digestive system and pancreatic cancer progression 62

3.1 Summary 62

3.2 Introduction 63

3.3 Results 65

3.3.1 Tissue-specific tolerance mechanism, subcellular source of self-antigen and antigen dose dictate T cell fate of self-reactive $CD4^+$ T cells at homeostasis 65

3.3.2 Type 1 and but not type 2 intestinal infections shifts exocrine-pancreas-reactive T cell fate in LNs shared between the pancreas and duodenum 68

3.3.3 Intestinal reovirus-induced exocrine pancreas-reactive pro-inflammatory T cells migrate to the pancreas, leading to exocrine tissue destruction 70

3.3.4 Intestinal reovirus leads to accelerated tumor progression in a genetic PDAC model 71

3.3.5 Intestinal reovirus infection enhances T cell infiltration and tumor control in an orthotopic PDAC model 73

3.3.6 Intestinal reovirus infection renders liver-specific T cells more pro-inflammatory leading to liver damage 75

3.3.7 Hepatotoxic concanavalin A induces pancreas- and gut-reactive Th1 cells and reduces pTreg cells 76

3.4 Discussion 78

3.5 Limitations of the study 82

3.6 Figures and figure legends 84

3.7 Material and methods 98

Chapter 4. Inducible, but not constitutive, pancreatic *REG/Reg* isoforms are regulated by intestinal microbiota and pancreatic diseases 114

4.1 Summary 114

4.2 Introduction 114

4.3 Results 116

4.3.1 Mouse and human Reg/REG gene family members are structurally conserved but differ in their ligand binding domains and expression pattern between pancreas and gut 116

4.3.2 Gut enterocytes and pancreatic acinar cells are enriched for REG/Reg transcripts and the upstream signaling receptor IL22RA1/Il22ra1 119

4.3.3 Pancreatic and intestinal Reg gene family transcripts correlate and are regulated by microbial colonization 121

4.3.4 Murine PDAC triggers Reg upregulation in pancreas but not gut 125

4.3.5 Cerulein-induced pancreatitis triggers upregulation of Reg genes in pancreas and modifies the duodenal microbiome 128

4.4 Disccusion 130

4.4.1 Evolution of divergent REG isoforms and inter-species differences in pancreatic and intestinal usage 131

4.4.2 Conservation of REG/Reg prosegment and its relation to trypsin 132

4.4.3 Microbe-induced IL-22, REG/Reg, and pancreatic disease 134

4.4.4 Lack of reciprocity between pancreas versus gut initiated Reg upregulation 135

4.5 Limitations of the study 136

4.6 Figures and figure legends 138

4.7 Material and methods..... 153

Chapter 5. Thesis Discussion.....166

Bibliography 168

List of Figures

Figure 2.1 Chapter 2 Graphical Abstract 8

Figure 2.2 Generation and characterization of mice expressing OVA in different subcellular epithelial cell compartments. 29

Figure 2.3 Antigen presentation by $ROR\gamma t^{+}MHC\text{-}II^{+}$ APCs is dispensable for pTreg cell induction and systemic tolerance to gut self-antigens. 30

Figure 2.4 BATF3-dependent APCs are required for pTreg cell induction to gut self-antigens.. 31

Figure 2.5 Intestinal viral infection impacts epithelial self-antigen and oral antigen-specific T cell fate similarly..... 32

Figure 2.6 Intestinal viral infection leads to comparable pro-inflammatory T cell infiltration and tissue damage following oral and self-antigen recognition..... 33

Figure 2.7 Secreted but not cytosolic self-antigens induce Th2 cells in response to helminth infection in a cDC2-dependent manner. 34

Figure 2.8 Helminth infection triggers breakdown in tolerance and anaphylaxis in response to secreted but not cytosolic gut self-antigen or dietary antigen..... 35

Figure 2.9 Generation and characterization of mice expressing OVA in different subcellular epithelial cell compartments. 36

Figure 2.10 Antigens with different subcellular compartments are taken up by APCs through distinct mechanisms. 37

Figure 2.11 cDC1s are required while Thetis cells are dispensable for the generation of gut self-antigen specific FOXP3+ T cells. 38

Figure 2.12 $FOXP3^{+}$ and FOXP3- OT-II cells diverge in their proliferation patterns. 39

Figure 2.13 Intestinal viral infection impacts epithelial self-antigens and oral antigen-specific T cell fate similarly..... 40

Figure 2.14 Intestinal viral infection leads to comparable pro-inflammatory T cell infiltration of the gut following oral and self-antigen recognition and helminth infection triggers breakdown in tolerance and anaphylaxis in response to secreted but not cytosolic OVA. 41

Figure 2.15 Secreted but not cytosolic self-antigens induce Th2 cells in response to helminth infection in a cDC2-dependent manner. 42

Figure 3.1 Chapter 3 Graphical Abstract 62

Figure 3.2 Tissue-specific tolerance mechanism, subcellular source of self-antigen and antigen dose dictate T cell fate of self-reactive CD4+ T cells at homeostasis. 84

Figure 3.3 Type 1 and but not type 2 intestinal infections shifts exocrine-pancreas-reactive T cell fate by LN co-drainage..... 85

Figure 3.4 Intestinal reovirus-induced pro-inflammatory T cells infiltrate the pancreas and cause tissue destruction..... 86

Figure 3.5 Intestinal reovirus infection exacerbates pancreatic tumor growth in a genetic PDAC model by a CD8+ T cell-dependent manner..... 87

Figure 3.6 Intestinal reovirus infection enhances T cell infiltration and tumor control in an orthotopic PDAC model. 88

Figure 3.7 Intestinal reovirus infection induces liver-reactive T cells and hepatic damage by LN co-drainage. 89

Figure 3.8 Con A-induced liver injury promotes pro-inflammatory conversion of pancreas- and gut-reactive T cells..... 90

Figure 3.9 Tissue-specific tolerance mechanism, subcellular source of self-antigen and antigen dose dictate T cell fate of self-reactive CD4+ T cells at homeostasis. 91

Figure 3.10 Type 1, but not type 2, intestinal infection renders pancreas-reactive T cells pro-inflammatory..... 92

Figure 3.11 Intestinal reovirus infection renders pancreas-reactive T cells pro-inflammatory by LN co-drainage. 93

Figure 3.12 Intestinal reovirus-induced pro-inflammatory T cells infiltrate the pancreas and cause severe tissue destruction..... 94

Figure 3.13 Intestinal reovirus infection enhances T cell infiltration and tumor control in an orthotopic PDAC model. 95

Figure 3.14 Intestinal reovirus infection induces liver-reactive T cells and hepatic damage by LN co-drainage. 96

Figure 3.15 Con A-induced liver injury promotes pro-inflammatory conversion of pancreas- and gut-reactive T cells..... 97

Figure 4.1 Mouse and human *Reg/REG* gene family members are structurally highly conserved but differ in their expression patterns between pancreas and gut. 138

Figure 4.2 Gut and pancreas are enriched for *Reg* transcripts and the upstream signaling receptors..... 139

Figure 4.3 Pancreatic and intestinal *Reg* gene family transcripts correlate and are regulated by microbial colonization. 140

Figure 4.4 Differential IL-22 producers in the pancreas and gut upon antibiotics and SFB-colonization suggests context-dependent production. 141

Figure 4.5 A mouse model of primary pancreatic ductal adenocarcinoma triggers *Reg* upregulation in pancreas but not gut. 142

Figure 4.6 Cerulein induced pancreatitis triggers upregulation of *Reg* genes in pancreas and modifies the gut microbiome. 143

Figure 4.7 Mouse *Reg* and human *REG* gene family members are structurally conserved..... 144

Figure 4.8 Mouse *Reg* and human *REG* gene family members differ in their expression patterns between pancreas and gut. 145

Figure 4.9 Gut and pancreas are enriched for *Reg* transcripts and the upstream signaling receptors. 146

Figure 4.10 Dependence of baseline pancreatic and intestinal *Reg* expression on IL-22 and postnatal environmental exposure..... 147

Figure 4.11 Transcription binding site analysis of *REG/Reg* family members. 148

Figure 4.12 A mouse model of primary pancreatic ductal adenocarcinoma triggers *Reg* upregulation in pancreas but not gut. 149

Figure 4.13 Human PDAC scRNAseq analysis for *REG* genes and murine duodenal microbiome upon PDAC induction. 150

Figure 4.14 Cerulein induced pancreatitis triggers upregulation of *Reg* genes in pancreas but not gut. 151

Figure 4.15 Cerulein induced pancreatitis modifies the gut microbiome. 152

List of Tables

Table 2.1 KEY RESOURCES TABLE 43

Table 3.1 KEY RESOURCES TABLE 98

Table 4.1 Primer list..... 157

Acknowledgements

The journey of the past six years has been nothing short of a transformative experience for me, both personally and professionally. I would like to express my gratitude to many people in my life whose support served as essential co-stimulatory signals, preventing this graduate student from undergoing terminal exhaustion.

I would like to begin by thanking my mentor, Dr. Daria Esterházy. Her scientific passion, vision and rigor, along with her unwavering support, have shaped every stage of this thesis and my PhD career. Daria is never short of brilliant and intriguing scientific questions. She trained me to think beyond the data in front of me and to appreciate the broader significance and implications of our work. I would not be the scientist I am today without her guidance and example.

I want to thank my parents for always believing in me and supporting me in every way they could. As a first-generation college student and the first in my family to complete a doctoral-level education, I owe this achievement to their support sacrifices and unconditional support. They navigated social and economic challenges to pave a path for me that they had never experienced themselves yet never hesitated to encourage me to keep going. Their hard work, resilience, and faith in me made this journey possible, and I carry that with me in everything I do.

I also thank my thesis committee, Dr. Peter Savage, Dr. Justin Kline, and Dr. Yuxuan Phoenix Miao for their insightful feedback, thoughtful questions and continued support through my PhD. Their perspectives challenged me to think more deeply and strengthened this work in meaningful ways. I am grateful to the Committee on Immunology community and my cohort for creating such a vibrant and supportive environment. It has been a privilege to grow alongside such talented and kind individuals. A special thank you to my friend Angie, for always listening to my

rants and for being spontaneously on board with any of my questionable ideas, academic or non-academic—you made this journey far more enjoyable.

To all the current and previous members of the lab, thank you so much for your collaboration and constant willingness to help. Whether through discussions during lab meetings, troubleshooting experiments, or simply being super approachable whenever I needed help, you made the lab an incredibly supportive place to work and learn.

To my friends outside of lab, especially Tong and Hang, thank you for everything you've been to me during this time. From traveling together to sharing countless everyday moments, and for always listening to my rants, no matter how repetitive or dramatic, they meant more than you know. Being roommates in San Diego and then now in Chicago was something I never expected, but it became one of the most meaningful parts of my PhD years. Somehow, our paths converged far more than any of us planned, and I'm incredibly grateful for that. Let's keep it that way.

I begin with gratitude to everyone who supported this work, especially those who assured me that, eventually, the experiments would stop failing. I want to take this opportunity to tell you that you are only partially correct. I have grown immensely over the course of my PhD, and I truly believe it takes a village to accomplish anything worth pursuing, and I could not be more grateful for mine.

Chapter 1. Introduction

1.1 Determinants of T cell fate in peripheral tissues

The differentiation of naïve $CD4^+$ T cells into effector or tolerogenic states is a central process in adaptive immunity, particularly in the gastrointestinal tract, ensuring protection against pathogens while preventing autoimmunity. Essential to this discriminatory capacity is the priming of naïve $CD4^+$ T cells within gLNs, where specialized APCs integrate environmental cues to direct differentiation toward either effector or regulatory lineages(Kedmi & Littman, 2024). Classical models of T cell fate determination emphasize TCR affinity to antigen, antigen persistence, co-stimulation and cytokine milieu at the time of priming(Zehn et al., 2009; J. Zhu & Paul, 2010). However, these models largely treat antigen as a uniform entity and do not fully account for how antigen origin or its subcellular localization influence immune outcomes. Therefore, while broad principles of T cell differentiation are well defined, the rules governing how distinct antigen sources instruct specific immune outcomes remain incomplete.

1.1.1 T cell activation and differentiation

It is well established that antigen dose and persistence critically shape $CD4^+$ T cell fate by tuning the strength and integration of the three canonical activation signals. Signal 1**,** delivered through TCR recognition of peptide-MHC II, is highly dependent on antigen abundance and duration of presentation. High antigen dose and sustained peptide availability prolong TCR signaling, driving strong activation of NFAT, AP-1, and NF-κB pathways and promoting effector differentiation(Zehn et al., 2009). In contrast, low-dose or transient antigen exposure generates weaker, discontinuous TCR signals that fail to fully induce IL-2 production and metabolic reprogramming, predisposing cells to anergy or deletion(Malherbe et al., 2004). Signal 2, mediated

by costimulatory and coinhibitory pathways, further calibrates T cell activation. Engagement of CD28 by CD80/CD86 amplifies TCR signaling via PI3K–Akt–mTOR, supporting proliferation and effector differentiation(S. Wang et al., 2024). Conversely, limited co-stimulation results in incomplete activation and promotes tolerance. Signal 3**,** composed of polarizing cytokines, provides instructive cues for lineage commitment. IL-12 promotes Th1 differentiation via STAT4 and T-bet, IL-4 drives Th2 via STAT6 and GATA3, while TGF-β with IL-6 induces Th17 through STAT3 and RORγt(Seki et al., 2004; Yamashita et al., 2011; J. Zhu et al., 2012; J. Zhu & Paul, 2010). In the absence of inflammatory cytokines, TGF-β favors FOXP3$^+$ Treg induction(S. Fu et al., 2004; J. Wang et al., 2023). Together, these signals integrate and collectively determine whether antigen exposure elicits sufficient T cell activation and to instruct the specific lineage that T cells ultimately adopt.

1.1.2 Distinct APC subsets specialize immune outcomes

Specialized APC subsets play nonredundant roles in directing T cell fate. Conventional dendritic cells (cDCs) are broadly divided into two subsets. cDC1s, defined by their dependence on BATF3 and expression of markers such as XCR1, are uniquely efficient at cross-presentation of exogenous antigens on MHC class I and are therefore critical for CD8$^+$ T cell priming(Hildner et al., 2008a; Murphy et al., 2016). In addition to cytotoxic T cell responses, cDC1s produce IL-12 and type I interferons, promoting Th1 polarization of CD4$^+$ T cells during infection(Mashayekhi et al., 2011; Murphy et al., 2016). Under steady-state conditions, however, cDC1s can also contribute to tolerance by inducing Treg cells, particularly in contexts where co-stimulatory signals are limited, highlighting their functional plasticity(Esterházy et al., 2016a).

cDC2s, in contrast, are specialized for priming CD4$^+$ T helper responses and can be further subdivided into cDC2A and cDC2B subsets with distinct immunological roles. cDC2A cells are

associated with Th2 differentiation, particularly in response to helminths and allergens, through production of cytokines such as IL-4 and IL-10(Gao et al., 2013), as well as T follicular helper (Tfh) responses(Xiao et al., 2024). cDC2B cells, often linked to inflammatory environments, promote Th17 responses via IL-6 and IL-23 production(Durai & Murphy, 2016).

In the intestine, additional APC populations such as RORγt^{+}MHC-II^{+} cells have been shown to enforce tolerance to commensal microbiota and dietary antigens by promoting Treg differentiation(Cabric, Franco Parisotto, et al., 2025; Cabric & Brown, 2025; Kedmi & Littman, 2024; Parisotto et al., 2024). Despite these advances, a major unresolved question is how different antigen sources preferentially engage specific APC subsets.

1.1.3 Mechanisms of oral tolerance to dietary antigens

Oral tolerance is the active suppression of systemic immune responses to ingested antigens and represents a cornerstone of mucosal immunology. This process is primarily mediated by migratory cDCs in the intestinal lamina propria, which capture luminal antigens and traffic to mesenteric LNs, where they induce Tregs through mechanisms dependent on TGF-β and retinoic acid(Coombes et al., 2007; Pabst & Mowat, 2012). In addition to cDCs, RORγt^{+}MHC-II^{+} APCs have been shown to restrain CD4^{+} T cell responses to dietary antigens and contribute to intestinal immune homeostasis(Abramson et al., 2023; Cabric, Franco Parisotto, et al., 2025; Parisotto et al., 2024; Rodrigues et al., 2025). Together, these systems ensure that dietary proteins are generally perceived as tolerogenic rather than immunogenic.

1.2 Tissue-specific immunity and the impact of shared lymphatic drainage

The liver, pancreas, and intestine form an interconnected unit within the upper digestive system, both anatomically and immunologically, however, these organs maintain highly specialized immune environments tailored to their physiological functions. At the same time, these organs are linked through common lymph nodes. This creates a complex system in which immune responses are influenced by the antigen-originating tissue as well as co-drained tissues. Understanding how these features are reconciled is essential for explaining both immune homeostasis and the emergence of multi-organ inflammatory disease.

1.2.1 The liver, pancreas and intestine exhibit distinct immune landscape

Each organ within the upper digestive system maintains a distinct immune profile adapted to its functional role. The intestine is continuously exposed to dietary antigens and commensal microbiota and is therefore enriched in regulatory mechanisms that promote tolerance. Specialized APCs, including $CD103^+$ cDC1s and $ROR\gamma t^+MHC\text{-}II^+$ populations, drive Treg differentiation and suppress excessive inflammation(Akagbosu et al., 2022a; Coombes et al., 2007; Hepworth et al., 2013). The pancreas, by comparison, is relatively immune-quiescent under homeostasis but highly sensitive to inflammatory disruption. It contains fewer resident immune cells and maintains a higher activation threshold(Glaubitz et al., 2023), yet rapidly becomes inflamed in disease states such as pancreatitis(Pandol et al., 2007). In contrast, the liver is intrinsically tolerogenic, functioning as a filter for portal blood. Antigen presentation in the liver often leads to tolerogenic responses, including incomplete T cell activation, exhaustion or abortive proliferation(Crispe, 2014; Thomson & Knolle, 2010). These differences underscore that T cell responses are strongly shaped by tissue context, raising the question of how such specialization is maintained across co-drained organs.

1.2.2 The liver, pancreas and intestine share LNs

Despite their distinct immune environments, the liver, pancreas, and proximal intestine share lymphatic drainage into common regional LNs(H. Brown et al., 2023a; Deki & Sato, 1988). These sites serve as hubs for antigen presentation, where T cells can encounter antigens derived from multiple tissues within the same microenvironment. This anatomical organization creates the potential for cross-tissue immune interactions. T cells primed in these LNs may integrate signals from different organs, allowing inflammatory cues from one tissue to influence responses to another(H. Brown et al., 2023a). Conversely, tolerogenic signals may also propagate across tissues, suppressing immune activation. However, the functional consequences of shared lymphatic drainage remain unclear. It is not known whether T cell fate is primarily dictated by the tissue of antigen origin or by the shared lymph node environment. Resolving this question is essential for understanding how immune tolerance and activation are coordinated across the digestive system.

1.3 Additional routes of communications between gut and pancreas and their impact on tissue innate immunity

1.3.1 Routes of communications between gut and pancreas

The portal circulation represents a major conduit through which gut-derived signals reach the pancreas. Microbial products, metabolites, and inflammatory mediators from the intestine can enter the bloodstream and influence distal tissues, including the pancreas(Tripathi et al., 2018), thereby providing a mechanism for systemic immune calibration. A second route of communication is ductal reflux through the pancreaticobiliary system. The anatomical continuity

between the duodenum and pancreatic ducts allows for the potential retrograde flow of duodenal contents into the pancreas(MCCUTCHEON, 1964; Taylor & Rimmer, 1980). Together, these pathways suggest that intestinal-derived signals can modulate pancreatic innate immune responses, establishing gut-pancreas axis.

1.3.2 REG/Reg isoforms and regulation

The *REG/Reg* gene family encodes secreted C-type lectins with roles in antimicrobial defense, epithelial repair, and inflammation. Multiple isoforms, including *Reg1*, *Reg2*, *Reg3* and *Reg4* family members, exhibit distinct tissue distributions and ligand engagement(Cash, Whitham, & Hooper, 2006; Sun et al., 2021). In the intestine, REG3γ is a key antimicrobial effector that limits bacterial contact with the epithelium, and its expression is tightly controlled by IL-22–STAT3 signaling downstream of microbial sensing(Vaishnava et al., 2011; Zheng et al., 2008a). In the pancreas, REG proteins have been primarily associated with regeneration and disease, particularly in the context of pancreatitis(Chen et al., 2023). However, it remains unclear whether individual *REG/Reg* isoforms are regulated synchronously. Moreover, whether their expression is coordinated between the pancreas and intestine is largely unexplored. Addressing this question is critical, as coordinated regulation would support a model in which the gut and pancreas engage in a shared innate defense program, enabling rapid and integrated responses to microbial or inflammatory perturbations originating in the intestine.

1.4 Summary

The immune system must continuously balance protective responses against pathogens and malignancies with the preservation of tolerance to self and innocuous environmental antigens. This

challenge is particularly pronounced in the upper digestive system, where the intestine, pancreas, and liver are exposed to diverse antigenic inputs yet must maintain coordinated immune homeostasis. While substantial progress has been made in defining the molecular and cellular mechanisms governing T cell activation and tolerance, a unifying framework that integrates antigen origin, tissue imprint, and inter-organ communication remains lacking.

This thesis addresses this gap by identifying antigen origin as a primary determinant of $CD4^+$ T cell fate**,** extending beyond traditional models that emphasize antigen dose and inflammatory cues. By distinguishing between dietary antigens and epithelial self-antigens, as well as resolving self-antigens by subcellular localization, this thesis demonstrates that antigen source dictate access to specialized APC subsets and bias the selection of T cell lineages. These findings provide a mechanistic basis for understanding how immune responses are differentially programmed toward tolerance or pathology in complex tissue environments.

In parallel, this work establishes that inter-organ communication mediated through shared lymphatic drainage emerges as another critical layer of immune regulation. Shared LNs enable inflammatory signals originating in one tissue to shape immune responses in another, leading to pathological outcomes and altering disease progression.

Additionally, this thesis also highlights the coordinated innate responses, namely antimicrobial peptide production, between the gut and pancreas in response to change in gut microbiota via the IL-22 pathway, further supporting the notion that the gut–pancreas–liver axis as a multi-tissue process governed by both local antigen context and systemic connectivity.

Chapter 2. T cell fate is dictated by different antigen presenting cells in response to dietary *versus* gut epithelial self-antigen

2.1 Summary

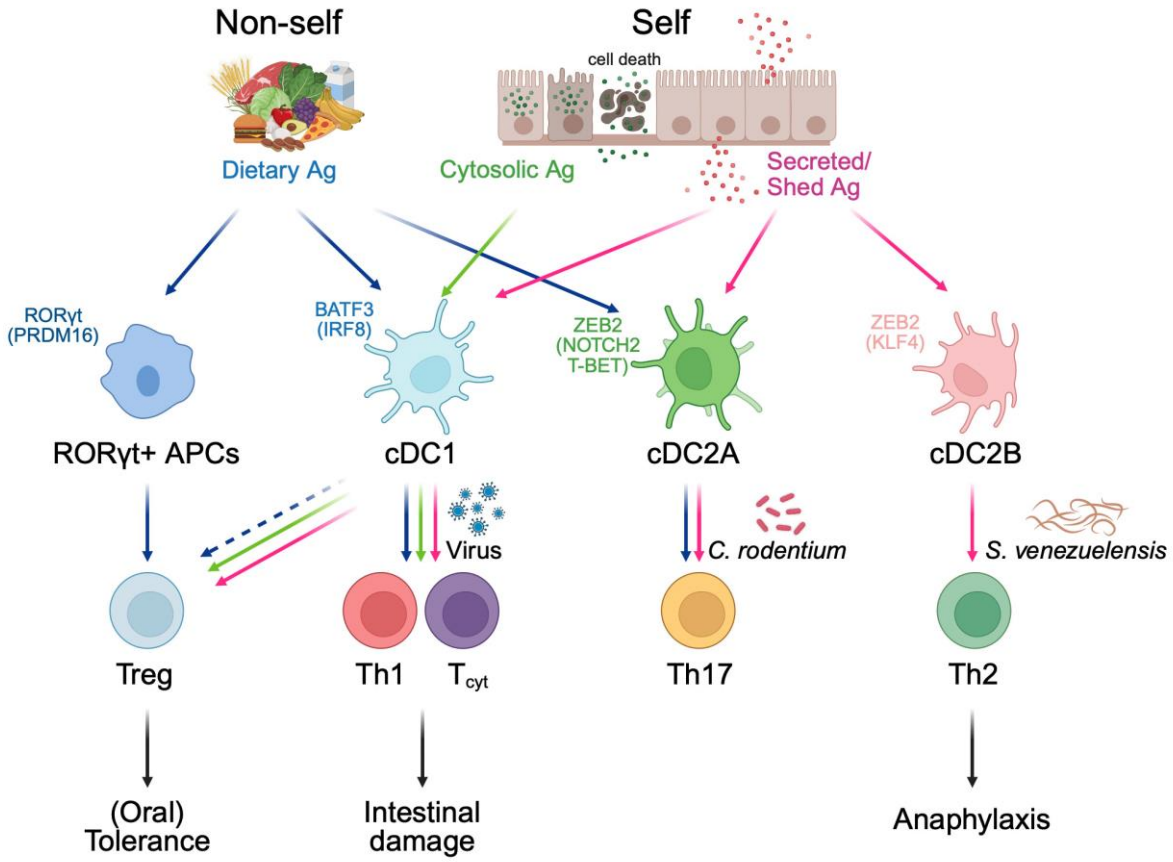


Figure 2.1 Chapter 2 Graphical Abstract

We investigated whether T cell responses and antigen-presenting cell (APC) requirements in gut-draining lymph nodes differ by antigen source, diet *versus* epithelium. Using mice fed ovalbumin (OVA) or expressing secreted (s), cytosolic (c), or transmembrane (tm) epithelial OVA, we compared OVA-specific T cell fates. At baseline and after reovirus infection, T cell responses were comparable across models. However, helminth infection induced Th2 cell polarization in sOVA and tmOVA but not cOVA or OVA-fed mice. $BATF3^+$ APCs were indispensable for $CD4^+$

T cell proliferation only in cOVA mice yet drove Treg cell differentiation across all epithelial OVA models. In contrast, antigen presentation by RORγt^{+}MHC-II^{+} APCs was exclusively required for Treg cell induction by dietary OVA. These distinct APC dependencies correlated with susceptibility to pathology elicited by dietary *versus* epithelial self-antigens. Thus, antigen origin and presentation context are integrated to shape T cell fate, a new framework for predicting gut immune outcomes.

2.2 Introduction

The intestinal immune system is constantly exposed to dietary and microbial antigens. Although less studied, it also encounters self-antigens, which are likely presented in abundance due to the epithelium's large surface area, rapid turnover rate, the absorptive nature of intestinal epithelial cells, and the vast lymphatics. The reaction to dietary antigens is well characterized: Under homeostatic conditions, food proteins elicit peripheral Treg (pTreg) cell induction, leading to their tolerance. In contrast, viral, helminthic, and bacterial infections lead to a Th1, Th2, or often Th17/22 cell response, respectively, required for pathogen clearance(Bouziat et al., 2017; Canesso et al., 2025; Esterházy et al., 2019a; Ivanov et al., 2009; Zheng et al., 2008b). The default pTreg cell response to dietary antigens and corresponding oral tolerance can be diminished if food antigens are encountered for the first time during any of these infections(Bouziat et al., 2017; Esterházy et al., 2019a; Fonseca et al., 2015), and this may contribute to diseases like celiac disease (CD) or food allergies. Since antigen presenting cells (APCs) in the gut-draining lymph nodes (gLNs) determine T cell fate, the impact of infections on how food antigens are reacted to reflects a switch in the APC subset presenting these antigens or changes in the APC transcriptional and

functional profiles(Bouziat et al., 2017; Canesso et al., 2025; Fonseca et al., 2015). Additionally, recent work has shown that dietary antigen is loaded onto various APC subtypes(Canesso et al., 2025), including conventional dendritic cells type 1 and 2 (cDC1 and cDC2) and RORγt^{+}MHC-II^{+} APCs (recently more commonly referred to as Thetis cells (TCs)), all of which are capable of inducing pTreg cells *in vitro*(Akagbosu et al., 2022b; Esterházy et al., 2016b). However *in vivo*, only a subset of TCs, the PDRM16^{+} subset TC IV, appears absolutely indispensable for generating food antigen-specific pTreg cells(Cabric, Parisotto, et al., 2025; L. Fu et al., 2025; Rodrigues et al., 2025).

Whether the same principles for Treg induction in the periphery apply to self-antigens is unknown. In fact, T cell responses to another major source of antigens in the gut, the commensal microbiota, are highly strain specific, and while when pTreg cells to commensals are induced this process seems to also depend on TC IVs(L. Fu et al., 2025), not all commensals induce pTreg cells. For example, segmented filamentous bacteria (SFB) drive Th17 cell differentiation(Ivanov et al., 2009), *Helicobacter hepaticus* promotes RORγt^{+} pTreg cell induction in gLNs(Xu et al., 2018), and *Akkermansia muciniphila* elicits a Tfh cell-dominated response, primarily in the Peyer's Patches(Ansaldo et al., 2019). As observed for dietary antigens, these dominant T cell fates can shift when antigen presentation occurs in a different inflammatory or tissue context(Ansaldo et al., 2019; Xu et al., 2018; Y. Yang et al., 2014). The differences in the nature of the T cell response to dietary and microbial antigens or between microbial strains can only to some extent be explained by the different locations along the gastrointestinal tract at which the antigens are encountered(Esterházy et al., 2019a), as homeostatic T cell responses can differ at the same location. Thus, these different responses likely also reflect the selective access of APC subsets to specific antigens and adjuvants that come with these antigens, shaping the functional

profiles of the APCs. It is therefore not evident what the rules governing self-reactive T cell fate would be. While central tolerance eliminates most self-reactive T cell clones or redirects them into the Treg cell lineage, additional peripheral tolerance mechanisms are required to prevent autoimmunity. Indeed, studies using mice expressing cytosolic OVA have found that OVA-specific $CD8^+$ T cells develop and home to the gut but acquire a $CD8^+$ Treg cell phenotype rather than destroying the epithelium(Joeris et al., 2021; Vezys et al., 2000). On the other hand, conditions like gluten-evoked autoimmunity in CD(Bouziat et al., 2017; Caio et al., 2019), autoantibodies and self-reactive T cells in inflammatory bowel disease(Kuwada et al., 2021), and the destruction of gut epithelium in patients treated with immune checkpoint inhibitors(Vezys et al., 2000) illustrate the consequences of failed tolerance to intestinal self-antigens. Thus, there is a need to better understand what determines T cell fate to gut self-antigens, which include a large repertoire of secreted, membrane-bound, and cytosolic proteins.

In this study, we asked whether T cell responses and APC requirements differ between epithelial self- and diet-derived antigens, and among epithelial antigens, whether the subcellular compartment of antigen origin influences immune outcomes. We hypothesized that any such distinctions would result in differential susceptibility to collateral damage following infections or the loss of specific APC subtypes. More broadly, our goal was to uncover principles linking antigen source and presentation context to T cell fate in the gut.

2.3 Results

2.3.1 Intestinal epithelial self-antigens and oral antigen induce similar antigen-specific $FOXP3^+$ T cell levels in an antigen dose-dependent manner

To directly compare T cell fate and APC requirements following exposure to dietary and self-antigens without confounding factors such as differential T cell receptor (TCR) affinity, we engineered mice that express the dietary antigen ovalbumin (OVA) as a self-antigen. We cloned full-length secreted OVA (sOVA) after a loxP-flanked STOP cassette, allowing tissue-specific Cre recombinase to excise the cassette and place *OVA* under the control of the artificial CAG promoter(Chu et al., 2016). We inserted the construct into the *Rosa26* locus using CRISPR (Fig. 2.2A). We also engineered a version that lacked the internal secretion signal, rendering OVA cytosolic (cOVA), as well as a version lacking the signal peptide but N-terminally fused to the transferrin receptor (TFR) transmembrane domain (tmOVA)(Joeris et al., 2021; Kurts et al., 1996; Vezys et al., 2000). Each construct included a C-terminal 3×FLAG tag for protein detection purposes. Correct targeting to the mouse genome was confirmed by PCR (Fig. 2.9A) and sequencing. Mice with these *OVA* transgenes did not stimulate the proliferation of adoptively transferred, OVA-specific $CD4^+$ T cells (OT-II cells) in the gLNs (Fig. 2.9B) and did not express *OVA* in any tissue tested (Fig. 2.9C-E). However, following interbreeding with $Villin^{CRE\text{-}ERT2}$ mice(El Marjou et al., 2004), in which *Cre* is expressed in intestinal epithelial cells and translocates to the nucleus after tamoxifen administration, all three *OVA* mouse lines robustly expressed *OVA* along the gut. The mRNA expression levels were comparable between the three lines, albeit trended to be lower in $Villin^{cOVA}$ and $Villin^{tmOVA}$ than $Villin^{sOVA}$ mice (Fig. 2.9F, G). The expected protein sizes were confirmed by immunoblotting, with higher OVA abundance in the jejunal lysates from $Villin^{sOVA}$ mice than the other two lines that appeared to attain similar levels (Fig. 2.9H), potentially because the latter two are less stable. Immunofluorescence staining suggested by contrast suggested comparable epithelial expression between $Villin^{tmOVA}$ and $Villin^{sOVA}$ mice, and expected localization across all lines (Fig. 2.9I). While quantifying how much OVA would be

available to APCs from each mouse line is not possible, the combined analysis of mRNA expression and protein staining by Western blot and immunofluorescence suggest that at the same tamoxifen dose, sOVA, the native form, consistently tends to be more highly expressed than cOVA and tmOVA, while cOVA and tmOVA display more similar levels.

To assess whether the subcellular origin of epithelial antigen influences T cell stimulation, we adoptively transferred CFSE loaded OT-II cells into *Villin*^{sOVA}, *Villin*^{cOVA}, and *Villin*^{tmOVA} mice and quantified their proliferation in gLNs as an activation proxy. In all three mouse lines, OT-II cells proliferated in the gLNs but not the non-draining liver and inguinal LNs (Fig. 2.2B, C). However, while OT-II cell division was comparable between *Villin*^{sOVA} and *Villin*^{tmOVA} mice, it was much lower in *Villin*^{cOVA} mice. We thought it was unlikely that this result was due to the slightly lower OVA expression in these mice (Fig. 2.9F-H). Rather, we hypothesized that accessing cytosolic OVA requires epithelial turn over. Consistent with this hypothesis, pharmacological inhibition of apoptosis using a pan-caspase inhibitor (Fig. 2.10A, B) in *Villin*^{cOVA} mice almost completely abrogated OT-II proliferation (Fig. 2.2D, Fig. 2.10C). However, proliferation in *Villin*^{sOVA} mice was unaffected and only partially reduced in *Villin*^{tmOVA} mice by caspase inhibition (Fig. 2.10D, E), suggesting that antigen access was either independent or only partially dependent on cell death, respectively, in these two mouse lines. As OT-II proliferation in *Villin*^{tmOVA} mice displayed an intermediate phenotype compared to *Villin*^{sOVA} and *Villin*^{cOVA} mice, we tested whether tmOVA also is released from epithelial cells. One potential mechanism is exosomal secretion of transmembrane proteins. However, treating mice with exosome inhibitor GW4869(Luberto et al., 2002) had no impact on OT-II division (Fig. 2.10F), arguing against this pathway. Ectodomain shedding is an alternative mechanism that does not require cell death. The tmOVA construct used in our experiments, based on published tmOVA constructs(Joeris et al., 2021; Kurts et al., 1996;

Vezys et al., 2000), retains the ADAM protease cleavage site (Arg100)(Kaup et al., 2002) within the TFR transmembrane stalk (amino acids 1-116 of the full-length 760-aa human TFR). To test whether ectodomain shedding is the responsible mechanism, we overexpressed sOVA, cOVA, or tmOVA in Caco-2 or HEK293T cells and probed the cell lysates with an antibody specific for the N-terminal domain of TFR(Kaup et al., 2002). In tmOVA-expressing cells, TFR antibody detected the expected ~50 kDa full-length tmOVA protein as well as two lower-molecular weight species, one at ~13 kDa, the size of the N-terminal cleavage product, and another at ~25 kDa likely representing its dimer(Kaup et al., 2002) (Fig. 2.2E, Fig. 2.10G). However, in the supernatant of HEK293T cells, much less OVA shed from tmOVA was present relative to sOVA (Fig. 2.10H), indicating that while tmOVA can be shed, sOVA remains the more abundant soluble form.

We next addressed if the subcellular compartment of epithelial OVA influences $CD4^+$ T cell fate at homeostasis and how it compares with the response to dietary OVA. Naïve OT-II cells were simultaneously transferred into C57Bl/6 mice fed OVA via oral gavage and drinking water and into *Villin*^{sOVA}, *Villin*^{cOVA}, and *Villin*^{tmOVA} mice. Cells in the gLNs were analyzed four days later for proliferation and the expression of activation, lineage and anergy markers: CD44 (early activation), FOXP3 (pTreg), TBET (Th1), GATA3 (Th2), RORγt (Th17), PD-1 and CXCR5 (Tfh), and FR4 and CD73 (anergy). Nearly all OT-II cells acquired CD44, indicating that they had encountered cognate antigen (*data not shown*). Of all lineages, only $FOXP3^+$ cells were recovered among OT-II cells at percentages above 2-4%, and the OT-II cells failing to upregulate any lineage-defining transcription factors adopted an anergic phenotype (Fig. 2.2F, and *data not shown*). Oral OVA and sOVA elicited similar percentages of $FOXP3^+$ OT-II cells, with higher induction in small-intestine relative to large-intestine draining LNs (Fig. 2.2F), as previously reported(Esterházy et al., 2019a). By contrast, cOVA and tmOVA induced only about half the

amount of FOXP3^{+} cells (10% of OT-II cells), and this induction was the same across all gLNs. Within a mouse model, the OT-II cell division index inversely correlated with the percentage of FOXP3^{+} OT-II cells (Fig. 2.10I), suggesting that the gradient of pTreg cells between gLNs results in graded T cell suppression of T cell proliferation; differences between mouse models in cell division were most easily explained by antigen availability (Fig. 2.10I, in line with Fig. 2.2B, C). Total OT-II cell numbers reflected this finding also within each OVA delivery model (Fig. 2.10J). However surprisingly OT-II cell counts were not lower in *Villin*^{cOVA} mice compared to OVA fed or *Villin*^{sOVA} and *Villin*^{tmOVA} mice (Fig. 2.10J), illustrating that total cell counts are determined by the combination of antigen availability, suppression of proliferation and potentially other mechanisms not explored here such as deletion. We reasoned that the reduced and regionally uniform pTreg cell induction in cOVA and tmOVA mice relative to OVA-fed and sOVA mice could reflect differences in antigen dose rather than subcellular compartment. To test this hypothesis, we matched the antigen levels by using a dose of tamoxifen in *Villin*^{sOVA} mice that resulted in similar gut OVA protein levels across the OVA lines (Fig. 2.10K) and comparable OT-II cell division following transfer as in *Villin*^{cOVA} mice (compare Fig. 2.10L to Fig. 2.10I or Fig. 2.2C). We also fed less OVA, which reduced OT-II cell division to *Villin*^{cOVA}-like levels (compare Fig. 2.10L to 2.10I or Fig. 2.2C). Under these conditions, pTreg cell induction dropped to ~4-8% of OT-II cells, comparable to *Villin*^{cOVA} and *Villin*^{tmOVA} mice, and was uniform across all gLNs (Fig. 2.2G, compare to Fig. 2.2F).

In sum, we have generated mice that permit the expression of OVA in different subcellular compartments under the control of tissue-specific Cre recombinase of choice. In the context of gut epithelium, the compartment of origin influences antigen availability at steady state, but when

antigen dose is matched, epithelial self-antigens and dietary antigen drive comparable pTreg cell differentiation.

2.3.2 Antigen presentation by RORγt⁺MHC-II⁺ APCs is dispensable for pTreg cell induction and systemic tolerance to gut self-antigens

Two APC subtypes have been implicated as primarily responsible for pTreg cell induction in response to oral antigens: TC IVs, whose ablation or loss of MHC-II expression abolishes pTreg cell generation(Cabric, Parisotto, et al., 2025; L. Fu et al., 2025; Rodrigues et al., 2025), and cDC1s, whose loss, except in very young mice(Cabric, Parisotto, et al., 2025), leads to up to 50% reduction of pTreg cells, in part through a role in pTreg cell maintenance(Cabric, Parisotto, et al., 2025; Esterházy et al., 2016b; Rudnitsky et al., 2025). To assess whether the same APC requirements apply to the differentiation of pTreg cells recognizing self-antigens, we first generated bone marrow chimeras (BMCs) using *MHCII*$^{\Delta Rorc}$ marrow, which lack MHC-II expression on RORγt⁺ cells, including TC IVs. Of note, while *MHCII*$^{\Delta Rorc}$ mice also lack MHC-II expression on ILC3s, other groups have engineered *Rorc* enhancer-knockout mice(Guo et al., 2025; Rodrigues et al., 2025) that formally exclude the contribution of ILC3s to Treg cell induction, as ILC3s are not targeted in these systems. These mice are currently not publicly available. We confirmed that only the targeted APC indeed lacked MHC-II in the mLNs of these mice (Fig. 2.11A-F). Using the same bone marrow donors, we confirmed that pTreg cell induction following oral OVA administration was blunted in all gLNs, irrespective of antigen dose (Fig. 2.3A, B). However, loss of antigen presentation by TC IVs only marginally affected pTreg cell differentiation in high-dose tamoxifen-treated *Villin*^{sOVA} mice, and, if anything, was associated with a slight increase in pTreg frequencies in *Villin*^{cOVA}, *Villin*^{tmOVA} and low-dose tamoxifen-treated *Villin*^{sOVA} mice (Fig. 2.3C-F), suggesting that in these models, TC IVs may exert an indirect

restraint on pTreg cell induction. Across models, proliferation correlated inversely with pTreg cell frequency: proliferation increased following oral OVA and in high-dose tamoxifen-treated *Villin*^{sOVA} mice (Fig. 2.11G-I), which also translated into higher OT-II numbers (*data not shown*). In contrast, proliferation was relatively unaffected in low-dose tamoxifen-treated *Villin*^{sOVA} and *Villin*^{tmOVA} mice and was reduced in *Villin*^{cOVA} mice, the model in which pTreg cell induction increased upon loss of MHC-II expression on RORγt^{+} cells (Fig. 2.11J-L). The increased proliferation was attributable to selective expansion of FOXP3^{-} OT-II cells, which divided in response to oral and high but not low dose self-OVA. FOXP3^{-} OT-II cells divided less in *Villin*^{cOVA} mice in the absence of MHC-II on TC IVs (Fig. 2.12A-F).

Induction of pTreg cells recognizing oral antigens establishes systemic suppression of pro-inflammatory responses to the same antigen, a phenomenon described as oral tolerance. Antigen presentation by TC IVs, being indispensable for the differentiation of oral antigen-specific pTreg cells, is required for oral tolerance(Cabric, Parisotto, et al., 2025; L. Fu et al., 2025; Rodrigues et al., 2025). By contrast, we hypothesized that systemic tolerance to gut self-antigens should be independent of TC IVs, since pTreg cell induction by epithelium-derived OVA was preserved in their absence. To compare the requirement for TCs in oral *versus* self-antigen induced systemic tolerance, we generated BMCs using *MHCII*$^{\Delta Rorgt}$ or *MHCII*$^{fl/fl}$ (WT) bone marrow transferred into either *Villin*^{sOVA} mice that were later tamoxifen-treated, or C57Bl/6 recipients that were later administered oral OVA. All mice were then immunized with Alum-OVA and challenged with intranasal OVA (Fig. 2.3G), and we quantified lung immune cell infiltrates and serum anti-OVA IgE and IgG1 levels. OVA feeding in the absence of antigen presentation by TCs led to increased immune cell infiltrates in the bronchioalveolar lavage fluid (BALF) and lungs and elevated anti-OVA IgE and IgG1 serum concentrations compared WT BM recipients (Fig. 2.3H-O, oral OVA

groups), as reported previously(L. Fu et al., 2025; Rodrigues et al., 2025). In contrast, these parameters remained low in *Villin*^{sOVA} recipients of *MHCII*$^{\Delta Rorgt}$ BM and indistinguishable from WT BM recipients (Fig. 2.3H-O, *Villin*^{sOVA} group), demonstrating that systemic suppression of allergic anti-OVA responses remained intact.

These data show differential APC requirements for inducing pTreg cells specific for oral *versus* gut epithelium-derived self-antigen (Fig. 2.3A-F), which translate into their requirement for systemic tolerance.

2.3.3 BATF3-dependent APCs are required for pTreg cell induction to gut self-antigens

We next sought to determine the contribution of cDC1s to pTreg cell induction in response to self-antigens. To this end, we interbred *Batf3*$^{-/-}$ mice, which are devoid of cDC1s(Hildner et al., 2008b) (Fig. 2.11A-F), with our *Villin*^{OVA} lines, adoptively transferred OT-II cells and analyzed their fate in the gLNs in comparison to heterozygous littermates. Ablation of cDC1 completely prevented OT-II proliferation and expansion in *Villin*^{cOVA} mice, but only partially impaired proliferation in *Villin*^{sOVA} and *Villin*^{tmOVA} mice (Fig. 2.4A), which led to OT-II cell numbers only being notably affected in this model (Fig. 2.4D). As anticipated, the small fraction of T-BET^{+} cells observed at homeostasis was reduced in *Batf3*$^{-/-}$ compared to WT mice across all OVA models (Fig. 2.4B). Consistent with previous reports(Cabric, Parisotto, et al., 2025; Esterházy et al., 2016b; Rudnitsky et al., 2025), we confirmed that pTreg OT-II cells were partially reduced in OVA fed *Batf3*$^{-/-}$ mice (Fig. 2.4C). By contrast, FOXP3^{+} OT-II cells were reduced by 50-75% in high-dose tamoxifen-treated *Villin*^{sOVA} and *Villin*^{tmOVA} mice (Fig. 2.4C) and were almost absent in low-dose tamoxifen-treated *Villin*^{sOVA} mice (Fig. 2.4E). Again, cell division, when affected, was decreased in the FOXP3^{+} and increased in the FOXP3^{-} compartment (Fig. 2.12G, H). These data suggest that presentation of cytosolic antigen is strictly dependent on cDC1s, while secreted

antigens are accessed by additional APC subsets. Moreover, unlike luminal, foreign antigens, which rely primarily on presentation by TCs for pTreg cell induction, epithelial self-antigens induce pTreg cells predominantly via cDC1s, with TCs contributing only under conditions of high antigen abundance.

2.3.4 Intestinal viral infection similarly alters epithelial self- and oral antigen-specific T cell fate

We next predicted that adverse immune outcomes dependent on cDC1s would be similar when stimulated by oral OVA or any *Villin*^{OVA} derived antigen. Since cDC1s are critical for inducing antiviral Th1 cells and cytotoxic CD8$^+$ T (T_{cyt}) cells, we first tested if infection with reovirus T1L(Bouziat et al., 2017; H. Brown et al., 2023a; Medina Sanchez et al., 2023) would induce ectopic OVA-specific T-BET$^+$ Th1 and T_{cyt} cells and concomitantly reduce FOXP3$^+$ Treg cells equivalently when the antigen was dietary and gut epithelium derived.

Indeed, following OT-II transfer into mice fed OVA or all three *Villin*^{OVA} lines, T1L infection induced comparable percentages of T-BET$^+$ OT-II cells and reduced FOXP3$^+$ OT-II cells across all gLNs relative to vehicle controls (Fig. 2.5A-D). Similarly, naïve OVA-specific CD8$^+$ T (OT-I) cells became cytotoxic in the gLNs of all groups after T1L infection, as assessed by the robust emergence of granzyme B (GzmB)$^+$ and interferon γ (IFNγ)$^+$ OT-I cells (Fig. 2.13A-D). An increase in OVA-specific T_{cyt} and Th1 cells, accompanied by a decrease in Treg cells, was detected within the endogenous repertoire using OVA tetramers (Fig. 2.5E-I, Fig. 2.13E, F), indicating that this response also occurred in the endogenous T cell pool. Using *Villin*^{sOVA} crossed to *Batf3*$^{-/-}$ mice, we verified that the observed T-BET induction in OT-II cells and GzmB and IFNγ in OT-I cells was dependent on cDC1s (Fig. 2.14A, B).

Thus, gastrointestinal viral infection leads to similar pro-inflammatory type 1 T cell responses to oral and gut-self antigens in the gLNs. This finding also confirms that oral and self-antigens from any compartment are efficiently presented by cDC1s.

2.3.5 Intestinal viral infection drives pro-inflammatory T cell infiltration of the gut and comparable tissue damage upon oral and self-antigen recognition

We next determined whether the adverse T cell responses to dietary and self-OVA observed in gLNs following T1L infection translated into the T cell landscape in gut tissue, and if so, whether these responses contributed to gut pathology. OT-I and OT-II cells were adoptively transferred at the time of T1L inoculation, and their abundance and phenotype in the small and large intestine analyzed 7 days later. We used *Villin*^{sOVA} mice as a representative for self-antigen, while dietary antigen recognition was modeled by continuous OVA feeding. In both cases, T1L infection led to a higher abundance of OT-I and OT-II cells (Fig. 2.14C, D), increased GzmB^{+} OT-I cells and T-BET^{+} OT-II cells, and reduced FOXP3^{+} cells in T1L-infected mice than in vehicle controls (Fig. 2.6A-C, Fig. 2.14E). Gut tissue destruction by T cells requires both effector T cell infiltration and local inflammatory cues. T1L alone does not lead to sufficient local inflammation to elicit overt pathology(Bouziat et al., 2017; J. J. Brown et al., 2018), likely because viral clearance precedes the return of effector T cells to the gut. However, in the presence of local IL-15, T1L infection can elicit gluten-specific T cells to mediate tissue destruction(Abadie et al., 2020; Bouziat et al., 2017). To test whether T1L-induced OVA-specific Th1 and T_{cyt} cells similarly exacerbate tissue pathology, we administrated indomethacin, a non-steroidal anti-inflammatory drug that induces local gut injury(Nadatani et al., 2019) to mice fed OVA, *Villin*^{sOVA} or *Villin*^{cOVA} mice 10 days after T1L inoculation and OVA-specific T cell transfer (Fig. 2.6D). Indomethacin alone caused few mucosal lesions, regardless of whether the transferred T cells encountered

cognate antigen or not (Fig. 2.6E, F). However, if the mice had been inoculated with T1L 10 days prior to indomethacin commencement, the gut of infected mice displayed two to three times as many lesions and was shortened (Fig. 2.6E-H), with the effects slightly stronger in OVA-fed and *Villin*^{sOVA} than *Villin*^{cOVA} mice, correlating with the lower antigen dose and slightly lower number of Th1 cells induced in this latter model (see Fig. 2.5B). The exacerbated gut pathology occurred in an antigen-specific manner, since T1L failed to aggravate indomethacin-induced pathology in the absence of OVA, even after transfer of OVA-specific T cells (Fig. 2.6E-H, no OVA group). These results demonstrate that the comparable induction of antigen-specific Th1 and T_{cyt} cells upon oral versus self-antigen in the gLNs translate into similar, antigen-driven gut pathology.

2.3.6 Secreted but not cytosolic self-antigen induces Th2 cells in response to helminth infection in a cDC2-dependent manner

We next speculated that secreted antigen, like oral antigen(Canesso et al., 2025), would be presented by the other major APCs in gLNs, cDC2s. cDC2s have several subtypes(C. C. Brown et al., 2019; Minutti et al., 2024). In the gut, *Klf4*-dependent cDC2Bs are required for in response to allergens and helminths(Tussiwand et al., 2015), while *Notch2*-dependent cDC2As respond to bacteria and fungi and their absence leads to a loss of Th17/22 cells(Satpathy et al., 2013). Thus, GATA3 and RORγt induction in CD4 T cells mark cDC2B- and cDC2A-mediated presentation, respectively. We therefore inoculated mice with *S. venezuelensis*, a strong Th2-inducing helminth, and examined OT-II fate in *Villin*^{OVA} lines. Notably, dietary OVA does not elicit an interaction between Th2-inducing cDC2s and T cells(Canesso et al., 2025). However, when OVA came from the epithelium, over 20% of transferred cells became GATA3^{+} in the gLNs draining the upper small intestine, the site of helminth infection, in *Villin*^{sOVA} and *Villin*^{tmOVA} mice (Fig. 2.7A, B). Analogous to the response to oral antigen, relative frequencies but not total numbers of FOXP3^{+}

OT-II cells were diminished in those LNs (Fig. 2.7A, C-E), likely due to the relative but not absolute exclusion of cDC1s from the gut in the context of *S. venezuelensis(Canesso et al., 2025)*. As expected, OT-II cells in *Villin*^{cOVA} mice remained unaffected (Fig. 2.7A-C), consistent with the conclusion that presentation of cytosolic self-antigen is primarily dependent on cDC1s. To further validate that secreted but not cytosolic self-OVA is presented by cDC2s, we ablated this lineage using *Zeb2* enhancer-knockout (*Zeb2*$^{\Delta 1+2+3}$) mice(Canesso et al., 2025; T. T. Liu et al., 2022), in which cDC2s are reduced by over 80% (Fig. 2.11A, C, E). The loss of cDC2s did not impact the low levels of GATA3^{+} OT-II or the FOXP3^{+} cells in the gLNs at homeostasis (Fig. 2.15A, B). However, during *S. venezuelensis* infection, *Zeb2*$^{\Delta 1+2+3}$ mice interbred with *Villin*^{sOVA} and *Villin*^{tmOVA} mice displayed a blunted OVA-specific Th2 response (Fig. 2.7A, B). The blunted Th2 response also was associated with restored relative pTreg cell induction (Fig. 2.7C) and even an increase in their total numbers (Fig. 2.7E), indicating that cDC1s remain competent to drive tolerance when antigen access is preserved, even during helminth infection. Finally, *S. venezuelensis* also induced a Tfh response in *Villin*^{sOVA} mice, which was reversed in *Zeb2*$^{\Delta 1+2+3}$ mice interbred with *Villin*^{sOVA} mice (Fig. 2.15C-E), demonstrating Tfh cells in this setting are equally dependent on cDC2s.

We next tested whether secreted but not cytosolic self-antigens are capable of inducing RORγt^{+} CD4 T cells, a fate endowed by cDC2As and observed in the context of luminally-sourced OVA(Esterházy et al., 2019a). Following infection with *C. rodentium*, a colonic pathogen, the frequency of RORγt^{+} OT-II cells increased and that of FOXP3^{+} decreased in the ceco-colonic LN of *Villin*^{sOVA}, mirroring responses to oral OVA(Esterházy et al., 2019a), but not *Villin*^{cOVA} mice (Fig. 2.15F, G). *Zeb2*$^{\Delta 1+2+3}$ mice succumbed to *C. rodentium* infection by day 8 post infection (Fig.

2.15H), preventing direct assessment of cDC2s in the induction of RORγt$^+$ CD4 T cells, but highlighting their critical role in the response to this pathogen.

Collectively, these findings indicate that secreted but not cytosolic self-antigen from the gut epithelium is presented by cDC2 subsets capable of polarizing CD4 T cells towards GATA3$^+$, RORγt$^+$ or Tfh cell fates following pathogen infection. This response contrasts with that elicited by dietary antigen, which fails to induce GATA3$^+$ T cells during helminth infection(Canesso et al., 2025; Esterházy et al., 2019a) but is capable of inducing RORγt$^+$ cells.

2.3.7 Helminth infection triggers breakdown of tolerance and anaphylaxis in response to secreted but not cytosolic gut-self antigen or dietary antigen

Finally, we assessed whether the induction of Th2 cells recognizing secreted but not cytosolic self-antigen or oral antigen by *S. venezuelensis* leads to differential susceptibility to systemic allergic responses, such as elevated levels of allergic IgE and IgG1 antibodies and anaphylaxis. We exposed mice continuously to OVA either by gavage and drinking water or administration of tamoxifen to *Villin^{sOVA}* or *Villin^{cOVA}* mice starting from the peak of infection (day 5 post-inoculation). We compared serum anti-OVA IgE and IgG1 titers and systemic anaphylaxis (drop in body temperature and survival) following intraperitoneal OVA challenge. Uninfected mice served as controls, and the experiments were conducted both with and without OT-II transfer at the time of OVA exposure (Fig. 2.8A). Of all groups, only *Villin^{sOVA}* mice infected with *S. venezuelensis* developed signs of anaphylaxis, manifested by a decrease in body temperature of 4°C within 30 min (Fig. 2.8B, Fig. 2.15I), markedly reduced survival (Fig. 2.8C), and an increase in anti-OVA IgG1 and IgE levels from almost non-detectible to levels comparable to Alum immunization(Esterházy et al., 2016b; L. Fu et al., 2025) (Fig. 2.8D, E). OT-II transfer produced a more severe phenotype (Fig. 2.8B-E), but these cells were not required, indicating that

endogenous OVA-reactive $CD4^+$ T cells were sufficient. Finally, since anaphylaxis is IgE-mediated and IgE class switching largely depends on Th2 cells, we asked whether these two responses to *S.venezuelensis* infection are dependent on cDC2s. In WT mice, *S.venezuelensis* led to a strong polyclonal Th2 response in the duodenal LNs and high total IgE titers. These responses where abrogated in $Zeb2^{\Delta 1+2+3}$ mice (Fig. 2.8F, G).

In conclusion, these experiments demonstrate that the Th2 response to secreted, but not cytosolic or oral antigen, results in a unique susceptibility to allergic reactions.

2.4 Discussion

In this study, we discovered that gut-derived antigens elicit different T cell fates depending on the compartment from which they originate, whether luminal (dietary and presumably bacterial) or epithelial, and if epithelial, whether secreted or cytosolic. We found that each antigen source has different APC requirements for stimulating T cell responses, which leads to corresponding disease susceptibilities. Finally, by engineering Cre-inducible *OVA*-expressing mice, we developed new tools that will allow definition of the rules governing tissue-specific autoimmunity *versus* self-tolerance beyond the gut (Fig. 2.2A).

Our findings have major implications for understanding the general principles dictating T cell fate decisions in the gut and the potential contribution of autoimmunity to gastrointestinal diseases. The default T cell fate in the gut is Treg differentiation, with reprogramming to pro-inflammatory lineages occurring only when adjuvants or infections alter the APC profile. This mechanism likely evolved to prevent adverse reactions to food and commensal microbes while preserving host defense against pathogens or symbionts that breach the intestinal barrier, a paradigm supported by our findings. However, while responses to a single antigen like dietary

OVA can be pleiotropic, and OVA-specific T cells interact with many APC subtypes when OVA is a dietary antigen(Canesso et al., 2025), we found that differential antigen access by distinct APCs is another critical and previously underappreciated determinant of T cell polarization. This became evident especially upon perturbations, where the immune system deviates from the pTreg cell default. Thus, the logic for predicting T cell fate is not simply determined by which adjuvants ("signal 3") are present but also dictated by the dominant APC subset with access to the given antigen.

This mechanism connects to another key concept from our study: access to an antigen is determined by antigen biology- whether it is cytosolic and accessible only following cell death, secreted and readily available, and, while not formally tested in our study, potentially whether it is intact or partially degraded, or more apical or basolateral. Each type of antigen may be preferentially sampled by different APC subset repertoire, thereby shaping the ensuing T cell responses. Whether antigen access is regulated by anatomical location of the antigen relative to an APC or by cargo-selective endocytic machineries remains to be determined. While we observed this phenomenon using self-antigens, it is likely that the same rules apply to bacterial and dietary antigens that directly interact with the epithelium, such that these antigens can behave like intracellular or secreted OVA rather than like luminal antigens. For T cell responses to bacteria, which appear to be diverse even when elicited by commensals, this mechanism suggests that in addition to the adjuvant provided by a given bacterial strain, the nature of the bacterial interaction with the epithelium and consequently the APC that presents the antigen contributes to determining the dominant T cell fate in response to that strain. Finally, these concepts of APC access and antigen biology contributing to shaping the nature of the T cell response also likely apply to other

tissues, particularly those at barrier sites such as the lung and skin that also regularly encounter foreign antigens.

Another striking discovery made in our experiments is that even baseline pTreg cell induction is not universally dependent on one APC subtype. Instead, the main APC required for pTreg cell induction varies with antigen source. TCs are strictly required for developing pTreg cells that recognize dietary and commensal bacterial antigens(Cabric, Parisotto, et al., 2025; L. Fu et al., 2025; Rodrigues et al., 2025). However, this is not the case for pTreg cells recognizing self-antigens, for which antigen presentation by TCs plays a minor role, contributing only when secretory antigen is highly abundant (Fig. 2.3C). This finding suggests that TCs have access to luminal antigens in a manner that does not extend to self-antigens. TCs are thought to be largely LN-resident, and therefore likely acquire antigens *in situ* rather than by migration from the gut. It is possible that their exposure to dietary and bacterial antigens, which are at least partially digested, occurs through delivery in acellular lymph, whereas secreted self-antigens may only spill into this compartment once the antigen-loading capacity of gut cDCs is saturated. Conversely, such a dual-antigen access system for pTreg cell induction may in itself support the tolerogenic default to dietary and benign commensal antigens by also enabling a temporally controlled dominance of tolerance: Postprandial lymph and lymph-borne antigens reach the LNs within 30-60 min after ingestion, while DC migration can take up to 24 h. Future research on the role of digestive enzyme-mediated antigen preprocessing, as well as antigen state and concentration in lymph, will be required to test these hypotheses. Similarly, how pTreg cell induction by TCs is suppressed in the context of infections remains unresolved. In addition to the potential reprogramming of TCs, our data suggest that antigen could alternatively be diverted to migratory DCs in such contexts (Fig. 2.5), but this idea also requires additional experimental confirmation. Finally, these rules may

differ for pTreg cell induction outside the gut, where antigen processing by digestive enzymes is absent and lymph production and flow rates are lower.

Our data also imply that gut-self recognizing Th1/T_{cyt} cells contribute to autoimmune gut pathology more than previously appreciated. *Bona fide* gut autoimmunity may in fact be underrecognized, as self-reactivity is not routinely monitored and the rapid turnover of intestinal epithelial cells may obscure its detection, particularly in the context of inflammatory bowel disease or immune checkpoint inhibitor-induced colitis. In both settings, it remains unclear whether pathology is primarily driven by pro-inflammatory T cell responses directed against the microbiota(Rojas et al., 2018)or self-antigens.

While such self-recognizing Th1/T_{cyt} cells in the gut may be detrimental in the presence of pro-inflammatory cues such as tissue damage, these cells could provide a beneficial first line of defense against a previously unencountered type 1-inducing pathogen through the secretion of inflammatory cytokines. Similarly, secreted self-antigen-elicited Th2 cells could contribute to type 2 responses in the gut. Analogous to control of Th1/T_{cyt} cells, there likely are mechanisms to ensure that such cells do not cause damage in the absence of local gut insults. Nonetheless, it is conceivable that the persistence of these cells has been evolutionarily favored to allow rapid reinvigoration during new type 2-inducing infections. Experimentally dissecting these potentially beneficial gut self-recognizing T helper cells is another important future direction.

The findings made here challenge paradigms of how pTreg cell induction is governed in the gut and offer a unifying framework to explain how different T cell fates arise in response to intestinal antigens. Our work places self-antigens into the broader context of gut antigen recognition and establishes a universal system to study autoantigens in tissue-specific immunity.

2.5 Limitations of the study

Most of our experiments rely on a single antigen, OVA, and cognate T cell clones, OT-I and OT-II cells. While we do report the phenomenon of pTreg cell induction also holds true in the polyclonal OVA reactive T cell pool, we cannot evaluate what fraction of Treg cells in the gut is self-reactive and generated through the peripheral mechanisms described in this study rather than in the thymus. Epithelial cells are heterogeneous, and Vil^{Cre} drives *OVA* expression in all subtypes, making it unclear which epithelial population drives the observed phenotypes. APC access to OVA from different sources is inferred indirectly through the impact of APC subtype loss or lack of presentation via MHC-II on T cell fates known to depend on each APC type. We only show that antigen presentation by TCs is not required for the generation of self-reactive pTreg cells, but do not formally rule out the possibility that TCs contribute to this process through other mechanisms. Though it is likely only TC IVs among all cell types targeted in $MHCII^{\Delta Rorgt}$ mice are also responsible for the small contribution to pTreg cell induction in the situation of high dose secreted self OVA, we cannot formally exclude other cells affected contribute too. Conversely, depleting cDC1s or cDC2s altogether does not permit us to resolve whether it is the loss of their antigen presentation capacity or another function such as cytokine secretion *in trans* that leads to defective T cell polarization in their absence.

2.6 Figures and figure legends

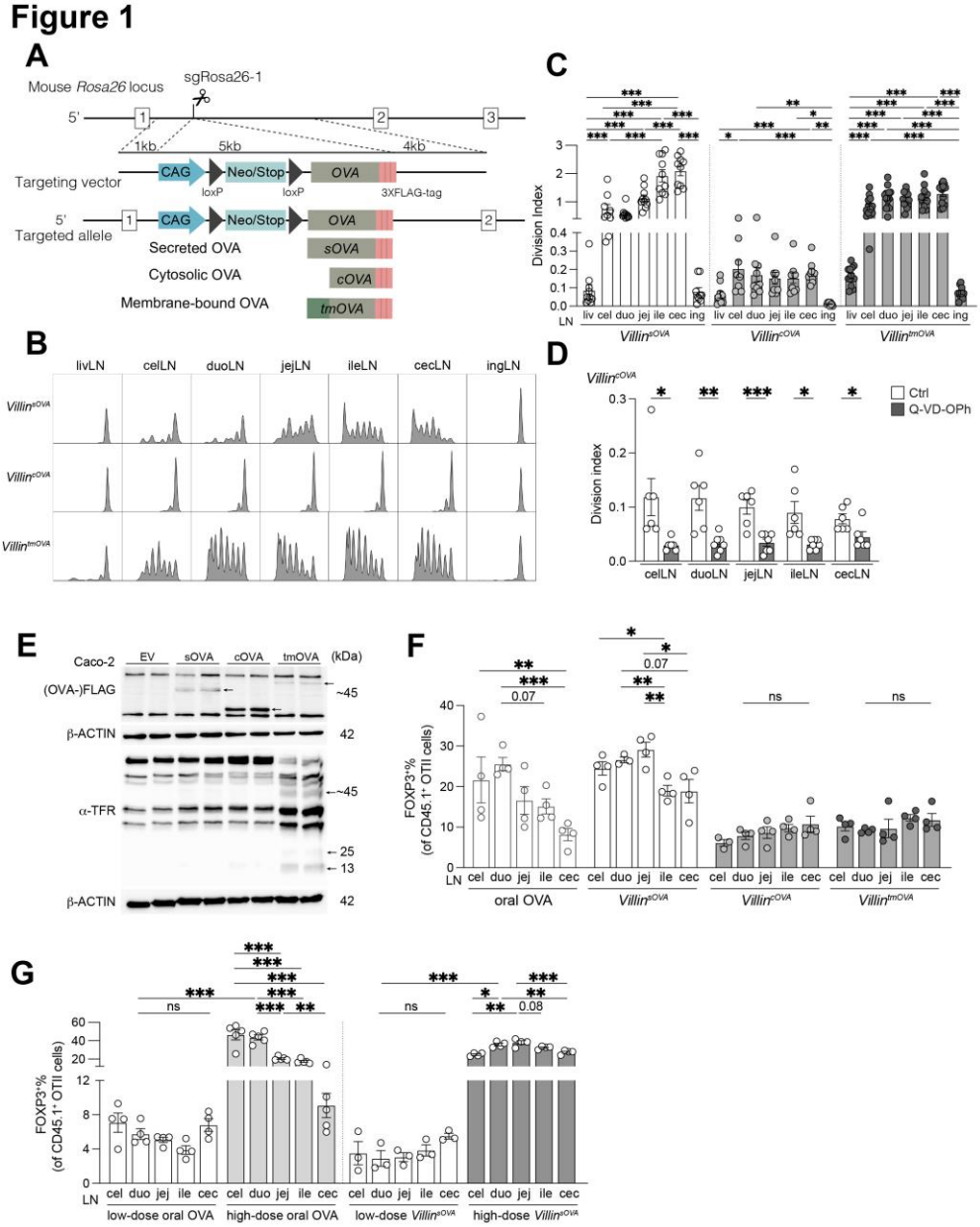


Figure 2.2 Generation and characterization of mice expressing OVA in different subcellular epithelial cell compartments.
A. Scheme of transgenic mouse generation. Targeted allele with the indicated transgene was inserted into the *Rosa26* locus using CRISPR/Cas9. **B-C**. CFSE dilution flow plots (**B**) and division index (**C**) of OT-II cells in the indicated LNs 96 h after transfer into *Villin*^{sOVA}, *Villin*^{cOVA} or *Villin*^{tmOVA} mice (n = 10-16 per group). **D**. Division index of OT-II cells 96 h after transfer into *Villin*^{cOVA} mice treated with pan-caspase inhibitor Q-VD-OPh (n = 6 per group). **E**. Western blot of cell lysates of Caco-2 cells transduced with lentivirus encoding empty vector, *sOVA*, *cOVA* or *tmOVA* blotted using antibodies against FLAG, α-TFR and β-ACTIN. Arrows indicate OVA signals. **F**. Frequencies of FOXP3$^+$ among total OT-II cells in the indicated LNs 96 h after transfer into mice fed OVA or *Villin*^{sOVA}, *Villin*^{cOVA} and *Villin*^{tmOVA} mice (n = 4 per group, as indicated by symbols). **G**. Frequencies of FOXP3$^+$ among total OT-II cells in the indicated LNs 96 h after transfer into mice fed high- or low-dose OVA or mice with high or low expression of sOVA (n = 4-5 per group, as indicated by symbols). Data are pooled from two or three independent experiments in C, D. Data are representative of two independent experiments in F, G. * p<0.05, ** p<0.01, *** p<0.001 by one-way ANOVA and t-test.

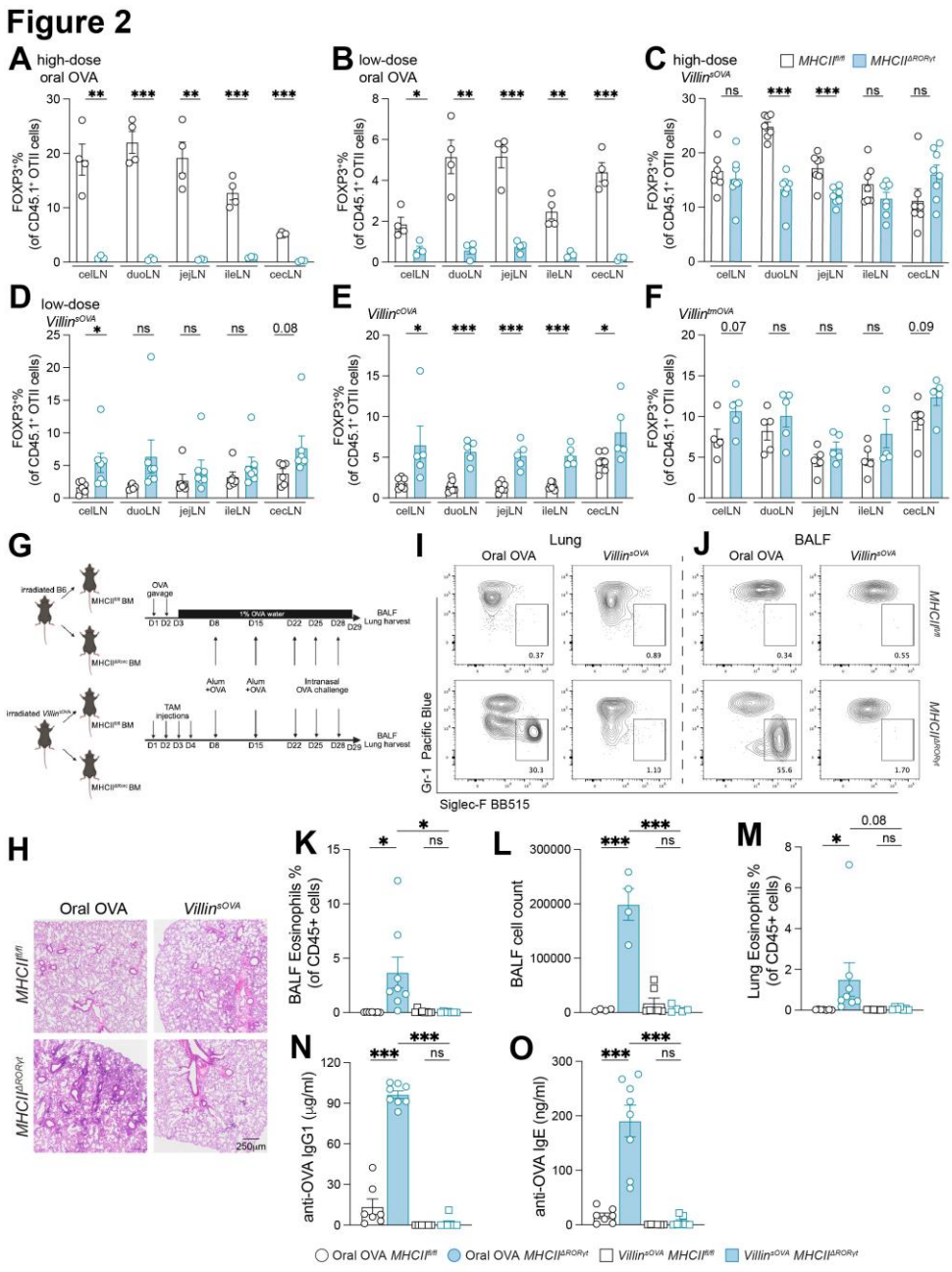


Figure 2.3 Antigen presentation by RORγt$^+$MHC-II$^+$ APCs is dispensable for pTreg cell induction and systemic tolerance to gut self-antigens.

A-F. Frequencies of FOXP3$^+$ among total OT-II cells in the indicated LNs 96 h after transfer into BMC receiving *MHCII$^{fl/fl}$* or *MHCII$^{\Delta ROR\gamma t}$* BM fed high-dose (**A**) or low-dose OVA (**B**), or mice expressing high-dose sOVA (**C**), low-dose sOVA (**D**), cOVA (**E**) and tmOVA (**F**) in the epithelium. **G**. Experimental scheme for the establishment of tolerance to alum-mediated immunity. **H**. H&E staining of lung tissue from BMC receiving *MHCII$^{fl/fl}$* or *MHCII$^{\Delta ROR\gamma t}$* BM fed high-dose OVA or expressing sOVA in the epithelium. The scale bar represents 250 μm. **I-M**. Flow plots of CD45$^+$SSC^{hi}MHCII$^-$CD11b$^+$Ly6G^{int} cells in lung (**I**) and BALF (**J**) from mice in **H**. Frequency (**K**) and total number (**L**) of SiglecF$^+$Gr-1$^-$ cells (eosinophils) among total CD45$^+$ cells in BALF and frequency of eosinophils in lung tissue (**M**) of mice in **H**. **N-O**. Serum concentration of OVA-specific IgG1 (**N**) and IgE (**O**) in mice in **H**. Data are pooled from two independent experiments in I-O (n = 6-8 per group, as indicated by symbols). Data represent one experiment in A-F (n = 3-7 per group, as indicated by symbols). * p<0.05, ** p<0.01, *** p<0.001 by t-test.

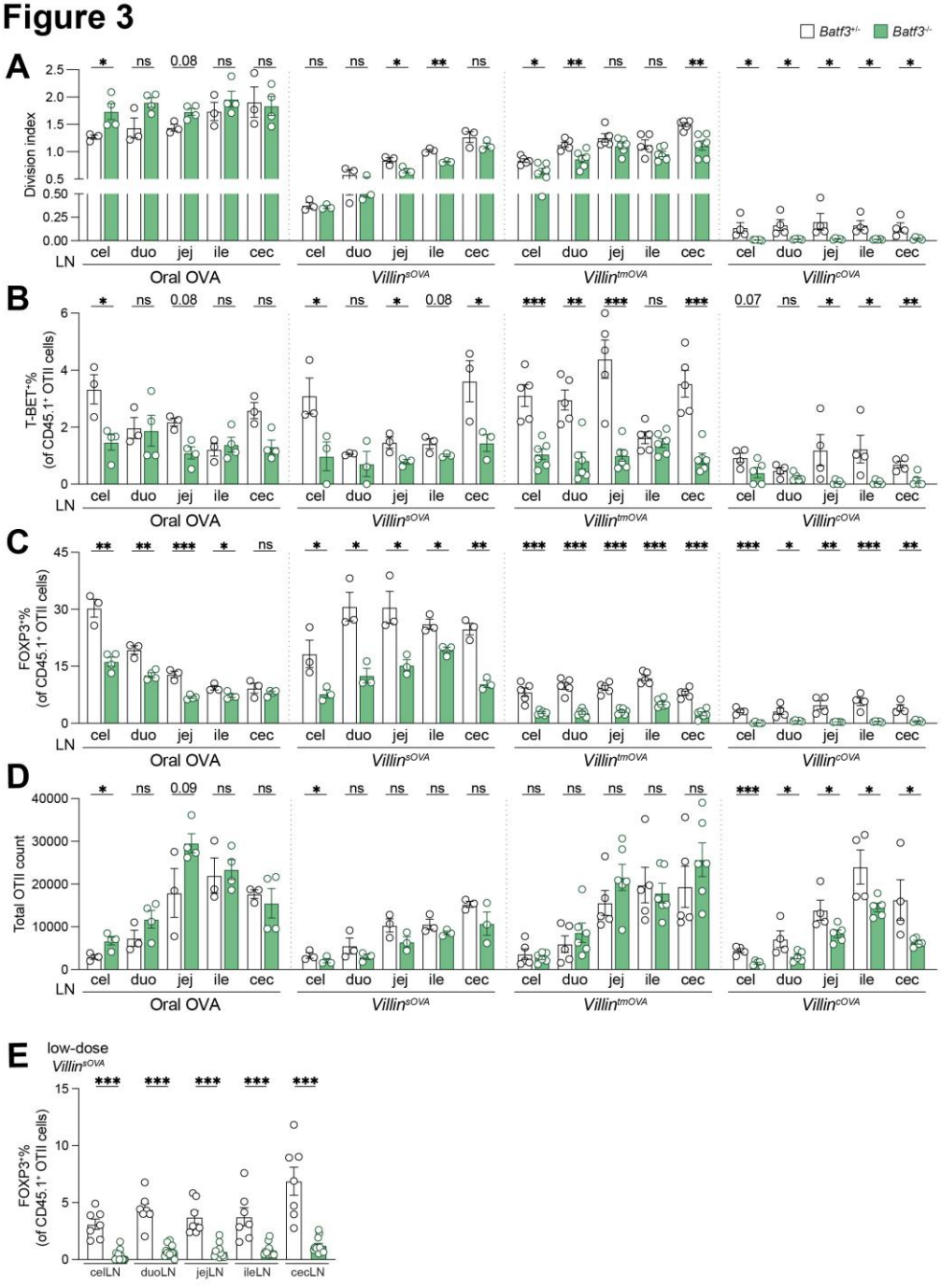


Figure 2.4 BATF3-dependent APCs are required for pTreg cell induction to gut self-antigens.
A. Division index of OT-II cells 96 h after transfer into high-dose OVA-fed, *Villin*^{sOVA}, *Villin*^{tmOVA} or *Villin*^{cOVA} mice that are *Batf3*-proficient or -deficient. **B-D**. Frequencies of T-BET$^+$ (**B**), FOXP3$^+$ (**C**) among total OT-II cells and total OT-II number (**D**) in the indicated LNs 96 h after transfer into *Batf3*-proficient or -deficient mice expressing sOVA, tmOVA or cOVA in the epithelium or fed high-dose OVA (n = 3-7 per group, as indicated by symbols). **D**. Frequencies of FOXP3$^+$ among total OT-II cells in the indicated LNs 96 h after transfer into *Batf3*-proficient or -deficient mice expressing low-dose sOVA (n = 7-9 per group, as indicated by symbols). Data are representative of two independent experiments in A-E. * p<0.05, ** p<0.01, *** p<0.001 by t-test.

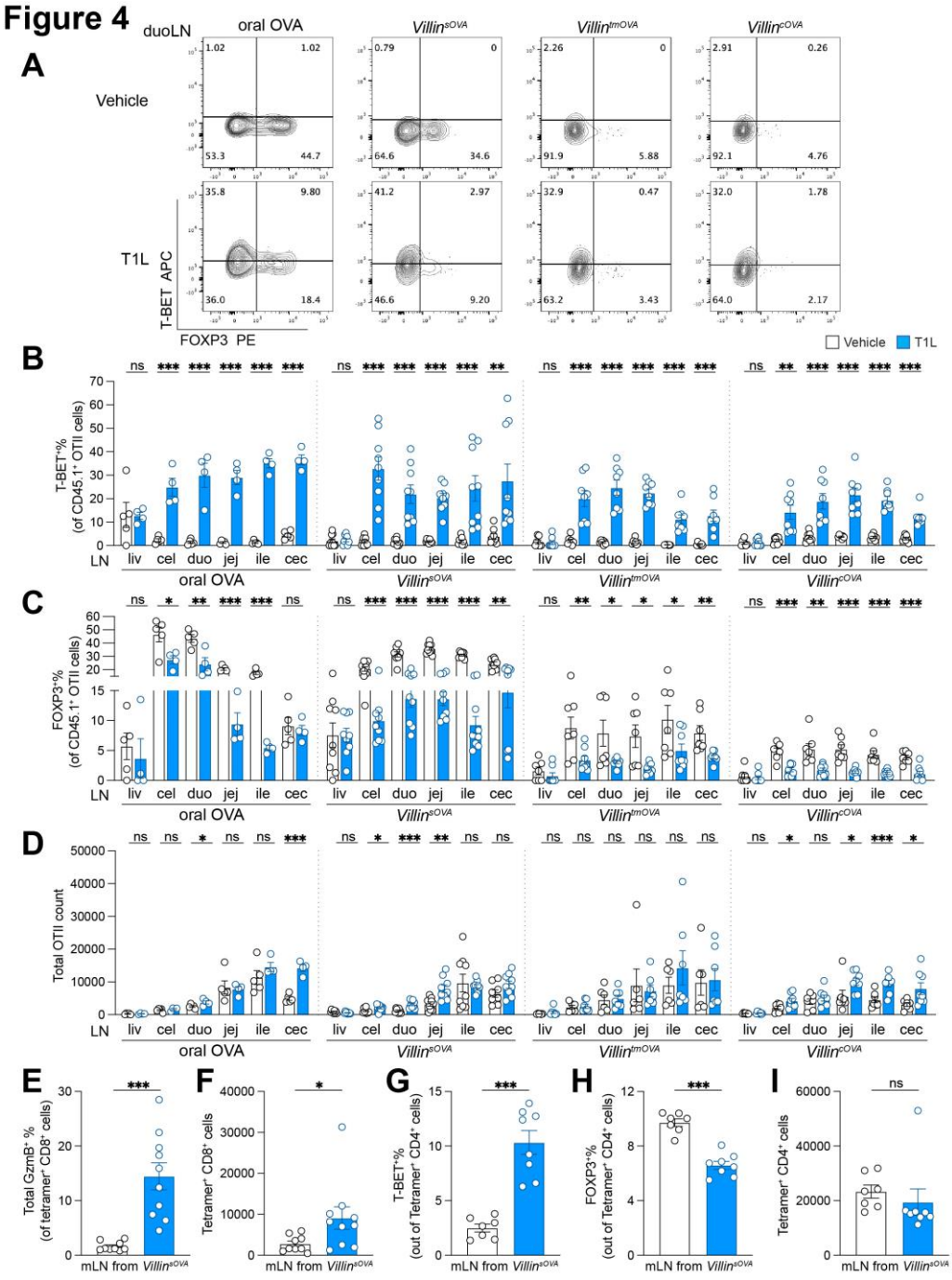


Figure 2.5 Intestinal viral infection impacts epithelial self-antigen and oral antigen-specific T cell fate similarly.
A. Flow plots of OT-II cells in duodenal LNs of T1L- or vehicle-infected mice that were fed high-dose OVA or express sOVA, tmOVA or cOVA in the epithelium. **B-D.** Frequencies of T-BET$^+$ (**B**) or FOXP3$^+$ (**C**) among total OT-II cells and total OT-II numbers (**D**) in the indicated LNs 72 h after transfer into T1L- or vehicle-infected mice that were fed high-dose OVA or express sOVA, tmOVA or cOVA in the epithelium (n = 4-9 per group, as indicated by symbols). **E-F.** Frequencies of GzmB$^+$ among total OVA-tetramer$^+$CD8$^+$ T cells (**E**) and total numbers of OVA-tetramer$^+$CD8$^+$ T cells (**F**) in the mLNs of T1L- or vehicle-infected *Villin^{sOVA}* mice (n = 9-10 per group, as indicated by symbols). **G-I.** Frequencies of T-BET$^+$ (**G**) or FOXP3$^+$ (**H**) among total OVA-tetramer$^+$ CD4$^+$ T cells and total numbers of OVA-tetramer$^+$CD4$^+$ T cells (**I**) in the mLNs of T1L- or vehicle-infected *Villin^{sOVA}* mice (n = 7-8 per group, as indicated by symbols). Data are pooled from two independent experiments in B-I. * p<0.05, ** p<0.01, *** p<0.001 by t-test.

Figure 5

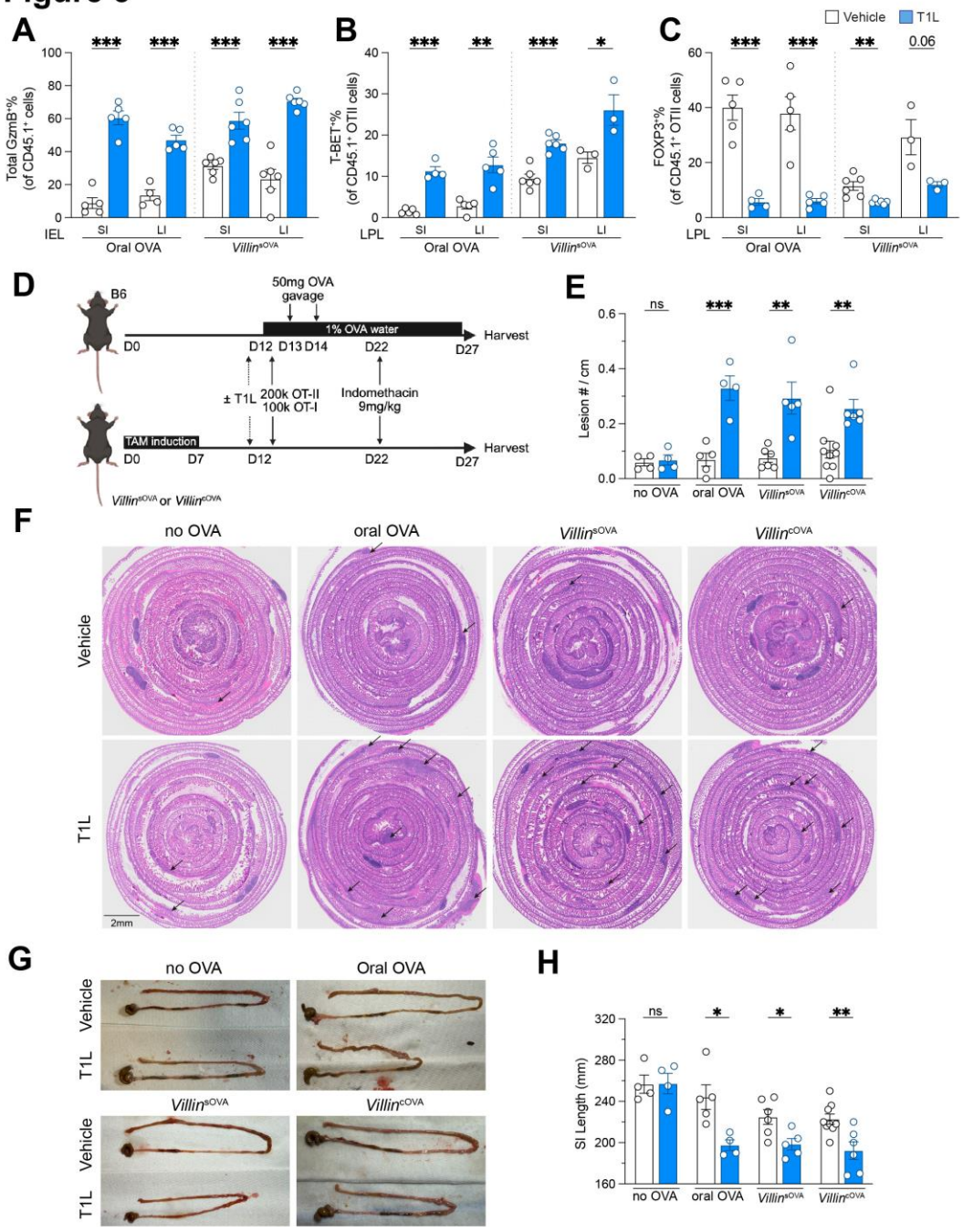


Figure 2.6 Intestinal viral infection leads to comparable pro-inflammatory T cell infiltration and tissue damage following oral and self-antigen recognition.

A-C. Frequencies of GzmB$^+$ among total OT-I cells (**A**) in the IEL fraction or T-BET$^+$ (**B**) or FOXP3$^+$ (**C**) among total OT-II cells in the LPL fraction of the gut tissue of T1L- or vehicle-infected mice that were either fed high-dose OVA or express sOVA in the epithelium (n = 3-6 per group, as indicated by symbols). **D**. Experimental scheme of small intestine damage model. **E**. Lesion number per cm of gut length in each indicated treatment group (n = 4-9 per group, as indicated by symbols). **F**. Representative H&E staining of small intestine Swiss roll from each indicated treatment group. The scale bar represents 2 mm. **G**. Representative pictures of small intestines from each indicated treatment group. **H**. Small intestine length of each indicated treatment group (n = 4-9 per group, as indicated by symbols). Data are pooled from two independent experiments in A-C. Data represent one experiment in E, H. * p<0.05, ** p<0.01, *** p<0.001 by t-test.

Figure 6

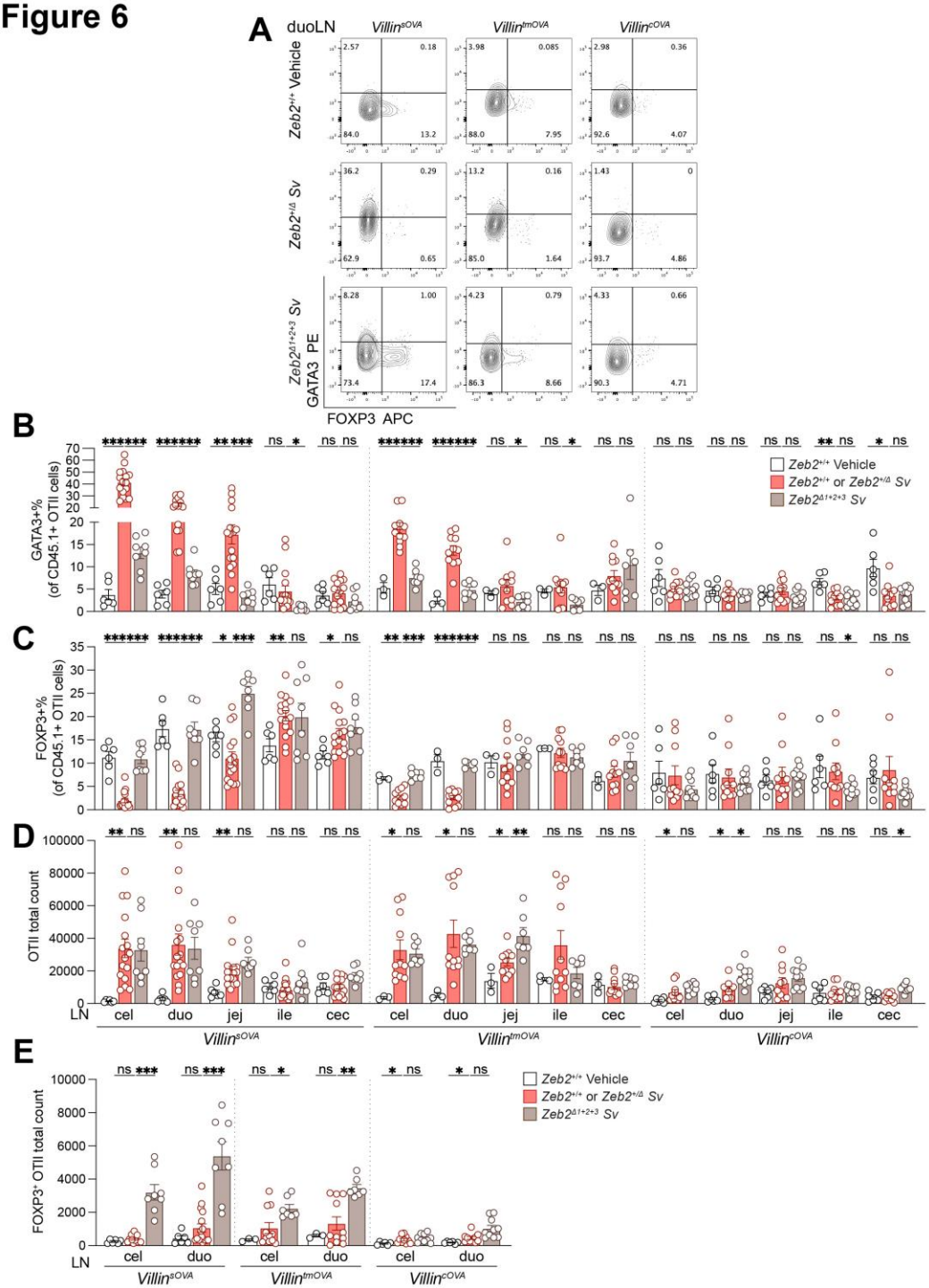


Figure 2.7 Secreted but not cytosolic self-antigens induce Th2 cells in response to helminth infection in a cDC2-dependent manner. **A.** Flow plots of OT-II cells in duodenal LNs of OVA-expressing mice with the indicated genotypes and *S. venezuelensis* infection status. **B-D.** Frequencies of GATA3$^+$ (**B**) or FOXP3$^+$ (**C**) among total OT-II cells and total OT-II numbers (**D**) 72 h after transfer into non-infected WT, *S. venezuelensis*-infected WT or *S. venezuelensis*-infected *Zeb2* enhancer-knockout mice expressing sOVA, cOVA or tmOVA (n = 6-15 per group, as indicated by symbols). **E**. Total FOXP3$^+$ OT-II cell numbers in the indicated LNs of mice in **B-D**. Data are pooled from four independent experiments in B-E. * p<0.05, ** p<0.01, *** p<0.001 by t-test.

Figure 7

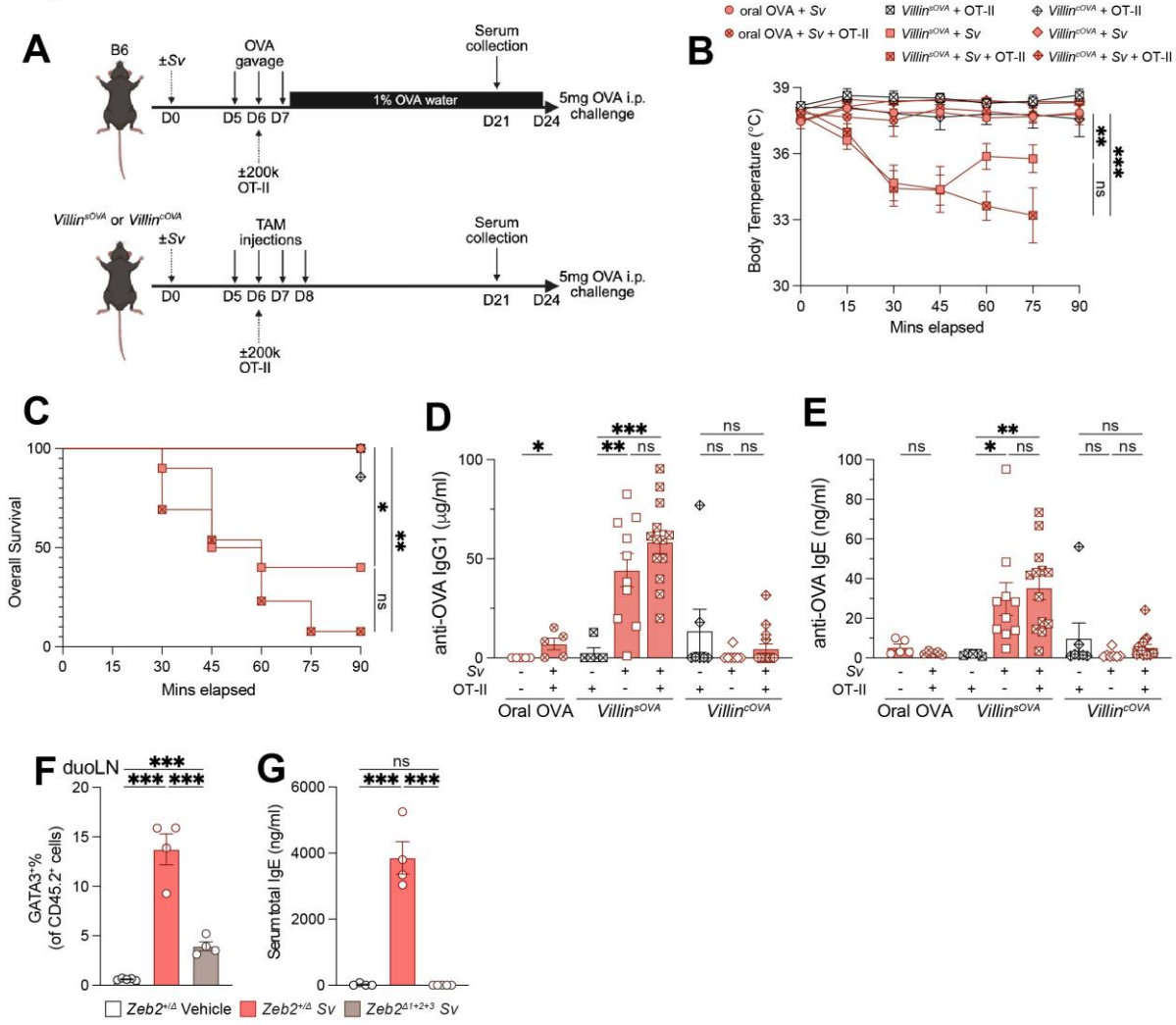


Figure 2.8 Helminth infection triggers breakdown in tolerance and anaphylaxis in response to secreted but not cytosolic gut self-antigen or dietary antigen.

A. Experimental scheme for systemic anaphylaxis model. **B**. Body temperature measurements of indicated groups every 15 min post 5 mg i.p. OVA challenge. **C**. Anaphylaxis as measured by survival of mice at the indicated times after 5 mg i.p. OVA challenge. **D-E**. Serum concentration of OVA-specific IgG1 (**D**) and IgE (**E**) in mice as in **A**. **F**. Frequencies of GATA3$^+$ cells among total CD4$^+$ T cells in duodenal LNs of non-infected *Zeb2*$^{+/\Delta}$, *S. venezuelensis*-infected *Zeb2*$^{+/\Delta}$ or *S. venezuelensis*-infected *Zeb2*$^{\Delta 1+2+3}$ mice 8 days post infection. **G**. Serum concentration of total IgE in mice in **F at** 16 days post infection. Data are pooled from two independent experiments in B-E (n = 5-12 per group, as indicated by symbols). Data represent one experiment in F, G. * p<0.05, ** p<0.01, *** p<0.001 by Logrank test and t-test.

Figure S1

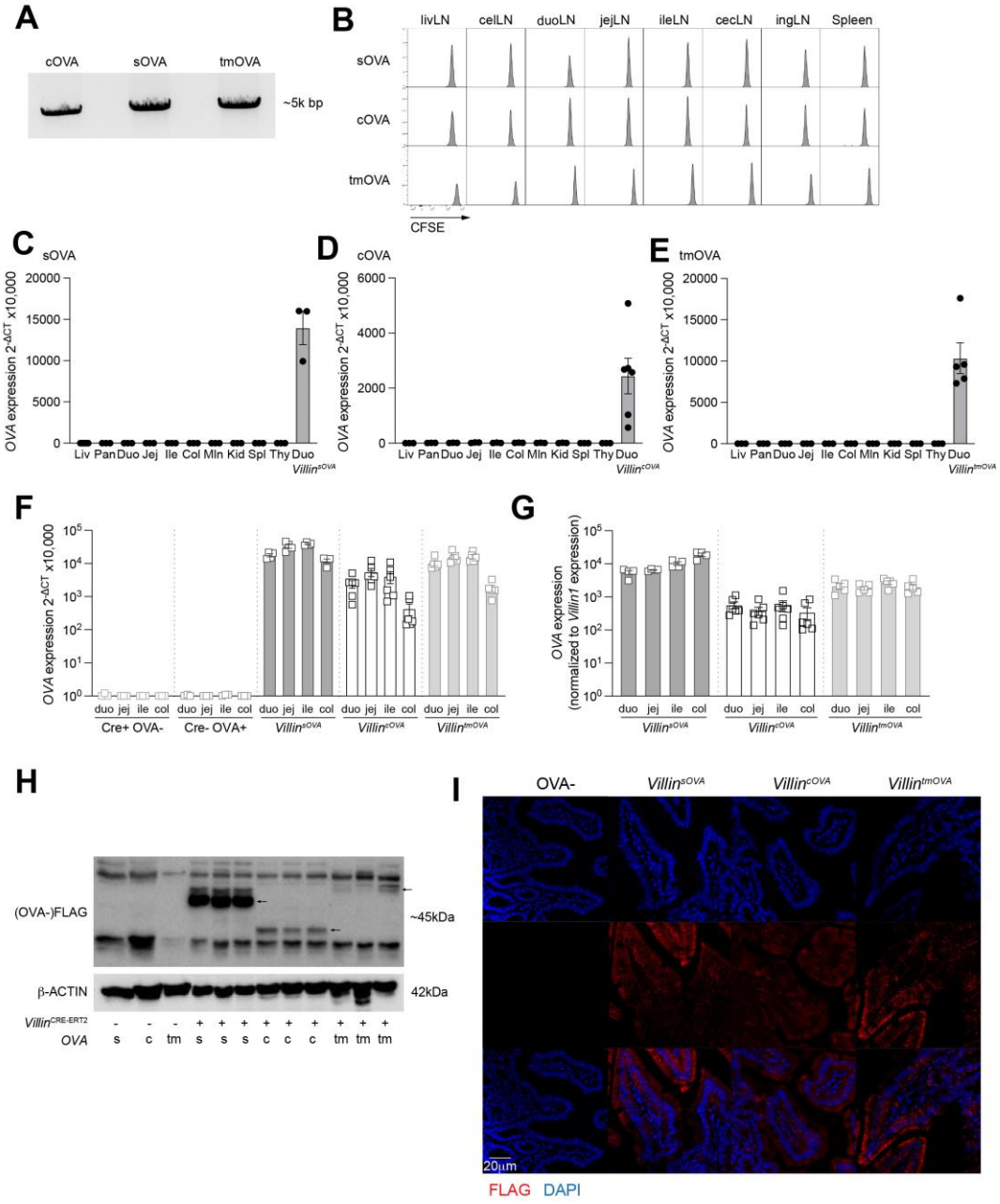


Figure 2.9 Generation and characterization of mice expressing OVA in different subcellular epithelial cell compartments.
A. PCR amplification of the *Rosa26* locus between the homology arms from founders of each OVA line. The bands were sent for sequencing to confirm the correct sequences. **B**. CFSE dilution flow plots of OT-II cells in the indicated LNs 96 h after transfer into $sOVA^{+/w}$, $cOVA^{+/w}$ and $tmOVA^{+/w}$ mice. **C-E**. *OVA* expression levels in the indicated tissues of $sOVA^{+/w}$ (**C**), $cOVA^{+/w}$ (**D**) and $tmOVA^{+/w}$ (**E**) mice. Duodenum from each line crossed to $Villin^{CRE\text{-}ERT2}$ mice was used as a positive control (n = 3-6 per group, as indicated by symbols). **F-G**. *OVA* expression (**F**), and their normalization to *Villin1* (**G**), in the different gut segments of mice with indicated genotypes (n = 3-6 per group, as indicated by symbols). **H**. Western blot of tissue lysates of jejunum from $Villin^{sOVA}$, $Villin^{cOVA}$ and $Villin^{tmOVA}$ mice and their CRE-negative controls, immunoblotted using antibodies against FLAG and β-ACTIN. Arrows indicate OVA signals. **I**. Jejunal sections from $Villin^{sOVA}$, $Villin^{cOVA}$ and $Villin^{tmOVA}$ mice and their CRE-negative control stained for FLAG and DAPI (nuclei). The scale bar represents 20 μm. Data represent one experiment in C-G.

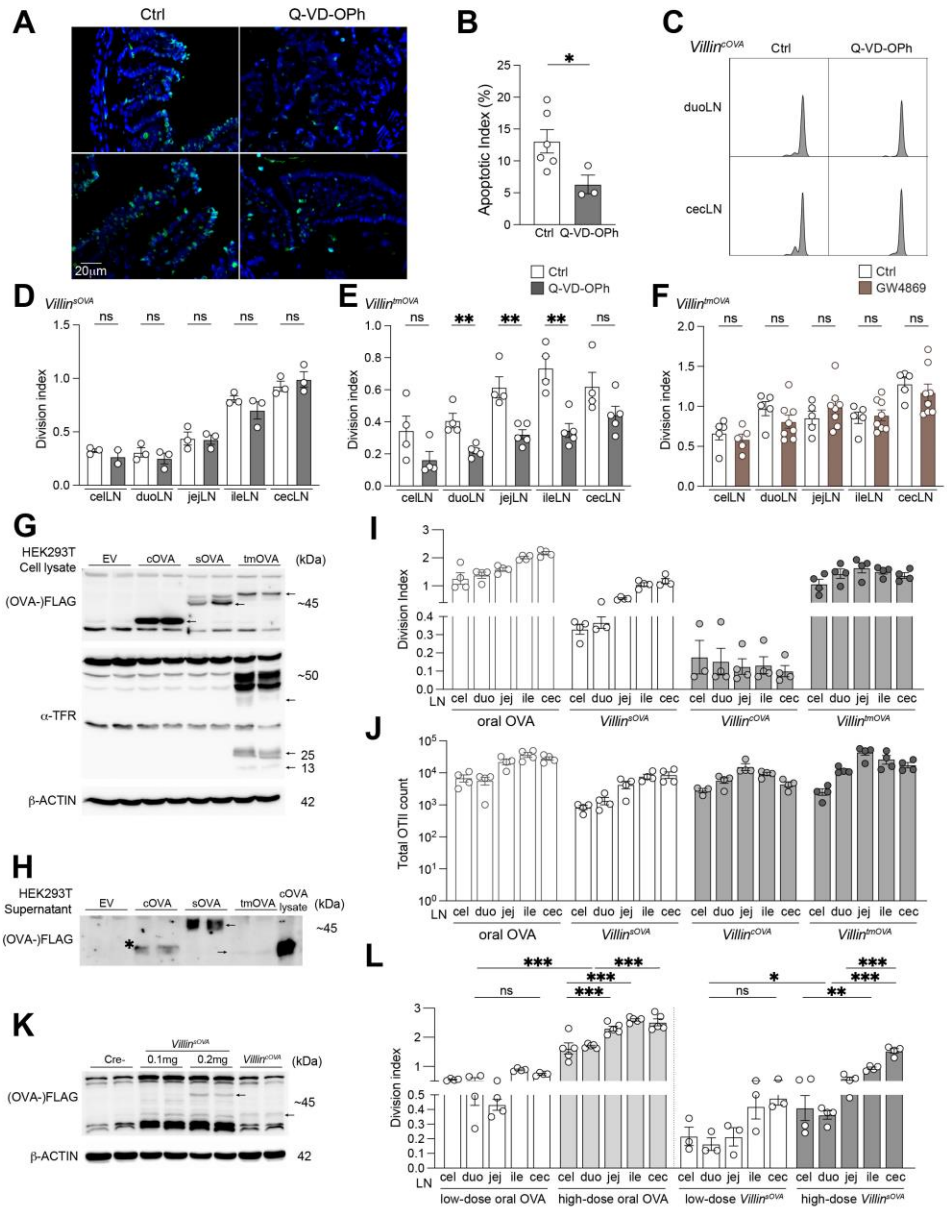


Figure 2.10 Antigens with different subcellular compartments are taken up by APCs through distinct mechanisms.
A-B. Jejunal sections from C57Bl/6 mice treated with Q-VD-OPh or vehicle control stained for apoptotic cells and DAPI (nuclei) (**A**). Apoptotic index of A (**B**) (n = 3-6 per group, as indicated by symbols). **C**. Representative CFSE dilution flow plots of OT-II cells in duoLNs and cecLNs 96 h after transfer into *Villin*^{cOVA} mice treated with Q-VD-OPh or vehicle control. **D-F**. Division index of OT-II cells 96 h after transfer into *Villin*^{sOVA} (**D**) and *Villin*^{tmOVA} (**E**) mice treated with Q-VD-OPh or vehicle control and *Villin*^{tmOVA} mice treated with exosomal biogenesis inhibitor GW4869 (**F**) (n = 3-8 per group, as indicated by symbols). **G-H**. Western blot of cell lysates (**G**) and supernatants (**H**) of HEK293T cells transduced with lentivirus encoding empty vector, *sOVA*, *cOVA*, or *tmOVA* immunoblotted using antibodies against FLAG, α-TFR, and β-ACTIN. Arrows indicate OVA signals, asterisk possible signal from dead cells. **I-J.** Division index (**I**) and total OT-II cells (**J**) in the indicated LNs from mice fed high-dose OVA or *Villin*^{sOVA}, *Villin*^{cOVA} and *Villin*^{tmOVA} mice (n = 4 per group). **K**. Western blot of jejunal tissue lysates from *Villin*^{sOVA} mice treated with low-dose of tamoxifen immunoblotted using antibodies against FLAG and β-ACTIN. Jejunal lysates from *Villin*^{cOVA} mice receiving full tamoxifen diet regime were used as a reference. Arrows indicate OVA signals. **L**. Division index of OT-II cells in the indicated LNs 96 h after transfer into mice fed high- or low-dose oral OVA or mice with high or low expression of sOVA (n = 3-5 per group, as indicated by symbols). Data are representative of two independent experiments in B, D-F. Data represent one experiment in I, J, L.* p<0.05, ** p<0.01, *** p<0.001 by one-way ANOVA test and t-test.

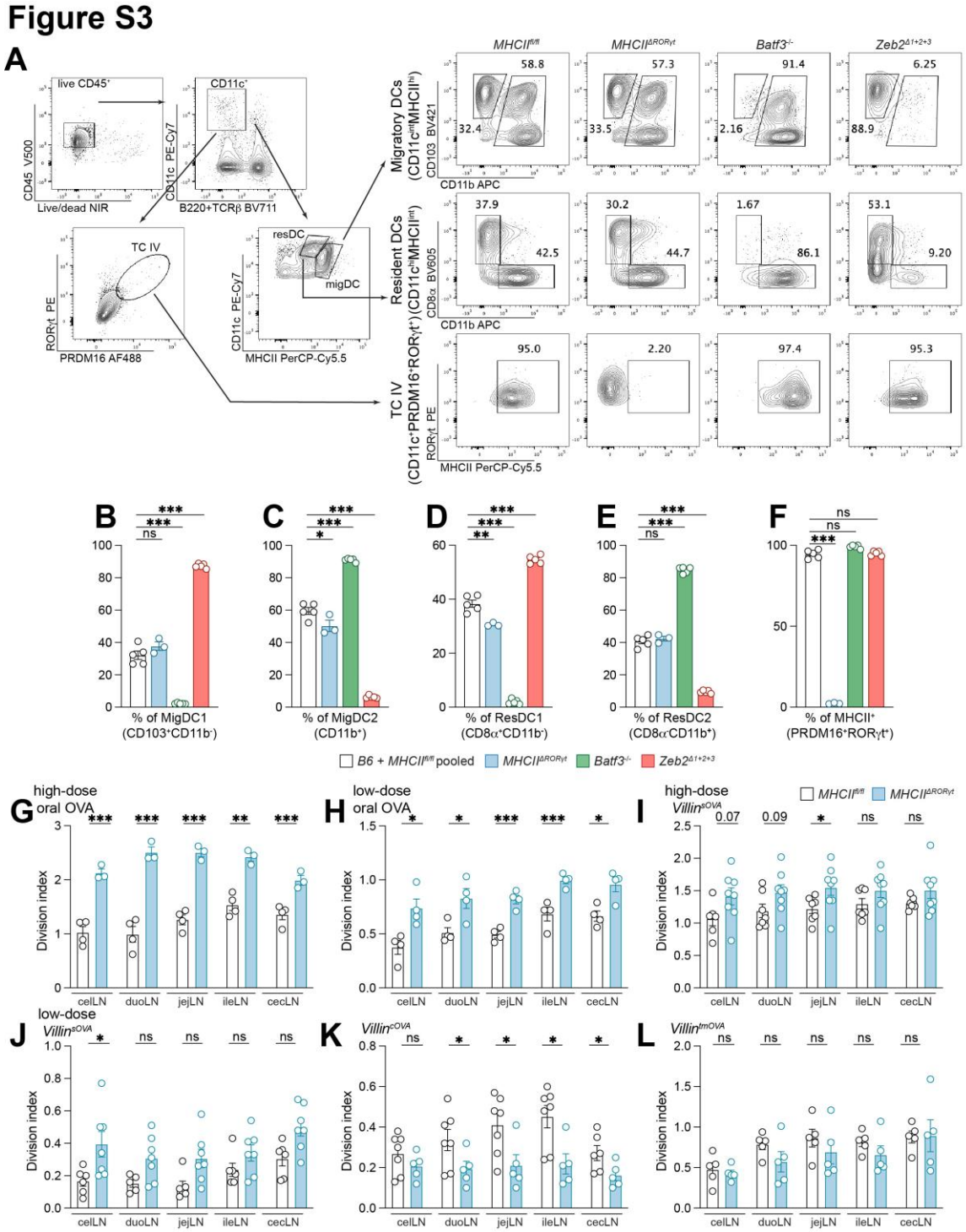


Figure 2.11 cDC1s are required while Thetis cells are dispensable for the generation of gut self-antigen specific FOXP3+ T cells.
A-F. Gating strategy (**A**, left) and representative flow plots (**A**, right) of mLNs from mice with indicated genotypes showing APC frequencies, along with quantification of migDCs (**B, C**), resDCs (**D, E**) and MHCII expression on TC IVs (**F**) (n = 3-5 per group, as indicated by symbols). **G-L**. Division index of OT-II cells in the indicated LNs 96 h after transfer into BMC receiving *MHCII*$^{fl/fl}$ or *MHCII*$^{\Delta ROR\gamma t}$ BM fed high-dose (**G**) or low-dose OVA (**H**), or mice expressing high-dose sOVA (**I**), low-dose sOVA (**J**), cOVA (**K**) and tmOVA (**L**) in the epithelium (n = 3-7 per group, as indicated by symbols). Data represent one experiment in B-L.* p<0.05, ** p<0.01, *** p<0.001 by t-test.

Figure S4

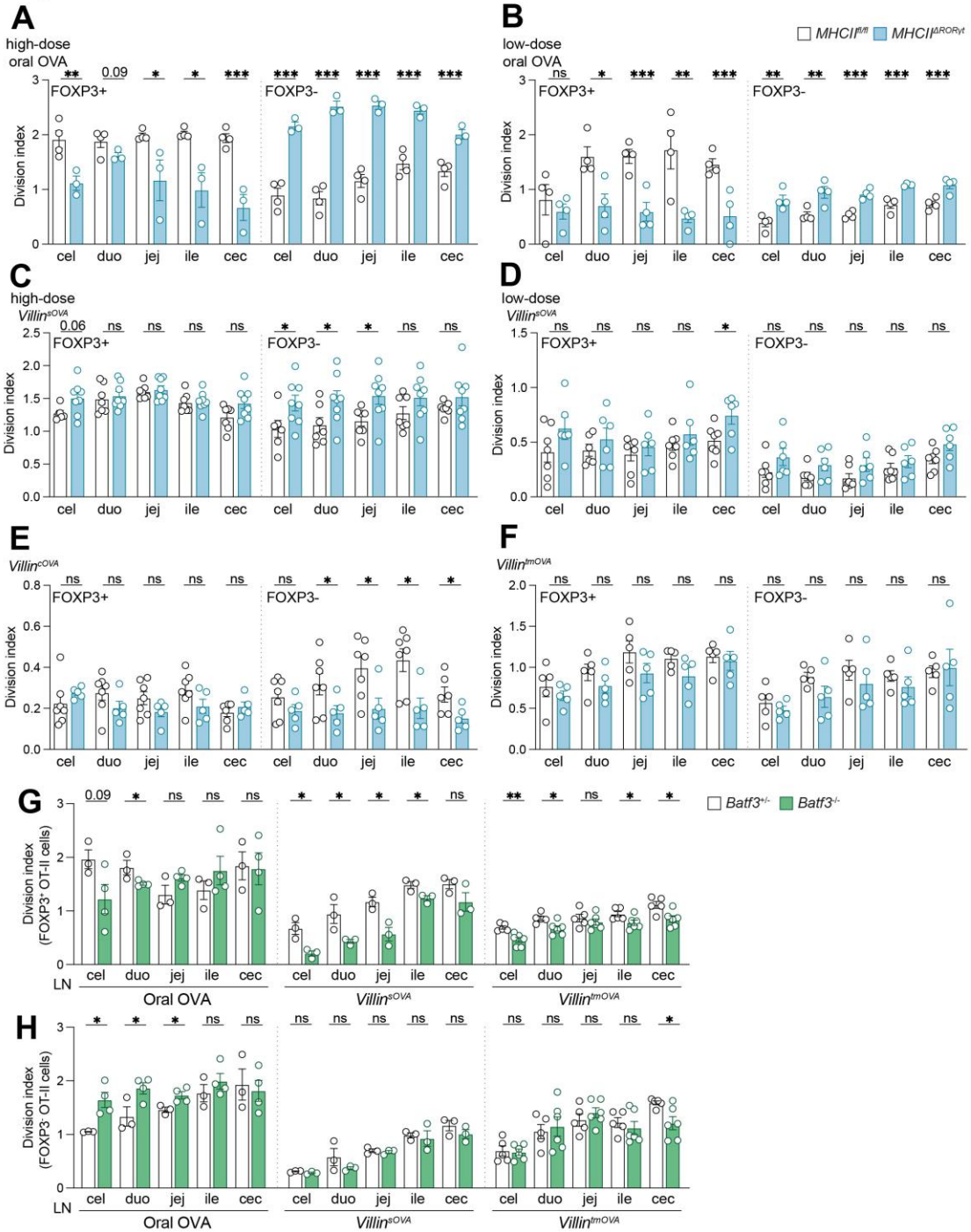


Figure 2.12 FOXP3$^+$ and FOXP3- OT-II cells diverge in their proliferation patterns.
A-F. Division index of FOXP3$^+$ and FOXP3$^-$ OT-II cells in the indicated LNs 96 h after transfer into BMC receiving *MHCII*$^{fl/fl}$ or *MHCII*$^{\Delta ROR\gamma t}$ BM fed high-dose (**A**) or low-dose OVA (**B**), or mice expressing high-dose sOVA (**C**), low-dose sOVA (**D**), cOVA (**E**) and tmOVA (**F**) in the epithelium (n = 3-7 per group, as indicated by symbols). **G-H.** Division index of FOXP3$^+$ (**G**) and FOXP3$^-$ (**H**) OT-II cells 96 h after transfer into high-dose OVA-fed, *Villin*^{sOVA}, or *Villin*^{tmOVA} mice that are *Batf3*-proficient or -deficient. Data represent one experiment in A-F. Data are representative of two independent experiments in G, H. * p<0.05, ** p<0.01, *** p<0.001 by t-test.

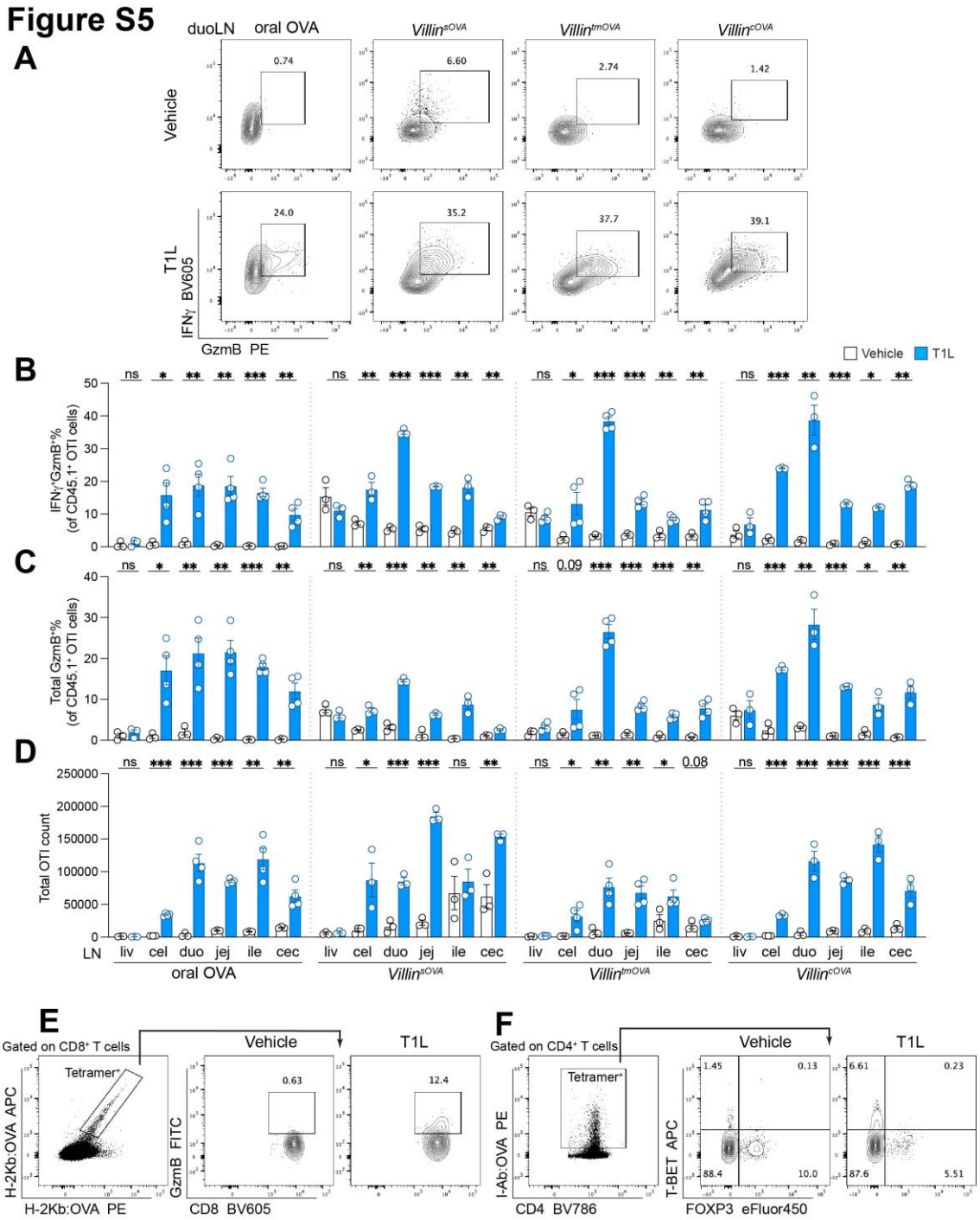


Figure 2.13 Intestinal viral infection impacts epithelial self-antigens and oral antigen-specific T cell fate similarly.
A. Flow plots of OT-I cells in duodenal LNs of T1L- or vehicle-infected mice that were fed high-dose OVA or express sOVA, tmOVA or cOVA in the epithelium. **D.** Frequencies of cytotoxic cells among total OT-I cells in the indicated LNs 72 h after transfer into T1L- or vehicle-infected mice that were fed oral OVA or express sOVA, tmOVA or cOVA in the epithelium (n = 3-4 per group, as indicated by symbols). **D-E.** Frequencies of IFNγ$^+$GzmB$^+$ (**B**), total GzmB$^+$ cells (**C**) among total OT-I cells and total OT-I cell numbers (**D**) in the indicated LNs 72 h after transfer into T1L- or vehicle-infected mice in **A** (n = 3-4 per group, as indicated by symbols). **E-F.** Flow plots of H-2Kb:OVA$^+$ (**E**) and I-Ab:OVA$^+$ (**F**) cells in total mLNs of T1L- or vehicle-infected *Villin^{sOVA}* mice. Data represent one experiment in B-D. * p<0.05, ** p<0.01, *** p<0.001 by t-test.

Figure S6

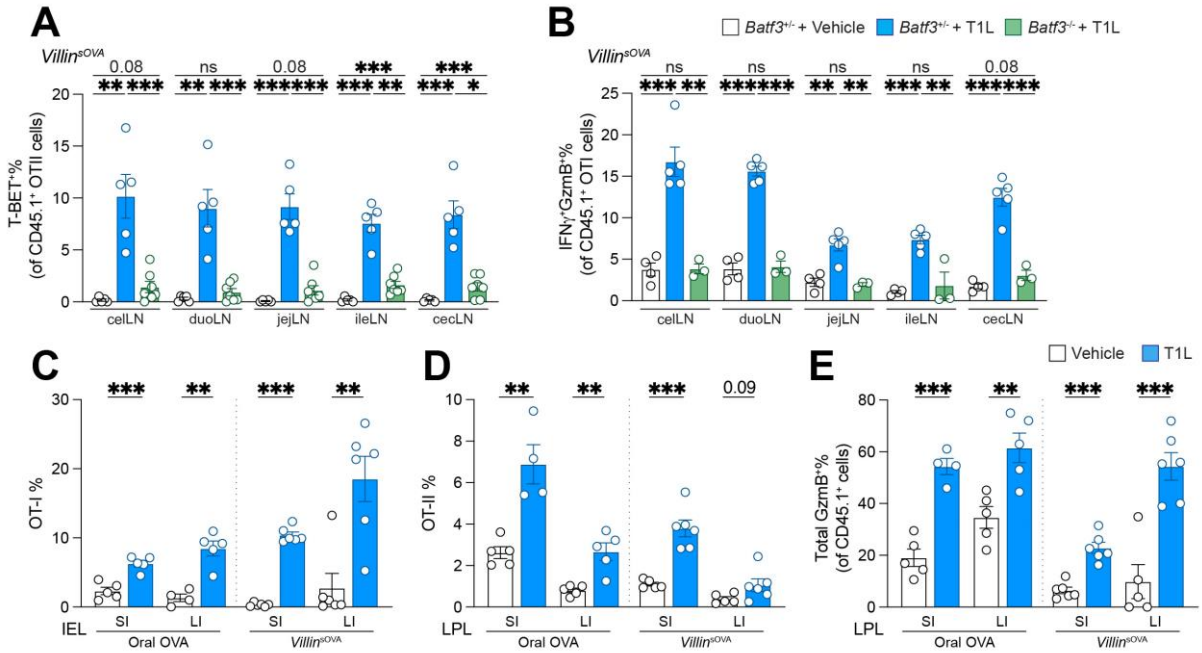


Figure 2.14 Intestinal viral infection leads to comparable pro-inflammatory T cell infiltration of the gut following oral and self-antigen recognition and helminth infection triggers breakdown in tolerance and anaphylaxis in response to secreted but not cytosolic OVA. **A-B.** Frequencies of T-BET$^+$ among total OT-II cells (**A**) and IFNγ$^+$GzmB$^+$ among total OT-I cells (**B**) in indicated LNs 72hr after transfer into T1L- or vehicle-infected *Villin*^{sOVA} mice that are *Batf3*-proficient or -deficient. **C-E.** Frequencies of OT-I among total CD8$^+$ T cells (**C**) in the IEL fraction, OT-II among total CD4$^+$ T cells (**D**) or GzmB$^+$ OT-I among total OT-I cells (**E**) in the LPL fraction of the gut tissue of T1L- or vehicle-infected mice that were fed OVA or express sOVA (n = 4-6 per group, as indicated by symbols). Data are pooled from two independent experiments in C-E. Data represent one experiment in A, B. * p<0.05, ** p<0.01, *** p<0.001 by t-test.

Figure S7

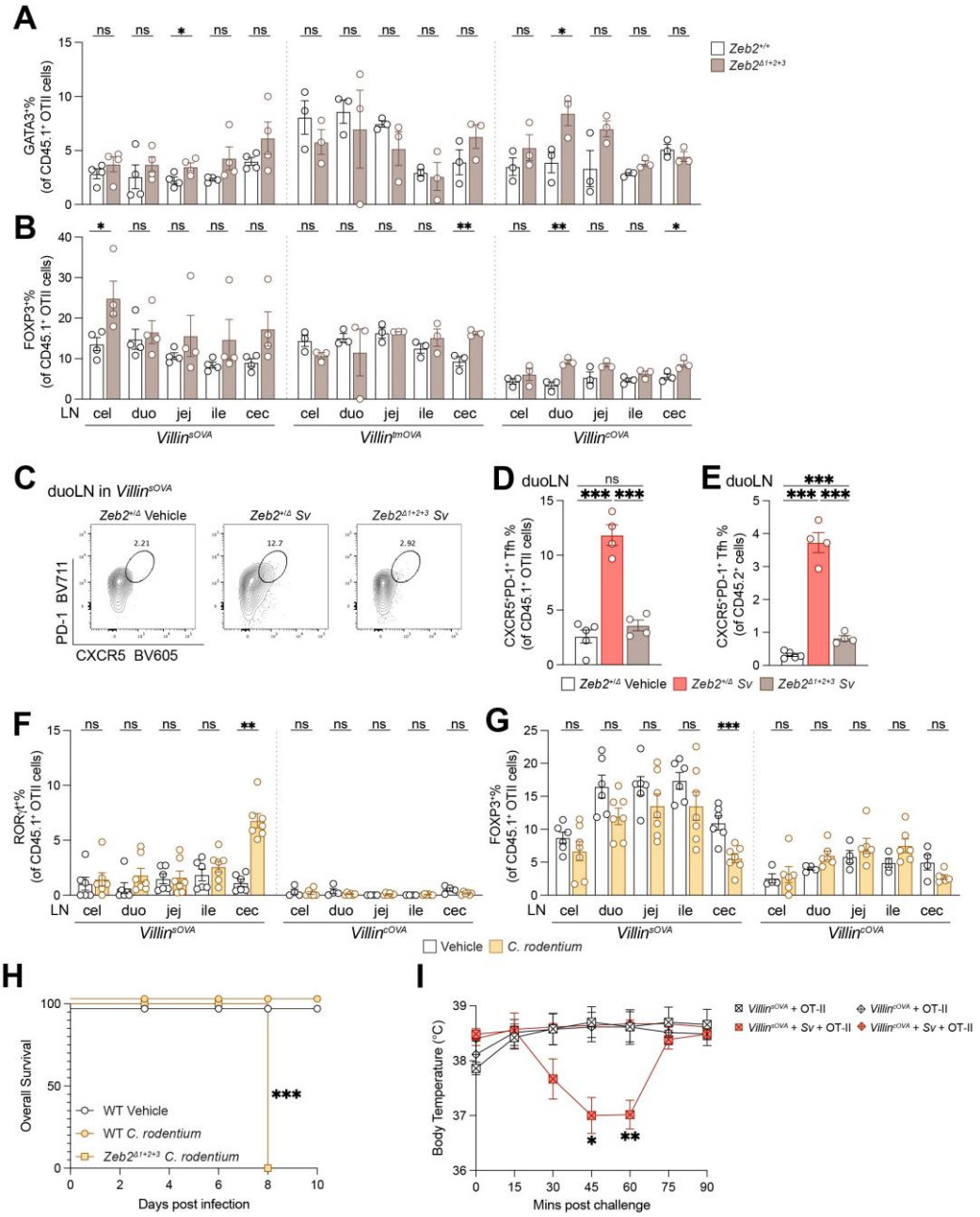


Figure 2.15 Secreted but not cytosolic self-antigens induce Th2 cells in response to helminth infection in a cDC2-dependent manner. **A-B.** Frequencies of GATA3$^+$ (**A**) and FOXP3$^+$ (**B**) among total OT-II cells in the indicated LNs from bone marrow chimera (received *Zeb2*$^{+/+}$ or *Zeb2*$^{\Delta 1+2+3}$ bone marrow) mice expressing OVA (n = 3-4 per group, as indicated by symbols). **C-E.** Flow plot of OT-II cells in duodenal LNs of sOVA-expressing non-infected *Zeb2*$^{+/\Delta}$, *S. venezuelensis*-infected *Zeb2*$^{+/\Delta}$ or *S. venezuelensis*-infected *Zeb2*$^{\Delta 1+2+3}$ mice (**C**). Frequencies of Tfh among total OT-II cells (**D**) or total endogenous CD4 T cells (**E**) in the duodenal LNs of mice in **C** (n = 4-5 per group, as indicated by symbols). **F-G.** Frequencies of RORγt$^+$ (**F**) and FOXP3$^+$ (**G**) among total OT-II cells in the indicated LNs 72 h after transfer into *C. rodentium*-infected *Villin*^{sOVA} and *Villin*^{cOVA} mice (n = 4-7 per group, as indicated by symbols). **H.** Overall survival of *C. rodentium*-infected WT or *Zeb2*$^{\Delta 1+2+3}$ mice over a duration of 10 days (n = 5-7 per group). **I**. Body temperature measurements of indicated groups every 15 min post 50 μg i.p. OVA challenge (n = 5-7 per group, as indicated by symbols). Data are pooled from two independent experiments in F, G. Data represent one experiment in A, B, D, E, H, I. * p<0.05, ** p<0.01, *** p<0.001 by t-test or Logrank (Mantel-Cox) test.

2.7 Material and methods

Table 2.1 KEY RESOURCES TABLE

REAGENT or RESOURCE	SOURCE	IDENTIFIER
Antibodies		
APC anti-mouse Granzyme B (clone QA16A02)	Biolegend	Cat#372204; RRID: AB_2687028
APC anti-mouse T-bet (clone 4B10)	Biolegend	Cat#644814; RRID: AB_10901173
APC anti-mouse FoxP3 (clone FJK-16S)	eBioscience	Cat#17-5773-82; RRID: AB_469457
APC anti-mouse IFNγ (clone XMG1.2)	Biolegend	Cat#505810; RRID: AB_315404
APC anti-mouse CD4 (clone RM4.5)	BD Biosciences	Cat#553051; RRID: AB_398528
APC/Cyanine7 anti-mouse TCRβ (clone H57-597)	Biolegend	Cat#109220; RRID: AB_893624
APC/Cyanine7 anti-mouse B220 (clone RA2-6B2)	Biolegend	Cat#103224; RRID: AB_313007
APC/Cyanine7 anti-mouse NK1.1 (clone PK136)	Biolegend	Cat#108724; RRID: AB_830871
Pacific Blue anti-mouse Ly6G/Ly-6c (Gr-1) (clone RB6-8C5)	Biolegend	Cat#108430; RRID: AB_893556
PE anti-mouse FOXP3 (clone FJK-16S)	eBioscience	Cat#12-5773-82; RRID: AB_465936
PE anti-mouse T-bet (clone O4-46)	BD Biosciences	Cat#561268; RRID: AB_10564071
PE anti-mouse TNFα (clone MP6-XT22)	BD Biosciences	Cat#554419; RRID: AB_395380
PE anti-mouse GATA3 (clone TWAJ)	eBioscience	Cat#12-9966-42; RRID: AB_1963600
PE anti-mouse CD8α (clone 53-6.7)	Biolegend	Cat#100708; RRID: AB_312747
PE anti-mouse RORγT (clone Q31-378)	BD Biosciences	Cat#562607; RRID: AB_11153137
PE anti-mouse Granzyme B (clone QA16A02)	Biolegend	Cat#372208; RRID: AB_2687032
PE/Cyanine5 anti-mouse CD11c (clone N418)	Biolegend	Cat#117316; RRID: AB_493566
PE/Cyanine5 anti-mouse CD44 (clone IM7)	eBioscience	Cat# 15-0441-82; RRID: AB_468749
PE/Cyanine7 anti-mouse CD45.1 (clone A20)	eBioscience	Cat#25-0453-82; RRID: AB_469629
PE/Cyanine7 anti-mouse CD45 (clone 30-F11)	eBioscience	Cat#25-0451-82; RRID: AB_2734986
PE/Cyanine7 anti-mouse CD11c (clone N418)	eBioscience	Cat#25-0114-82; RRID: AB_469590
PE/Fire810 I-A/I-E (clone M5/114.15.2)	Biolegend	Cat#107667; RRID: AB_2894690
FITC anti-mouse CD4 (clone RM4-5)	Biolegend	Cat#100510; RRID: AB_312713
FITC anti-mouse CD279 (PD-1) (clone RMP1-30)	eBioscience	Cat#11-9981-82; RRID: AB_465467
FITC anti-mouse Granzyme B (clone NGZB)	eBioscience	Cat#11-8898-82; RRID: AB_10733414
Spark Blue™ 550 anti-mouse CD45 (clone 30-F11)	Biolegend	Cat#103166; RRID: AB_2832300
PerCP/eFluor™710 anti-mouse I-A^b (MHCII) (clone M5/114)	eBioscience	Cat#46-5321-82; RRID: AB_1834439
PerCP/eFluor™710 anti-mouse Vβ5.1/5.2 (clone MR9-4)	eBioscience	Cat#46-5796-82; RRID: AB_10853817
eFluor™ 450 anti-mouse FOXP3 (clone FJK-16s)	eBioscience	Cat#48-5773-82; RRID: AB_1518812
BUV563 anti-mouse CD11b (clone M1/70)	BD Biosciences	Cat#741242; RRID: AB_2870793
BUV661 anti-mouse CD103 (clone M290)	BD Biosciences	Cat#741504; RRID: AB_2870960
BUV737 anti-mouse CD127 (clone SB/199)	BD Biosciences	Cat#612841; RRID: AB_2870163
BB515 anti-mouse Siglec F (clone E50 2440)	BD Biosciences	Cat#564514; RRID: AB_2738833

REAGENT or RESOURCE	SOURCE	IDENTIFIER
eFluor 450 anti-mouse FoxP3 (clone FJK-16S)	eBioscience	Cat#48-5773-82; RRID: AB_1518812
BV421 anti-mouse CD103 (clone OX-62)	BD Biosciences	Cat#566297; RRID: AB_2739670
BV421 anti-mouse TNFα (clone MP6-XT22)	BD Biosciences	Cat#563387; RRID: AB_2738173
BV421 anti-mouse RORγT (clone Q31-378)	BD Biosciences	Cat#562894; RRID: AB_2687545
V500 anti-mouse CD4 (clone RM4-5)	BD Biosciences	Cat#560782; RRID: AB_1937315
V500 anti-mouse CD45 (clone 30-F11)	BD Biosciences	Cat#561487; RRID: AB_10697046
BV605 anti-mouse CD44 (clone IM7)	BD Biosciences	Cat#563058; RRID: AB_2737979
BV605 anti-mouse CD8α (clone 53-6.7)	Biolegend	Cat#100744; RRID: AB_2562609
BV605 anti-mouse IFNγ (clone XMG1.2)	Biolegend	Cat#505839; RRID: AB_2561438
BV605 anti-mouse CD185 (clone L138D7)	Biolegend	Cat#145513; RRID: AB_2562208
BV711 anti-mouse TCRβ (clone H57-597)	Biolegend	Cat#109243; RRID: AB_2629564
BV711 anti-mouse B220 (clone RA2-6B2)	Biolegend	Cat#103255; RRID: AB_2563491
BV711 anti-mouse CD279 (clone 29F.1A12)	Biolegend	Cat#135231; RRID: AB_2566158
BV785 anti-mouse CD8α (clone 53-6.7)	Biolegend	Cat#100749; RRID: AB_11218801
BV786 anti-mouse CD45 (clone 30-F11)	BD Biosciences	Cat#564225; RRID: AB_2716861
AF488™ anti-mouse F4/80 (clone BM8)	Biolegend	Cat#123120; RRID: AB_893479
AF647™ anti-mouse CD11b (clone M1/70)	Biolegend	Cat#101218; RRID: AB_389327
Biotin anti-mouse B220 (clone RA3-6B2)	BD Biosciences	Cat#553086; RRID: AB_394616
Biotin anti-mouse CD11c (clone HL3)	BD Biosciences	Cat#553800; RRID: AB_395059
Biotin anti-mouse NK1.1 (clone PK136)	BD Biosciences	Cat#553163; RRID: AB_394675
Biotin anti-mouse CD4 (clone GK1.5)	BD Biosciences	Cat#553728; RRID: AB_395012
Biotin anti-mouse CD8α (clone 53-6.7)	BD Biosciences	Cat#553029; RRID: AB_394567
Biotin anti-mouse CD11b (clone M1/70)	BD Biosciences	Cat#553309; RRID: AB_394773
Biotin anti-mouse CD25 (clone 7D4)	BD Biosciences	Cat#553070; RRID: AB_394602
Biotin anti-mouse TER-119 (clone TER-119)	BD Biosciences	Cat#553672; RRID: AB_394985
PRDM16 (clone EPR24315-59)	Abcam	Cat#ab303534; RRID: AB_3662673
FLAG, polyclonal	Millipore Sigma	Cat#F7425; RRID: AB_439687
DDDDK tag, polyclonal	Abcam	Cat#ab95045; RRID: AB_10676074
DDDDK tag, polyclonal	Abcam	Cat#ab1257; RRID: AB_299216
Transferrin receptor (clone H68.4)	Invitrogen	Cat#13-6800; RRID: AB_2533029
Beta-actin (C4) HRP	Santa Cruz Biotechnology	Cat#sc-47778 HRP; RRID: AB_2714189
Peroxidase AffiniPure goat anti-mouse IgG (H+L)	Jackson Immunoresearch	Cat#115-035-003; RRID: AB_10015289
Peroxidase AffiniPure goat anti-rabbit IgG (H+L)	Jackson Immunoresearch	Cat#111-035-144; RRID: AB_2307391
Alexa Fluor 488 AffiniPure donkey anti-rabbit IgG (H+L)	Jackson Immunoresearch	Cat#711-545-152; RRID: AB_2313584
Donkey anti-Goat IgG (H+L) Highly Cross-Adsorbed Secondary Antibody, AF™568	Invitrogen	Cat#A11057; RRID: AB_2534104
Bacterial and virus strains		
Type 1 Lang (T1L) virus	Dermody Lab (University of Pittsburgh)	N/A
S. venezuelensis	Galli Lab (Stanford University)	N/A
C. rodentium DBS100	Jabri Lab (University of Chicago)	N/A

REAGENT or RESOURCE	SOURCE	IDENTIFIER
NEB Stable Competent DH5α *E. coli* (High Efficiency)	New England Biolabs	Cat#C3040H
Biological samples		
Bovine serum albumin (BSA)	Thermo Fisher	Cat#BP1600-100
Normal donkey serum (NDS)	Jackson ImmunoResearch	Cat#017-000-121
Newborn calf serum (NCS)	GeminiBio	Cat#100-504
Foundation B FBS	GeminiBio	Cat#900-208
Penicillin-streptomycin solution	Corning	Cat#30001CI
Collagenase, Type IV	Thermo Fisher	Cat#17104019
Collagenase, Type D	Millipore Sigma	Cat#11088866001
Collagenase, Type VIII	Millipore Sigma	Cat#C2139
DNase I, Amplification Grade	Invitrogen	Cat#18068015
DNase I	Millipore Sigma	Cat#10104159001
Albumin from chicken egg white	Millipore Sigma	Cat#A5378
Ovalbumin, Low Endo, Purified	Worthington Biochemical	Cat#LS003062
Ovalbumin EndoFit™	InvivoGen	Cat#vac-pova
Chemicals, peptides, and recombinant proteins		
TRIzol™ Reagent	Thermo Fisher	Cat#15596018
DNaseI	Millipore Sigma	Cat#10104159001
Histopaque-1077	Millipore Sigma	Cat#10770
RNAlater	Millipore Sigma	Cat#R0901
GW4869	MedChemExpress	Cat#HY-19363
Q-VD-OPh	MedChemExpress	Cat#HY-12305
Alhydrogel adjuvant 2%	InvivoGen	Cat#vac-alu-50
Tamoxifen	Millipore Sigma	Cat#T5648
cOmplete Protease Inhibitor Cocktail, EDTA-free, Tablets	Roche	Cat#11873580001
PMSF	Millipore Sigma	Cat#10837091001
TAM diet (500, 2016, Red)	Envigo	Cat#TD.130858
Alt-R S.p. Cas9 Nuclease V3	Integrated DNA Technologies	Cat#292647563
Dulbecco's Modified Eagle Medium (DMEM)	Thermo Fisher	Cat#11965118
Joklik's modified Eagle's minimal essential medium (SMEM)	Lonza Bioscience	Cat#BE15-375k
LB Broth, Lennox (Powder)	Thermo Fisher	Cat#BP1427-2
Penicillin-Streptomycin Solution, 100x	Corning	Cat#30-002-CI
0.05% Trypsin/0.53mM EDTA in HBSS	Corning	Cat#25-051-CI
Ampicillin sodium salt	Thermo Fisher	Cat#BP176025
Puromycin Ready Made Solution	Millipore Sigma	Cat#P4512-1MLX10
Dapi Fluoromount G Clear Mounting Media	Thermo Fisher	Cat#OB010020
2-mercaptoethanol	Sigma Aldrich	Cat#M7522
RPMI 1640, powder	Thermo Fisher	Cat#31800105
Percoll	GE Healthcare	Cat#17089109
HEPES Buffer	Corning	Cat#25060CI
LIVE/DEAD™ Fixable Near-IR	Thermo Fisher	Cat#L10119

REAGENT or RESOURCE	SOURCE	IDENTIFIER
LIVE/DEAD™ Fixable Aqua	Thermo Fisher	Cat#L34965
Zombie NIR™	Biolegend	Cat#423105
CellTrace™ CFSE	Thermo Fisher	Cat#C34554
PE-conjugated H2-Kb chicken ova 257-264 SIINFEKL	NIH Tetramer Core Facility	N/A
APC-conjugated H2-Kb chicken ova 257-264 SIINFEKL	NIH Tetramer Core Facility	N/A
PE-conjugated I-Ab chicken ova 328-337 HAAHAEINEA	NIH Tetramer Core Facility	N/A
APC-conjugated I-Ab chicken ova 328-337 HAAHAEINEA	NIH Tetramer Core Facility	N/A
Trypan blue solution, 0.4%	Thermo Fisher	Cat#15250061
Buffer TCL	Qiagen	Cat#1031576
Critical commercial assays		
Fixation/permeabilization Concentrate	Thermo Fisher	Cat#00-5123-43
Fixation/permeabilization Diluent	Thermo Fisher	Cat#00-5223-56
Cytofix/cytoperm™ Fixation and Permeabilization Solution	BD Biosciences	Cat#554722
Permeabilization Buffer (10X)	Thermo Fisher	Cat#00-8333-56
GolgiPlug™ Protein Transport Inhibitor	BD Biosciences	Cat#555029
eBioscience™ Cell Stimulation Cocktail	Thermo Fisher	Cat#00-4975-93
Lipofectamine 3000 Transfection Reagent	Thermo Fisher	Cat#L3000008
SuperScript™ III One-Step RT-PCR System with Platinum™ *Taq* High Fidelity DNA Polymerase	Thermo Fisher	Cat#12574035
Maxima H Minus Reverse Transcriptase (200 U/μL)	Thermo Fisher	Cat#EP0753
RNasin™ Plus RNase Inhibitor	Promega	Cat#N2611
HiFi HS Ready Mix 2X	KAPA Biosystems	Cat#K2601K
T cell enrichment kit	Beckman Coulter	Cat#A63987
Anti-Ovalbumin IgG1 (mouse) ELISA Kit	Cayman Chemical Company	Cat#500830
Iegend MAX™ Mouse OVA Specific IgE ELISA Kit with Pre-coated Plates	Biolegend	Cat#439807
Mouse IgE ELISA Kit	Invitrogen	Cat#EMIGHE
ApopTag Fluorescein In Situ Apoptosis Detection Kit	EMD Millipore	Cat#S7110
Clarity Western ECL Substrate	Bio-Rad	Cat#1705061
Clarity Max Western ECL Substrate	Bio-Rad	Cat#1705062
Anti-biotin Microbeads	Miltenyi Biotec	Cat#130090485
QIAprep Spin Miniprep Kit (50)	Qiagen	Cat#27104
QIAquick Gel Extraction Kit (50)	Qiagen	Cat#28704
Invitrogen PureLink HiPure Plasmid Filter Midiprep Kit	Invitrogen	Cat#210014
Experimental models: Organisms/strains		
Mouse: C57BL/6J (B6)	Jackson Laboratory	RRID: IMSR_JAX:000664
Mouse: B6.Cg-Tg(TcraTcrb)425Cbn/J (OT-II)	Jackson Laboratory	RRID: IMSR_JAX:004194
Mouse: C57BL/6-Tg(TcraTcrb)1100Mjb/J (OT-I)	Jackson Laboratory	RRID: IMSR_JAX:003831

REAGENT or RESOURCE	SOURCE	IDENTIFIER
Mouse: C57B6/6J-*Ptprc*^{em6Lutzy}/J (CD45.1)	Jackson Laboratory	RRID: IMSR_JAX:033076
Mouse: B6.Cg-Tg(Vil1-cre/ERT2)23Syr/J (Villin^{CreERT2})	Jackson Laboratory	RRID: IMSR_JAX:020282
Mouse: B6. 129S(C)-*Batf3*^{tm1Kmm}/J (*Batf3*$^{-/-}$)	Jackson Laboratory	RRID: IMSR_JAX:013755
Mouse: C57BL/6-*Rr253*^{em6Kmm}/J (*Zeb2*$^{Δ1+2+3}$)	Jackson Laboratory	RRID: IMSR_JAX:037704
Mouse: B6.129X1-*H2-Ab1*$^{b-tm1Koni}$/J (*MHCII*$^{fl/fl}$)	Jackson Laboratory	RRID: IMSR_JAX:013181
Mouse: B6.FVB-Tg(Rorc-cre)1Litt/J (Rorc^{CRE})	Jackson Laboratory	RRID: IMSR_JAX:022791
Mouse: Rosa26-*sOVA*	This manuscript	N/A
Mouse: Rosa26-*cOVA*	This manuscript	N/A
Mouse: Rosa26-*tmOVA*	This manuscript	N/A
Cell line: Caco-2	ATCC	Cat#HTB-37
Cell line: HEK293T	ATCC	Cat#CRL-3216
Cell line: L cell, L929	ATCC	Cat#CCL-1
Oligonucleotides		
OVA1F	Integrated DNA Technologies	AAACAGCTGCAGATCAAGCC
OVA1R	Integrated DNA Technologies	CATGCTCATTGTCCCACTGG
OVA2F	Integrated DNA Technologies	GGGACAATGAGCATGTTGGT
OVA2R	Integrated DNA Technologies	ACCTCTCTGCCTGCTTCATT
TFR_OVA_F	Integrated DNA Technologies	GTTGGTGCTGTTGCCTGATG
TFR_OVA_R	Integrated DNA Technologies	AGAAGAGAACGGCGTTGGTT
R26_3v2_F	Integrated DNA Technologies	GTTGCCAGCCATCTGTTGTTT
R26_3v1_R	Integrated DNA Technologies	GCTCGCACCAACACAAAAGT
R26_3v1_F	Integrated DNA Technologies	CAAGGGGGAGGATTGGGAAG
R26_3v2_R	Integrated DNA Technologies	GAGGGCAATCTGGGAAGGTT
pLJM1_sOVA_FLAG_F	NEBuilder	CAGAGCTGGTTTAGTGAACCGTC AGATCCGATGGGCTCCATCGGTG CAG
pLJM1_sOVA_FLAG_R	NEBuilder	GATCTGAGTCCGGACTTGTACCC GGTAGCGTTACTTGTCATCGTCAT CCTTGTAATC
pLJM1_cOVA_FLAG_F	NEBuilder	CAGAGCTGGTTTAGTGAACCGTC AGATCCGATGGGCTCCATCGGCG CAG
pLJM1_cOVA_FLAG_R	NEBuilder	GATCTGAGTCCGGACTTGTACCC GGTAGCGTTACTTGTCATCGTCAT CCTTGTAATCG
pLJM1_tmOVA_FLAG_F	NEBuilder	CAGAGCTGGTTTAGTGAACCGTC AGATCCGATGATGGATCAAGCTA GATCAG

REAGENT or RESOURCE	SOURCE	IDENTIFIER
pLJM1_tmOVA_FLAG_R	NEBuilder	GATCTGAGTCCGGACTTGTACCC GGTAGCGTTACTTGTCATCGTCAT CCTTG
OVA_F	Integrated DNA Technologies	CTTCAAAGGACTGTGGGAGAAA
OVA_R	Integrated DNA Technologies	CTCCATCTTCATGCGAGGTAAG
CRISPR crRNA	Integrated DNA Technologies	ACTCCAGTCTTTCTAGAAGA
Software and algorithms		
GraphPad Prism (v10.6.1)	GraphPad	https://www.graphpad.com/
FlowJo (v10.10.0)	Tree Star	https://www.flowjo.com/
QuPath (v0.5.1)	Bankhead et. al(Bankhead et al., 2017)	https://qupath.github.io/
Adobe Illustrator (v29.0)	Adobe	www.adobe.com/products/illustrator
Devices		
BD LSRII	BD Biosciences	N/A
5-laser Aurora spectral flow cytometer	Cytek Bioscience	N/A
EVOS^{TM} FL fluorescent microscope	Invitrogen	N/A
SP8 confocal microscope	Leica	N/A
TP500 Temperature Programmable Transponder	Avidity Science	Cat#TP-500

Mice

C57BL/6J, CD45.1 congenic (C57B6/6J-*Ptprc*^{em6Lutzy}/J), *Villin*$^{CRE-ERT2}$ (B6.Cg-Tg(Vil1-cre/ERT2)23Syr/J), *Batf3*$^{-/-}$ (B6. 129S(C)-*Batf3*^{tm1Kmm}/J), *Zeb2*$^{\Delta 1+2+3}$ (C57BL/6-*Rr253*^{em6Kmm}/J), *Rorc*^{CRE} (B6.FVB-Tg(Rorc-cre)1Litt/J), and *MHCII*$^{fl/fl}$ (B6.129X1-*H2-Ab1*$^{b-tm1Koni}$/J), B6.Cg-Tg(TcraTcrb)425Cbn/J (OT-II) and C57BL/6-Tg(TcraTcrb)1100Mjb/J (OT-I) mice were purchased from The Jackson Laboratory and maintained at the University of Chicago animal facility under specific pathogen-free (SPF) conditions, confirmed to be free of segmented filamentous bacteria. OT-I and OT-II mice were crossed to CD45.1$^{+/+}$ mice to introduce a congenic marker. All experiments were performed in accordance with AICUC protocols.

Engineering *OVA* expression vectors and Rosa26 targeting constructs

Full length *ovalbumin* (*OVA*) and transmembrane *OVA* were amplified from Addgene plasmids #64599 and #64600, respectively, and cloned into pcDNA3.1 upstream of a C-terminal 3xFLAG tag using the In-Fusion cloning kit (Takara) with *NotI* as the restriction site. Cytosolic *OVA*, lacking amino acids 18-143 relative to the full-length sequence, was amplified from a construct provided by Seungmin Hwang and similarly inserted into pcDNA-3xFLAG. Plasmids were introduced into chemically competent *E. coli* DH5α by heat-shock transformation. Transformed bacteria were plated onto LB plates supplemented with ampicillin. Single colonies were cultured, expanded and plasmids extracted by Miniprep (Qiagen). Expression of each OVA variant was validated by transient transfection of HEK293T cells using Lipofectamine 3000 Transfection Reagents (Thermo Fisher) followed by immunoblotting.

For *Rosa26* targeting, the *OVA*-3xFLAG sequences were PCR-amplified from the respective expression construct and cloned into the *MluI/AsiSI* site of the pR26-CAG-AsiSI/MluI (Addgene #74286). All constructs were verified by Sanger sequencing. Plasmids were introduced into chemically competent *E. coli* DH5α by heat-shock transformation. Single colonies harboring pR26 targeting constructs were selected using ampicillin-supplemented LB plates and cultured overnight (≤12 h). Plasmid DNA was prepared using anion-exchange midi columns (Invitrogen). Purified DNA was ethanol-precipitated and resuspended in nuclease-free water. On the injection day, the CRISPR injection mix was prepared 2 h prior to use(Chu et al., 2016). Briefly, 5 µl crRNA (5'-ACTCCAGTCTTTCTAGAAGA, 1µg/µl; IDT) and 10µl tracrRNA (1µg/µl; IDT) were annealed in a thermocycler (95°C with a ramp down to 25°C at 5°C/min). Cas9 protein (10 µl, 1 µg/µl; IDT) was then complexed with 10 µl of annealed crRNA:tracrRNA and 30 µl of water for 15 min at 25°C. Midi-prepped plasmid DNA was added to the RNP complex at a final concentration of 15

μg/μl in a total volume of 100 μl. The mixture was spun at 20,000 x g for 20 min, and the upper 65 μl was transferred to a fresh tube and provided to the University of Chicago Transgenic Mouse Facility.

Fertilized C57BL/6 oocytes were microinjected with the mixture and reimplanted into pseudopregnant CD-1 females. Tail biopsies were collected from pups at 2 weeks of age for genotyping. Integration of *OVA* sequences was confirmed by PCR using primers OVA1F, OVA1R, OVA2F, OVA2R, TFR_OVA_F and TFR_OVA_R. Correct targeting to the *Rosa26* locus was validated with primer pairs R26_3v2F and R26_3v1R, followed by R26_3v1F and R26_3v2R. The resultant PCR products were analyzed by agarose gel electrophoresis to confirm expected size and subsequently validated by Sanger sequencing. Successful founders were isolated in quarantine for SFB removal and bred to C57BL/6 mice for two generations before crossing onto Cre driver lines. The sequences of mentioned primers are listed in the Key Resource Table.

Induction of ovalbumin self-antigen in the intestine by tamoxifen administration

Rosa26-*OVA* mice were crossed to *Villin*$^{CRE\text{-}ERT2}$ mice. Offspring were administrated tamoxifen-containing diet (TAM diet, Envigo) for 7 consecutive days or by daily intraperitoneal injection of 1mg tamoxifen (TAM) (Sigma) dissolved in 100 μl corn oil for 5 consecutive days at 4-6 weeks of age to induce for OVA self-antigen expression in the intestinal epithelium. Following TAM administration, mice were returned to a normal Chow diet for 4-7 days before use in experiments. For low-TAM administration, the mice were given one injection of 0.2mg TAM dissolved in 100 μl corn oil.

Oral ovalbumin administration

For high-dose regimen, OVA (Sigma) was diluted in sterile PBS or water, filter-sterilized and administered by oral gavage at 50mg in 200 µl PBS daily for 2-3 consecutive days. In addition, OVA was provided continuously in the drinking water at a concentration of 1% w/v until harvest. For low-dose regimen, 10mg OVA in 200 µl PBS was administered for 2 consecutive days with no OVA water given.

Segmentation of gut-draining lymph nodes

Gut-draining LNs were harvested as previously described(Esterházy et al., 2019a). Briefly, the LNs that are relevant for this study include: the hepatic-pancreatic (liv) LN that have little drainage from the gut as a negative control, the hepatic–coeliac (cel) LN along the portal vein, the pancreatic–duodenal (duo) LN draining the duodenum, the upper portion of the main mLN chain (jej) draining the distal duodenum and jejunum, the lower portion of the main mLN chain (ile) draining the ileum, as well as a separate LN (cec) at end of the mLN chain that drains the caecum and colon.

Adaptive T cell transfer and CFSE tracing

Naïve T cells were isolated from pooled LNs and spleens by negative selection using biotinylated antibodies against NK1.1, B220, CD11c, CD11b, TER119 and either CD8α or CD4, followed by anti-biotin MACS beads (Miltenyi Biotec). Purity of transgenic cells was confirmed by flow cytometry ($CD45.1^+V\beta5^+TCR\beta^+CD4^+$ for OT-II cells or $CD45.1^+V\beta5^+TCR\beta^+CD8\alpha^+$ for OT-I cells). Cell viability was determined by Trypan blue staining.

For experiments probing T cell outcomes in the dLNs, OT-II cells were labeled with CFSE Cell Proliferation Kit (Life Technologies) according to the manufacturer's protocol, incubating cells

for 3-5 mins at 37°C, followed by a wash in PBS. A total of 750,000 OT-II or OT-I cells was transferred by retro-orbital injections under isoflurane anesthesia, and LNs harvested 3 (after infections) or 4 (at homeostasis) days post-transfer, as indicated. For experiments probing T cell responses in the intestine, transgenic cells were not CFSE-labeled. On the day of transfer, 200,000 OT-II and 50,000 OT-I cells were injected retro-orbitally. Intestines were procured 7 days post-transfer.

Immunofluorescence staining

Tissues were fixed in 4% PFA/PBS for 2 h at RT and subjected to paraffinization. Paraffin-embedded tissue sections (5μm) were heated at 65°C for 20min, deparaffinized twice in xylene (10 min each), and rehydrated through a graded ethanol series. Sections were permeabilized with 0.1% Triton X-100, blocked for 30 min at RT with blocking buffer (5% donkey serum, 2.5% BSA in PBS) before overnight incubation at 4°C in a humidified chamber with primary antibodies in blocking buffer (see Antibodies section). The following day, slides were washed three times with PBST (PBS with 0.05% Tween-20) for 15 min each, incubated with appropriate secondary antibodies in blocking buffer for 1 h at RT, washed again three times in PBST, and mounted with DAPI Fluoromount G Clear Mounting Media (SouthernBiotech). Images were acquired using an SP8 Lightning confocal microscope (Leica) at the University of Chicago Microscopy Core.

Immunoblotting

Whole-cell or whole-tissue lysates were prepared in RIPA lysis buffer (20 mM HEPES, 0.2 mM EDTA, 300 mM NaCl, 1.5 mM $MgCl_2$, 1% Triton X-100) supplemented with protease inhibitor (Roche) and 1 mM phenylmethylsulphonyl fluoride (PMSF; Sigma). Supernatant from cultured

cells were concentrated using Amicon Ultra Centridugal Filter, 10kDa MWCO (Millipore) and mixed with Laemmli buffer. Samples were separated by SDS-PAGE and transferred onto nitrocellulose membranes (Millipore). Membranes were probed with the indicated primary and secondary antibodies (see Key Resource Table).

Isolation of cells from lymph nodes

For T cell analysis, LNs were dissected into RPMI supplemented with 2% NCS and 1mM EDTA, disrupted using two frosted glass slides, and filtered into 96-well plates. Cells were immediately subjected to Live/Dead and surface marker staining. For APC analysis, LNs were dissected into RPMI supplemented with 2% NCS and 1% HEPES, finely minced, and digested with 2.5 mg/ml Collagenase D (Roche) for 30 min at 37°C. Resulting single-cell suspensions were directly used for Live/Dead and surface marker staining.

Isolation of lymphocytes from small and large intestines

The small intestine was excised, cleared of mesentery, Peyer's patches and fecal contents. Intestines were cut longitudinally and washed three times in PBS containing 1μM DTT to remove mucus. Tissue was cut into ~1cm pieces and incubated in PBS with 30 mM EDTA for 10 min at 37°C with shaking at 230 rpm, followed by a vigorous shake after the incubation. Tissue samples were filtered through a metal sieve and the flow through was collected as intraepithelial fraction (IEL). Tissues were transferred to a new tube containing fresh PBS without EDTA and incubated for another 10 min at 37°C at 230 rpm. Tissues were washed with PBS on a metal sieve, finely chopped and digested in RPMI containing 2% FCS, 1% HEPES, and 2 mg/ml Collagenase 8 (Roche), 200 μg/ml DNase I (Roche) for 30 min at 37°C with gentle agitation at 80 rpm. Digests

were quenched in cold RPMI containing 2% FCS and cell pellets were resuspended in 40% Percoll. Lymphocytes were enriched at the interphase of a discontinuous Percoll gradient (80%/40%) by centrifugation at 2300 rpm for 23 min at RT with slow acceleration and deceleration. Cells were washed and used for flow cytometry analysis.

T cell stimulation

For the detection of OT-I cytokine production, single cell suspensions of isolated lymphocytes were pelleted by centrifugation and resuspended in T cell media containing cell stimulation cocktail (1:500; eBioscience). Cultures were incubated for 4 h at 37°C. Following stimulation, cells were pelleted, washed once with fresh medium, and processed for cell staining.

Flow cytometry

Single-cell suspensions were first stained with LIVE/DEAD™ Fixable Near-IR Dead Cells Stain kits (Invitrogen) in PBS for 10 min at 4°C, followed by surface staining with antibody cocktails (in 1:200 dilution) in FACS buffer (PBS, 1% BSA, 2 mM EDTA) for 20 min at 4°C. For intracellular cytokine detection, cells were fixed and permeabilized with Cytofix/cytoperm™ solution (BD Biosciences) for 20 min prior to staining with intracellular antibodies overnight at 4°C. For transcription factor analysis, cells were incubated in Fixation/permeabilization solution (eBiosciences) for 30 min to 2 h, and subsequently stained with nuclear antibodies overnight at 4°C. All intracellular and nuclear antibodies were diluted 1:100 in 1x Permeabilization buffer (eBiosciences). Fluorescent signals were acquired on an LSR II (BD Biosciences) or a 5-laser Aurora spectral flow cytometer (Cytek) and analyzed using FlowJo software. Cell division index was calculated using FlowJo formula as described

(http://www.flowjo.com/v765/en/proliferation.html), whereby the index represents the fraction of total cell divisions normalized to the estimated starting cell number.

OVA tetramer staining

Single-cell suspensions were enriched for T cells using EasySep™ Mouse T Cell Isolation Kit (Stemcell Technologies) and then incubated with Fc block for 10 min at 4°C to prevent nonspecific binding. For detection of OVA-specific $CD8^+$ T cells, H-2Kb:OVA (SIINFEKL) PE- and APC-conjugated tetramers (NIH Tetramer Core Facility) were added at 1:200 in FACS buffer and incubated for 20 min at RT in the dark. For detection of OVA-specific $CD4^+$ T cells, I-Ab:OVA (HAAHAEINEA) PE- or APC-conjugated tetramers (NIH Tetramer Core Facility) were added at 1:100 in T cell medium and incubated for 2 h at RT in the dark(L. Fu et al., 2025; Rudnitsky et al., 2025). Cells were then washed with FACS buffer before staining with surface antibody cocktail. Each tetramer lot was validated using OVA-immunized mice before use. Tetramer-positive gates were defined using OVA-naïve mice and fluorescence-minus-one controls.

Cell lines

HEK293T cells and Caco-2 cells were cultured in high glucose Dulbecco's Modified Eagle Media (DMEM; Gibco) supplemented with 10% FBS and 100 U/mL penicillin/streptomycin. Spinner-adapted murine L929 cells were maintained in either suspension or monolayer cultures in Joklik's modified Eagle's minimal essential medium (SMEM; Lonza) supplemented to contain 5% fetal bovine serum (FBS; Gibco), 2 mM L-glutamine, 100 U/ml of penicillin, 100 µg/ml of streptomycin (Gibco), and 25 ng/ml of amphotericin B (Sigma). Cultures were maintained at 37°C in a humidified incubator with 5% CO_2.

Lentiviral transduction of ovalbumin expression

pLJM1-Empty (Addgene #91980) plasmid was used as lentiviral vector, which was linearized by Nhel-HF (NEB) at 37°C for 20min and gel purified. Primers were designed using NEBuilder (https://nebuilder.neb.com/#!/) to create the necessary overlap with the plasmid. Insert fragments were created using the designed primers (listed in Key Resource Table) and Phusion High-fidelity DNA polymerase (NEB). The fragments were gel purified. Gibson assembly reaction was set up and the molar ratio for insert-to-vector set to be 1:1. The reaction was incubated at 50°C for 2 h and the product was transformed into *E. coli* DH5α according to the manufacturers' protocol. Transformed *E. coli* cells were plated onto selection agar plates and single colonies were picked and sequences. The correct colonies were expanded, and plasmids were extracted using QIAGEN Plasmid Mini Kit.

Lentivirus was produced in HEK293T cells transfected at 80-90% confluency using Lipofectamine 3000 (Invitrogen) as recommended by the manufacturer using psPAX2 (Addgene) and pMD2.G (Addgene) packaging vectors. Medium was changed 8-12 hours after transfection and supernatant was collected after 48-72 h. Viral media was passed through a 0.45μm filter and mixed with 10 μg ml^{-1} Polybrene (Sigma Aldrich) before being added to recipient cells. Infected cells were treated with puromycin to generate stable cell populations. OVA expression was verified by immunoblotting.

Quantitative real-time PCR

Total RNA from samples was extracted using TRIzol (Thermo Fisher Scientific), treated with DNase I (Invitrogen), and reverse transcribed into cDNA using SuperScript IV kit (Thermo Fisher

Scientific) according to the manufacturer's protocol. Quantitative real-time PCR was performed using Power SYBR Green PCR Master Mix (Applied Biosystems) on Quanstudio 6 Flex machine (Thermo Fisher Scientific). The relative expression of target genes was determined by normalization to housekeeping gene *36B4* and calculated using the formula of $2^{-\Delta Ct} \times 10000$. All data were averaged from at least 2 replicates.

Infections

Reovirus strain type 1 Lang was recovered using plasmid-based reverse genetics(Kobayashi et al., 2007) and purified using $CsCl_2$ gradient centrifugation(Fiske et al., 2024). Titers of purified virus stocks were determined by plaque assay using L929 cells. Mice were inoculated with 10^9 PFU of purified T1L diluted in 100 µL PBS by oral gavage(Fiske et al., 2024). OT-II or OT-I cells were transferred at the time of infection.

S. venezuelensis was maintained in NSG mice by subcutaneous infection with 10,000-30,000 larvae. Fecal pellets from infected NSG mice were collected and spread on Whatman paper, and incubated in water at 28°C. Larvae emerging over 3-4 days were collected to reinitiate the infection cycle or to be used for infection of experimental mice. For experimental mouse infection, 1000 larvae were administrated subcutaneously to male mice. Successful infection was confirmed by appearance of eggs in the fecal content of the infected mice. OT-II cells were transferred 5 days post infection.

C. rodentium was first cultured in 5 ml of LB overnight and then sub-cultured in 200 ml of LB on the next day for 4 h until OD600 reached 0.75 (exponential growth phase). The bacteria were spun down and resuspended in PBS. Mice were gavaged with 1×10^9 CFU in 200 µl, and OT-II cells transferred 8 days later.

Bone marrow chimeras

Recipient mice were lethally irradiated with two doses of 550 rads, 4 h apart, and reconstituted with 2×10^6 to 5×10^6 bone marrow cells delivered by retro-orbital injection under isoflurane anesthesia. Chimeras were used for experiments ≥8 weeks post-transfer.

ApopTag staining and apoptotic index

Apoptosis was detected using ApopTag Fluorescein In Situ Apoptosis Detection Kit (Sigma). Paraffin sections were deparaffinized and rehydrated as described for immunofluorescence staining, followed by ApopTag staining according to the manufacturer's protocol. The stained slides were scanned and analyzed in QuPath. Apoptotic index represents the percentage of $ApopTag^+$ cells over total cell number.

Q-DV-OPh *in vivo* treatment

Mice were treated with the pan-caspase inhibitor Q-VD-OPh dissolved in DMSO and diluted in sterile corn oil. A final concentration of 10 mg/kg was administered by intraperitoneal injection once daily for 5 days, starting 3 days prior to OT-II cell transfer. Control animals received vehicle (DMSO in corn oil) by the same route and schedule.

GW4869 *in vivo* treatment

Mice were treated with exosomal biogenesis inhibitor GW4869 reconstituted in DMSO and then diluted in 300 µl sterile PBS before treatment. GW4869 was administered intraperitoneally at a

dose of 2.5 mg/kg every day for the duration of the experiment, beginning 3 days prior to OT-II cell transfer. Control animals received vehicle injections on the same schedule.

Indomethacin-induced gut injury post intestinal viral infection

Indomethacin was dissolved in sterile sodium carboxymethyl cellulose and administered at 9 mg/kg by oral gavage in a volume of 200 µl 7 days post transgenic T cell transfer and T1L infection. Mice were monitored daily for weight loss and clinical adverse events (which did not occur). Five days after treatment, small intestines were harvested, rolled into "Swiss-rolls", fixed and Hematoxylin and Eosin (H&E)-stained for histological assessment of mucosal injury.

Alum immunization and airway challenge

Seven days after the first oral OVA administration or first tamoxifen treatment, mice were intraperitoneally immunized with 10µg endotoxin-free OVA adsorbed to 100 µl Alhydrogel adjuvant 2% (InvivoGen) in a final volume of 400 µl PBS. Immunization was repeated after 7 days. To induce airway inflammation, mice were anesthetized and intranasally administered 10 µg endotoxin-free OVA in 50 µl PBS (25 µl per nostril) on days 14, 17, and 21 following the first intraperitoneal immunization. Mice were sacrificed one day after the last intranasal challenge.

Bronchoalveolar lavage, lung histology, and infiltrate analysis by flow cytometry

Mice were euthanized, the trachea cannulated, and lungs were lavaged first with 0.5 ml and then 1.0 ml PBS. Total BAL cells were counted after erythrocyte lysis, and stained for flow cytometry. Lungs were perfused via the left ventricle with 10 ml saline to remove residual blood. One lobe

was digested in 400 U/ml collagenase D in HBSS for flow cytometry analysis; eosinophils were identified as $CD45^{+}SSC^{hi}MHCII^{-}CD11b^{+}Ly6G^{int}SiglecF^{+}$. Another lobe was fixed in 4% PFA, embedded in paraffin, sectioned at 5μm, and stained with H&E.

Anti-OVA IgG1, anti-OVA IgE and total IgE ELISA

Mouse sera were collected and stored at -80°C until use. ELISAs were performed according to the manufacturer's protocols using Anti-Ovalbumin IgG1 (mouse) ELISA Kit (Cayman Chemical), Legend MAX™ Mouse OVA Specific IgE ELISA Kit (BioLegend) and Mouse IgE ELISA Kit (Invitrogen). Samples were diluted 1:1000 for anti-OVA IgG1 detection, 1:3 for anti-OVA IgE detection and 1:1000 for total IgE detection.

Allergy and systemic anaphylaxis model

Mice received 1000 *S. venezuelensis* larvae 5 days prior to the first OVA gavage or tamoxifen injection. 200,000 OT-II cells were optionally transferred at 6 days post infection. Sera were collected 21 days post infection. Mice were implanted with subcutaneous electronic temperature probes (Avidity TP-500) one or two days prior to OVA challenge. 24 days post infection, mice were then challenged intraperitoneally with 50 μg or 5 mg endotoxin-low OVA, and body temperature was recorded every 15 min for 90 min to assess anaphylactic responses. Death by anaphylactic shock was also recorded.

Statistical analysis

All statistical analyses were performed using GraphPad Prism 10. Error bars represent the standard error of the mean (s.e.m.). For comparisons involving more than two groups, one-way

ANOVA with Tukey's multiple-comparison *post hoc* test was applied. Comparisons between two groups were performed using a two-tailed unpaired Student's t-test assuming a Gaussian distribution. Survival curves were analyzed using log-rank tests. P-values or representative symbols are noted when differences are less than or equal to 0.1; all other differences were not found to be significant (n.s., $p > 0.1$). Throughout, $*$ designates $p < 0.05$, $**$ $p < 0.01$, and $***$ $p < 0.001$.

Chapter 3. Tissue-specific tolerance mechanisms and lymph node co-drainage shape T cell immunity in the upper digestive system and pancreatic cancer progression

3.1 Summary

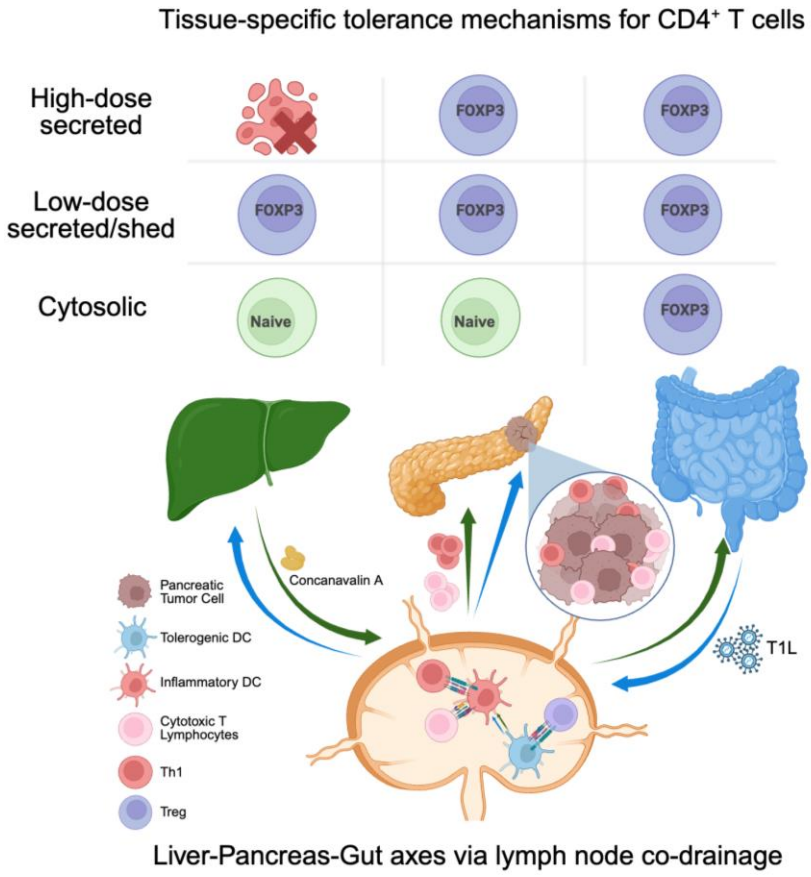


Figure 3.1 Chapter 3 Graphical Abstract

The liver, pancreas, and duodenum share lymph nodes (LNs), providing a unique system to examine how tissue origin of self-antigens shapes T cell fate. Comparing mice expressing ovalbumin (OVA) from distinct subcellular compartments, we found that cytosolic OVA from liver or pancreas, but not gut, was immunologically ignored. High-dose hepatic secreted OVA triggered antigen-specific T cell deletion, whereas secreted pancreatic and intestinal OVA induced regulatory T (Treg) cells, revealing immunological ignorance, clonal deletion and Treg cell

generation as tissue-specific tolerance mechanisms. Of these, LN co-drainage only influenced Treg cell induction, establishing gut-pancreas-liver axes: Intestinal viral infection rendered hepatocyte- and exocrine pancreas-specific T cells inflammatory; liver injury promoted pancreas- and gut-directed responses. These self-reactive T cells caused tissue destruction but enhanced pancreatic tumor control when neoantigen OVA was secreted but not cytosolic. Thus, LN co-drainage and tissue-specific tolerance mechanisms jointly shape immune homeostasis and disease susceptibility in the upper digestive system.

3.2 Introduction

The immune system must balance protective reactions against microbial pathogens and malignancies with tolerance to self and innocuous foreign antigens. Achieving this balance requires finely tuned responses tailored to the distinct environments of individual organs, underscoring the importance of compartmentalization in immunity. Immune cells acquire organ-specific transcriptional and functional profiles shaped by local cues such as antigen exposure, cytokines, and stromal signals(Pao et al., 2018; Weisberg et al., 2021). Similarly, lymph nodes (LNs) draining different tissues provide specialized niches where adaptive immune responses are initiated in a context-dependent manner(Hu & Pasare, 2013). Immune compartmentalization exists even within a single organ, with the regionalization of gut draining LNs being a prime example(Esterházy et al., 2019b). LNs along the gut are immunologically distinct: in response to dietary antigens, proximal gut-draining LNs favor peripheral regulatory T (pTreg) cell induction, whereas distal LNs favor pro-inflammatory RORγt^{+} T cells. These differences parallel distinct dendritic cell profiles(Esterházy et al., 2019b) and stromal cell milieus(Fatkhullina et al., 2025).

The strong influence of the gut LN milieu is further exemplified by LN sharing between organs. The duodenum, liver and pancreas share LNs, with liver LN (livLN) draining the liver and pancreas, celiac LN (celLN) draining all three and duodenal LN (duoLN) draining the pancreas and duodenum(H. Brown et al., 2023b). This anatomical arrangement biases pancreatic β-cell-specific T cells toward the Treg cell lineage under steady state but can redirect them towards pro-inflammatory lineages during duodenal viral infection(H. Brown et al., 2023b). In addition, we recently found that the subcellular origin of intestinal self-antigens influences T cell fate within the same gut-draining LNs(Zhou et al., 2025) and that this effect is mediated by distinct dependencies on antigen-presenting cell subsets and translate into differential disease susceptibilities(H. Brown et al., 2023b; Zhou et al., 2025): When antigen is cytosolic, its presentation strictly depends on cDC1s; when it is secreted or shed from the cell surface it can additionally be loaded onto cDC2s; the generation of self-antigen reactive pTreg cells is largely independent of RORγt^{+} antigen presenting cells(H. Brown et al., 2023b; Zhou et al., 2025). Since pancreatic and hepatic antigens are likely presented primarily by cDC1, the only migratory APC subset in these tissues(H. Brown et al., 2023b), it remains unclear whether the same rules governing antigen access and T cell fate in the gut also apply to antigens derived from these tissues. Understanding this is critical, as it will determine the circumstances under which the liver and pancreas are susceptible to T cell-mediated autoimmunity or cancer control, and when these responses can be shaped by LN co-drainage. This question is particularly relevant in the context of pancreatic ductal adenocarcinoma (PDAC), a malignancy with poor prognosis, frequent hepatic metastasis, and limited responsiveness to immunotherapies(Ullman et al., 2022).

LN sharing provides an excellent platform to interrogate whether T cell outcomes in response to self-antigens are primarily shaped by the tissue of origin or by the environment of the

draining LN. In this study, we investigated whether the default peripheral tolerance mechanism of the gut, pTreg cell induction, also applies to self-antigens derived from the liver and pancreas when assessed within the same, shared LNs and using a standardized antigen, ovalbumin (OVA). We then examined how tolerance programs can be perturbed by selectively inducing inflammation either in the antigen-expressing tissue or in a co-drained organ. Finally, we assessed how tissue origin, subcellular localization and LN co-drainage intersect in dictating the susceptibility to T cell rewiring in the context of PDAC.

3.3 Results

3.3.1 Tissue-specific tolerance mechanism, subcellular source of self-antigen and antigen dose dictate T cell fate of self-reactive CD4$^+$ T cells at homeostasis

To determine how the same self-antigen shapes T cell responses when expressed in different tissues within a shared lymphatic network, we engineered three mouse lines that express OVA in distinct forms, secreted (sOVA), cytosolic (cOVA), or transmembrane (tmOVA), under control of tissue-specific Cre drivers(Zhou et al., 2025). Using inducible *Alb$^{Cre\text{-}ERT2}$* for hepatocytes and *Ptf1a$^{Cre\text{-}ERT2}$* for exocrine pancreas, we expressed OVA in the liver, exocrine and endocrine pancreas, respectively (Fig. 3.9A-D). Immunofluorescence imaging confirmed the subcellular distribution of each OVA variant (Fig. 3.9E), and no cross-expression was detected in non-target tissues within the triad (Fig. 3.9F-H).

To assess homeostatic CD4$^+$ T cell responses, we adoptively transferred OT-II cells into OVA-expressing mice and quantified their proliferation in draining LNs 96 h after transfer. At steady state, tmOVA induced robust OT-II proliferation in liver and pancreas-draining LNs, whereas cOVA did not (Fig. 3.2A-D). The degree of OT-II proliferation mirrored the relative

drainage of each tissue into the co-drained LNs (Fig. 3.2B, D) as previously identified(H. Brown et al., 2023b), and in line with the observation that tmOVA is seen by the immune system through ectodomain shedding(Zhou et al., 2025). A similar drainage hierarchy was observed for β-cell self-antigens, using *Ins1*$^{Cre\text{-}ERT2}$, in which only sOVA and tmOVA elicited detectable proliferation (Fig. 3.9I). However, the number of OT-II cells recovered from each LN was insufficient to allow phenotypic analysis. To overcome this problem, we used streptozotocin (STZ) in the subsequent experiments to selectively induce β-cell death, enhancing antigen availability in draining LNs for phenotypic profiling. In contrast, all three OVA forms expressed in the gut elicit strong T cell proliferation(Zhou et al., 2025), consistent with the constant tissue turnover in the intestine, suggesting immune ignorance as the main mechanism for cytosolic self-antigen tolerance in tissues such as liver and pancreas with low cell turnover. When hepatocyte or pancreatic acinar cell death was induced in mice expressing cOVA, OT-II cells proliferated in the respective draining LNs, reinforcing this notion (Fig. 3.2E, F).

Pancreatic sOVA led to stronger OT-II proliferation than tmOVA (Fig. 3.2C, D), in line with the observation that OVA released from tmOVA is present at lower levels than sOVA(Zhou et al., 2025). In contrast, hepatic sOVA, but not tmOVA, induced rapid OT-II clonal deletion (Fig. 3.2A, B). Since within the liver we observed that much more sOVA than tmOVA was expressed on the protein level (Fig. 3.9C), we speculated that hepatic antigen dose, rather than an inherent difference between secreted and transmembrane-shed antigen, was responsible for this striking difference in effect on $CD4^+$ T cells. To test if antigen alone drove this deletion, we first attempted to lower OVA expression by reducing tamoxifen dosing. However, we discovered that *Alb*$^{Cre\text{-}ERT2}$ exhibits sufficient basal Cre activity even without tamoxifen to induce *OVA* expression (Fig. 3.9J, K). The expression level was comparable to that in tamoxifen-induced *Ptf1a*^{sOVA} mice (Fig. 3.9K,

L), which is a pertinent comparison since the liver and pancreas share similar LN drainage pattern, and was sufficient to delete OT-II cells (Fig. 3.2G). Such leakiness is not uncommon for tamoxifen-inducible Cre systems(Álvarez-Aznar et al., 2020), though not previously reported for $Alb^{Cre\text{-}ERT2}$. In our system, high *Alb* expression and close loxP spacing likely both contribute to spontaneous recombination. We therefore delivered an adeno-Cre virus to the liver of Cre-negative sOVA mice by tail-vein injection instead. We chose an adenovirus dose that does not prevent OT-II cell deletion in Alb^{sOVA} mice (Fig. 3.2H, I), as we discovered that high-dose viral infection can break this tolerance mechanism (*data not shown*). This resulted in hepatic OVA expression that was much lower than that in Alb^{sOVA} mice (Fig. 3.9K). This level triggered robust OT-II proliferation in liver-draining LNs with no evidence of T cell deletion (Fig. 3.2H, I). These data together indicate that the liver, a tissue with tolerogenic nature(Calne et al., 1969; Fumagalli & Iannacone, 2024; Kawashima et al., 2024), has a mechanism that distinguishes high-dose from low-dose self-antigen and selectively deletes T cells recognizing high-dose antigen at homeostasis. Notably, this liver-specific tolerance mechanism was disrupted when the liver was perturbed by the hepatotoxic agent carbon tetrachloride (Fig. 3.2J).

Given that pTreg cell induction is the dominant peripheral tolerance program for intestinal self-antigens(Zhou et al., 2025), we next examined whether hepatic and pancreatic self-antigens utilize a similar program by assessing OT-II cell fate in Alb^{tmOVA}, $Ptf1a^{sOVA}$, $Ptf1a^{tmOVA}$ and $Ins1^{sOVA}$ mice in the shared LNs. The frequencies of T-BET$^+$ Th1 cell were consistently highest in the liver LN (livLN), which receives the greatest lymphatic drainage from the liver and pancreas (Fig. 3.10A, B). FOXP3$^+$ pTreg cell percentages also were highest in livLN when OVA originated from the liver, but also when it came from exocrine pancreas. This was in contrast to when OVA was expressed in pancreatic β cells, which led to the highest abundance of pTreg cells in duodenal LN

(duoLN) (Fig. 3.2K), mirroring the distribution of pTreg cells specific for native islet antigens(H. Brown et al., 2023b). We hypothesized that this difference in response to exocrine versus endocrine antigen may be because if antigen is limiting, pTreg cell induction reflects antigen availability and that the use of STZ to release β-cell antigen in a burst overcame this limitation, revealing the superior pTreg induction potential of the duoLN. Indeed, when we used cerulein to acutely damage the exocrine pancreas in *Ptf1a*^{sOVA} mice, presumably leading to a pulse of antigen release, we observed a pTreg cell pattern similar to that seen with endocrine sOVA (Fig. 3.2L).

Overall, our data show that each tissue, depending on its physiological function and immune characteristics, employs distinct tolerance mechanisms toward self-antigens from different subcellular compartments. These factors, together with the amount of antigen delivered to LNs, dictate T cell fates at homeostasis.

3.3.2 Type 1 and but not type 2 intestinal infections shifts exocrine-pancreas-reactive T cell fate in LNs shared between the pancreas and duodenum

Intestinal infections have been shown to reprogram T cell responses against dietary and self-antigens in the gut(Bouziat et al., 2017; Zhou et al., 2025). We previously demonstrated that certain intestinal viral infections, such as with reovirus strain type 1 Lang (T1L) and murine norovirus, can render islet-specific T cells more pro-inflammatory without spreading beyond the intestine(H. Brown et al., 2023b). This occurs via changes in the transcriptional profile of cDC1s through LN co-drainage(H. Brown et al., 2023b). cDC1s are the main migratory dendritic cell population in the pancreas and liver and sample islet antigens(H. Brown et al., 2023b), and are also the primary DC subset that induces Th1 and CTLs. By contrast, migratory cDC2s, abundant in the gut, promote Th2 and Th17 differentiation but are virtually absent in pancreas (and liver)(H. Brown et al., 2023b). Based on this, we hypothesized that only cDC1-dependent, type 1 intestinal

infections would alter T cell outcomes in the pancreas. To test this, we first infected *Ins1*^{sOVA} and *Ptf1a*^{sOVA} mice with the helminth *S. venezuelensis*, a type 2 infection. In both models, *S. venezuelensis* had no major impact on the frequencies of GATA3^{+} and FOXP3^{+} OT-II cells (Fig. 3.10C-F), as opposed to a significant increase of GATA3^{+} and decrease of FOXP3^{+} OT-II in *Villin*^{sOVA} mice(Zhou et al., 2025). This strongly suggests that pancreatic antigen is not loaded onto cDC2s, at least not cDC2B cells. By contrast, when we inoculated *Ins1*^{sOVA} perorally (a term used interchangeably here with intragastric infection using a gavage needle) with T1L, we observed a marked increase in OVA-specific Th1 cells and a corresponding decrease in pTreg cells in the celiac (cel-) and duo-LNs (Fig. 3.10G, H), consistent with our previous findings with endogenous islet antigens(H. Brown et al., 2023b).

To determine whether this LN-co-drainage-driven regulation of endocrine pancreas-reactive T cells can be extended to the exocrine pancreas, we inoculated *Ptf1a*^{sOVA} and *Ptf1a*^{tmOVA} mice perorally with T1L. We again observed increased Th1 cell differentiation of OT-II cells in the same co-drained LNs, although with variable concomitant reduction in pTreg cell numbers (Fig. 3.3A-D, Fig. 3.11A-C). In parallel, OT-I cells in these LNs of T1L-infected mice acquired enhanced cytotoxic features, including expression of granzyme B (GzmB), interferon-γ (IFNγ), and tumor necrosis factor-α (TNFα) (Fig. 3.3E-I, Fig. 3.10A, 3.11D-G). We also used OVA tetramers to identify endogenous OVA-specific T cells. Again, we observed an increase in GzmB^{+}CD8^{+} and T-BET^{+}CD4^{+} T cells and a modest reduction in FOXP3^{+}CD4^{+} T cells among tetramer^{+} cells in the co-drained LNs (Fig. 3.3J-P). Notably, in both the OT-I/OT-II and endogenous OVA-specific T cell contexts, this pro-inflammatory shift was absent in the livLN (Fig. 3.3A, E, J, M), a major pancreatic LN that however does not drain the gut. This finding highlights the specificity of the inter-organ crosstalk in that it occurs only in LNs that are co-

drained by the tissue expressing the antigen and the tissue being perturbed. Furthermore, we hypothesized that LN co-drainage would only influence T cell fate for antigens that are actively being surveyed. Consistent with this, OT-II cells remained non-proliferative even in T1L-infected *Ptf1a*^{cOVA} mice (Fig. 3.11H). These findings indicate that when an exocrine pancreatic self-antigen is available for immune presentation and recognition, intestinal infection can modulate exocrine-pancreas-specific T cell immunity, promoting inflammatory phenotypes.

To further solidify the requirements for LN co-drainage and regionality of the infection, we inoculated *Ptf1a*^{sOVA} mice intranasally with T1L(Nygaard et al., 2013), a route that targets the lung, an organ not co-drained with the pancreas. As anticipated, we observed increased CTLs cells among endogenous CD8$^+$ T cells in the mediastinal LN (mtLN), confirming successful infection (Fig. 3.12E). However, we did not detect major changes in the frequencies of CTLs in the pancreatic LNs of intranasally inoculated mice, in contrast to the robust response observed following peroral inoculation (Fig. 3.12A-D). Similarly, OVA-specific Th1 cells did not increase in the pancreatic LNs (Fig. 3.12F, G), despite intranasal T1L inoculation inducing more Th1 cells in the polyclonal compartment in the mtLN (Fig. 3.12H).

Together, these findings establish the requirements for immune crosstalk between gut and pancreas through LN co-drainage(H. Brown et al., 2023b), while expanding it to the exocrine pancreas.

3.3.3 Intestinal reovirus-induced exocrine pancreas-reactive pro-inflammatory T cells migrate to the pancreas, leading to exocrine tissue destruction

To determine whether the T cells activated by reovirus T1L in LNs migrate to the pancreas and mediate pathological effects, we inoculated *Ptf1a*^{sOVA} mice perorally with T1L at the time of OT-I and OT-II co-transfer. Immune cells isolated from the pancreas 7 days later had a substantial

increase in the percentage and total number of OT-I and OT-II cells (Fig. 3.4A-D). In parallel, we detected increased infiltration of endogenous $CD4^+$ and $CD8^+$ T cells (Fig. 3.12I, J). Phenotypic analysis showed a higher proportion of $GzmB^+$ OT-I cells and $T\text{-}BET^+$ OT-II cells (Fig. 3.4E, F), indicating an inflammatory signature in the pancreas. Similar trends were observed among endogenous T cells, with a significantly higher percentage of $CD8^+$ T cell expressing GzmB and an elevated Th1/pTreg cell ratio (Fig. 3.12K-O). Immunofluorescence staining confirmed widespread infiltration of both OVA-specific and polyclonal T cells into the pancreatic parenchyma (Fig. 3.4G). Histological analysis showed severe tissue damage, characterized by immune cell infiltration, necrosis, and interstitial edema (Fig. 3.4H, I). The percentage of apoptotic cells in the pancreas following T1L infection also was significantly increased (Fig. 3.4J, K). Of note, in the gut T1L infection in combination with OVA reactive cell transfer is not sufficient to cause measurable pathology(Zhou et al., 2025), suggesting that the pancreas, perhaps because it is inherently less regenerative than the gut epithelium, is more susceptible to damage. However, these pancreatic effects were not observed in the absence of OVA-specific T cell transfer (Fig. 3.4H, I), suggesting that while exogenous OT-I and OT-II transfer may overwhelm any pre-existing OVA-specific Treg cells in the pancreas, it remains a strong peripheral tolerance program to prevent pancreatic auto-destruction in responses to gastrointestinal infections.

These findings demonstrate that the intestinal reovirus infection-induced increase of inflammatory pancreas-reactive T cells in co-drained LNs correlates with the subsequent emergence of these activated autoreactive T cells in the pancreas where they mediate tissue destruction in the absence of pancreatic infection(H. Brown et al., 2023b).

3.3.4 Intestinal reovirus leads to accelerated tumor progression in a genetic PDAC model

PDAC, the most common cancer of the exocrine pancreas, is an aggressive malignancy characterized by poor prognosis and low lymphocyte infiltration(Ullman et al., 2022). The PDAC microenvironment is immunosuppressive, with increased tumor-associated macrophages and Treg cells and diminished Th1 and CTL cell numbers, contributing to impaired anti-tumor immunity(J. Zhang et al., 2022). We therefore hypothesized that LN co-drainage could be exploited to modulate disease outcome by rewiring T cells recognizing tumor cells. To this end, we interbred KPC mice (*Ptf1a*$^{Cre\text{-}ERT2/w}$*p53*$^{fl/fl}$*Kras*^{G12D}) with sOVA mice to produce animals in which sOVA is expressed in transformed pancreatic acinar cells (PDAC-sOVA mice). Tumor initiation was induced with tamoxifen containing diet at 3.5 weeks of age, followed by a 14-day period of tumor establishment. At that point, we adoptively transferred OVA-specific T cells into the mice, inoculated them perorally with reovirus T1L and either assessed T cell fate in the pancreatic LNs 3 days later or tumor burden 3 weeks later (Fig. 3.5A). As observed in *Ptf1a*^{sOVA} mice, T1L robustly induced the generation of cytotoxic OT-I cells (Fig. 3.5B) and T-BET^{+} OT-II cells at the expense of pTreg cells in the co-drained LNs of PDAC-sOVA mice (Fig. 3.5C, D), showing that intestinal infection can induce type 1 immunity to pancreatic neoantigen in the context of PDAC. Perhaps unexpectedly, however, T1L infection was associated with significantly accelerated tumor progression, as assessed by the percentage of tumor area within the pancreas (Fig. 3.5E-H). This effect was also evident without transferring OVA-recognizing T cells, suggesting that the endogenous repertoire of OVA-reactive cells was sufficient to mediate accelerated tumor progression in the presence of LN perturbation. T1L-infected mice that received OT-I or both OT-I and OT-II cells showed the most severe pathology, with 95-100% lesion area (Fig. 3.5F-H), indicating that CD8^{+} T cells are primary mediators of this effect. To directly test the impact of CD8^{+} T cells on the oncogenesis of PDAC-sOVA mice, we administered a CD8β-neutralizing

antibody beginning 7 days after T1L inoculation, to allow time for viral clearance, and continued antibody administration every 4 days. CD8-depleted mice showed significantly reduced tumor burden relative to isotype-treated controls (Fig. 3.5I, J), confirming that $CD8^+$ T cells are the primary mediators of reovirus-mediated tumor acceleration. We concluded that the tumor-promoting effect of T1L in the genetic PDAC model was caused by the ubiquitous expression of OVA, which rendered nearly all pancreatic acinar cells susceptible to attack by OVA-specific T cells, including those that had not yet undergone full transformation and pushing them toward dedifferentiation. In addition, fully transformed pancreatic carcinoma cells employ multiple immunosuppressive mechanisms, making them less susceptible to T cell-mediated killing than pre-neoplastic or early-stage cells. However, these results underscore the capacity of intestinal viral infection to reshape pancreatic T cell immunity through shared LNs, with a potent influence on PDAC progression.

3.3.5 Intestinal reovirus infection enhances T cell infiltration and tumor control in an orthotopic PDAC model

In human PDAC, tumor initiation occurs neither uniformly in all acinar cells simultaneously, nor do all acinar cells express neoantigens. Therefore, to model a scenario in which only tumor cells express a neoantigen and not all acinar cells have transformation potential, we employed an orthotopic system using a syngeneic KPC-derived tumor cell line(Apiz Saab et al., 2023). This system also permitted us to easily test if the subcellular compartment in which a tumor antigen is expressed dictates the capacity of the adaptive immune system to exert anti-tumor control. To this end, we stably transduced KPC cells with either a control lentiviral vector (empty vector, EV) or a vector encoding sOVA, cOVA or tmOVA, whereby sOVA and cOVA were expressed at similar protein levels and therefore used for subsequent analyses (Fig. 3.13A). The

KPC cells were injected into the pancreas of B6 mice, and tumors were allowed to develop for 11 days. In the absence of further experimental interference, all three KPC lines gave rise to similarly sized tumors (Fig. 3.13B, C). To confirm antigen drainage and T cell priming in the LNs, mice were administered OT-I and OT-II cells and inoculated perorally with reovirus T1L or not (Fig. 3.6A). We observed robust proliferation of OT-II cells in pancreatic LNs only when KPC-sOVA but not when KPC-cOVA cells were injected, with OT-II cells in livLN showing the highest proliferation, followed by celLN and duoLN (Fig. 3.13D), mirroring the previously mapped pancreatic drainage(H. Brown et al., 2023b). Although proliferation did not significantly change following T1L infection (Fig. 3.13D), we detected increased frequencies of $GzmB^+$ OT-I and $T\text{-}BET^+$ OT-II cells in co-drained LNs, indicating that T1L infection led to inflammatory T cell polarization in the orthotopic setting (Fig. 3.6B, C, 3.13E-H).

We next tested the effect of T1L infection on tumor control. Mice were injected orthotopically with either 50,000 KPC-EV, KPC-sOVA or KPC-cOVA cells. On day 11, when tumors were similarly established in all groups (Fig. 3.13B, C), mice were administered OT-I and OT-II cells and inoculated perorally with T1L (Fig. 3.6D). T1L infection reduced tumor burden in KPC-sOVA but not KPC-cOVA or KPC-EV tumor-bearing mice relative to the uninfected controls (Fig. 3.6E-G), in congruence with the observations in the LNs where KPC-cOVA elicited no OVA-specific T cell responses (Fig. 3.6B, C). Immunofluorescence staining revealed significantly increased infiltration of both OVA-specific and endogenous T cells in the pancreas of T1L-infected mice with KPC-sOVA tumors but not KPC-EV or KPC-cOVA mice (Fig. 3.6H and *data not shown*). To confirm that LN co-drainage was required for this effect, we compared tumor outcomes in mice inoculated with T1L either intragastrically or intranasally. Intragastric

inoculated showed superior tumor control than that following intranasal inoculation, supporting the requirement for direct gut-to-pancreas immune interaction for this modulation (Fig. 3.6I, J).

In the next series of experiments, we determined whether peroral administration of a tumor-associated neoantigen could enhance anti-tumor immunity in the presence of an intestinal infection (Fig. 3.13I). A single dose of oral OVA was sufficient to increase the number of $GzmB^+$ OVA-specific T cells in pancreatic draining LNs (Fig. 3.13J, K), which reduced tumor size, particularly in T1L-infected mice with KPC-sOVA tumors (Fig. 3.13L, M). Given the aggressive nature of this tumor cell line, we hypothesized that the intervention might be more effective if the initial tumor burden was lower. Therefore, we repeated the experiment using a lower tumor inoculum (5,000 cells; Fig. 3.13I). In this setting, we again observed a reduction in tumor burden, with the T1L-infected, sOVA-tumor-bearing group having the most significant response, as approximately 25% of the mice achieved complete tumor clearance at the end point of the experiment (Fig. 3.13N, O). Together, these data demonstrate that intestinal infection can enhance tumor-specific T cell responses and reduce tumor burden in PDAC through LN co-drainage when the antigen is confined to the tumor cells.

3.3.6 Intestinal reovirus infection renders liver-specific T cells more pro-inflammatory leading to liver damage

In our previous experiments we largely ignored the role of liver in tri-organ immune crosstalk, despite it being a major lymph-producing organ. To assess whether immune-modulation by intestinal type 1 infections extends to the liver, we perorally inoculated Alb^{sOVA} and Alb^{tmOVA} mice with T1L, followed by OT-II transfer. In Alb^{sOVA} mice, T1L did not reverse OT-II clonal deletion (Fig. 3.14A, B), reinforcing our suspicion that this is a liver-intrinsic phenomenon. In Alb^{tmOVA} mice however, we observed increased Th1 and reduced pTreg cell frequencies specifically

in the celLN, the primary LN co-draining the liver and gut (Fig. 3.7A-C, 3.14C). In the $CD8^+$ T cell compartment, OT-I cells from infected mice displayed an enhanced cytotoxic profile in both celLN and duoLN (Fig. 3.7D-G, 3.14D). We suspect that the duoLN response reflects a combination of greater $CD8^+$ T cell sensitivity to antigen and possible shifts in hepatic drainage patterns under inflammatory conditions.

As seen in the pancreas, activated T cells also subsequently migrated to the liver. Both OT-I and OT-II cells accumulated in the liver following perioral T1L inoculation, with increases observed in both the percentage and absolute number of each (Fig. 3.7H, I, 3.14E, F). Endogenous $CD8^+$ but not $CD4^+$ T cells also infiltrated the liver in greater numbers (Fig. 3.14G, H). Phenotypic analysis using flow cytometry showed higher frequencies of hepatic $GzmB^+$ OT-I and $T\text{-}BET^+$ OT-II cells upon T1L infection (Fig. 3.7J, K). Endogenous $CD8^+$ T cells also increased in number and cytotoxicity (Fig. 3.14G, I, J), while the effect on endogenous $CD4^+$ T cells was more limited (Fig. 3.14H, K-M). Histological analysis of liver sections revealed localized immune cell aggregates accompanied by tissue damage (Fig. 3.7L). Immunofluorescence staining showed extensive infiltration of both OVA-specific transferred T cells and endogenous T cells throughout the hepatic parenchyma (Fig. 3.7M), while ApopTag staining demonstrated a marked increase in apoptotic cells, notably in areas densely populated by immune infiltrates (Fig. 3.7N).

Collectively, these findings demonstrate that intestinal reovirus infection impact T cell immunity not only in the endocrine(H. Brown et al., 2023b) and exocrine pancreas but also in the liver, revealing a gut-to-liver immune axis through LN sharing.

3.3.7 Hepatotoxic concanavalin A induces pancreas- and gut-reactive Th1 cells and reduces pTreg cells

We finally sought to determine whether perturbations of the liver induce immune shifts in the pancreas or intestine through shared LNs, thus, if immunological liver-to-gut or -pancreas axes exist. Since human hepatitis viruses do not infect mice(Lanford et al., 2011; Winer et al., 2016), current mouse models for hepatitis viruses rely on humanized systems(Dorner et al., 2011; Winer et al., 2016) or other hepatotropic viruses that also infect the pancreas(Burch et al., 1973; Tomasiewicz et al., 2005; L. Yang et al., 2024). Therefore, we instead used a non-viral model: Concanavalin A (conA), which induces autoimmune hepatitis and causes liver-specific damage by a Kupffer cell- and T cell-dependent type 1 immune response(Marlies Ballegeer and Claude Libert, 2016). We first tested the effect of conA on T cell responses in Alb^{tmOVA} mice. Following conA administration, we observed significant liver injury (Fig. 3.8A) and increased OT-II proliferation in liver-draining LNs, as well as ectopic drainage into duoLN (Fig. 3.15A). Notably, pTreg cell induction was suppressed in livLN and celLN, and Th1 cells increased in these nodes (Fig. 3.8B, C), establishing conA as an agent for probing liver-driven immune regulation by LN co-drainage.

To determine whether conA-induced liver inflammation alters T cell responses to pancreatic and intestinal self-antigens, we treated $Ptf1a^{tmOVA}$ or $Villin^{tmOVA}$ mice, which express the same antigen as Alb^{tmOVA}, with conA and monitored T cell differentiation. In $Ptf1a^{tmOVA}$ mice, conA treatment led to an increase in Th1 cells and a reduction in pTreg cells within livLN (Fig. 3.8D-G), the LN with the highest shared drainage between liver and pancreas. Similarly, in $Villin^{tmOVA}$ mice, conA treatment led to an increase in Th1 cells and a reduction in pTreg cells, specifically within the celLN, which is the only LN shared by liver and duodenum (Fig. 3.8H-K). Comparable results were obtained in experiments using $Ptf1a^{sOVA}$ (Fig. 3.15B-C) and $Villin^{sOVA}$ (Fig. 3.15D-E) mice. Although pancreatic antigens are also drained into celLN and duoLN, and gut antigens are drained into multiple gut draining LNs, no significant T cell phenotypic changes were observed in

those LNs. This result suggests that the observed effects are confined to the LNs co-drained with the liver and are not systemic, excluding the possibility that our observations are due to conA directly affecting T cells.

Thus, liver perturbation also reciprocally regulates T cell immunity of other co-drained tissues, establishing liver-to-gut/pancreas axes and highlighting LN co-drainage as a critical immunological mechanism for inter-organ immune crosstalk.

3.4 Discussion

In this study, we uncovered that tissue-specific tolerance mechanisms and LN co-drainage collectively dictate T cell immune outcomes in the upper digestive system. By standardizing the antigen and T cell receptor affinity, and leveraging the fact that the liver, pancreas and duodenum drain into the same LNs, we disentangled the contribution of LN environment and tissue source to T cell polarization. Specifically, we discovered that liver and pancreas, which are functionally and immunologically different from the gut, adopt distinct tissue-specific mechanisms for maintaining tolerance to self-antigens from different subcellular compartments and with different dosages at homeostasis. Using an intestinal perturbation, we expanded on our previous findings(H. Brown et al., 2023b) and showed that one of tolerance programs, pTreg cell differentiation, can also be disrupted in the exocrine pancreas (and liver) through LN sharing. While this disruption can result in pancreatic autoimmunity, it has the potential of being harnessed to enhance PDAC tumor control. Finally, our study identified reciprocal immune regulation between the liver and gut through LN co-drainage, establishing liver-pancreas-gut axes.

Maintaining tolerance to self-antigens is critical for preventing autoimmunity. Because central tolerance is incomplete(Xing & Hogquist, 2012), multiple peripheral tolerance mechanisms

have evolved to prevent aberrant responses to self. However, it remains unclear whether all tissues preferentially employ a common mechanism, or whether, analogous to inflammatory responses, they adapt their tolerance mechanisms to their physiological roles. We found that peripheral tolerance is sculpted jointly by tissue of origin and the subcellular localization of antigens. Cytosolic self-antigens in tissues with low cell turnover, like the pancreas and liver, are tolerated through immune ignorance, as antigen levels remained below the threshold required for T cell activation. In contrast, secreted or membrane-shed self-antigens preferentially induced pTreg cell differentiation, particularly in the gut(Zhou et al., 2025). Interestingly, high levels of secreted self-antigen from the liver triggered pruning of antigen-specific T cells, suggesting a liver-specific, dominant deletional strategy when encountering highly expressed hepatic self-antigens. These differences likely reflect tissue-specific immune pressures. The gut, continuously exposed to foreign antigens, relies heavily on active suppression to maintain immune quiescence, favoring pTreg cell induction, which enables flexible rewiring of immune responses during inflammatory events such as epithelial breach. The pancreas, physically connected to the duodenum and susceptible to pancreatic ductal reflux, may employ a similar mechanism to coordinate local immune responses with the gut. In contrast, the liver is largely sterile, so immune responses there, besides systemic infections, may be primarily triggered by local self-antigens or systemic antigens in the serum, including those derived from the gut. As a key site for producing highly abundant serum proteins and sampling blood-borne antigens of other origins(Jenne & Kubes, 2013), clonal T cell deletion in response to the most abundant secreted proteins may be the most efficient strategy for maintaining tolerance in the liver, although the precise mechanism or cellular contributors remain to be defined in future investigation. Immunosuppressive outcomes such as chronic infections(Ferri et al., 2010; Vento et al., 1984) or tumor outgrowth(Huang et al., 2022) could be

a consequence of “mistaking” pathogens or cancer cells for liver-self, and, on the flipside, if this tolerance mechanism is broken, hepatic autoimmunity could ensue(Ferri et al., 2010; Vento et al., 1984). Thus, identical antigens can induce distinct T cell fates in the same LNs depending on tissue origins, underscoring that tissues employ specialized tolerance programs based on their antigen accessibility, local immune environment, and physiological function. Understanding these tissue-specific mechanisms has broad implications: Autoimmune diseases may emerge when these programs fail, while cancers may exploit them to evade immune detection. By defining how tolerance varies by tissue, we can design more precise immunotherapeutics that either reinforce these programs to prevent autoimmunity or temporarily override them to boost anti-tumor immunity.

Our study also expands the physiological relevance of LN co-drainage by establishing liver-pancreas-gut axes and demonstrating the reciprocal immune regulation between these organs. The bidirectional communication introduces an additional layer of immune modulation that must be considered alongside local and systemic factors. Our disease studies were mostly conducted with OVA-specific T cell transfer and in the presence of relatively recently introduced self-antigens. tetramer staining of OVA-specific T cells revealed that the endogenous repertoire can also react to OVA under these conditions and participate in pathology. This may model the rare instances of autoimmunity in humans. From a translational perspective, this mechanism presents exciting therapeutic opportunities. The gut, which is readily accessible, may serve as a non-invasive entry point for modulating immune responses in more secluded organs like the liver or pancreas through shared lymphatic drainage. This anatomic and immunologic connection opens the possibility of developing new strategies to either dampen unwanted autoimmune responses or enhance anti-tumor or anti-viral immunity by targeting the immune system at a regional level.

Another notable finding in this study is that the pancreas is markedly more susceptible to autoimmune destruction than the liver (Fig. 3.4 and Fig. 3.5) and gut(Zhou et al., 2025), even when exposed to the same number of antigen-specific T cells and equivalent inflammatory stimuli. Although differences in the number of infiltrating T cells per gram of tissue or variation in local tolerogenic milieu may contribute, these results also suggest that the consequences of LN co-drainage are not uniform across organs. Instead, they appear to be shaped by each tissue's intrinsic regenerative and immunological capacities. The pancreas, with its limited regenerative ability compared to the liver or gut, appears particularly vulnerable to immune-mediated injury once an autoimmune response is initiated. Consequently, the inflammation mediated by shared LNs exerts more destructive and lasting effects on the pancreas than on more regenerative tissues. Physiologically, this distinction may help explain the higher incidence and chronicity of autoimmune diseases targeting the pancreas, such as type 1 diabetes, whereas comparable insults in the liver are more often transient or self-resolving. Exploring the impact of LN co-drainage on primary or metastatic liver tumors represents an interesting direction for future investigation.

In our experiments, genetically engineered and orthotopic PDAC mouse models had markedly different outcomes in response to elevated antigen-specific T cell infiltration (Fig. 3.5 and Fig. 3.6), highlighting the importance of choosing suitable models for studies of PDAC immunobiology. Genetically engineered mouse models (GEMMs), like the KPC model, recapitulate the gradual tumor evolution and desmoplastic stroma formation characteristic of human PDAC, but fail to capture the stochastic nature of tumor initiation in humans, in which only a subset of acinar cells gradually dedifferentiates and adopt ductal features. Since the pancreas is a tissue prone to stress(Kubisch & Logsdon, 2008), acinar cells have the capacity to partially dedifferentiate under stress conditions(Backx et al., 2022; Rooman & Real, 2012). In this context,

indiscriminate killing by antigen-specific T cells, due to the ubiquitous expression of the model neoantigen, may exacerbate tissue stress and inadvertently accelerate acinar-to-ductal metaplasia, thereby worsening PDAC progression. In contrast, orthotopic transplantation mouse models offer synchronized tumor onset and tighter temporal control and limit the expression of neoantigens to tumor cells. As such, only malignant cells become targets of immune cells, allowing more specific T cell-mediated tumor cell killing. Our data also emphasize the importance of intervention timing. While boosting antigen-specific T cell infiltration can be beneficial, the therapeutic effect diminishes as the tumor burden increases. This phenomenon is likely due to physical and immunological barriers established by the stroma, including extracellular matrix deposition and exclusion of effector cells from tumor nests(Kabacaoglu et al., 2018). Moreover, advanced lesions may develop additional resistance mechanisms, such as antigen loss or immune checkpoint upregulation(Kabacaoglu et al., 2018). Collectively, our findings suggest that model selection and timing of immune intervention must be carefully aligned with the specific biological question being addressed in PDAC research.

Collectively, our study reveals the complexity of forces shaping adaptive immune outcomes in the upper digestive system, offering insights into hitherto idiopathic diseases like autoimmunity and cancer, as well as their heterogeneity and interindividual variability.

3.5 Limitations of the study

Our studies rely on a model antigen, OVA. While we were able to confirm key results using tetramers that detect endogenous OVA-reactive T cells, it is likely that the mechanisms we reveal are not as active as when we deliberately transfer OVA reactive T cells. This is a general limitation in adoptive transfer systems used in immunology. We concentrated the current study on exploring

the consequences of the combined effect of LN co-drainage and antigen source to pancreatic diseases, leaving understanding the liver's potentially unique deletion-inducing mechanisms to handle high dose self-antigens and the implications of LN co-drainage for liver disease for future investigations. That antigen dose may influence T cell response, and that tamoxifen-inducible system do not permit antigen dose control in the liver, were both unanticipated findings. Consequently, our experimental design was not suited to formally address the antigen dose-T cell response relationship. We predict that doxycycline- rather than a tamoxifen-inducible system would be required to formally answer this intriguing question in the future.

3.6 Figures and figure legends

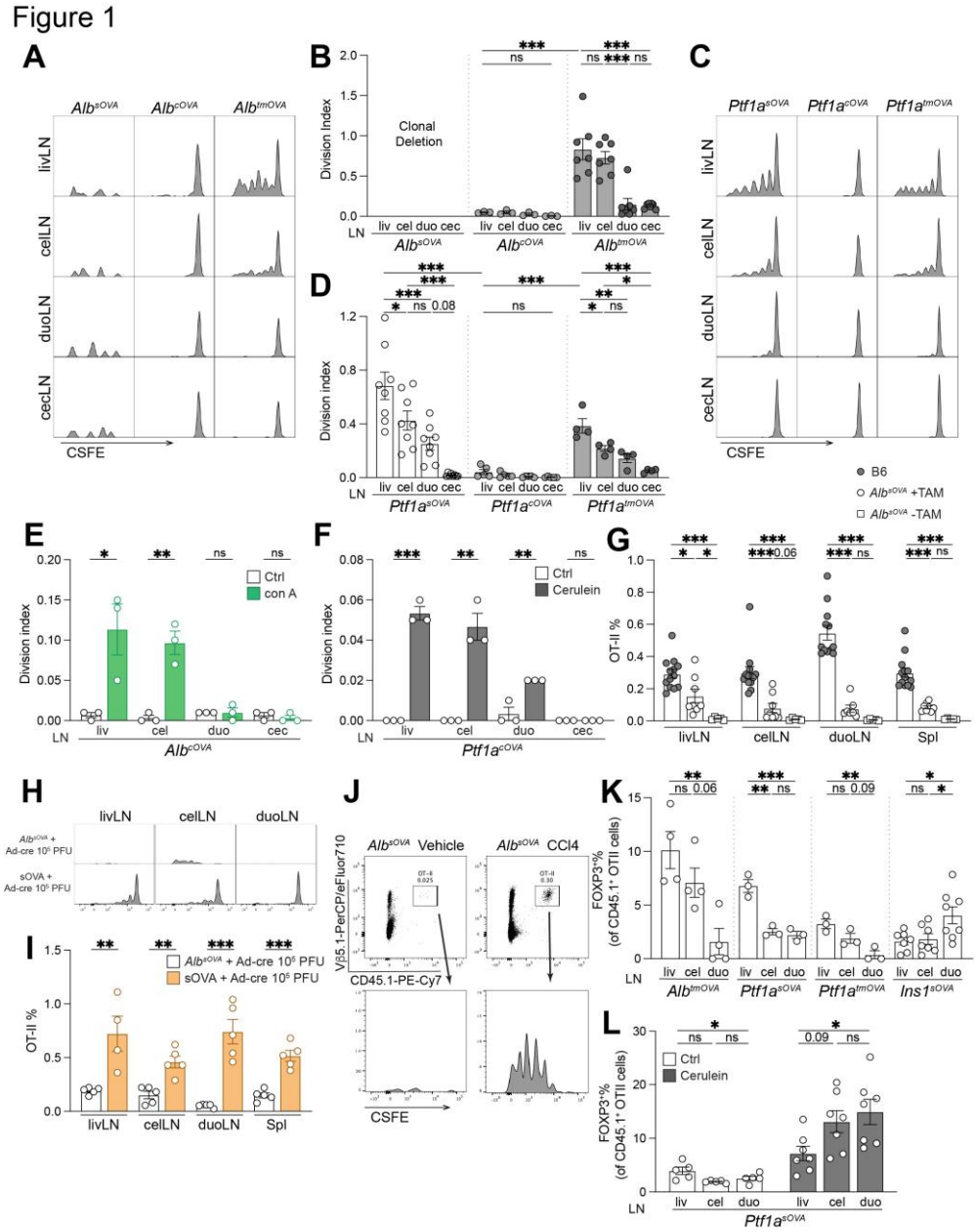


Figure 3.2 Tissue-specific tolerance mechanism, subcellular source of self-antigen and antigen dose dictate T cell fate of self-reactive CD4+ T cells at homeostasis.

A-B. CFSE dilution flow plots (**A**) and division index (**B**) of OT-II cells in the indicated LNs 96 h after transfer into Alb^{sOVA}, Alb^{cOVA} or Alb^{tmOVA} mice (n = 3-7 per group, as indicated by symbols). **C-D**. CFSE dilution flow plots (**C**) and division index (**D**) of OT-II cells in the indicated LNs 96 h after transfer into $Ptf1a^{sOVA}$, $Ptf1a^{cOVA}$ or $Ptf1a^{tmOVA}$ mice (n = 4-8 per group, as indicated by symbols). **E**. Division index of OT-II cells in the indicated LNs 96 h after transfer into Alb^{cOVA} mice treated with con A (n = 3 per group). **F**. Division index of OT-II cells in the indicated LNs 96 h after transfer into $Ptf1a^{cOVA}$ mice treated with cerulein (n = 3 per group). **G.** Frequencies of OT-II among total $CD4^+$ T cells in the indicated LNs and spleen 96 h after transfer into OVA-naïve, tamoxifen-induced and non-induced Alb^{sOVA} mice (n = 7-11 per group, as indicated by symbols). **H-I.** CFSE dilution flow plots (**H**) and frequencies of OT-II among total $CD4^+$ T cells (**I**) in the indicated LNs of adeno-infected Alb^{sOVA} and adeno-infected sOVA mice (n = 5 per group). **J.** Flow plots of OT-II cells in livLN of Alb^{sOVA} mice treated with CCl_4. **K**. Frequencies of $FOXP3^+$ among total OT-II cells in the indicated LNs 96 h after transfer into Alb^{tmOVA}, $Ptf1a^{sOVA}$, $Ptf1a^{tmOVA}$ and $Ins1^{sOVA}$ mice (n = 3-8 per group, as indicated by symbols). **L**. Frequencies of $FOXP3^+$ OT-II cells in the indicated LNs 96 h after transfer into $Ptf1a^{sOVA}$ mice treated with cerulein (n = 5-7 per group, as indicated by symbols). Data are representative of two independent experiments in B, D, E-G, K, L. * p<0.05, ** p<0.01, *** p<0.001 by one-way ANOVA and t-test.

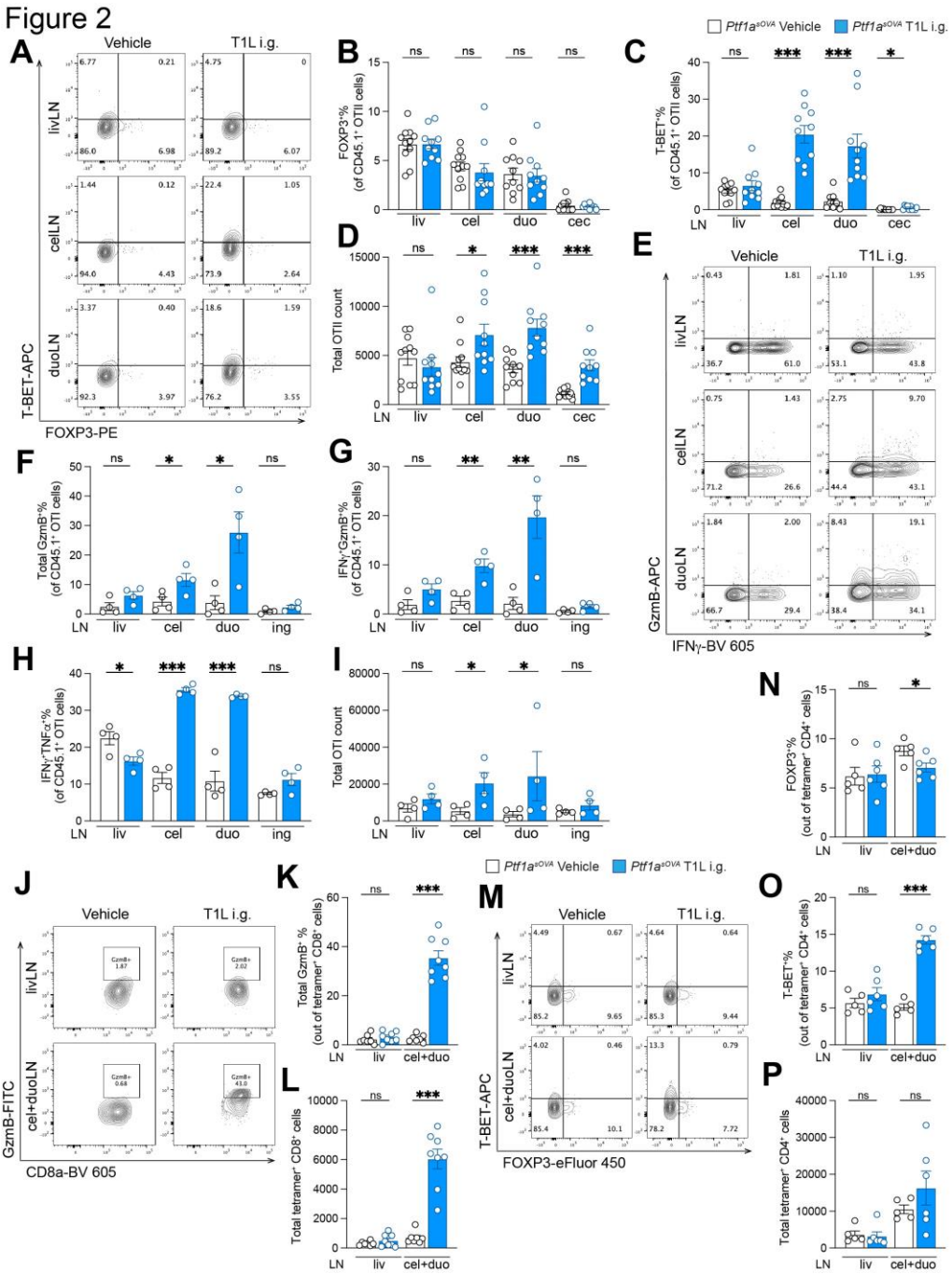


Figure 3.3 Type 1 and but not type 2 intestinal infections shifts exocrine-pancreas-reactive T cell fate by LN co-drainage.
A. Flow plots of OT-II cells in LNs of *Ptf1a*^{sOVA} mice inoculated perorally with T1L or vehicle control. **B-D.** Frequencies of FOXP3$^+$ (**B**) or T-BET$^+$ (**C**) among total OT-II cells and total OT-II count (**D**) in indicated LNs 72 h after transfer into mice in (**A**) (n = 10-11 per group, as indicated by symbols). **E.** Flow plots of OT-I cells in LNs of *Ptf1a*^{sOVA} mice inoculated perorally with T1L or vehicle control. **F-I.** Frequencies of Total GzmB$^+$ (**F**), IFNγ$^+$GzmB$^+$ (**G**) or IFNγ$^+$TNFα$^+$ (**H**) among total OT-I cells and total OT-I count (**I**) in indicated LNs 72 h after transfer into mice in (**D**) (n = 4 per group). **J-L.** Flow plots (**J**), frequencies of GzmB$^+$ among total OVA-tetramer$^+$CD8$^+$ T cells (**K**) and total tetramer+ CD8 T cell count (**L**) in LNs of T1L-infected or vehicle-infected *Ptf1a*^{sOVA} mice in the absence of adoptive transfer (n = 7-8 per group, as indicated by symbols). **M-P.** Flow plots (**M**), frequencies of FOX3$^+$ (**N**) or T-BET$^+$ (**O**) among total OVA-tetramer$^+$CD4$^+$ T cells and total tetramer$^+$ CD4 T cell count (**P**) in LNs of T1L- or vehicle-infected *Ptf1a*^{sOVA} mice in the absence of adoptive transfer (n = 3 per group). Data are representative of two independent experiments in B-D, F-I, K, L, N-P. * p<0.05, ** p<0.01, *** p<0.001 by t-test.

Figure 3

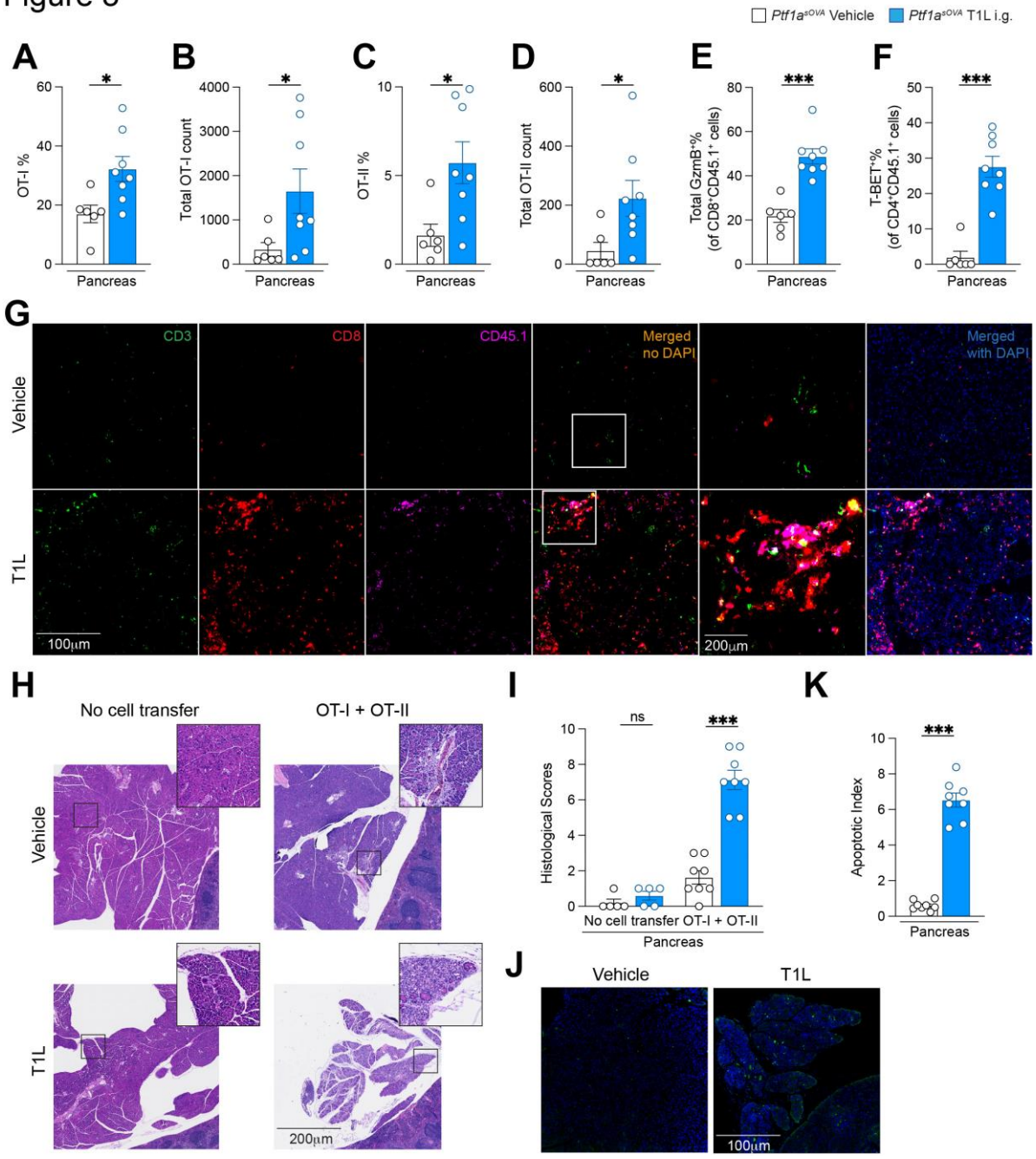


Figure 3.4 Intestinal reovirus-induced pro-inflammatory T cells infiltrate the pancreas and cause tissue destruction.
A-F. Frequencies of OT-I cells among total CD8$^+$ cells (**A**), total OT-I cell count (**B**), OT-II cells among total CD4$^+$ cells (**C**), total OT-II cell count (**D**), GzmB$^+$ among total OT-I cells (**E**) and T-BET$^+$ among total OT-II cells (**F**) in the pancreas of orally T1L-infected or vehicle-infected *Ptf1a*^{sOVA} mice 7 days post transfer (n = 6-8 per group, as indicated by symbols). **G.** Frozen sections of the pancreas from T1L-infected or vehicle-infected *Ptf1a*^{sOVA} mice 14 days post transfer stained for CD3, CD8, CD45.1 and DAPI (nuclei). Scale bar represents 100 µm. Enlarged area are indicated by white boxes. Scale bar for enlarged images represents 200 µm. **H-J.** Sections of the pancreas from T1L- or mock-infected *Ptf1a*^{sOVA} mice 14 days post transfer stained with H&E (**H**) or stained for apoptotic cells and DAPI (**J**). Scale bars represent 200 µm and 100 µm, respectively. Enlarged area are indicated by black boxes and shown on the upper right corner of corresponding images. Quantification of histological score (**I**) and apoptotic index (**K**) (n = 5-8 per group, as indicated by symbols). Data are pooled from two independent experiments in A-E, I, K. * p<0.05, ** p<0.01, *** p<0.001 by t-test.

Figure 4

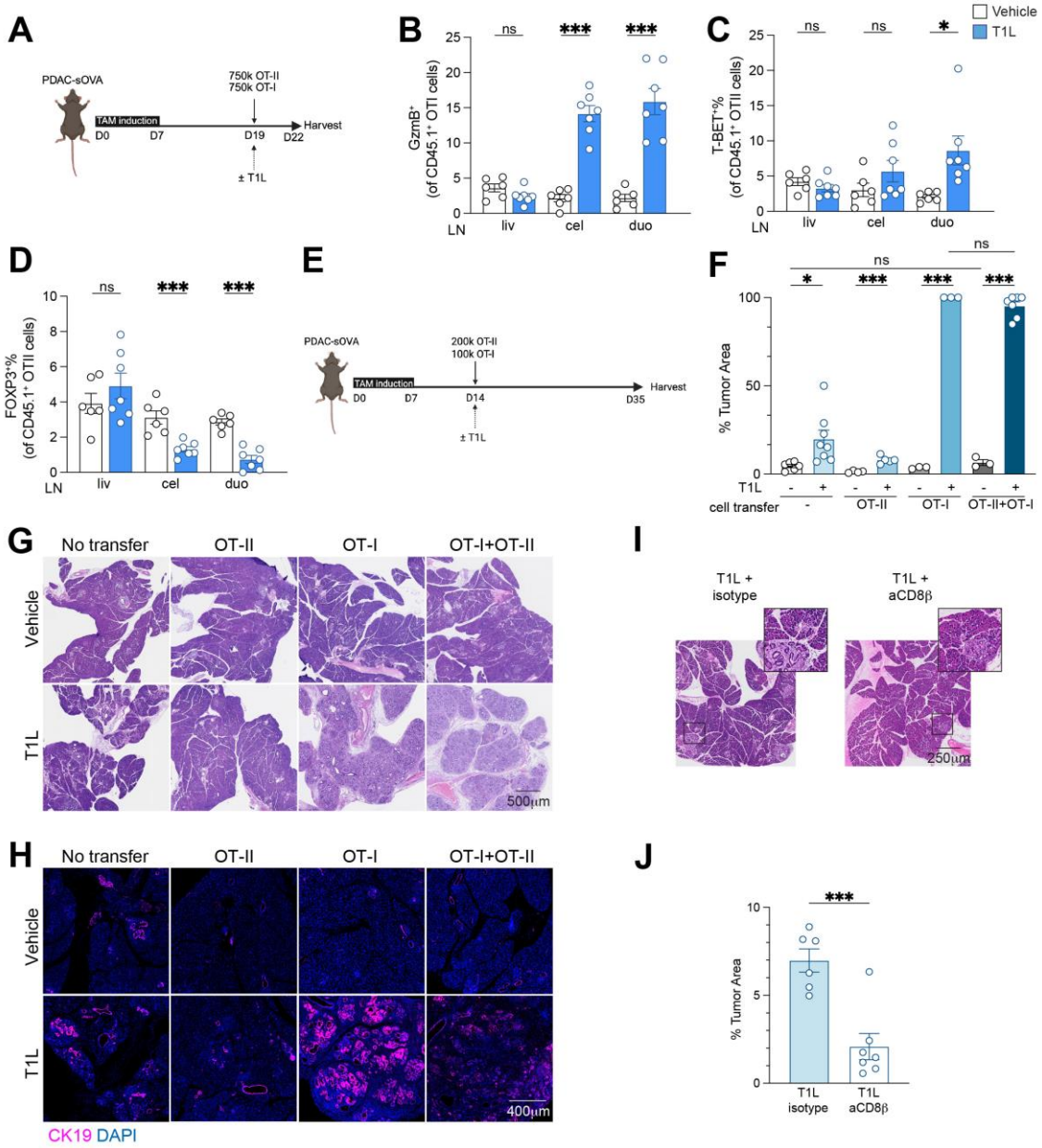


Figure 3.5 Intestinal reovirus infection exacerbates pancreatic tumor growth in a genetic PDAC model by a CD8+ T cell-dependent manner.

A. Experimental scheme for tumor development, cell transfer and detection of T cell fate in the LNs. **B-D**. Frequencies of $GzmB^+$ among total OT-I cells (**B**), $T\text{-}BET^+$ (**C**) or $FOXP3^+$ (**D**) among total OT-II cells in indicated LNs 72 h after co-transfer into T1L-infected or vehicle-infected PDAC-sOVA mice (n = 6-7 per group, as indicated by symbols). **E.** Experimental scheme for tumor development, cell transfer and analysis of tumor area. **F-H**. Sections of pancreas from PDAC-sOVA mice with indicated cell transfer and T1L infection status stained with H&E (**G**) or CK19 antibody (**H**). The percentage of tumor area out of total tissue area from each section was quantified (**F**) (n = 3-8 per group, as indicated by symbols). Scale bar represents 500 μm (**G**) and 400 μm (**H**). **I-J**. Sections of pancreas from T1L-infected PDAC-sOVA mice treated with a CD8β neutralizing antibody or isotype control stained with H&E (**I**). Enlarged area are indicated by black boxes and shown on the upper right corner of corresponding images. The percentage of tumor area from each section was quantified (**J**) (n = 6-7 per group, as indicated by symbols). Scale bar represents 400 μm. Data are pooled from two independent experiments in B-D, F, J. * $p<0.05$, ** $p<0.01$, *** $p<0.001$ by t-test.

Figure 5

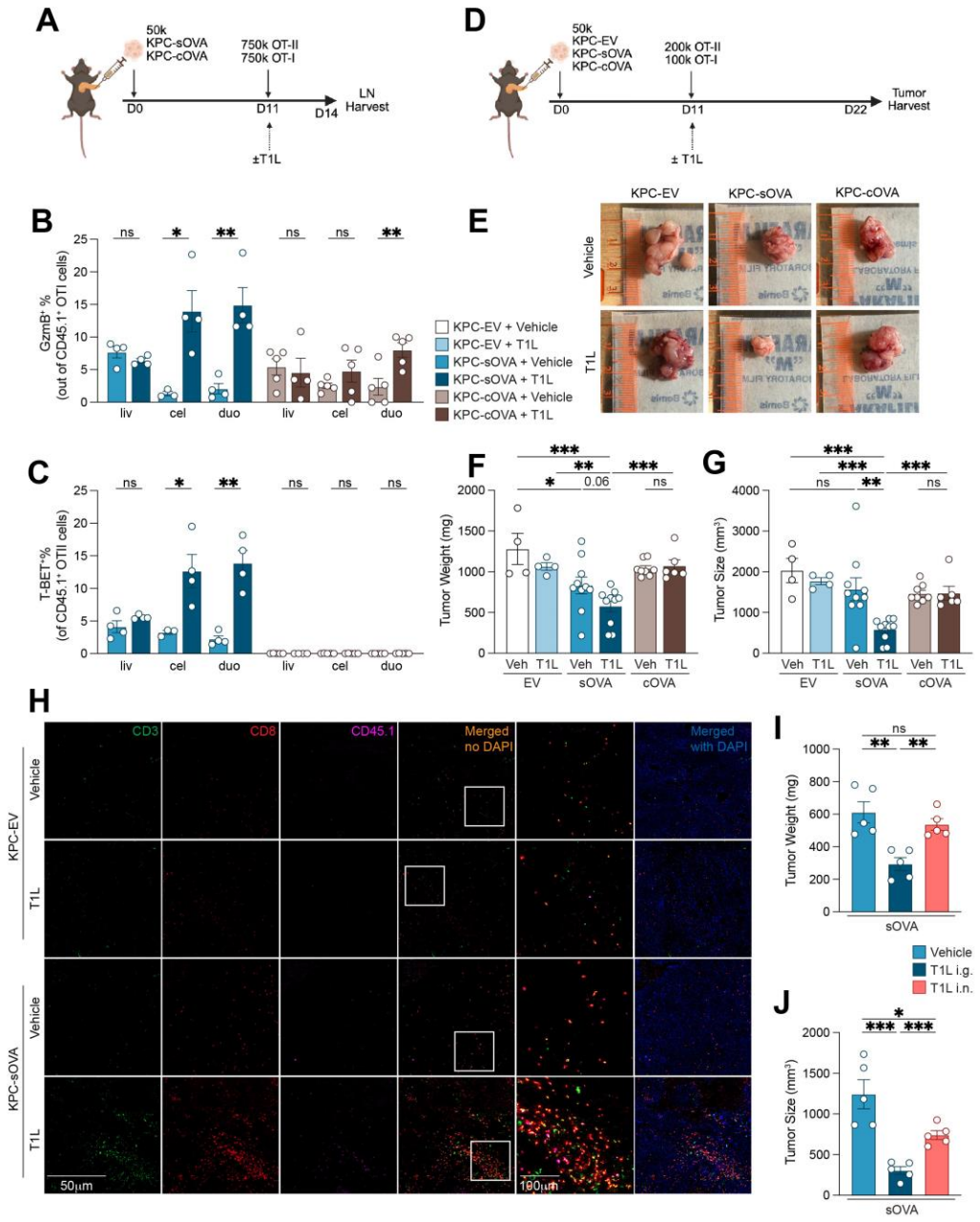


Figure 3.6 Intestinal reovirus infection enhances T cell infiltration and tumor control in an orthotopic PDAC model.
A, D. Schematic of orthotopic PDAC model for assessing T cell fate in the LNs (**A**) and tumor progression (**D**). **B-C**. Frequencies of GzmB$^+$ among total OT-I cells (**B**) or T-BET$^+$ among total OT-II (**C**) cells in indicated LNs of mice receiving sOVA- or cOVA-expressing tumor cells (n = 4-5 per group, as indicated by symbols). **E.** Representative photographs of tumors removed from mice with indicated tumor implants and T1L infection status. **F-G.** Weights (**F**) and sizes (**F**) of tumors from mice in (**E**) (n = 4-10 per group, as indicated by symbols). **H.** Tumor frozen sections from mice in (**E**) were stained for CD3, CD8, CD45.1 and DAPI (nuclei). Scale bar represents 50 μm. Enlarged area are indicated by white boxes. Scale bar for enlarged images represents 100 μm. **I-J.** Weights (**I**) and sizes (**J**) of tumors from mice receiving sOVA-expressing KPC cells intragastrically or intranasally infected with T1L (n = 5 per group). Data are pooled from two independent experiments in F, G. Data represent one experiment in B, C, I, J. * p<0.05, ** p<0.01, *** p<0.001 by t-test.

Figure 6

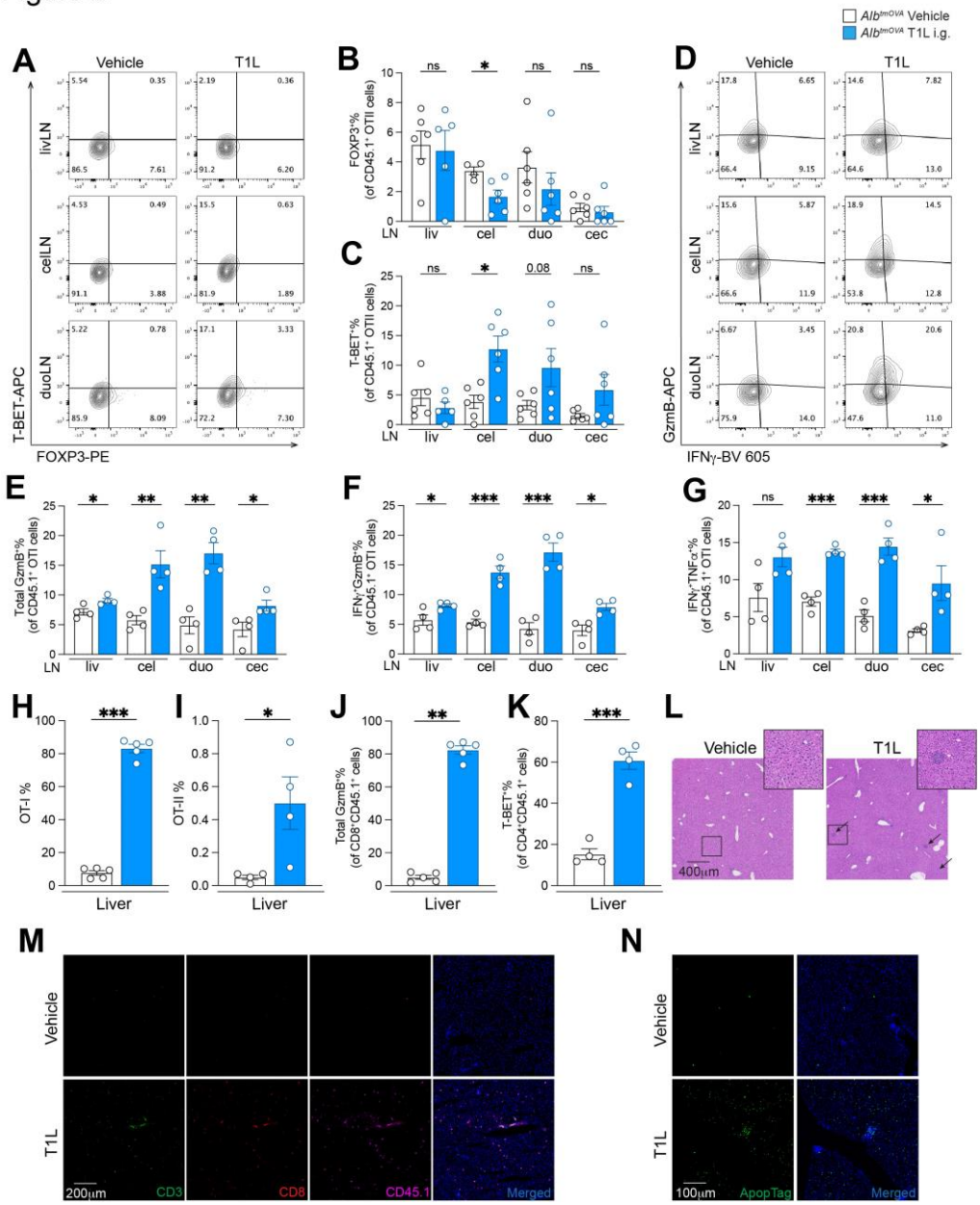


Figure 3.7 Intestinal reovirus infection induces liver-reactive T cells and hepatic damage by LN co-drainage.
A. Plots of OT-II cells in indicated LNs of orally T1L-infected or vehicle-infected *Alb*^{tmOVA} mice, representative of gating applies in (**B**) and (**C**). **B-C.** Frequencies of FOXP3$^+$ (**B**) or T-BET$^+$ (**C**) among total OT-II cells in indicated LNs 72 h after transfer into mice in (**A**) (n = 5-6 per group, as indicated by symbols). **D.** Plots of OT-I cells in indicated LNs of T1L- or vehicle-infected *Alb*^{tmOVA} mice, representative of gating applied in (**E**) – (**G**). **E-G.** Frequencies of total GzmB$^+$ (**E**), IFNγ$^+$GzmB$^+$ (**F**) or IFNγ$^+$TNFα$^+$ (**G**) among total OT-I cells in indicated LNs 72 h after transferred into mice in (**D**) (n = 4 per group). **H-K**. Frequencies of OT-I cells among total CD8$^+$ cells (**H**), OT-II cells among total CD4$^+$ cells (**I**), GzmB$^+$ among total OT-I cells (**J**) and T-BET$^+$ among total OT-II cells (**K**) in the liver of T1L- or mock-infected *Alb*^{tmOVA} mice 7 days post transfer (n = 5 per group). **L.** Sections of the liver from orally T1L-infected or vehicle-infected *Alb*^{tmOVA} mice 14 days post transfer stain with H&E. Scale bar represents 400 μm. Necrotic clusters are indicated by arrows. Enlarged area are indicated by black boxes and shown on the upper right corner of corresponding images. **M.** Frozen sections of the liver from T1L-infected or vehicle-infected *Ptf1a*^{sOVA} mice stained for CD3, CD8, CD45.1 and DAPI (nuclei). Scale bar represents 200 μm. **N.** Sections of the liver from T1L-infected or vehicle-infected *Alb*^{tmOVA} mice 14 days post infection stained for apoptotic cells. Scale bar represents 100 μm. Data are representative of two independent experiments in B, C, E-K. * p<0.05, ** p<0.01, *** p<0.001 by t-test.

Figure 7

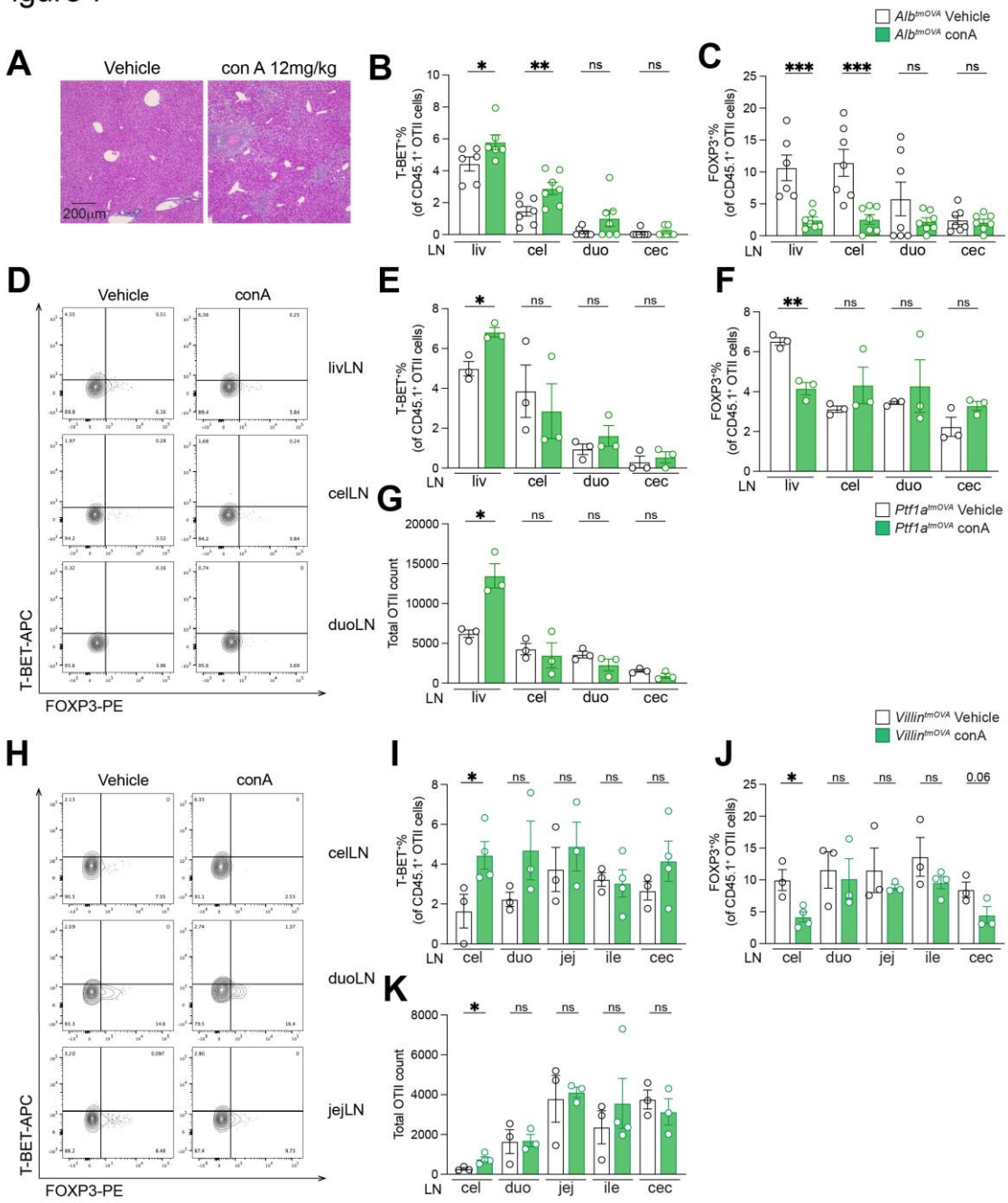


Figure 3.8 Con A-induced liver injury promotes pro-inflammatory conversion of pancreas- and gut-reactive T cells.
A. Sections of the liver from con A- or vehicle-treated *Alb*^{tmOVA} mice stained with H&E. Scale bar represents 200 μm. **B-C.** Frequencies of T-BET$^+$ (**B**) or FOXP3$^+$ (**C**) among total OT-II cells in indicated LNs 96 h after transfer into mice in (**A**) (n = 6 per group). **D.** Plots of OT-II cells in indicated LNs of con A- or vehicle-treated *Ptf1a*^{tmOVA} mice, representative gating applied in (**E**) and (**F**) (n = 3 per group). **E-G.** Frequencies of T-BET$^+$ (**E**) or FOXP3$^+$ (**F**) among total OT-II cells and total OT-II count (**G**) in indicated LNs 96 h after transfer into mice in (**D**). **H.** Plots of OT-II cells in indicated LNs of con A- or vehicle-treated *Villin*^{tmOVA} mice, representative gating applied in (**H**) and (**I**). **I-K.** Frequencies of T-BET$^+$ (**I**) or FOXP3$^+$ (**J**) among total OT-II cells and total OT-II count (**K**) in indicated LNs 96 h after transfer into mice in (**H**) (n = 3-4 per group, as indicated by symbols). Data are representative of two independent experiments in B, C, E-G, I-K. * p<0.05, ** p<0.01, *** p<0.001 by t-test.

Figure S1

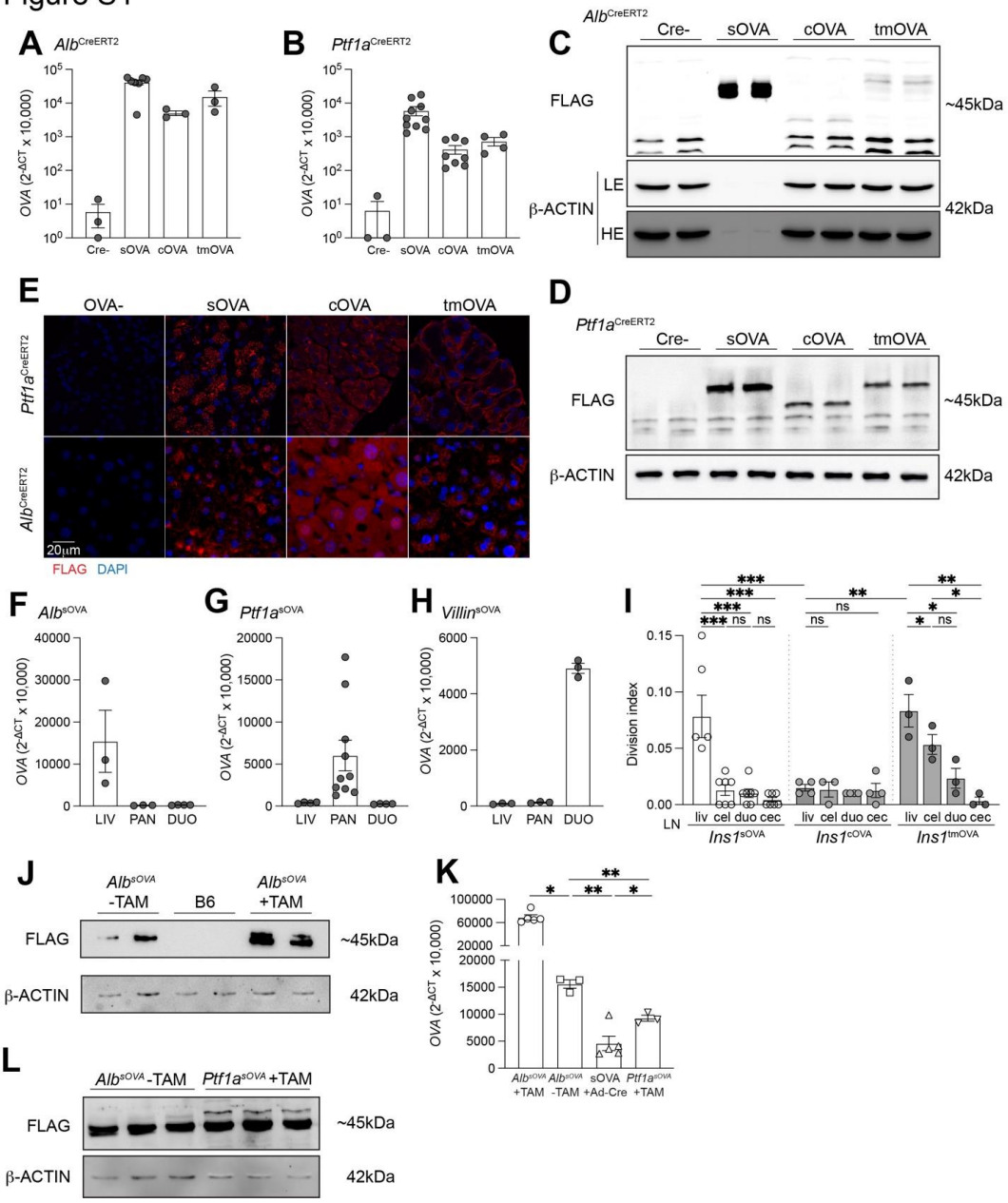


Figure 3.9 Tissue-specific tolerance mechanism, subcellular source of self-antigen and antigen dose dictate T cell fate of self-reactive CD4+ T cells at homeostasis.

A-B. Expression levels of *OVA* in the liver (**A**) and pancreas (**B**) of mice with indicated genotypes (n = 3-10 per group, as indicated by symbols). **C-D**. Hepatic (**C**) and pancreatic (**D**) tissue lysates from mice with indicated OVA form and their CRE-negative controls were immunoblotted using antibodies against FLAG, and β-ACTIN as a loading control. **E**. Sections of pancreas (top) and liver (bottom) from mice with indicated genotypes stained for FLAG and DAPI (nuclei). Scale bar represents 20μm. **F-H.** *OVA* expression levels in the liver, pancreas and duodenum tissue of mice with indicated genotypes, showing tissue-specific expression restricted to the intended sites (n = 3-10 per group, as indicated by symbols). **I.** Division index of OT-II cells in the indicated LNs 6 days after transfer into $Ins1^{sOVA}$, $Ins1^{cOVA}$ and $Ins1^{tmOVA}$ mice (n = 4-7 per group, as indicated by symbols). **J**. Hepatic tissue lysates from Alb^{sOVA} mice treated with or without tamoxifen and B6 mice were immunoblotted using antibodies against FLAG and β-ACTIN. **K.** *OVA* expression levels in liver tissue of Alb^{sOVA} mice treated with or without tamoxifen and sOVA mice infected with adeno-Cre virus and pancreas of $Ptf1a^{sOVA}$ mice (n = 3-5 per group, as indicated by symbols). **L**. Hepatic tissue lysates from Alb^{sOVA} mice without tamoxifen treatment and pancreatic lysates from tamoxifen-treated $Ptf1a^{sOVA}$ mice were immunoblotted using antibodies against FLAG and β-ACTIN. Data are pooled from two independent experiments in A, B, F-I. * p<0.05, ** p<0.01, *** p<0.001

Figure S2

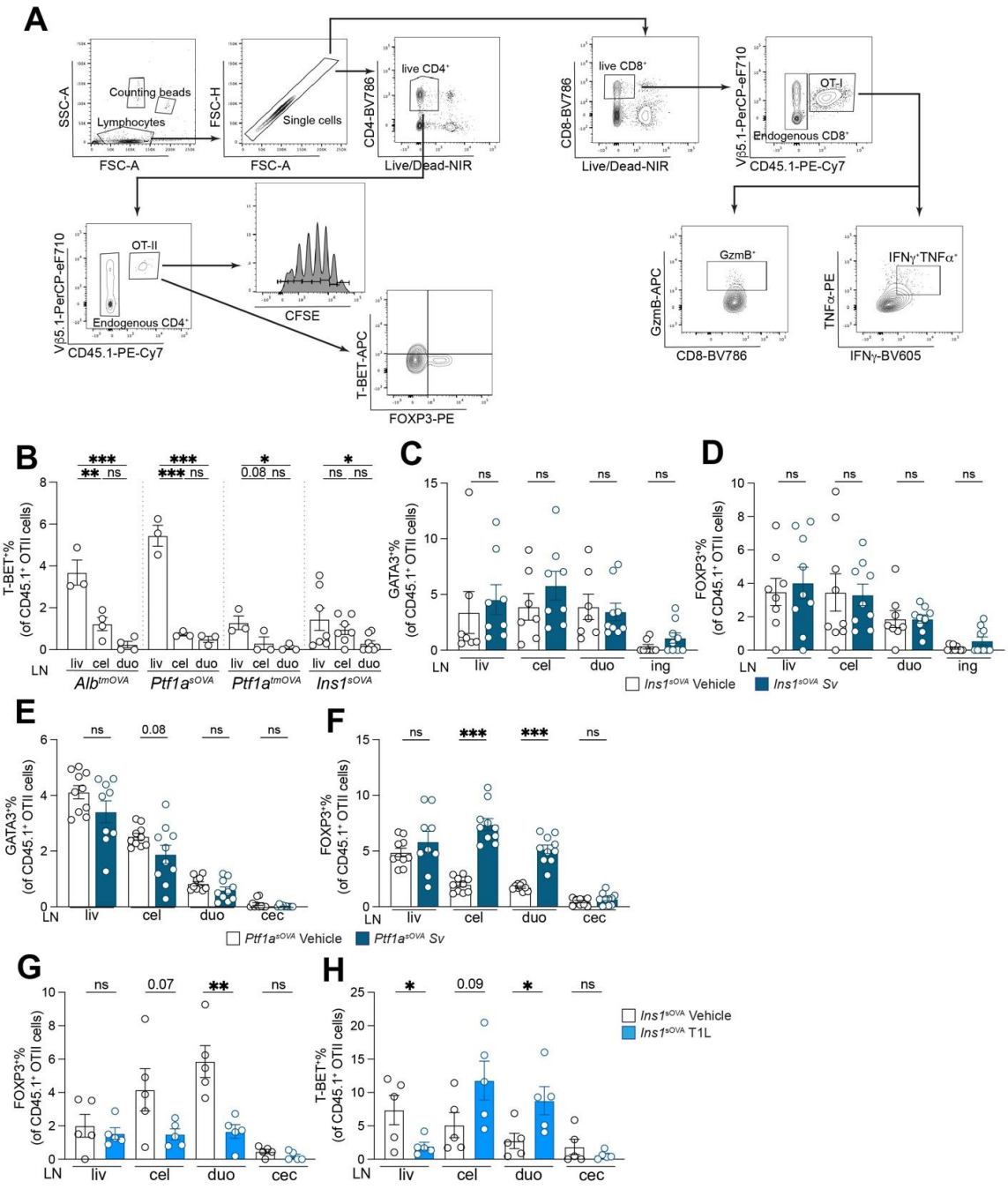


Figure 3.10 Type 1, but not type 2, intestinal infection renders pancreas-reactive T cells pro-inflammatory.
A. Gating strategy for OT-II proliferation and cell fate of both OT-I and OT-II cells. **B.** Frequencies of T-BET$^+$ among total OT-II cells in the indicated LNs 96 h after transfer into *Alb*^{tmOVA}, *Ptf1a*^{sOVA}, *Ptf1a*^{tmOVA} and *Ins1*^{sOVA} mice (n = 3-8 per group, as indicated by symbols). **C-F.** Frequencies of GATA3$^+$ (**C, E**) or FOXP3$^+$ (**D, F**) among total OT-II cells 72 h after transfer into *Ins1*^{sOVA} (**C-D**) or *Ptf1a*^{sOVA} (**E-F**) mice that were *S. venezuelensis*- or mock-infected (n = 8-10 per group, as indicated by symbols). **G-H.** Frequencies of FOXP3$^+$ (**G**) or T-BET$^+$ (**H**) among total OT-II cells in indicated LNs 72 h after transfer into T1L- or mock-infected *Ins1*^{sOVA} mice (n = 5 per group). Data are pooled from two independent experiments in B-H. * p<0.05, ** p<0.01, *** p<0.001 by t-test.

Figure S3

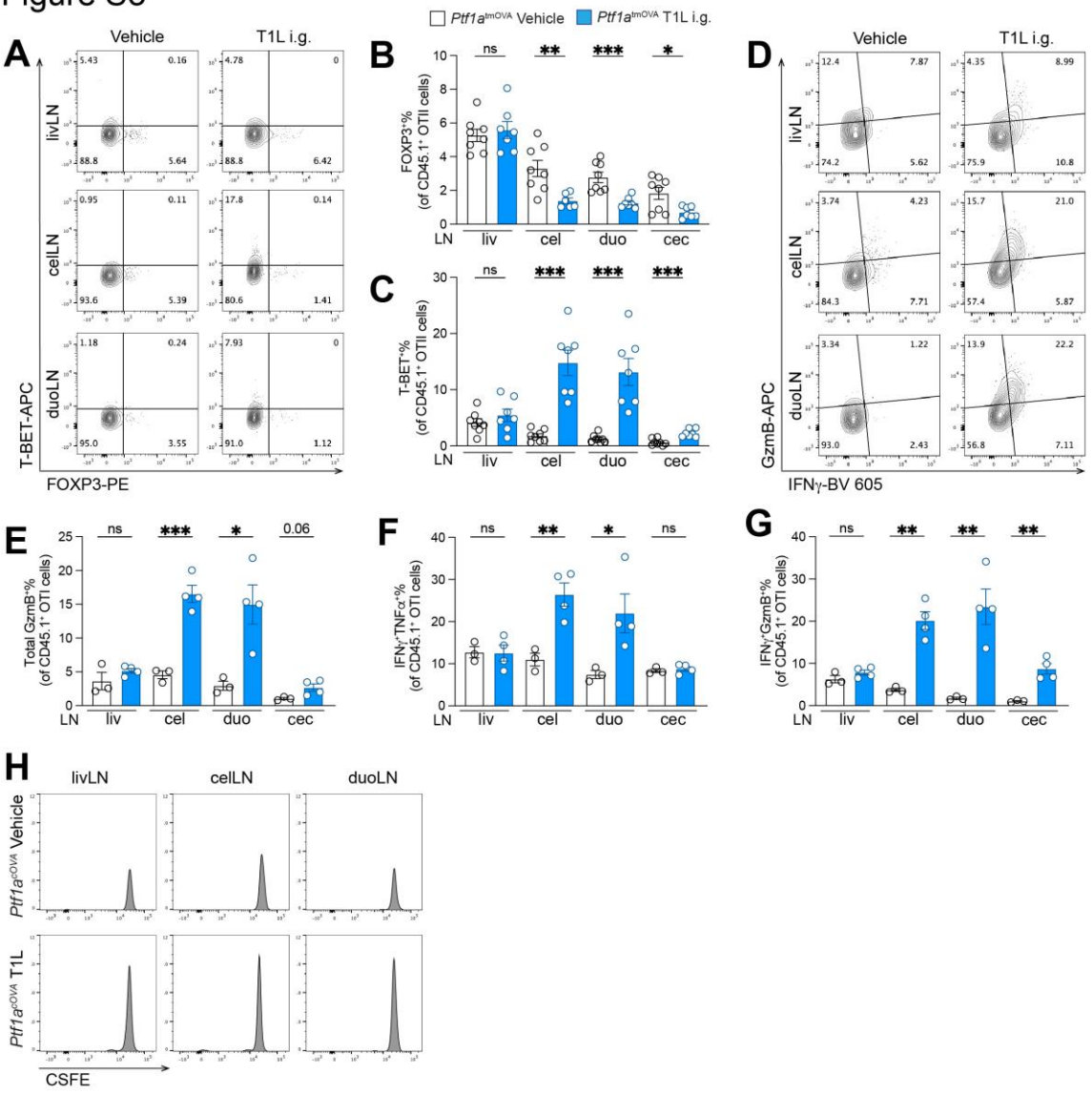


Figure 3.11 Intestinal reovirus infection renders pancreas-reactive T cells pro-inflammatory by LN co-drainage.
A. Plots of OT-II cells in LNs of *Ptf1a*^{tmOVA} mice that are inoculated perorally with T1L or vehicle control, representative gating applied in (**B**) and (**C**). **B-C.** Frequencies of FOXP3$^+$ (**B**) or T-BET$^+$ (**C**) among total OT-II cells in indicated LNs 72 h after transfer into mice in (**A**) (n = 7-8 per group, as indicated by symbols). **D.** Plots of OT-I cells in LNs of *Ptf1a*^{tmOVA} mice that are inoculated perorally with T1L or vehicle control. **E-G.** Frequencies of total GzmB$^+$ (**E**), IFNγ$^+$GzmB$^+$ (**F**) or IFNγ$^+$TNFα$^+$ (**G**) among total OT-I cells in indicated LNs 72 h after transfer into mice in (**D**) (n = 3-4 per group, as indicated by symbols). **H.** CFSE flow plots of OT-II cells in indicated LNs from *Ptf1a*^{cOVA} mice orally infected with T1L or given vehicle control. Data are pooled from two independent experiments in B, C. Data represent one experiment in E-G. * p<0.05, ** p<0.01, *** p<0.001 by t-test.

Figure S4

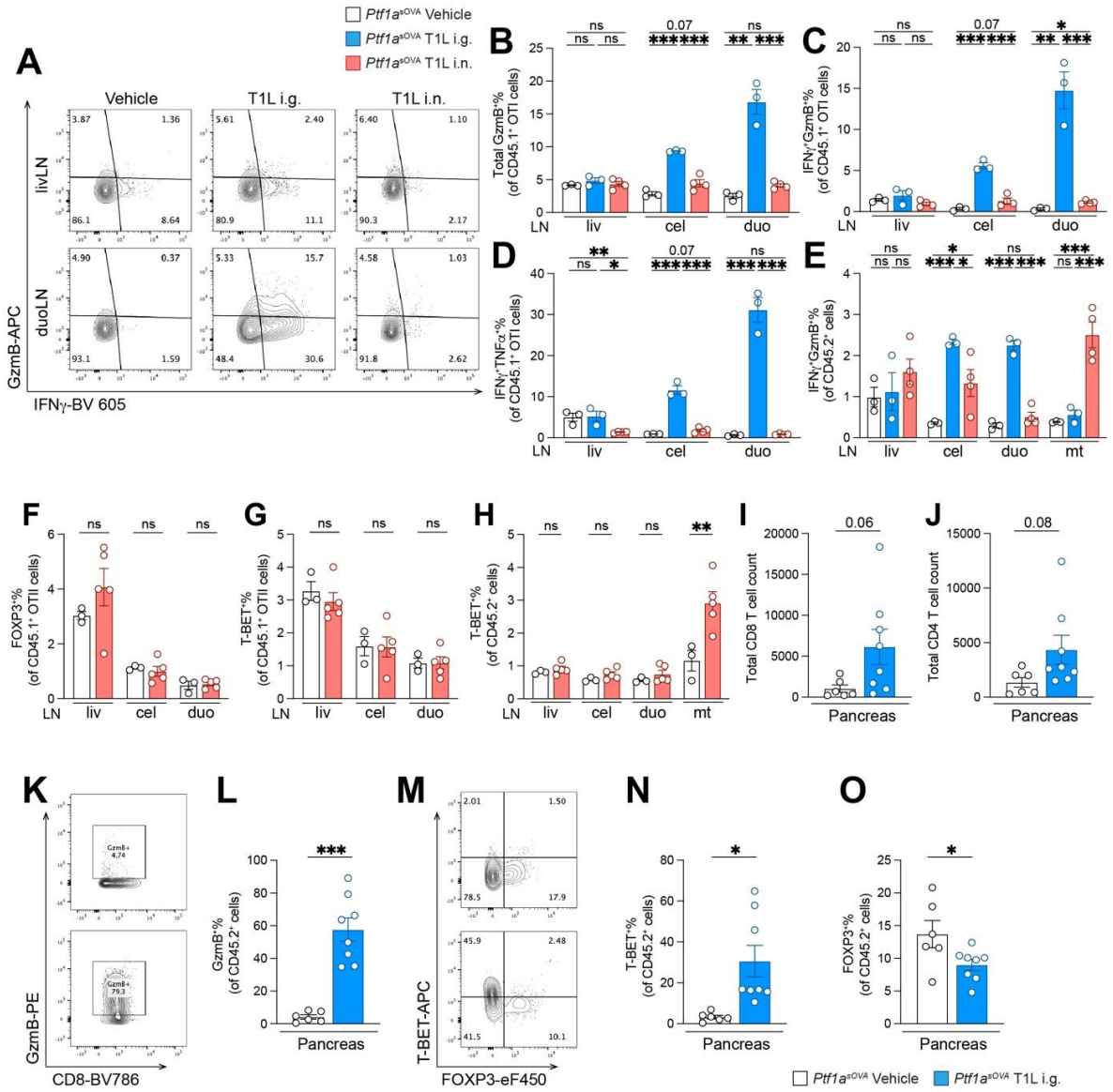


Figure 3.12 Intestinal reovirus-induced pro-inflammatory T cells infiltrate the pancreas and cause severe tissue destruction.
A. Flow plots of OT-I cells in LNs of *Ptf1a*^{sOVA} mice that were either intragastrically or intranasally infected with T1L. **B-E.** Frequencies of Total GzmB$^+$ (**B**), IFNγ$^+$GzmB$^+$ (**C**) or IFNγ$^+$TNFα$^+$ (**D**) among total OT-I cells and IFNγ$^+$GzmB$^+$ among total CD8$^+$ cells (**E**) in the indicated LNs 72 h after transfer into mice in (**A**) (n = 3-4 per group, as indicated by symbols). **F-H.** Frequencies of FOXP3$^+$ (**F**), T-BET$^+$ (**G**) among total OT-II cells or endogenous T-BET$^+$ among total CD4$^+$ cells (**H**) in indicated LNs of T1L-infected or vehicle-infected *Ptf1a*^{sOVA} mice (n = 3-5 per group, as indicated by symbols). **I-J.** Total CD8$^+$ (**I**) and CD4$^+$ (**J**) T cell numbers in the pancreas of orally T1L-infected or vehicle-infected *Ptf1a*^{sOVA} mice 7 days post transfer. **K-L.** Representative plots of endogenous CD8$^+$ T cells (**K**) and frequencies of GzmB$^+$ among total CD8$^+$ T cells (**L**) in the pancreas of T1L-infected or vehicle-infected *Ptf1a*^{sOVA} mice. **M-O.** Representative flow plots of endogenous CD4$^+$ T cells (**M**) and frequencies of T-BET$^+$ (**N**) or FOXP3$^+$ among total CD4$^+$ T cells (**O**) in the pancreas of T1L-infected or vehicle-infected *Ptf1a*^{sOVA} mice. Data are pooled from two independent experiments (n = 6-8 per group, as indicated by symbols) in I, J, L, N, O. Data represent one experiment in B-H. * p<0.05, ** p<0.01, *** p<0.001 by t-test.

Figure S5

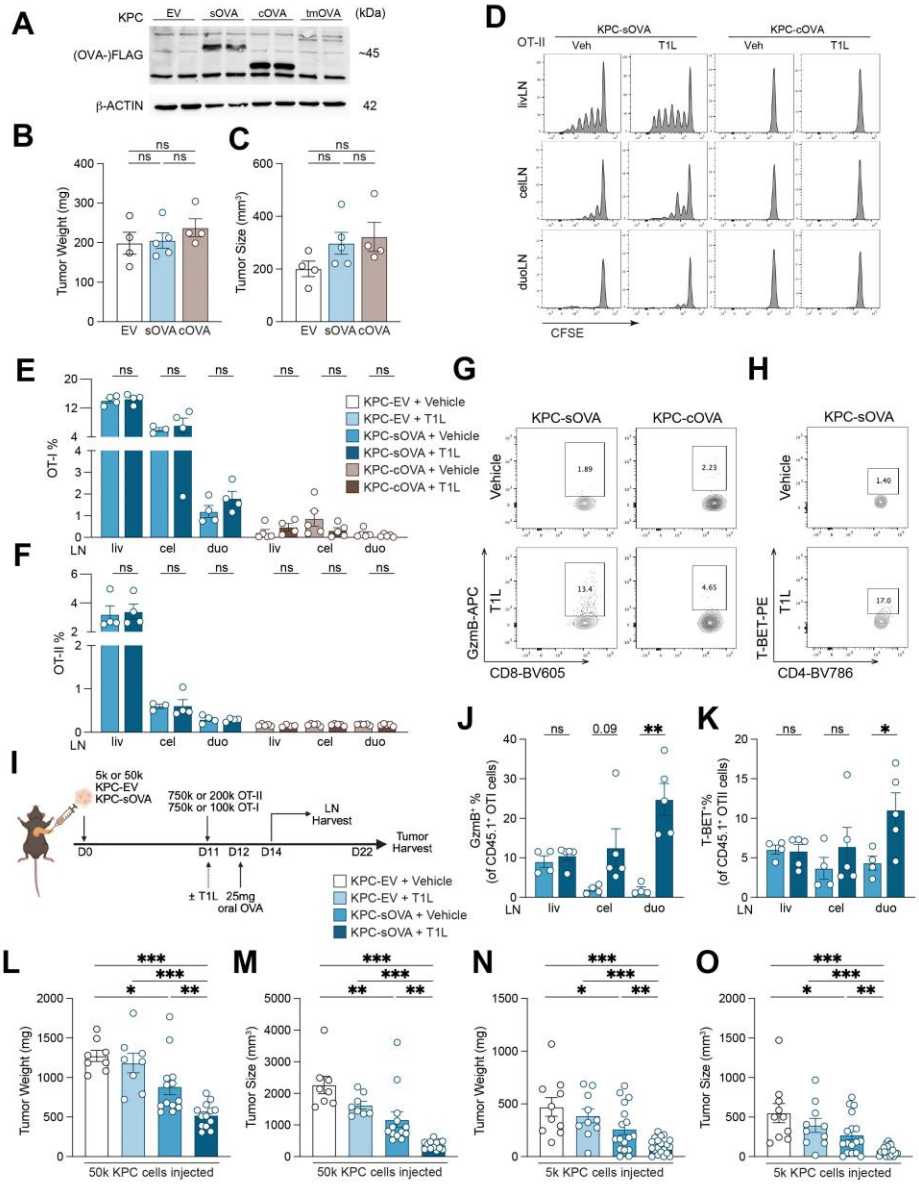


Figure 3.13 Intestinal reovirus infection enhances T cell infiltration and tumor control in an orthotopic PDAC model.
A. Western blot of cell lysates of KPC cells expressing indicated OVA forms or empty vector control using antibodies against FLAG and β-ACTIN. **B-C.** Tumor weights (**B**) and sizes (**C**) at day 11 post KPC cell injection were measured to confirm that OVA expression does not alter tumor growth (n = 4-5 per group, as indicated by symbols). **D.** CFSE dilution flow plots of OT-II cells in the indicated LNs from orally T1L-infected or mock-infected mice receiving sOVA- or cOVA-expressing KPC tumor cells. **E-F**. Frequencies of OT-I among total $CD8^+$ cells (**E**) or OT-II among total $CD4^+$ (**F**) cells in indicated LNs of mice receiving sOVA- or cOVA-expressing KPC tumor cells (n = 4-5 per group, as indicated by symbols). **G-H**. Plots of OT-I cells (**G**) or OT-II (**H**) cells in duoLNs of mice receiving sOVA- or cOVA-expressing tumor cells. **I**. Schematic of orthotopic PDAC model for assessing T cell fate in the LNs and tumor progression. **J-K**. Frequencies of $GzmB^+$ among total OT-I cells (**J**) or $T\text{-}BET^+$ among total OT-II (**K**) cells in indicated LNs of mice receiving 50k sOVA-expressing KPC tumor cells with one dose of OVA oral gavage 1 day post cell transfer (n = 4-5 per group, as indicated by symbols). **L-M.** Weights (**L**) and sizes (**M**) of tumors from mice receiving standard 50k indicated tumor cells and one dose of OVA gavage 1 day post cell transfer (n = 8-13 per group). **N-O.** Weights (**N**) and sizes (**O**) of tumors from mice receiving a lower dose of 5k indicated tumor cells and one dose of OVA oral gavage 1 day post cell transfer (n = 10-20 per group, as indicated by symbols). Data are pooled from two independent experiments in L-O. Data represent one experiment in B, C, E, F, J, K. * p<0.05, ** p<0.01, *** p<0.001 by t-test.

Figure S6

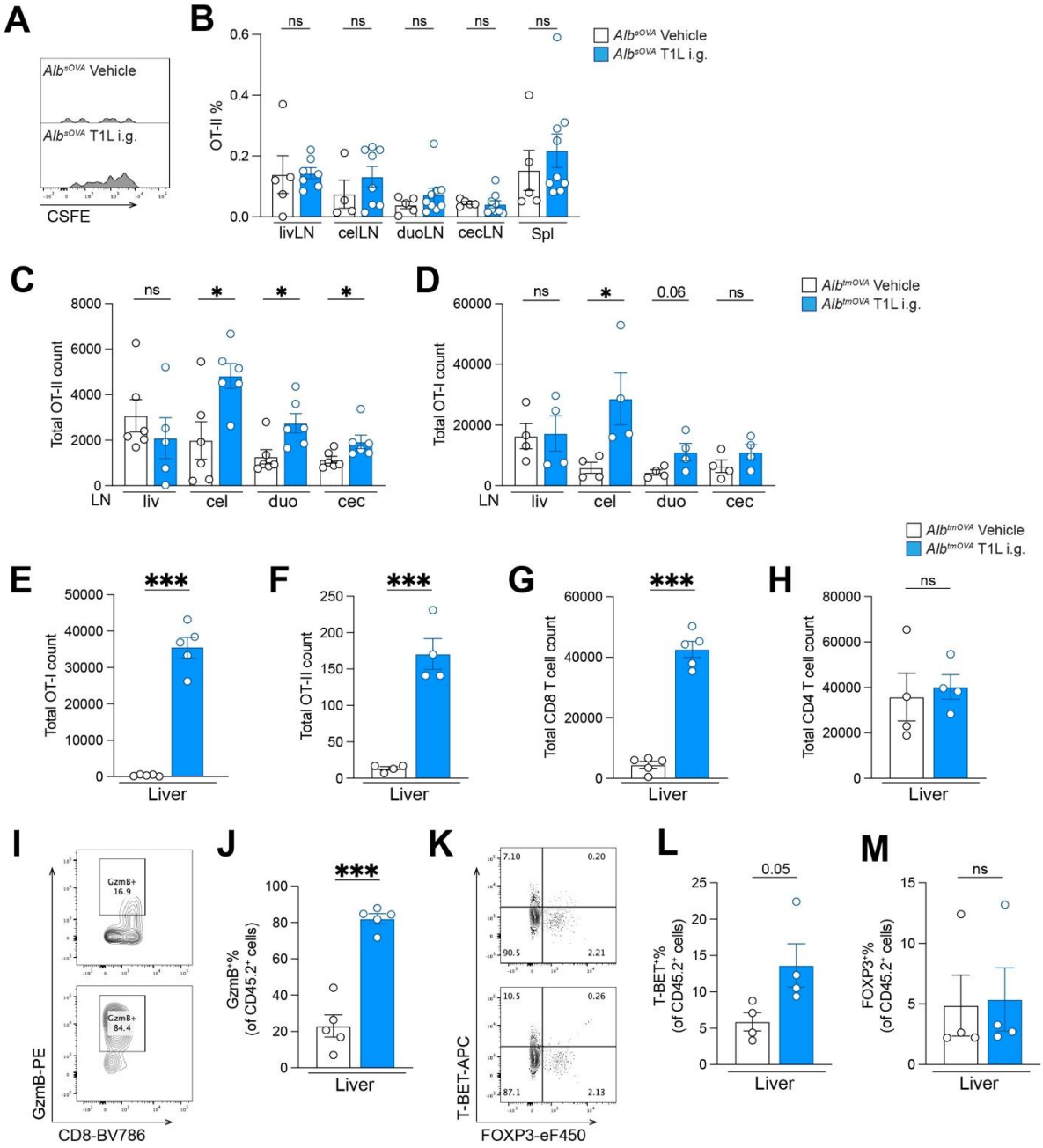


Figure 3.14 Intestinal reovirus infection induces liver-reactive T cells and hepatic damage by LN co-drainage.
A-B. CFSE flow plots (**A**) and frequency of OT-II among total CD4$^+$ cells (**B**) in indicated LNs and spleen from *Alb^{sOVA}* mice orally infected with T1L or treated with vehicle control (n = 5-9 per group, as indicated by symbols). **C-D.** Total OT-II (**C**) and OT-I (**D**) count in indicated LNs 72 h after transfer into orally T1L-infected or vehicle-infected *Alb^{tmOVA}* mice (n = 4-6 per group, as indicated by symbols). **E-H.** Total OT-I (**E**), OT-II (**F**), CD8$^+$ (**G**) and CD4$^+$ (**H**) T cell numbers in the liver of T1L- or vehicle-infected *Alb^{tmOVA}* mice 7 days post transfer. **I-J.** Representative plots of endogenous CD8$^+$ T cells (**I**) and frequencies of GzmB$^+$ among total CD8$^+$ T cells (**J**) in the liver of T1L- or mock-infected *Alb^{tmOVA}* mice. **K-M.** Representative plots of endogenous CD4$^+$ T cells (**K**) and frequencies of T-BET$^+$ (**L**) or FOXP3$^+$ among total CD4$^+$ T cells (**KM**) in the liver of T1L- or mock-infected *Alb^{tmOVA}* mice. Data are pooled from two independent experiments in A-B. Data are representative of two independent experiments in C-H, J, L, M. * p<0.05, ** p<0.01, *** p<0.001 by t-test.

Figure S7

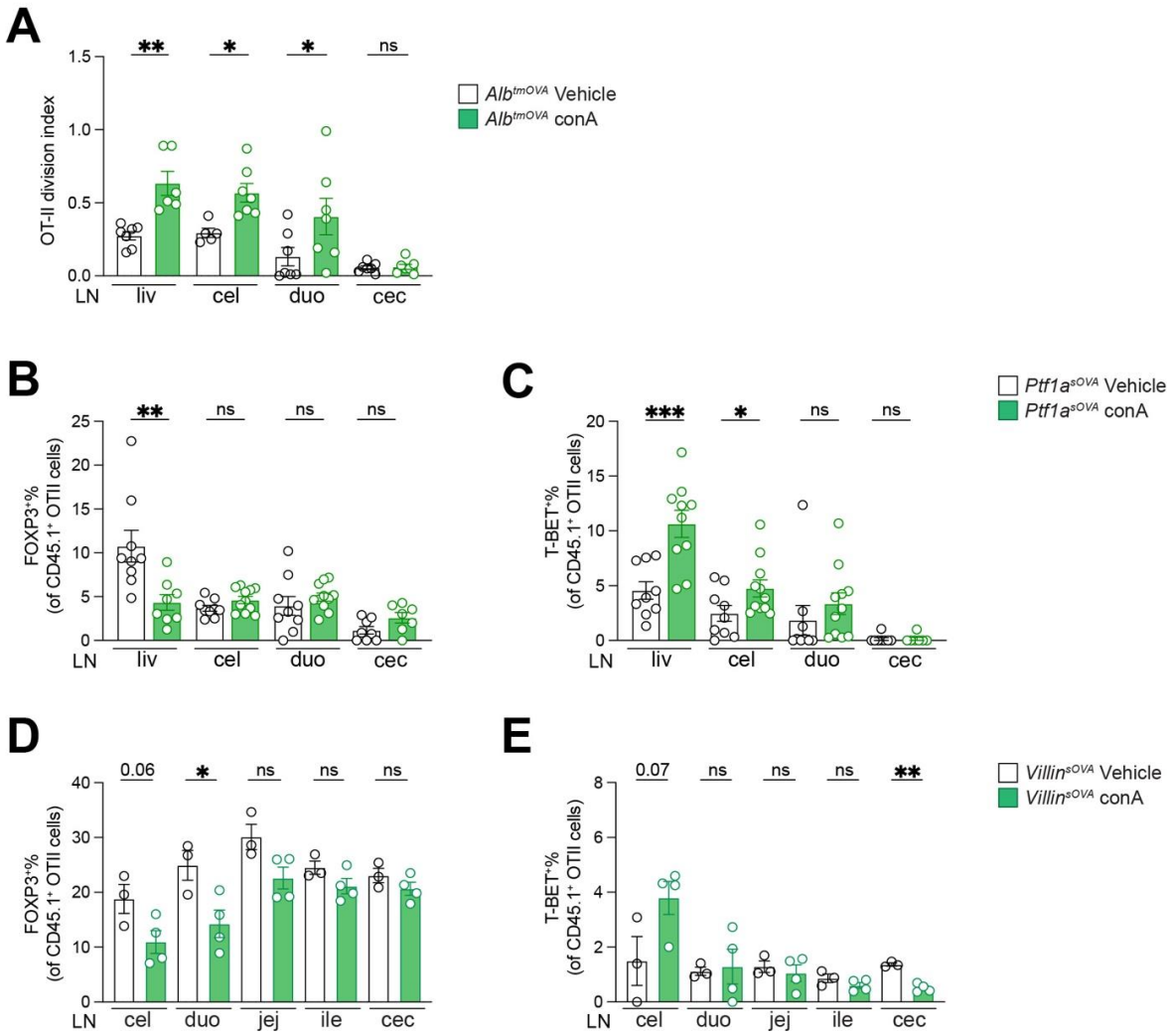


Figure 3.15 Con A-induced liver injury promotes pro-inflammatory conversion of pancreas- and gut-reactive T cells.
A. Division index of OT-II cells in indicated LNs 96 h after transfer into con A- or vehicle-treated *Alb*^{tmOVA} mice (n = 6 per group). **B-C.** Frequencies of FOXP3$^+$ (**B**) or T-BET$^+$ (**C**) among total OT-II cells in indicated LNs 96 h after transfer into con A- or vehicle-treated *Ptf1a*^{sOVA} mice (n = 9-10 per group, as indicated by symbols). **D-E.** Frequencies of FOXP3$^+$ (**B**) or T-BET$^+$ (**C**) among total OT-II cells in indicated LNs 96 h after transfer into con A- or vehicle-treated *Villin*^{sOVA} mice (n = 3-4 per group, as indicated by symbols). Data are pooled from two independent experiments in A-C. Data represent one experiment in D-E. * p<0.05, ** p<0.01, *** p<0.001 by t-test.

3.7 Material and methods

Table 3.1 KEY RESOURCES TABLE

REAGENT or RESOURCE	SOURCE	IDENTIFIER
Antibodies		
APC anti-mouse Granzyme B (clone QA16A02)	Biolegend	Cat#372204; RRID: AB_2687028
APC anti-mouse T-bet (clone 4B10)	Biolegend	Cat#644814; RRID: AB_10901173
APC anti-mouse FoxP3 (clone FJK-16S)	eBioscience	Cat#17-5773-82; RRID: AB_469457
APC anti-mouse IFNγ (clone XMG1.2)	Biolegend	Cat#505810; RRID: AB_315404
APC anti-mouse CD4 (clone RM4.5)	BD Biosciences	Cat#553051; RRID: AB_398528
APC anti-mouse CD45.1 (clone A20)	Tonbo Biosciences	Cat#20-0453; RRID: AB_2621575
APC/Cyanine7 anti-mouse TCRβ (clone H57-597)	Biolegend	Cat#109220; RRID: AB_893624
APC/Cyanine7 anti-mouse B220 (clone RA2-6B2)	Biolegend	Cat#103224; RRID: AB_313007
APC/Cyanine7 anti-mouse NK1.1 (clone PK136)	Biolegend	Cat#108724; RRID: AB_830871
PE anti-mouse FoxP3 (clone FJK-16S)	eBioscience	Cat#12-5773-82; RRID: AB_465936
PE anti-mouse T-bet (clone O4-46)	BD Biosciences	Cat#561268; RRID: AB_10564071
PE anti-mouse TNFα (clone MP6-XT22)	BD Biosciences	Cat#554419; RRID: AB_395380
PE anti-mouse GATA3 (clone TWAJ)	eBioscience	Cat#12-9966-42; RRID: AB_1963600
PE anti-mouse CD8α (clone 53-6.7)	Biolegend	Cat#100708; RRID: AB_312747
PE anti-mouse RORγT (clone Q31-378)	BD Biosciences	Cat#562607; RRID: AB_11153137
PE anti-mouse Granzyme B (clone QA16A02)	Biolegend	Cat#372208; RRID: AB_2687032
PE/Cyanine5 anti-mouse CD11c (clone N418)	Biolegend	Cat#117316; RRID: AB_493566
PE/Cyanine7 anti-mouse CD45.1 (clone A20)	eBioscience	Cat#25-0453-82; RRID: AB_469629
PE/Cyanine7 anti-mouse CD45 (clone 30-F11)	eBioscience	Cat#25-0451-82; RRID: AB_2734986
PE/Cyanine7 anti-mouse CD11c (clone N418)	eBioscience	Cat#25-0114-82; RRID: AB_469590
FITC anti-mouse CD4 (clone RM4-5)	Biolegend	Cat#100510; RRID: AB_312713
FITC anti-mouse Granzyme B (clone NGZB)	eBioscience	Cat#11-8898-82; RRID: AB_10733414
PerCP/eFluor™710 anti-mouse Vβ5.1/5.2 (clone MR9-4)	eBioscience	Cat#46-5796-82; RRID: AB_10853817
eFluor 450 anti-mouse FoxP3 (clone FJK-16S)	eBioscience	Cat#48-5773-82; RRID: AB_1518812
BV421 anti-mouse CD103 (clone OX-62)	BD Biosciences	Cat#566297; RRID: AB_2739670
BV421 anti-mouse TNFα (clone MP6-XT22)	BD Biosciences	Cat#563387; RRID: AB_2738173
BV421 anti-mouse RORγT (clone Q31-378)	BD Biosciences	Cat#562894; RRID: AB_2687545
BV605 anti-mouse CD44 (clone IM7)	BD Biosciences	Cat#563058; RRID: AB_2737979
BV605 anti-mouse CD8α (clone 53-6.7)	Biolegend	Cat#100744; RRID: AB_2562609
BV605 anti-mouse IFNγ (clone XMG1.2)	Biolegend	Cat#505839; RRID: AB_2561438
BV711 anti-mouse TCRβ (clone H57-597)	Biolegend	Cat#109243; RRID: AB_2629564
BV711 anti-mouse B220 (clone RA2-6B2)	Biolegend	Cat#103255; RRID: AB_2563491
BV785 anti-mouse CD8α (clone 53-6.7)	Biolegend	Cat#100749; RRID: AB_11218801
BV786 anti-mouse CD45 (clone 30-F11)	BD Biosciences	Cat#564225; RRID: AB_2716861
AF647™ anti-mouse CD11b (clone M1/70)	Biolegend	Cat#101218; RRID: AB_389327
Biotin anti-mouse B220 (clone RA3-6B2)	BD Biosciences	Cat#553086; RRID: AB_394616
Biotin anti-mouse CD11c (clone HL3)	BD Biosciences	Cat#553800; RRID: AB_395059
Biotin anti-mouse NK1.1 (clone PK136)	BD Biosciences	Cat#553163; RRID: AB_394675

REAGENT or RESOURCE	SOURCE	IDENTIFIER
Biotin anti-mouse CD4 (clone GK1.5)	BD Biosciences	Cat#553728; RRID: AB_395012
Biotin anti-mouse CD8α (clone 53-6.7)	BD Biosciences	Cat#553029; RRID: AB_394567
Biotin anti-mouse CD11b (clone M1/70)	BD Biosciences	Cat#553309; RRID: AB_394773
Biotin anti-mouse CD25 (clone 7D4)	BD Biosciences	Cat#553070; RRID: AB_394602
Biotin anti-mouse TER-119 (clone TER-119)	BD Biosciences	Cat#553672; RRID: AB_394985
Anti-mouse CD3 epsilon, monoclonal (clone SP7)	Abcam	Cat#ab16669; RRID: AB_443425
Anti-mouse CK19 (clone TROMA-III)	DSHB	Cat#TROMA-III; RRID: AB_2133570
Donkey anti-Goat IgG (H+L) Highly Cross-Adsorbed Secondary Antibody, AF^{TM}568	Invitrogen	Cat#A11057; RRID: AB_2534104
Donkey anti-Rat IgG (H+L) Highly Cross-Adsorbed Secondary Antibody, AF^{TM}568	Invitrogen	Cat#A78946; RRID: AB_2910653
Donkey anti-Rabbit IgG (H+L) Highly Cross-Adsorbed Secondary Antibody, AF^{TM}488	Invitrogen	Cat#A21206; RRID: AB_2535792
FLAG, polyclonal	Millipore Sigma	Cat#F7425; RRID: AB_439687
DDDDK tag, polyclonal	Abcam	Cat#ab95045; RRID: AB_10676074
DDDDK tag, polyclonal	Abcam	Cat#ab1257; RRID: AB_299216
Beta-actin (C4) HRP	Santa Cruz Biotechnology	Cat#sc-47778 HRP; RRID: AB_2714189
Peroxidase AffiniPure goat anti-rabbit IgG (H+L)	Jackson Immunoresearch	Cat#111-035-144; RRID: AB_2307391
Bacterial, virus and helminth strains		
Type 1 Lang (T1L) virus	Dermody Lab (University of Pittsburgh)	N/A
S. venezuelensis	Galli Lab (Stanford University)	N/A
NEB Stable Competent DH5α *E. coli* (High Efficiency)	New England Biolabs	Cat#C3040H
VQAd CMV Cre Virus	Antibodies Inc.	Cat#91-VQ004
Biological samples		
Bovine serum albumin (BSA)	Thermo Fisher	Cat#BP1600-100
Normal donkey serum (NDS)	Jackson ImmunoResearch	Cat#017-000-121
Newborn calf serum (NCS)	GeminiBio	Cat#100-504
Penicillin-streptomycin solution	Corning	Cat#30001CI
Collagenase, Type IV	Thermo Fisher	Cat#17104019
Collagenase, Type D	Millipore Sigma	Cat#11088866001
Collagenase, Type VIII	Millipore Sigma	Cat#C2139
DNase I, Amplification Grade	Invitrogen	Cat#18068015
Albumin from chicken egg white	Millipore Sigma	Cat#A5378
Chemicals, peptides, and recombinant proteins		
TRIzol^{TM} Reagent	Thermo Fisher	Cat#15596018
DNaseI	Millipore Sigma	Cat#10104159001
Histopaque-1077	Millipore Sigma	Cat#10770
RNAlater	Millipore Sigma	Cat#R0901
Concanavalin A	Millipore Sigma	Cat#234567
Carbon tetrachloride	Millipore Sigma	Cat#289116

REAGENT or RESOURCE	SOURCE	IDENTIFIER
Tamoxifen	Millipore Sigma	Cat#T5648
Streptozotocin (STZ)	Caymen Chemicals	Cat#13104
cOmplete Protease Inhibitor Cocktail, EDTA-free, Tablets	Roche	Cat#11873580001
PMSF	Millipore Sigma	Cat#10837091001
TAM diet (500, 2016, Red)	Envigo	Cat#TD.130858
Dulbecco's Modified Eagle Medium (DMEM)	Thermo Fisher	Cat#11965118
Joklik's modified Eagle's minimal essential medium (SMEM)	Lonza Bioscience	Cat#BE15-375k
LB Broth, Lennox (Powder)	Thermo Fisher	Cat#BP1427-2
Penicillin-Streptomycin Solution, 100x	Corning	Cat#30-002-CI
0.05% Trypsin/0.53mM EDTA in HBSS	Corning	Cat#25-051-CI
Ampicillin sodium salt	Thermo Fisher	Cat#BP176025
Puromycin Ready Made Solution	Millipore Sigma	Cat#P4512-1MLX10
Dapi Fluoromount G Clear Mounting Media	Thermo Fisher	Cat#OB010020
2-mercaptoethanol	Sigma Aldrich	Cat#M7522
RPMI 1640, powder	Thermo Fisher	Cat#31800105
Percoll	GE Healthcare	Cat#17089109
HEPES Buffer	Corning	Cat#25060CI
LIVE/DEAD™ Fixable Near-IR	Thermo Fisher	Cat#L10119
Zombie NIR™	Biolegend	Cat#423105
CellTrace™ CFSE	Thermo Fisher	Cat#C34554
Meloxicam Injection, 5 mg/ml, Solution for Injection	Covetrus	Cat#049755
Buprenorphine in Polymer Injection Solution 0.5 mg/ml	Wedgewood Pharmacy	Cat# BUPREN-INJ010VC
PE-conjugated H2-Kb chicken ova 257-264 SIINFEKL	NIH Tetramer Core Facility	N/A
APC-conjugated H2-Kb chicken ova 257-264 SIINFEKL	NIH Tetramer Core Facility	N/A
PE-conjugated I-Ab chicken ova 328-337 HAAHAEINEA	NIH Tetramer Core Facility	N/A
APC-conjugated I-Ab chicken ova 328-337 HAAHAEINEA	NIH Tetramer Core Facility	N/A
Trypan blue solution, 0.4%	Thermo Fisher	Cat#15250061
Buffer TCL	Qiagen	Cat#1031576
Critical commercial assays		
Fixation/permeabilization Concentrate	Thermo Fisher	Cat#00-5123-43
Fixation/permeabilization Diluent	Thermo Fisher	Cat#00-5223-56
Cytofix/cytoperm™ Fixation and Permeabilization Solution	BD Biosciences	Cat#554722
Permeabilization Buffer (10X)	Thermo Fisher	Cat#00-8333-56
GolgiPlug™ Protein Transport Inhibitor	BD Biosciences	Cat#555029
eBioscience™ Cell Stimulation Cocktail	Thermo Fisher	Cat#00-4975-93
SuperScript™ III One-Step RT-PCR System with Platinum™ *Taq* High Fidelity DNA Polymerase	Thermo Fisher	Cat#12574035
Maxima H Minus Reverse Transcriptase (200 U/μL)	Thermo Fisher	Cat#EP0753

REAGENT or RESOURCE	SOURCE	IDENTIFIER
RNasin™ Plus RNase Inhibitor	Promega	Cat#N2611
HiFi HS Ready Mix 2X	KAPA Biosystems	Cat#K2601K
EasySep Mouse T Cell Isolation Kit	Stemcell Technologies	Cat#19851
ApopTag Fluorescein In Situ Apoptosis Detection Kit	EMD Millipore	Cat#S7110
Anti-biotin Microbeads	Miltenyi Biotec	Cat#130090485
Clarity Western ECL Substrate	Bio-Rad	Cat#1705061
Clarity Max Western ECL Substrate	Bio-Rad	Cat#1705062
QIAprep Spin Miniprep Kit (50)	Qiagen	Cat#27104
QIAquick Gel Extraction Kit (50)	Qiagen	Cat#28704
Lipofectamine 3000 Transfection Reagent	Thermo Fisher	Cat#L3000008
Experimental models: Organisms/strains		
Mouse: C57BL/6J (B6)	Jackson Laboratory	RRID: IMSR_JAX:000664
Mouse: B6.Cg-Tg(TcraTcrb)425Cbn/J (OT-II)	Mucida Lab (Rockefeller University)	RRID: IMSR_JAX:004194
Mouse: C57BL/6-Tg(TcraTcrb)1100Mjb/J (OT-I)	Jackson Laboratory	RRID: IMSR_JAX:003831
Mouse: B6.SJL-Ptprca Pepcb/BoyJ (CD45.1)	Jackson Laboratory	RRID: IMSR_JAX:033076
Mouse: B6.129S6(Cg)-Ptf1a$^{tm2(cre/ESR1)Cvw}$/J (*Ptf1a^{CreERT2}*)	Jackson Laboratory	RRID: IMSR_JAX:036577
Mouse: B6(Cg)-*Ins1$^{tm2.1(cre/ERT2)Thor}$*/J (*Ins1^{CreERT2}*)	Jackson Laboratory	RRID: IMSR_JAX:026802
Mouse: B6.Cg-Tg(Vil1-cre/ERT2)23Syr/J (*Villin^{CreERT2}*)	Jackson Laboratory	RRID: IMSR_JAX:020282
Mouse: B6.Cg-*Speer6-ps1$^{Tg(Alb-cre)21Mgn}$*/J (*Alb^{Cre}*)	Jackson Laboratory	RRID: IMSR_JAX:003574
Mouse: B6.129S2-*Albtm1(cre/ERT2)Mtz*/J (*Alb^{CreERT2}*)	Mahan Lab (UT Health Houston)	RRID: IMSR_JAX:039060
Mouse: Rosa26-*sOVA*	Zhou et al.(Zhou et al., 2025)	N/A
Mouse: Rosa26-*cOVA*	Zhou et al.(Zhou et al., 2025)	N/A
Mouse: Rosa26-*tmOVA*	Zhou et al.(Zhou et al., 2025)	N/A
Cell line: KPC58	Muir Lab (University of Chicago)	N/A
Cell line: HEK293T	ATCC	Cat#CRL-3216
Cell line: L cell, L929	ATCC	Cat#CCL-1
Oligonucleotides		
OVA_F	Integrated DNA Technologies	CTTCAAAGGACTGTGGGAGAAA
OVA_R	Integrated DNA Technologies	CTCCATCTTCATGCGAGGTAAG
pLJM1_sOVA_FLAG_F	NEBuilder	CAGAGCTGGTTTAGTGAACCGTCAGATCCGATGGGCTCCATCGGTGCAG
pLJM1_sOVA_FLAG_R	NEBuilder	GATCTGAGTCCGGACTTGTACCCGGTAGCGTTACTTGTCATCGTCATCCTTGTAATC

REAGENT or RESOURCE	SOURCE	IDENTIFIER
pLJM1_cOVA_FLAG_F	NEBuilder	CAGAGCTGGTTTAGTGAACCGTC AGATCCGATGGGCTCCATCGGCG CAG
pLJM1_cOVA_FLAG_R	NEBuilder	GATCTGAGTCCGGACTTGTACCC GGTAGCGTTACTTGTCATCGTCAT CCTTGTAATCG
pLJM1_tmOVA_FLAG_F	NEBuilder	CAGAGCTGGTTTAGTGAACCGTC AGATCCGATGATGGATCAAGCTA GATCAG
pLJM1_tmOVA_FLAG_R	NEBuilder	GATCTGAGTCCGGACTTGTACCC GGTAGCGTTACTTGTCATCGTCAT CCTTG
Software and algorithms		
GraphPad Prism (v10.6.1)	GraphPad	https://www.graphpad.com/
FlowJo (v10.10.0)	Tree Star	https://www.flowjo.com/
QuPath (v0.5.1)	Bankhead et. al(Bankhead et al., 2017)	https://qupath.github.io/
Adobe Illustrator (v29.0)	Adobe	www.adobe.com/products/illustrator
Devices		
BD LSRII	BD Biosciences	N/A
5-laser Aurora spectral flow cytometer	Cytek Bioscience	N/A
EVOS^{TM} FL fluorescent microscope	Invitrogen	N/A
SP8 confocal microscope	Leica	N/A

Mice

All mouse studies were approved by The University of Chicago Institutional Animal Care and Use Committee under protocol number 72562. C57BL/6J, CD45.1 congenic (B6.SJL-Ptprc^{a} Pepc^{b}/BoyJ), *Villin*$^{CRE-ERT2}$ (B6.Cg-Tg(Vil1-cre/ERT2)23 Syr/J), *Ptf1a*$^{CRE-ERT2}$ (B6.129S6(Cg)-Ptf1a^{tm2}(cre/ESR1)Cvw/J), *Ins1*$^{CRE-ERT2}$ (B6(Cg)-Ins1$^{tm2.1(cre/ERT2)Thor}$/J), OT-I (C57BL/6-Tg(TcraTcrb) 1100Mjb/J), OT-II (B6.Cg-Tg(TcraTcrb)425Cbn/J), *Alb*^{Cre} (B6.Cg-Speer6-ps1^{Tg}(Alb-cre)21 Mgn/J), *p53*^{LOXP} (B6.129P2-*Trp53*^{tm1Brn}/J) and *Kras*$^{FSF-G12D}$ (B6(Cg)-*Kras*^{tm5Tyj}/J) were purchased from The Jackson Laboratory. *Alb*^{CreERT2} mice were gifted by Dr. Kristin E. Mahan (UT Health Houston) after obtaining an MTA from the original investigator (Dr. Pierre Chambon, IGBMC, Illkirch, France) and rederived at our facility. The 3 lines of OVA mice were engineered in house and characterized in Zhou et, al(Zhou et al., 2025). All mice were

maintained at the University of Chicago animal facility under specific pathogen-free (SPF) condition, confirmed to be free of segmented filamentous bacteria (SFB). Mice were used between 5-10 weeks of age. With the exception of *S. venezuelensis* infections (male mice only), a mix of male and female mice was used, with equal numbers of males and females in each experimental group.

Immunofluorescent staining of paraffin embedded slides

Tissues were fixed in 4% PFA/PBS for 2 h at RT and subjected to paraffinization. Paraffin-embedded tissue sections (5μm) were heated at 65°C for 20min, deparaffinized twice in xylene (10 min each), and rehydrated through a graded ethanol series. Sections were blocked for 30 min at RT with blocking buffer (5% donkey serum, 2.5% BSA in 1X PBS). Slides were permeabilized with 0.1% Triton X-100 before overnight incubation at 4°C in a humidified chamber with primary antibodies (see Antibodies section). The following day, slides were washed three times with PBST (PBS with 0.05% Tween-20) for 15 min each, incubated with appropriate secondary antibodies for 1 h at RT, washed again three times in PBST, and mounted with DAPI Fluoromount G Clear Mounting Media (SouthernBiotech). Images were acquired using SP8 Lightning confocal microscope (Leica) or Olympus VS200 Slideview Research Slide Scanner at the University of Chicago Microscopy Core.

Immunofluorescent staining of fresh frozen slides

Tissue was directly put into OCT compound and fresh frozen using pre-cooled 2-methylbutane bath and cut into 6-μm-thick sections. The slides were returned to RT right before staining and fixed in 1% PFA for 30 min. They were then blocked in 5% BSA + 0.1% Tween-20 in PBS for 1

hour at RT and incubated in primary antibodies diluted in blocking buffer overnight at 4°C. The slides were then washed, incubated with secondary antibodies (1:500 dilution) and mounted with DAPI Fluoromount G Clear Mounting Media. Stained slides were sent for whole slide scanning using Olympus VS200 Slideview Research Slide Scanner. Alternatively, pictures of slides were taken using SP8 Lightning Confocal Microscope (Leica).

Immunoblotting

Whole-cell or whole-tissue lysates were prepared in RIPA lysis buffer (20 mM HEPES, 0.2 mM EDTA, 300 mM NaCl, 1.5 mM $MgCl_2$, 1% Triton X-100) supplemented with protease inhibitor (Roche) and 1 mM phenylmethylsulphonyl fluoride (PMSF; Sigma). Samples were separated by SDS-PAGE and transferred onto nitrocellulose membranes (Millipore). Membranes were probed with the indicated primary and secondary antibodies (see Key Resource Table).

Cell culture

HEK293T cells were purchased from ATCC and were cultured in Dulbecco's Modified Eagle Media (DMEM; Gibco) supplemented with 10% FBS and 100 U/mL penicillin/streptomycin. KPC58 cell line was generously provided by Dr. Alexander Muir (University of Chicago)(Apiz Saab et al., 2023). KPC cells were grown in RPMI-1640 media supplemented with 10% FBS and 100 U/mL penicillin and streptomycin. Spinner-adapted murine L929 cells for T1L titer determination were maintained in either suspension or monolayer cultures in Joklik's modified Eagle's minimal essential medium (SMEM; Lonza) supplemented to contain 5% fetal bovine serum (FBS; Gibco), 2 mM L-glutamine, 100 U/ml of penicillin, 100 μg/ml of streptomycin

(Gibco), and 25 ng/ml of amphotericin B (Sigma). Cultures were maintained at 37°C in a humidified incubator with 5% CO_2.

Lentiviral transduction of ovalbumin expression

pLJM1-Empty (Addgene #91980) plasmid was used as lentiviral vector, which was linearized by Nhel-HF (NEB) at 37°C for 20min and gel purified. Primers were designed using NEBuilder (https://nebuilder.neb.com/#!/) to create the necessary overlap with the plasmid. Insert fragments were created using the designed primers (listed in Key Resource Table) and Phusion High-fidelity DNA polymerase (NEB). The fragments were gel purified. Gibson assembly reaction was set up and the molar ratio for insert-to-vector was set to be 1:1. The reactants were incubated at 50°C for 2 h and the product was transformed into NEB Stable Competent E. coli cells (NEB #C3040H) according to the manufacturers' protocol. Transformed E. coli cells were plated onto selection agar plates and single colonies were picked and sequences. The correct colonies were expanded, and plasmids were extracted using QIAGEN Plasmid Mini Kit.

Lentivirus was produced in HEK293T cells transfected at 80-90% confluency using Lipofectamine 3000 (Invitrogen) as recommended by the manufacturer and psPAX2 (Addgene) and pMD2.G (Addgene) packaging vectors. Medium was changed 8-12 hours after transfection and supernatant was collected after 48-72 h. Viral media was passed through a 0.45 μm filter and mixed with 10 μg ml^{-1} Polybrene (Sigma Aldrich) before being added to KPC cells. Infected cells were treated with puromycin to generate stable cell populations. OVA expression was verified by immunoblotting.

Flow Cytometry

Single-cell suspensions were first stained with LIVE/DEAD™ Fixable Near-IR Dead Cells Stain kits (Invitrogen) for 10 min at 4°C, followed by surface staining with antibody cocktails (1:200) for 20 min at 4°C. For intracellular cytokine detection, cells were fixed and permeabilized with Cytofix/cytoperm™ solution (BD Biosciences) for 20 min prior to staining with intracellular antibodies overnight at 4°C. For transcription factor analysis, cells were incubated in Fixation/permeabilization solution (eBiosciences) for 30 min to 2 hr, and subsequently stained with nuclear antibodies overnight at 4°C. All intracellular and nuclear antibodies were diluted 1:100 in 1x Permeabilization buffer (eBiosciences). Samples were acquired on an LSR II (BD Biosciences) or a 5-laser Aurora spectral flow cytometer (Cytek) and analyzed using FlowJo software. Cell division index was calculated using FlowJo formula as described (http://www.flowjo.com/v765/en/proliferation.html), whereby the index represents the fraction of total cell divisions normalized to the estimated starting cell number.

OVA tetramer staining

Single-cell suspensions were enriched for T cells using EasySep™ Mouse T Cell Isolation Kit (Stemcell Technologies) and then incubated with Fc block for 10 min at 4°C to prevent nonspecific binding. For detection of OVA-specific $CD8^+$ T cells, H-2Kb:OVA (SIINFEKL) PE- and APC-conjugated tetramers (NIH Tetramer Core Facility) were added at 1:200 in FACS buffer and incubated for 20 min at RT in the dark. For detection of OVA-specific $CD4^+$ T cells, I-Ab:OVA (HAAHAEINEA) PE- or APC-conjugated tetramers (NIH Tetramer Core Facility) were added at 1:100 in T cell medium and incubated for 2 h at RT in the dark. Cells were then washed with FACS buffer before staining with surface antibody cocktail. Each tetramer lot was validated using OVA-

immunized mice before use. Tetramer-positive gates were defined using OVA-naïve mice and fluorescence-minus-one controls.

Quantitative Real-time PCR

Total RNA from samples was extracted using TRIzol (Thermo Fisher Scientific), treated with DNase I (Invitrogen), and reverse transcribed into cDNA using SuperScript IV kit (Thermo Fisher Scientific) according to the manufacturer's protocol. Quantitative real-time PCR was performed using Power SYBR Green PCR Master Mix (Applied Biosystems) on Quanstudio 6 Flex machine (Thermo Fisher Scientific). The relative expression of target genes was determined by normalization to housekeeping gene *36B4* and calculated using the formula of $2^{-\Delta Ct} \times 10000$. All data were averaged from at least 2 replicates.

Adaptive T cell transfer and CFSE tracing

Naïve T cells were isolated from pooled LNs and spleens by negative selection using biotinylated antibodies against NK1.1, B220, CD11c, CD11b, TER119 and either CD8α or CD4, followed by anti-biotin MACS beads (Miltenyi Biotec). Purity of transgenic cells was confirmed by flow cytometry ($CD45.1^+V\beta5^+TCR\beta^+CD4^+$ for OT-II cells or $CD45.1^+V\beta5^+TCR\beta^+CD8\alpha^+$ for OT-I cells). Cell viability was determined by Trypan blue staining.

For experiments probing T cell outcomes in LNs, OT-II cells were labeled with CFSE Cell Proliferation Kit (Life Technologies) by incubating cells for 3-5 mins at 37°C, followed by a wash in PBS. A total of 750,000 OT-II or OT-I cells was transferred by retro-orbital injections under isoflurane anesthesia, and LNs harvested 4 days post-transfer. For experiments probing T

cell responses in the tissues, transgenic cells were not CFSE-labeled. On the day of transfer, 200,000 OT-II and 50,000 OT-I cells were injected retro-orbitally. Organs were procured at indicated timepoints.

Induction of ovalbumin self-antigen in the intestine by tamoxifen administration

Rosa26-*OVA* mice were crossed to mice expressing tissue-specific Cre. Offspring were administrated tamoxifen-containing diet (TAM diet, Envigo) for 7 consecutive days or by daily intraperitoneal injection of 1mg tamoxifen (TAM) (Sigma) dissolved in 100 µl corn oil for 5 consecutive days at 4-6 weeks of age to induce for OVA self-antigen expression in the tissue of interest. Following TAM administration, mice were returned to a normal Chow diet for 4-7 days before use in experiments.

Oral ovalbumin administration

OVA (Sigma) was diluted in sterile PBS and filter sterilized prior to administration. Mice received 25 mg OVA in 200 µl PBS by oral gavage one time, one day post OT-I/OT-II co-transfer.

Infections

Reovirus strain type 1 Lang was recovered using plasmid-based reverse genetics(Kobayashi et al., 2007) and purified using $CsCl_2$ gradient centrifugation(Fiske et al., 2024). Titers of purified virus stocks were determined by plaque assay using L929 cells. Intragastric infection was performed by oral gavage mice with 1×10^9 PFU T1L in 200 µl PBS(Fiske et al., 2024). Intranasal infection was performed by lightly anesthetizing mice with isoflurane and inoculating intranasally with 1 × 10^9 PFU of T1L diluted in PBS in a total volume of 50 µl (25 µl per nostril).

S. venezuelensis was maintained in NSG mice by subcutaneous infection with 10,000-30,000 larvae. Fecal pellets from infected NSG mice were collected and spread on Whatman paper, and incubated in water at 28°C. Larvae emerging over 3-4 days were collected to reinitiate the infection cycle or to be used for infection of experimental mice. For experimental mouse infection, 1000 larvae were administrated subcutaneously to male mice. Successful infection was confirmed by appearance of eggs in the fecal content of the infected mice. OT-II cells were transferred 5 days post infection.

Adeno-Cre virus was diluted in PBS to a final concentration of 5 × 10^5 PFU/ml. A total volume of 200 µl of the viral suspension was administered to mice via tail vein injection. OT-II cells were transferred 14 days post infection.

Carbon tetrachloride (CCl_4) administration

CCl_4 was diluted in corn oil at 20% (v/v). A 50 µl volume of this solution was administered intraperitoneally to a 20 g mouse, delivering a dose of 50 µl per kg body weight.

Concanavalin A (Con A) administration

Con A was reconstituted from lyophilized powder into a 2.4 mg/mL working stock using sterile PBS. 100 µl was administered retro-orbitally to a 20 g mouse, delivering a dose of 12 mg/kg.

Cerulein administration

6 hourly intraperitoneal injections of 50ug/kg cerulein (Bachem) on each injection day while control mice were injected with the same amount of saline. 3 injection days was performed at 7, 4, 1 day before OT-II cell transfer.

Streptozotocin (STZ) administration

Prior to STZ treatment, mice were fasted for 4-5 hours. STZ was dissolved in sterile sodium citrate buffer immediately prior to i.p. injection. Sodium citrate buffer was prepared by adding 1.47 g sodium citrate to 50 mL H2O and adjusting pH to 4.5 with citric acid. Mice were given a single high dose (150 mg/kg).

ApopTag staining and apoptotic index

Apoptosis was detected using ApopTag Fluorescein In Situ Apoptosis Detection Kit (Sigma, S7110). Paraffin sections were deparaffinized and rehydrated as described for immunofluorescence staining, followed by ApopTag staining according to the manufacturer's protocol. The stained slides were scanned and analyzed in QuPath. Apoptotic index represents the percentage of ApopTag$^+$ cells over total cell number.

Isolation of T cells from lymph nodes

For T cell analysis, LNs were dissected into RPMI supplemented with 2% NCS and 1mM EDTA, mashed between two frosted glass slides, and filtered into 96-well plates. Cells were immediately subjected to Live/Dead and surface marker staining.

Isolation of T cells from the liver and pancreas

For hepatic immune cell isolation, liver was perfused with approximately 3ml of collagenase D and DNase I in RPMI through the portal vein. The liver was then digested at 37°C for 16-18 min. The reaction was quenched with ice-cold RPMI with 10% FBS. Parenchymal cells were discarded

by centrifugation (75g for 1 min). The supernatant was centrifuged again at 800g for 2 min. The pellet was resuspended in 5 ml of Histopaque 1077 and gently overlayed with 10 ml of RPMI. Immune cells were enriched through gradient centrifugation at 900g for 18 min at RT with slow acceleration and deceleration.

For pancreatic immune cell isolation, pancreas was perfused with 2-3ml of collagenase IV and DNase I in HBSS with Ca and Mg through the bile duct. LNs were detached from the pancreas using forceps. The pancreas was then digested at 37°C for 25 min with repeated mechanical shacking every 5min throughout the digestion. The reaction was quenched with ice-cold RPMI with 10% FBS. The samples were filtered and centrifuged at 800g for 2 min. The pellet was resuspended in 5 ml of Histopaque 1077 and gently overlayed with 10 ml of RPMI. Immune cells were enriched through gradient centrifugation at 900g for 18 min at RT with slow acceleration and deceleration. Cells were immediately subjected to Live/Dead and surface marker staining.

T cell stimulation

For the detection of OT-I cytokine production, single cell suspension of isolated lymphocytes was pelleted by centrifugation and resuspended in T cell media containing cell stimulation cocktail (1:500; eBioscience). Cultures were incubated for 4 h at 37°C. Following stimulation, cells were pelleted, washed once with fresh medium, and processed for cell staining.

Pancreatic cancer induction

Ptf1a$^{CreERT2/w}$*Trp53*$^{fl/fl}$Kras$^{LSL-G12D/w}$sOVA$^{+/w}$ (PDAC-sOVA) mice were fed with tamoxifen-containing diet (Envigo # TD.130858) for 7 days at 3-4 weeks of age for induction of tumorigenesis and OVA expression. OT-I and OT-II cells were transfer at day 7 post induction.

For T cell analysis in the LNs, LNs were harvested at day 10 post termination of the tamoxifen diet. For tumor area analysis, pancreas was harvested at day 28 post induction.

Orthotopic model for pancreatic cancer

Mice were treated with Meloxicam (0.5 mg) and Buprenorphine (10 μg per mouse) prior to the surgery for pain management. Mice were then anesthetized using isoflurane. 5k or 50k of KPC cells expressing sOVA, cOVA or empty vector control were surgically implanted to the mid portion of the pancreas. Surgical incision was sutured, and mice were monitored for the need of further pain management. At day 11 post operation, OT-I and OT-II cells were co-transferred and mice were infected with T1L or vehicle control. For T cell analysis in the LNs, LNs were harvested at day 14 post operation. For tumor analysis, mice were sacrificed at day 22-23 post operation and tumor size / weight was measured. Tumor size was calculated as $0.5 \times \text{length} \times \text{width}^2$. Tumors were fresh frozen in OCT for downstream immunofluorescent analysis.

Pancreatic lesion quantification

Whole-pancreas H&E sections, including tumors, were scanned and analyzed using QuPath. Spleen and lymph node regions were excluded, and the total pancreatic tissue area was outlined and quantified. Each lesion was annotated, and lesion number and total lesion area were recorded. The percentage of lesion area was calculated relative to the total pancreatic area.

Administration of CD8b neutralizing antibody

One week after T1L infection, mice received 100 μg of CD8β-neutralizing antibody (SelleckChem) per mouse via intraperitoneal injection every 5 days. Control mice received 100 μg of isotype control antibody on the same schedule.

Statistical analysis

All data were analyzed with Prism software (GraphPad). Data is presented as average ± SEM. Comparison between two treatment conditions by two-tailed unpaired Student's t-test assuming a Gaussian distribution. Gaussian distribution tests appropriate for small sample sizes were applied for all datasets (Shapiro-Wilk and Kolmogorov-Smirnov test); all data sets passed the requirements for Gaussian distribution. P-values or representative symbols are noted when differences are less than or equal to 0.1; all other differences were not found to be significant (n.s., $p > 0.1$). $^{*}p < 0.05$, $^{**}p < 0.01$, $^{***}p < 0.001$). One-way ANOVA was used for multivariant comparisons between more than two groups. Two-tailed t-test was used to compare two groups (i.e. NI vs. infected LNs).

Chapter 4. Inducible, but not constitutive, pancreatic *REG/Reg* isoforms are regulated by intestinal microbiota and pancreatic diseases

4.1 Summary

The *REG*/*Reg* gene locus encodes for a conserved family of potent antimicrobial but also pancreatitis-associated proteins. Here we investigated whether *REG/Reg* family members differ in their baseline expression levels and abilities to be regulated in the pancreas and gut upon perturbations. We found, in human and mouse, pancreas and gut differed in *REG*/*Reg* isoform levels and preferences, with duodenum most resembling the pancreas. Pancreatic acinar cells and intestinal enterocytes were the dominant REG producers. Intestinal symbiotic microbes regulated the expression of the same, select *Reg* members in gut and pancreas. These *Reg* members had the most STAT3-binding sites close to the transcription start sites and were partially IL-22 dependent. We thus categorized them as "inducible" and others as "constitutive". Indeed, also in models of pancreatic-ductal adenocarcinoma and pancreatitis, only inducible *Reg* members were upregulated in pancreas. While intestinal *Reg* expression remained unchanged upon pancreatic perturbation, pancreatitis altered the microbial composition of the duodenum and feces shortly after disease onset. Our study reveals differential usage and regulation of *REG*/*Reg* isoforms as a mechanism for tissue-specific innate immunity, highlights the intimate connection of pancreas and duodenum, and implies a gut-to-pancreas communication axis resulting in a coordinated *Reg* response.

4.2 Introduction

Barrier sites of the body have the challenging task of maintaining a symbiotic relationship with commensal organisms while effectively killing pathogens. A broad set of innate and adaptive

immune cells has evolved to maintain this delicate equilibrium. At barrier sites, the cells directly interfacing with microbes, such as keratinocytes or gut epithelial cells, also possess antimicrobial activity. Though often requiring communication with hematopoietic immune cells, they substantially contribute to keeping the symbiotic microbiota in check and enhancing pathogen clearance.

In the gut epithelium, one mechanism is the secretion of antimicrobial peptides or small proteins including the C-type lectin family of REG proteins. In humans, this family includes *REG1A*, *REG1B* (*REG1* subfamily), *REG3A*, *REG3G* (*REG3* subfamily) clustered on Chromosome 2, and *REG4* on Chromosome 1. In mice, it consists of *Reg1* and *Reg2* (*Reg1* subfamily), *Reg3a*, *Regb3*, *Reg3g*, and *Reg3d* (*Reg3* subfamily) clustered on Chromosome 6 and *Reg4* on Chromosome 3. Better studied in murine intestine, REG3γ was found to spatially restrain the microbiota from contacting the epithelium and target gram-positive bacteria(Cash, Whitham, Behrendt, et al., 2006; Vaishnava et al., 2011b), while REG3β may bind both gram-positive and gram-negative(Stelter et al., 2011), and REG3A gram negative bacteria(Darnaud et al., 2018). Mechanistically, human REG3A has been found to form filaments of hexameric, pore-forming rings *in vitro* that insert into bacterial membranes to kill(Mukherjee et al., 2014) and REG3G to aggregate bacteria(Iovanna et al., 1991). *Reg3g* expression is regulated by microbial colonization and some bacterial infections(Keir et al., 2020; W. Yang et al., 2020; Zenewicz, 2018), particularly induced by flagellin in an IL-22 dependent manner(Kinnebrew et al., 2012), and upregulated by elevated IL-6, another infection-associated cytokine(Shaw et al., 2012). Both cytokine signaling pathways converge on STAT3 activation. In humans, intestinal *REG* expression is elevated in many patients with inflammatory bowel diseases(Tsuchida et al., 2017) and colorectal cancer(H. C. Zheng et al., 2011), suggesting a link with the microbiota and inflammation.

Surprisingly, such a bactericidal role for REG proteins has scarcely been proposed in the pancreas(Iovanna et al., 1991), even though the gene family was originally discovered there. REG proteins were initially observed to be upregulated upon pancreatitis (hence their alternative name, pancreatitis-associated protein, or PAP) and after partial pancreatectomy, where they were thought to aid beta cell regeneration(Okamoto, 1999) (from which the name REG is derived). REG1A, REG1B and REG3A are present in human pancreatic juice even under non-disease conditions(R. Chen et al., 2006; Doyle et al., 2012). However, elevated pancreatic *REG* expression is associated with poor prognosis in pancreatic ductal adenocarcinoma (PDAC)(Q. Li et al., 2016; Xie et al., 2003), and in mice overexpression of *Reg3g* is sufficient to aggravate PDAC in a genetic model(X. Liu et al., 2017). Knocking out the entire pancreatic *Reg* family is protective in cerulein-induced pancreatitis(W. Chen et al., 2023b). Overall, a pro-proliferative role has been assigned to REG proteins in the pancreas(Okamoto, 1999).

While C-type lectins can execute pleiotropic functions(Schnitger et al., 2009), a potential bactericidal role of pancreatic REG proteins and their transcriptional regulation by microbes remain unclear. Additionally, most studies focusing on the gut, even if occasionally also analyzing the pancreas, measure only *Reg3g* and *Reg3b*, which may not be the genes most relevant in the pancreas. Therefore, in this study, we performed a holistic investigation on all *Reg* family members' baseline expression profile in pancreas and gut and their abilities to be regulated upon intestinal and pancreatic perturbations.

4.3 Results

4.3.1 Mouse and human Reg/REG gene family members are structurally conserved but differ in their ligand binding domains and expression pattern between pancreas and gut

Most prior studies of REG proteins focused on the REG3 subfamily. To assess if other REG family members are likely to function similarly, we first took a bioinformatic approach. Amino acid sequence alignment of all murine and human REG isoforms revealed several conserved features (Fig. 4.7A): An inhibitory N-terminal prosegment followed by a trypsin cleavage site(Mukherjee et al., 2009) and characteristic features of C-type lectins(Gabba et al., 2021; Weis et al., 1991; Weis & Drickamer, 1996; Zelensky & Gready, 2005). The REG subgroups notably differed in the primary sequences of the three loops forming the carbohydrate recognition domain (CRD): REG3, but not REG1 and REG4, subfamily members possess a longer loop 1 that includes the classical mannose binding motif EPN. REG1 and REG4 members are also more similar to each other than to REG3 proteins in the backloop, while REG1 proteins resemble REG3 sequences more in loop 2. Additional subtle differences within REG subfamilies exist in the CRD region. To understand how these primary sequences may translate into three-dimensional differences, we simulated the structure of all REG proteins using AlphaFold, noting that the software cannot account for structural shifts upon prosegment removal(Mukherjee et al., 2009) (Fig. 4.7B). The prosegment was not folded onto the proteins as predicted by NMR(Mukherjee et al., 2009), but the heads representing mature REG proteins were similar to the experimentally solved REG3A structure(Abergel et al., 1999) and predicted to display the canonical C-type lectin fold with two alpha helices “sandwiching” antiparallel beta sheets, whose loops cluster on one side of the protein to form the CRD (Gabba et al., 2021; Weis et al., 1991; Weis & Drickamer, 1996; Zelensky & Gready, 2005). Notably, the CRD loops of the REG3 subfamily uniquely displayed one or two short beta strands and had a narrower binding cleft than subfamily REG1 and REG4. Scoring atomic distances within the REG proteins head regions (Fig. 4.1A) revealed structural similarity between members of the same REG subfamily regardless of species. The REG1 family

was equally similar to the REG3 and REG4 subfamilies, while the REG3 and REG4 subfamilies were the most dissimilar. This was also reflected at the amino acid sequence similarity level (Fig. 4.1A, Fig. 4.7C). Overall, this analysis suggests that the REG subfamilies bind different ligands, and REG proteins within subfamilies may bind ligands with different affinities (Cash, Whitham, Behrendt, et al., 2006; Vaishnava et al., 2011b).

Next, we compared isoform usage between the pancreas and different regions along the gut in B6 and NOD mice, as well as humans (Table 1). In both mouse strains, *Reg1*, *Reg2*, and *Reg3d* were more highly expressed in pancreas; *Reg3a* was highest in the jejunum, all other isoforms in the ileum. Within the gut, *Reg1*, *Reg2*, and *Reg3d* were most highly transcribed in the duodenum, while the colon consistently showed the lowest expression (Fig. 4.1B-E, Fig. 4.8A-J). The pancreas very lowly expressed *Reg4*, making it the most gut-specific isoform. Grossly, *Reg1* and *Reg3d* were the dominant pancreatic isoforms, *Reg1* and *Reg3b* were dominant in the duodenum, *Reg3b* and *Reg3g* in jejunum and ileum, and *Reg4* (B6 mice) or *Reg3b* and *Reg3*g (NOD mice) in the colon (Fig. 4.1I, J). The main difference between the mouse strains was that NOD mice had higher overall transcript levels, in line with previous reports on pancreas(Baeza et al., 2001). In humans the expression pattern was quite different. While *REG1* was highly expressed in the pancreas and displayed a proximal to distal gradient within the intestine (Fig. 4.1F), all other isoforms were lowly expressed despite robust pancreatic *CPA1* and intestinal *VILLIN1* expression, which rules out underrepresentation of acinar and gut epithelial cells, two cell types with previously reported *REG* expression(Tsuchida et al., 2017; H. Zhang et al., 2021; H. C. Zheng et al., 2011) (Fig. 4.1G, H; Fig. 4.8K-N). *REG4* was the second most highly expressed *REG* isoform in pancreas and gut, and no other isoform dominated the gut. Instead, the pancreas trended to

exhibit the highest *REG3A* and *REG3G* expression. Overall, *REG1A* was the dominant isoform of both human pancreas and gut (Fig. 4.1K).

These data suggest that the REG isoforms are utilized differently by the proximal gastrointestinal system (pancreas and duodenum) versus the distal gut, and are more tightly regulated in humans than mice, with the notable exception of *REG1A*.

4.3.2 Gut enterocytes and pancreatic acinar cells are enriched for REG/Reg transcripts and the upstream signaling receptor IL22RA1/Il22ra1

We sought to more comprehensively understand how unique *REG/Reg* expression is to gut and pancreas at homeostasis, which cell types within these tissues express them, and how likely it was for *REG/Reg* to be activated by IL-22 and IL-6 (Kinnebrew et al., 2012; X. Liu et al., 2015) across tissues. We first measured the expression of all seven mouse *Reg* isoforms in a 22-tissue panel from B6 mice, including other important barrier sites like lung, skin and bladder (Fig. 4.2A). In this panel, only the pancreas and gut expressed *Reg*. To determine if the confinement of *Reg* expression to the pancreas and gut correlated with IL-22 and/or IL-6 receptor expression, we measured the transcript abundance of the subunits of IL-6 receptor (*Il6r1* and *Il6st*) and IL-22 receptor (*Il22ra1* and *Il10rb*) in our tissue panel, along with the cytokines themselves (*Il6*, *Il22*) and IL-22BP, a soluble IL-22 decoy receptor that sequesters IL-22 (*Il22ra2*)(Huber et al., 2012) (Fig. 4.2B). *Il6r1* and *Il6st* were barely expressed in the gut; the pancreas displayed some expression, but similar levels were observed in organs that do not express *Reg* genes. By contrast, *Il22ra1* was enriched in the pancreas and small intestine (Fig. 4.2B, C), and its expression correlated more strongly with total *Reg* expression than did *Il6r1* and *Il6st* (Fig. 4.8P-R). In addition, *Il22ra2* was enriched in the colon compared to pancreas and small intestine (Fig. 4.2B, C), correlating with the lower expression of *Reg* genes in the colon. *Il6* and *Il22* transcripts were

very low, as typical for cytokines in whole tissue extracts, and their measurement was therefore omitted for the rest of this study. In human pancreas and gut, we found that *IL22R1* and *IL6ST* displayed higher transcript levels in the pancreas than gut and *IL22RA2* was the highest in the colon (Fig. 4.2D-G; Fig. 4.8O).

To pinpoint the cell types within pancreas and gut that express *REG*/*Reg* and assess whether this coincides with the expression of the IL22 receptor subunits, we re-analyzed published *scRNAseq* datasets. In mouse pancreas(Chondronasiou et al., 2022), the expression of *Reg* isoforms was largely restricted to acinar cells (Fig. 4.2H, I), displaying a pattern on a feature plot similar to the acinar cell marker *Amy2b*. The *Il22ra1* signal recovery was low but confined to acinar cells (Fig. 4.2J). By contrast, *Il10rb*, *Il6r1, Il6st* (Fig. 4.2J), as well as *Il17ra* and *Il17rc,* the receptors for IL-17, which is often co-secreted with IL-22 (Fig. 4.9A), were co-enriched in ductal, endothelial, and pancreatic stellate cells. Similarly, in human pancreas(Steele et al., 2020) *REG* and *IL22RA1* expression were confined to acinar cells (Fig. 4.2K-M). *REG1A* was the dominant pancreatic *REG* isoform (Fig. 4.2L), confirming our Q-PCR results. Ductal and acinar cells expressed comparable levels of *Il10RB*, *Il6R, Il6ST* (Fig. 4.2M), while *Il17RA* and *Il17RC* were enriched in ductal compared to acinar cells (Fig. 4.9B). In neither the mouse nor human *scRNAseq* did we observe noteworthy expression of the receptor genes in pancreatic endocrine cells, though this could in part be due to the low representation of these cells in the datasets.

For murine intestine, we analyzed a *scRNAseq* dataset that encompassed epithelial cells from different regions of the small intestine(Zwick et al., 2024) (Fig. 4.9C, D). Feature plots for single genes (Fig. 4.9E) and their relation to cell types and region (Fig. 4.9C, D) showed that *Reg1* expression was enriched in duodenal enterocytes. *Reg2* and *Reg3d* were barely expressed. *Reg3a*, *Reg3b* and *Reg3g* were enriched in enterocytes of all small intestinal regions, though lower levels

of *Reg3b* and *Reg3g* also mapped to virtually all cell types, including stem cells. *Reg4* was distinct, confined to goblet, Paneth, and enteroendocrine cells. Regarding cytokine receptor enrichment (Fig. 4.9F), *Il22ra1* and *Il17ra* were lowly expressed by nearly all cell types; *Il6ra* was enriched in endocrine cells. In human intestine, the scRNAseq dataset covered epithelial cells from the small and large intestine (Burclaff et al., 2022) (Fig. 4.9G, H). *REG1A* was the most abundant isoform, predominantly expressed by small intestinal epithelial cells, with much lower levels in large intestine (Fig. 4.9I). Small intestinal enterocytes were the dominant population expressing *REG1A* and *REG1B*; *REG3A* and *REG3G* were also expressed by small intestinal stem cells, and *REG4* was enriched in goblet, Paneth and enteroendocrine cells. For cytokine receptors (Fig. 4.9J), *IL22RA1* was again enriched in small intestinal enterocytes, with noteworthy expression in small intestinal transit amplifying, stem and goblet cells, and large intestinal enterocytes. Other receptors displayed broader distribution among the 17 cell types, though enterocytes were the most frequent cell type.

Taken together, these data identify small intestinal enterocytes and pancreatic acinar cells as the major cell types expressing most *REG/Reg* isoforms under non-disease conditions.

4.3.3 Pancreatic and intestinal Reg gene family transcripts correlate and are regulated by microbial colonization

The strong correlation of *REG/Reg* expression with that of *IL22RA1/Il22ra1*, but not IL-6 receptor subunits, suggested that IL-22 but not IL-6 contributes to baseline *REG/Reg* expression, though it could alternatively merely indicate a unique sensitivity of the pancreas and gut to IL-22. To determine whether the higher baseline expression of *REG/Reg* genes in pancreas and gut is driven by IL-22 as well as the gut microbiota, we first measured *Reg* gene expressions in pancreas, duodenum and colon of wildtype, heterozygous and *Il22* knockout mice (Fig. 4.3A, B, Fig. 4.10A).

The duodenum showed the greatest sensitivity to IL-22 deficiency, with a 5-fold decrease in *Reg3a*, *Reg3b*, *Reg3g* and a downward trend in *Reg2* expression in knockout mice compared to wildtype. Similar but less pronounced trends were observed in pancreas and colon. By contrast, *Reg1*, *Reg3d* and *Reg4* were unaffected. These findings suggest that while IL-22 contributes to baseline *Reg* expression of 4 isoforms in SPF mice, other, IL-22-independent mechanisms, must contribute to baseline *Reg* expression, especially for *Reg1*, *Reg3d* and *Reg4*. To address the involvement of microbiota, we treated adult mice with broad-spectrum antibiotics. This resulted in lower expression of *Reg2, Reg3a and Reg3b* in pancreas, with *Reg1* and *Reg3g* trending down (Fig. 4.3C). Although antibiotics had no impact on duodenal *Reg* levels (Fig. 4.9B), it reduced *Reg3b, Reg3g* and *Reg3d* expression in the ileum (Fig. 4.3D). Conversely, in comparing the pancreata of germ free (GF) mice and ex-GF (F2 generation of GF mice colonized with Jax microbiota) mice, we observed an upregulation of *Reg1* and *Reg3g* in ex-GF mice (Fig. 4.10C-E). To understand how early in life baseline *Reg* expression is established, we measured *Reg* expression in pancreas of one-day-old (P1, pre-microbial colonization) and 28-day-old (P28, post-microbial colonization) GF and ex-GF mice. P1 mice already exhibited robust *Reg1* expression independently of the microbiota (*data not shown*). The other *Reg* genes displayed low expression at P1, but increased by P28 in ex-GF but not GF mice, though *Reg2* also trended upward in GF mice (Fig. 4.10F-I).

The complex Jax microbiota likely increased pancreatic and intestinal *Reg* expression compared to GF mice through multiple IL-22 augmenting pathways, including increased abundance of microbe-dependent metabolites(Schiering et al., 2017; W. Yang et al., 2020) and PAMPs like flagellin(Kinnebrew et al., 2012; Y. Wang et al., 2019) that induce IL-23, IL-6, IL-1b and TGFb(Kinnebrew et al., 2012; X. Liu et al., 2015; Sano et al., 2015; Shaw et al., 2012) or

direct ligation of transcription factors (e.g. AhR, RORgt), which contribute to the differentiation of IL-22 producers (ILC3, Th17, TCRγδ T cells, NK cells and neutrophils)(Sabat et al., 2014; Zenewicz, 2018) or act on pre-existing tissue-resident immune cells. Additional IL-22 independent mechanisms by which microbes increase *REG/Reg* expression also exist(Choi et al., 2013; X. Liu et al., 2015; Parikh et al., 2012), though they often converge on STAT3 activation. Given that microbiota composition impacts how strongly these pathways are activated, we explored whether a microbiota enriched in SFB(Ivanov et al., 2009b), an ileum-resident, epithelium attaching, non-disseminating commensal known to rapidly induce IL-22 secretion by ILC3(Sano et al., 2015) and later by Th17 cells(Ivanov et al., 2009b), leads to a pancreatic *Reg* response in concert with the already reported intestinal upregulation of *Reg3g* and *Reg3b*. We compared the expression of all *Reg* family members in the pancreas, duodenum and ileum of age-matched B6 mice from Jax (SFB-free) versus mice from Taconic (SFB-bearing)(Ivanov et al., 2009b) and Jax mice co-housed Taconic mice for 4 weeks to account for the slight genetic difference between the B6 strains. All *Reg* genes were more expressed in the pancreas of Taconic than Jax mice (Fig. 4.3E), typically by over 10-fold, except for *Reg1* and *Reg3d*, which were about 3-fold higher. Jax mice co-housed with Taconic mice elevated their pancreatic *Reg* levels to resemble those of Taconic mice (Fig. 4.3E). Exposure to the Taconic microbiota in the gut led to a more select upregulation of *Reg* isoforms (Fig. 4.3F, Fig. 4.10J). *Reg2*, *Reg3b*, *Reg3g* increased in both duodenum and ileum while *Reg3d* increased only in ileum. Next, we asked to what extent these microbial effects depended on IL-22, using IL-22 deficient mice (*Il22*$^{-/-}$). Broad-spectrum antibiotics treatment of *Il22*$^{-/-}$ mice could not further reduce *Reg* expression in the pancreas or duodenum (Fig. 4.3G, Fig. 4.10K) and only had marginal effects on the ileum (Fig. 4.3H). Similarly, *Il22*$^{-/-}$ mice did not upregulate the *Reg* genes in pancreas, duodenum and ileum after co-housing with SFB positive Taconic mice

(Fig. 4.3I, J, Fig. 4.10L). These data strongly suggest IL-22 is a key mediator of the gut microbiota-induced *Reg* expression in pancreas and intestine. Finally, we asked which immune cell types were responsible for presumably differential IL-22 protein levels in pancreas and gut under vehicle versus antibiotics treatment conditions and after SFB colonization. Assessing the frequencies of the three main IL-22 producers, ILC3, Th17, TCRγδ T cells (Fig. 4.11A) revealed that after broad-spectrum antibiotics treatments all of them were lower in the pancreas, while in the gut the effect this was not the case (Fig. 4.3A-F), although the IL-22+ cells within the ILC3, Th17 populations trended down in the gut (Fig. 4.3B, D). In SFB+ Taconic mice (Fig. 4.3G-L) the main population increased compared to Jax mice in the pancreas were IL-22$^+$ Th17 cells (Fig. 4.3H), and co-housing of Jax with Taconic mice led to a trend to this effect; in the gut co-housing of Jax with Taconic mice also mainly led to an increase in IL-22$^+$ Th17 cells (Fig. 4.3G,H), while ILC3 and TCRγδ T cells were largely unaffected in frequency or IL-22 positivity (Fig. 4.3I-L).

When looking for the common denominator of all these experiments (Fig. 4.3-4.4, Fig. 4.10), it became evident that *Reg2, Reg3a, Reg3b* and *Reg3g* expression was more influenced by the microbiota and dependent on IL-22 in both gut and pancreas than *Reg1, Reg3d* and *Reg4*. This was in line with transcript factor binding site analysis showing that the more affected *Reg* genes have more STAT3 binding sites near the transcription start sites (Fig. 4.11A). Therefore, we categorized these highly regulated *Reg* genes as "inducible" and the others as "constitutive". Notably, in humans, REG1A, which is highly expressed at baseline, has 3 STAT3-binding sites. We thus predict it to be more regulated by environmental factors than its mouse counterpart (Fig. 4.11B).

All in all, these data strongly support that intestinal microbial colonization can selectively co-regulate inducible *Reg* gene expression in the pancreas and gut, with IL-22 as a crucial mediator of this effect.

4.3.4 Murine PDAC triggers Reg upregulation in pancreas but not gut

Poor prognosis in PDAC has been linked to increased *REG*3A and IL-22 levels(Perusina Lanfranca et al., 2020; Xie et al., 2003), though it is not clear whether this reflects the presence of a disease aggravating microbiota or is an independent feature of aggressive disease. To determine whether "primary pancreatic" diseases regulate *Reg* genes in pancreas and gut, we first utilized an inducible murine PDAC model with $Ptf1a^{CreERT2}$ mice on a $p53^{fl/fl}$ and $Kras^{G12D}$ background ("KPC" mice). In the pancreas, all *Reg* isoforms were upregulated in both the tumor and non-tumor tissues compared to controls as early as 4 weeks post-induction (Fig. 4.5A, B; Fig. 4.12A-E), when lesions start to appear (Fig. 4.12A). Notably, inducible *Reg* forms were the most drastically affected, increasing by almost 100-fold, while constitutive *Reg* forms, *Reg1* and *Reg3d*, were less impacted. Since *Reg3b* and *Reg3g* were strongly upregulated in the pancreas, we measured these genes in the gut as proxies for querying pancreas-to-gut regulation. However, even at 12 weeks, when the impact on these genes was the strongest in the pancreas (Fig. 4.5A, B, "non-tumor"), they were unchanged in the gut (Fig. 4.5C, D). This suggested that the mechanism upregulating *Reg* in primary PDAC stays local and is not transferred to the gut.

Additionally, we noticed that from week 8 onward all isoforms exhibited lower *Reg* levels in the "tumor" tissue than "non-tumor" tissue. Likely, as acinar cells increasingly lose their identity, they also lose *Reg* expression. These trends correlated with the loss of acinar markers *Cpa1* and *Ptf1a* and the gain of ductal markers *Krt19*, *Sox9* and *Car2* (Fig. 4.12F-J). Similarly, while most IL-6 or IL-22 receptor subunits remained unchanged in the pancreas of KPC mice (Fig.

4.12K-M), *Il22ra1* decreased in the tumor samples from week 8 (Fig. 4.12M), potentially reflecting the loss of acinar identity. To reconcile the finding that *Reg* in whole tissue extracts went up with a potential loss in their expression in advanced tumors, we took several approaches. First, we co-stained pancreatic sections of KPC mice and their littermate controls with antibodies against mouse REG3β, acinar marker CPA1 and ductal marker CK19 (Fig. 4.5E). The staining revealed both a much stronger staining intensity of REG3β on KPC pancreas and an exclusion of REG3β in the transformed, CK19-positive areas. We then queried a publicly available RNAseq dataset comparing acinar versus metaplastic cells from KPC mice(Backx et al., 2021) (Fig. 4.5F). All *Reg* genes were downregulated in metaplastic cells within the range of *Cpa1* and *Amy2a5* de-enrichment. To explore if this finding may be true in human PDAC as well, we compared the expression of *REG* genes and *IL22R1* in two human PDAC cell lines to that of healthy human primary acinar cells or pancreas (Fig. 4.5G, Fig. 4.12N), and found those genes downregulated while *KRT19* was upregulated. Additionally, we analyzed a publicly available scRNAseq dataset composed of PDAC tissue from 17 patients and 3 adjacent control tissues (ADJ)(Steele et al., 2020) (Fig. 4.13A, B). When focusing on ductal and acinar cells from PDAC and ADJ (Fig. 4.5H), *REG1A*, *REG1B* and *REG3A* were more highly expressed in acinar cells from PDAC tissue. Though acinar cell remained the major source of *REG* transcripts, the genes were also more highly expressed in the ductal cells of PDAC tissue, possibly due to a fraction of ductal cells being of acinar origin. To pursue this possibility, we generated a non-integrated UMAP of only the ductal and acinar cells in the dataset (Fig. 4.13C). Ductal cells were predominantly contributed by PDAC samples (Fig. 4.13D, E). When mapping *REG* genes along with *AMY2B* and *KRT19* onto this UMAP (Fig. 4.13F), it became clear that there was a zone of intermediate *REG* expression coinciding with a decrease in *AMYB2B* and gain of *KRT19*. Pseudotime analysis (Fig. 4.13G)

confirmed a trajectory from acinar clusters 1,4 and 10 (Fig. 4.13H, I) to ductal clusters 0, 2,3, 5, 7-12, 14, 15 and 17 passing through acinar-ductal hybrid clusters 6, 13, 19 and 20, matching decreasing *REG1A* expression (Fig. 4.13F). *IL22RA1* was lost in acinar and gained relatively in ductal cells in PDAC tissue, and IL-6 receptor subunit *IL6ST* were also upregulated in PDAC ducts (Fig. 4.5H), phenomena again pointing to an acinar origin of some "ductal" cells. This dataset also included some immune cell populations. Analysis of IL-6 and IL-22 producers (Fig. 4.5I) revealed an enrichment of antigen presenting cells (APCs), fibroblasts, B cells and granulocytes expressing *Il6*, as well as IL-22-producing CD4 T cells in PDAC tissues. This suggests that both IL-6 and IL-22 contribute to *REG* upregulation in human PDAC. Overall, the mouse and human data support a model in which *REG/Reg* genes are initially upregulated in acinar cells of PDAC, but they gradually lose the expression during acinar-to-ductal transformation (Fig. 4.12O).

Finally, we asked whether changes in pancreatic *Reg* expression in KPC mice affected the gut microbiome. We hypothesized that duodenal microbiome, either mucosa-associated or luminal, might be the most sensitive. However, 16S rRNA gene sequencing showed no difference between the duodenal microbiota of cancerous mice and their littermates at week 12 according to principal component analysis (PCA, Fig. 4.13J, K). Total bacterial load was also unchanged in duodenal mucosa or lumen. Fecal microbiome composition was also unaltered, as was the pancreatic microbiome, where both bacterial and fungal loads were very low (*data not shown*). Some variation was due to cage effects(Hildebrand et al., 2013; Russell et al., 2022) (Fig. 4.13J, K, bottom) but even within cages mice did not differ, though we could not exclude potential coprophagy(Bogatyrev et al., 2020a) counteracting any impact of PDAC on the gut microbiome.

In sum, primary pancreatic acinar-to-ductal transformation is sufficient to significantly upregulates inducible *Reg* genes, with a smaller effect on constitutive *Reg* genes, in PDAC without

affecting intestinal *Reg* expression. In human, PDAC acinar cells also upregulate *REG* genes. While PDAC progression in mice heavily depends on the presence of a microbiota(Kartal et al., 2022; Thomas et al., 2018) and IL-22(Perusina Lanfranca et al., 2020), our data show that an intestinal dysbiosis is not required as a triggering event for *Reg* upregulation in PDAC, nor does PDAC lead to a drastic gut microbial shift.

4.3.5 Cerulein-induced pancreatitis triggers upregulation of Reg genes in pancreas and modifies the duodenal microbiome

Pancreatitis, another major exocrine pancreatic disease, is a known context in which REG3A is upregulated(Iovanna et al., 1991). Chronic pancreatitis also poses a risk factor for PDAC development(Guerra et al., 2007; Yin et al., 2015). We therefore interrogated the *Reg* regulation pattern in the context of cerulein-induced pancreatitis. The pancreas displays enlarged acinar cells and signs of fibrosis as early as one week after cerulein treatment commencement (Fig. 4.14A). After 1 week of treatment, inducible *Reg* genes, *Reg2*, *Reg3a*, *Reg3b* and *Reg3g,* were 25- to 100-fold upregulated (Fig. 4.6A, B, 4.14B), while *Reg3d* was only doubled after 4 weeks and *Reg1* remained unchanged until downregulated at 8 weeks. IL-6 receptor subunits were upregulated from 4 weeks of treatment (Fig. 4.14C), suggesting that like in human PDAC, IL-6 contributes to *Reg* upregulation in pancreatitis. By contrast, *Il22ra1* was downregulated after 8 weeks (Fig. 4.14C). REG3b protein staining confirmed its restriction to acinar cells (Fig. 4.14E). Analysis of a publicly available scRNAseq dataset(Chondronasiou et al., 2022) (Fig. 4.14F, G) confirmed the upregulation of *Reg3g* and *Reg2* in acinar cells following acute cerulein treatment (Fig. 4.6C), though *Reg3d* was downregulated in this dataset. To test if the downregulation of *Reg1* and *Reg3d* (the two highest expressor at baseline) and *Il22ra1* after 8 weeks could be due to de-differentiation, similar to PDAC (Fig. 4.12O), we examined *Amy2b* and *Krt19* regulation in the

scRNAseq dataset and by Q-PCR along acinar and ductal markers (Fig. 4.14D). Acinar cells showed decreased *Amy2b* and increased *Krt19* expression (Fig. 4.5C), and in total pancreatic extracts, acinar marker *Cpa1* was downregulated while ductal markers *Sox9* and *Car2* were upregulated (Fig. 4.14D). Globally, the pancreas underwent substantial cellular redistribution following cerulein treatment (Fig. 4.14F, G). Despite the lack of access to human pancreatitis samples, we re-examined our pancreatic donor cohort (Table 1) and noticed potential splits by smoking status, cardiovascular disease (CVD), age over 50 and alcohol use, all of which have been proposed as risk factors for pancreatitis(Bexelius et al., 2013; Möller et al., 2023). *REG1A* and *REG4* levels were elevated in the CVD, smoking and age over 50 donors (Fig. 4.8S, T). Alcohol consumption had minimal impact (*data not shown*), possibly due to moderate use. However, increased expression of other acinar markers, like *CPA1*, *MIST1* (Fig. 4.8U, V) and *PTF1A* (*data not shown*), also co-segregated with these factors, indicating a more generic acinar renewal program may be at play.

Despite these dramatic pancreatic changes, the intestinal expression of the two proxy *Reg* isoforms, *Reg3b* and *Reg3g*, remained largely unaltered along the gut (Fig. 4.6D, E), with only ileal expression increasing 2-fold after 8 weeks. Thus, even in pancreatitis, the signal responsible for increased pancreatic *Reg* expression was not transmitted to the gut. Given the almost immediate effect of the cerulein treatment on *Reg* expression, we wondered if the duodenal microbiome might be affected in this setting. Notably, the fecal microbiome has been described to be altered by cerulein treatment(Wu et al., 2021), a finding we confirmed at all time points (Fig. 4.15A, B, Table 2, 3). When analyzing the microbiota of duodenal luminal contents and mucosal scrapes by 16S rRNA gene sequencing, we also found microbial differences between mock- and cerulein-treated animals by PCA as early as 1 week of cerulein treatment (Fig. 4.6F, G; Fig. 4.15C, D, Table 2,

Table 3). Beta diversity started to segregate by treatment after 4 and 8 weeks, despite cage effect (Fig. 4.6H, I; Fig. 4.15E, F). Total bacterial loads were unchanged (Fig. 4.15G, H), but the absolute abundance of distinct phyla was altered: After one week of treatment, several gram-positive phyla were enriched in the duodenal mucosa and lumen, including *Turicibacter*, *Lachnospiracea* and *Clostridia* (Fig. 4.15I, J). This enrichment persisted for *Turicibacter* and *Lachnospiracea* at later time points in the luminal contents, but from 4 weeks onwards, more phyla were depleted than enriched, representing a mix of gram positive and gram-negative bacteria (Fig. 4.6J-M). While most of these bacteria likely originated from coprophagia when recovered in the duodenum(Bogatyrev et al., 2020b), the results show that in the case of cerulein-induced pancreatitis, the upregulation of *Reg* genes in the pancreas correlates with a change in duodenal microbiome composition.

Thus, cerulein-induced pancreatitis, like PDAC, does not induce *Reg* expression in the gut despite strong induction of *Reg* in the pancreas. Though not necessarily mediated by pancreatic REG proteins, the abundance of select bacterial phyla in the duodenum changes in this setting.

4.4 Disccusion

In this study, we interrogated the baseline expression profile of all *REG/Reg* isoforms in the pancreas and gut, as well as their regulation upon intestinal and pancreatic perturbations. By analyzing the isoform usage and components of upstream signaling machineries, we uncovered the differential *REG/Reg* isoform usage between pancreas and gut, the similarity between pancreas and duodenum as well as between mice and humans, a common, unique sensitivity to IL-22 in these two organs, and the ability of the gut microbiome and its composition to match intestinal and pancreatic expression of select *Reg* genes. The findings thus suggest a deliberate and coordinated recruitment of pancreatic antimicrobial support by the gut and represent a hitherto

underappreciated gut-to-pancreas axis, by which intestinal microbiota regulates pancreatic innate immunity. Furthermore, we classified *Reg* genes into "inducible" and "constitutive" based on their overall regulation by the microbiota and enrichment for STAT3 binding sites. We encountered this classification also in two primary pancreatic diseases. In these settings, we found that *Reg* regulation remained local, possibly because they depended more on IL-6, which is primarily produced by tissue resident immune cells.

4.4.1 *Evolution of divergent REG isoforms and inter-species differences in pancreatic and intestinal usage*

In both species investigated here the *REG/Reg* family consists of three subfamilies. The similarity hierarchy aligns with *REG4/Reg4* being the evolutionarily most ancient isoform(Zelensky & Gready, 2005) that, via gene duplication onto another chromosome, gave rise to the *Reg1* and *Reg3* subfamilies. In both mice and humans, *REG1A/Reg1* dominated the pancreas and duodenum. In mice, the duodenum was also consistently the gut segment most similar to pancreas regarding all other *Reg* isoforms, while *Reg4* and the *Reg3* family, with exception of *Reg3d*, dominated the ileum. This suggest that, if all *Reg* isoforms bind microbial sugars, they are poised to respond to different microbes expected to be encountered in the different gut segments. The pancreas's similarity to duodenum could serve two purposes: keeping itself sterile from refluxing microbes via the pancreatic duct and supporting duodenal antimicrobial activity through REG1 secretion into the pancreatic juice. The stark difference between baseline *REG1A/Reg1* expression and other isoforms, even in GF mice, raises intriguing questions about what evolutionarily drove this difference. Assuming REG1 indeed has antimicrobial activity, it is possible that a high baseline in the upper intestinal tract guarantees the elimination of microbes at the site where they are least wanted, the gut segment with the highest nutrient levels and

absorption. REG1 may be targeting bacteria and fungi that would otherwise outgrow in the comparatively oxygen-rich, low pH environment of the duodenum. The relatively few symbiotic strains inhabiting the duodenum may have evolved resistance to this isoform. By contrast, the isoforms more enriched in the distal intestine would have to be more tightly controlled, as an abundant microbiome is desired in the ileum and colon, yet REG3 isoforms have been shown to target symbiotic bacteria when upregulated (Shin et al., 2022; Vaishnava et al., 2011b). Thus, REG3 may only be upregulated when the benefit of killing microbes prevails, though REG3-insensitive organisms like Salmonella appear to hijack the system and trigger *Reg3* upregulation to clear a niche for themselves(Behnsen et al., 2014; Stelter et al., 2011). Determining the ligand preferences of each isoform, as well as their oligomerization properties, will be crucial to fully appreciate the benefits of differential isoform usage along the gastrointestinal tract, but also how select isoforms could be blocked for therapeutic purposes. Similarly, promoter analysis of the different isoforms and cognate transcription factor levels in pancreas and along the gut warrant further investigation to understand the differences in baseline expression and sensitivity to IL-22.

Given the mouse is the most common model organism for human disease, it is reassuring that in both species *REG1A/Reg1* is the main isoform in the pancreas, total *REG* expression is higher in pancreas than gut with the colon as the lowest site. However, humans differ from mice in their low intestinal baseline expression of *REG3* isoforms, which is reported by others as well. Since newborn and GF mice display similar *REG3* expression patterns, it likely reflects an evolutionary adaptation of the murine gut, possibly driven by their natural coprophagic behavior.

4.4.2 *Conservation of REG/Reg prosegment and its relation to trypsin*

Trypsin is a critical activator of REG3A(Mukherjee et al., 2009) and likely other REG proteins, as the inhibitory pro-segment and trypsin cleavage site are conserved among all REG

proteins. Trypsin, produced as a zymogen with low autocatalytic capacity, requires activation by enterokinase(Kitamoto et al., 1994) and is inhibited by trypsin inhibitor proteins(Bohe et al., 1997; G.-P. Wang, 2010). This tightly regulated mechanism ensures controlled activation of REG proteins, potentially preventing self-damage that could occur if REG proteins interacted with the mammalian cell surface proteome, which is heavily glycosylated(Mukherjee et al., 2009). Of note, viral and bacterial pathogens use lectins to attach to or kill eukaryotic cells(Weis & Drickamer, 1996; Zelensky & Gready, 2005), and some eukaryotic DAMP receptors(Chiffoleau, 2018) and snake venoms(Eble, 2019), which bind to eukaryotic surface glycoproteins, are also C-type lectins. Therefore, at high concentrations, REG proteins could damage self-tissues through low-affinity but high-avidity binding to eukaryotic carbohydrates, tethering REG complexes to cell membrane. Trypsin, primarily generated in the pancreas, is expressed at lower levels in the gut epithelium(Bohe et al., 1997) and could activate REG proteins in gut segments beyond the reach of pancreatic juice. The unequal distribution of trypsin has two significant implications. One, that the difference in REG activity between duodenum versus distal intestine will be even bigger than the transcriptional analysis already predicted (Fig. 4.1I, J). Trypsin-digesting symbionts in the distal intestine(Y. Li et al., 2022) could further accentuate this difference. The other is that inappropriate activation of trypsin poses a higher risk of REG-mediated self-damage in the pancreas than gut. Indeed, pancreatitis, characterized by tissue trypsin activity and acinar self-damage(Hirota et al., 2006; Sendler & Lerch, 2020), is a predisposing risk factor for PDAC(Guerra et al., 2007; Yin et al., 2015). Increased trypsin activity has also been observed in inflammatory bowel diseases(Solà Tapias et al., 2021). Both are contexts in which *REG* are upregulated also. Attesting to the fatality of this combination, mice lacking all pancreatic *Reg* isoforms are protected from cerulein-induced pancreatitis(W. Chen et al., 2023b). The self-damaging potential of REG

proteins could unify the seemingly disparate roles of REG: mitogenic in the pancreas versus antimicrobial in the gut. Plasma membrane disruption elicits a cellular repair response and proliferation(Dias & Nylandsted, 2021), a phenotype that will be more apparent in the pancreas than the highly regenerative gut epithelium, though the mechanism could also contribute to gastrointestinal cancers. Additionally, since membrane disruption goes in hand with Ca^{2+} influx(Z. W. Li & Shaw, 2023), highly secretory and excitatory cells like pancreatic cells may be affected differently by REG proteins than others. The high trypsin activity associated with pancreatitis could also explain why cerulein-induced pancreatitis impacted the duodenal microbiome more than PDAC, possibly through more active REG proteins.

4.4.3 *Microbe-induced IL-22, REG/Reg, and pancreatic disease*

Baseline expression of *Reg* in pancreas and gut is partially independent of IL-22, as observed in GF mice with low IL-22 levels(Shaw et al., 2012; Stefka et al., 2014). However, microbial induction of REG proteins is largely IL-22 dependent: Many symbionts and pathogens(Sabihi et al., 2020; Y. Zheng et al., 2008c) or PAMPs(Kinnebrew et al., 2012) require IL-22 for their *Reg*-inducing effect in the gut. Our study focused on the role of the symbiotic gut microbiota in regulating pancreatic *Reg* expression. The extrapolation of our findings is that situations that drastically increase intestinal IL-22 production and *Reg* levels, such as certain pathogens, tissue damage or barrier breach, could similarly affect the pancreas, an inference that will be important to address experimentally in the future. Given the link between IL-22 and pancreatic diseases, whether pathobionts or gastrointestinal infections that trigger IL-22 are involved in the initiation or progression of chronic pancreatitis and PDAC in humans is of direct clinical relevance. Primary pancreatic disease was sufficient to increase *REG/Reg*; but the microbiota may set a “permissive tone”. GF and *Il22* knockout mice exhibit drastically slowed

PDAC progression(Perusina Lanfranca et al., 2020; Pushalkar et al., 2018) while *Reg3g* overexpression is sufficient to accelerate it(X. Liu et al., 2017). Mice lacking gut bacteria are also protected from developing pancreatitis(Zhu et al., 2019). However, primary dysbiosis, with an overrepresentation of strains efficient at triggering REG upregulation, could conceivably aggravate pancreatic disease progression. In our study, the pancreatic microbiome, which is low in abundance, remained unchanged upon PDAC, as did the duodenal and fecal microbiomes. However, dysbiosis was reported in a stochastic and slower KPC model(Kartal et al., 2022; Pushalkar et al., 2018), and fungi or bacteria enriched in the pancreas or feces of PDAC patients can accelerate the disease in the murine model(Aykut et al., 2019; Pushalkar et al., 2018; Riquelme et al., 2019), suggesting that in a "dysbiosis first" scenario, the microbiome composition can influence pancreatic disease outcome. Correlative studies with the microbiome in human pancreatitis further support this notion.(dos Santos et al., 2017; Tan et al., 2015) Notably, PDAC-aggravating bacteria can elicit IL-17(McAllister et al., 2014), and many IL-17 secreting cells co-produce IL-22(De Luca et al., 2010; Ivanov et al., 2009b), raising the possibility that the same gut bacteria could impact the pancreas via synergistic mechanisms, with IL-17 primarily targeting ductal cells and IL-22 targeting acinar cells, based on our *scRNAseq* analysis, to aggravate PDAC. Regardless of whether live duodenal microbes invade the pancreas, our data based on SFB with strict ileal tropism, suggest that direct invasion is not necessary for the gut microbiota to influence pancreatic innate immunity.

4.4.4 *Lack of reciprocity between pancreas versus gut initiated Reg upregulation*

While direct gut-pancreas cooperation is well known in the context of postprandial metabolism, our findings underscore that these organs also coordinate their immune responses(H. Brown et al., 2023c; Chandra et al., 2024; Kurashima et al., 2021; Thomas & Jobin, 2020). In our

study, the gut exerted a stronger impact on innate immunity of the pancreas than vice versa. This conceptually aligns with the need for antimicrobials and enzymes in pancreatic juice to support gut defenses. In addition, there is a real threat of ductal microbial reflux from gut to the pancreas. Anatomically and mechanistically, the stronger intestinal influence on the pancreas is logical. In the primary pancreatic diseases and models investigated here, the sources of IL-22 (or IL-6) that would induces *Reg/REG* upregulation are likely local, sparse tissue-resident cells that are unlikely to travel. The intestine, being a much larger organ, harbors the biggest and densest population of immune cells outside of lymphoid organs, contributes more lymph to shared LNs due to larger lymphatic output, and its venous drainage passes in part through the pancreas. Therefore, whether the coordinated *Reg* transcription is mediated via PAMPs, metabolites, blood-borne cytokines or gut-primed circulating immune cells traveling between organs, the potential influence is stronger if the gut is the source. Understanding the relative importance of each mentioned pathway in specific situations will be imperative for intercepting pathological gut-to-pancreas signals.

4.5 Limitations of the study

Our conclusions are largely based on transcriptional data rather than protein levels. The inferred relative abundances of *REG/Reg* transcripts within organs assume similar efficiency across all Q-PCR primers used. Although all primers were verified and *scRNAseq* data supported our conclusions, there may be slight variations in actual ratios due to subtle differences in primer performance. Our tissue panel reflects *Reg* family and cytokine receptor expression at homeostasis, however, others have reported increased IL-22 signaling upon injury/tissue damage in organs, like liver, skin and lung(Sabihi et al., 2020). Rare cell types within organs that express IL-22 receptors may be below the detection limit in whole tissue extracts, and low expression levels may even escape detection by *scRNAseq*. Finally, our study establishes the relationship between the gut

microbiota, inducible *Reg* isoforms in the pancreas and IL-22, but does not experimentally address the consequence of this relationship, detrimental or beneficial and whether different for the various isoforms.

4.6 Figures and figure legends

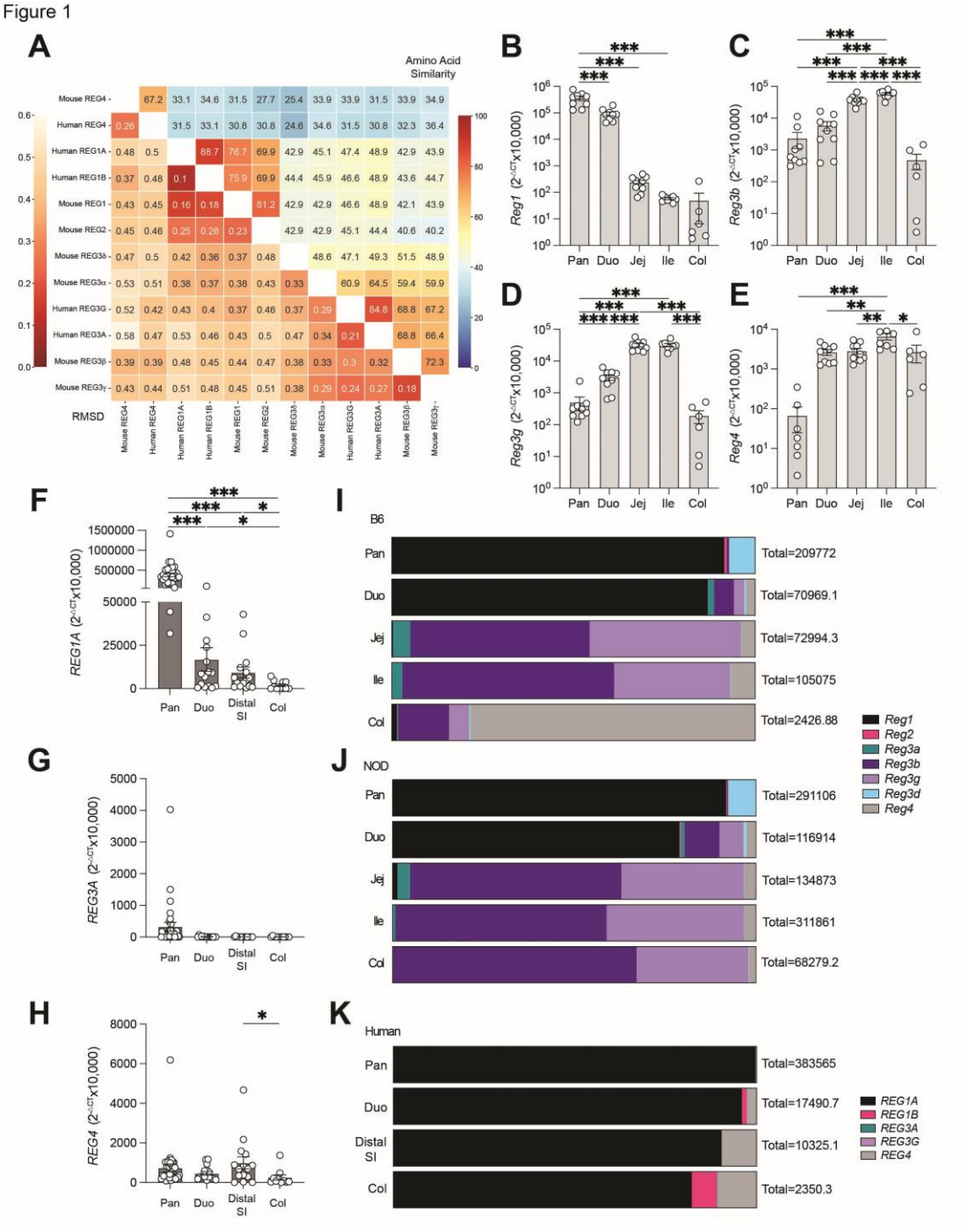


Figure 4.1 Mouse and human *Reg/REG* gene family members are structurally highly conserved but differ in their expression patterns between pancreas and gut.

A. Sequence similarity (upper right corner) and structural similarity (lower left corner) of all mouse and human REG proteins excluding pro-segment regions. **B-E**. Expression levels of indicated *Reg* genes in the pancreas (pan), duodenum (duo), jejunum (jej), ileum (ile) and colon (col) of C57Bl6 mice by Q-PCR (n=9 except colon, n=6). **F-H**. Expression levels of indicated *REG* genes in human pancreas (pan, n=31), duodenum (duo, n=15), distal small intestine (distal SI, n=14), and colon (col, n=11) by Q-PCR. **I-K**. Relative contribution of *Reg/REG* isoforms to total *Reg/REG* pool in C57Bl6 mice (**I**), NOD mice (**J**) and humans (**K**) based on data in Fig1B-H and S2A-J, M and N. The numbers on right indicate total expression of *Reg/REG* genes. * p<0.05, ** p<0.01, *** p<0.001 by ANOVA.

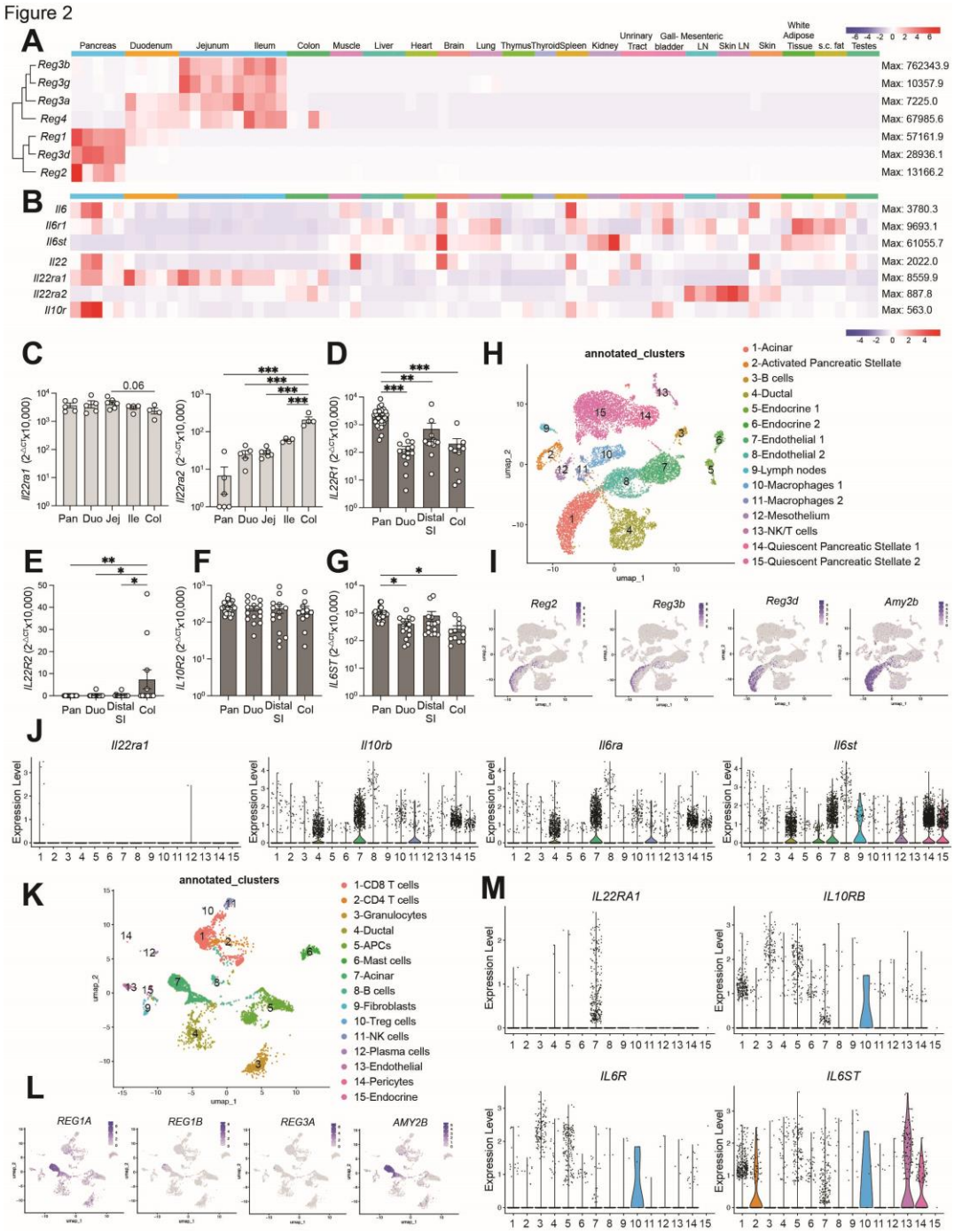


Figure 4.2 Gut and pancreas are enriched for *Reg* transcripts and the upstream signaling receptors.
A, B. Heatmap of *Reg* gene (**A**) and IL-6 or IL-22 receptor signaling gene (**B**) expression in indicated tissues from 8-week-old C57Bl6 mice measured by Q-PCR (*n*=2-5, see as indicated by box graph). Maximal expression level per row is indicated at the right of each row. **C.** Expression of *Il22ra1* and *Il22ra2* in pancreas (pan), duodenum (duo), jejunum (jej), ileum (ile) and colon (col) of C57Bl6 mice by Q-PCR (*n*=4). **D-G**. Expression levels of indicated IL6 or IL22 receptor signaling genes in human pancreas (pan, *n*=31), duodenum (duo, *n*=15), distal small intestine (distal SI, n=14), and colon (col, *n*=11) by Q-PCR. **H**. Annotated *scRNAseq* feature plot of mouse pancreas. **I**. Feature plots of mouse *Reg2, Reg3b, Reg3d* and *Amy2b*. **J**. Violin plots of IL-6 or IL-22 receptor subunit genes across mouse pancreatic cell types. **K**. Annotated *scRNAseq* feature plot of human pancreas. **L**. Feature plots of human *REG1A*, *REG1B*, *REG3A* and *AMY2B*. **M**. Violin plot of IL-6 or IL-22 receptor subunit genes across human pancreatic cell types. * p<0.05, ** p<0.01, *** p<0.001 by ANOVA.

Figure 3

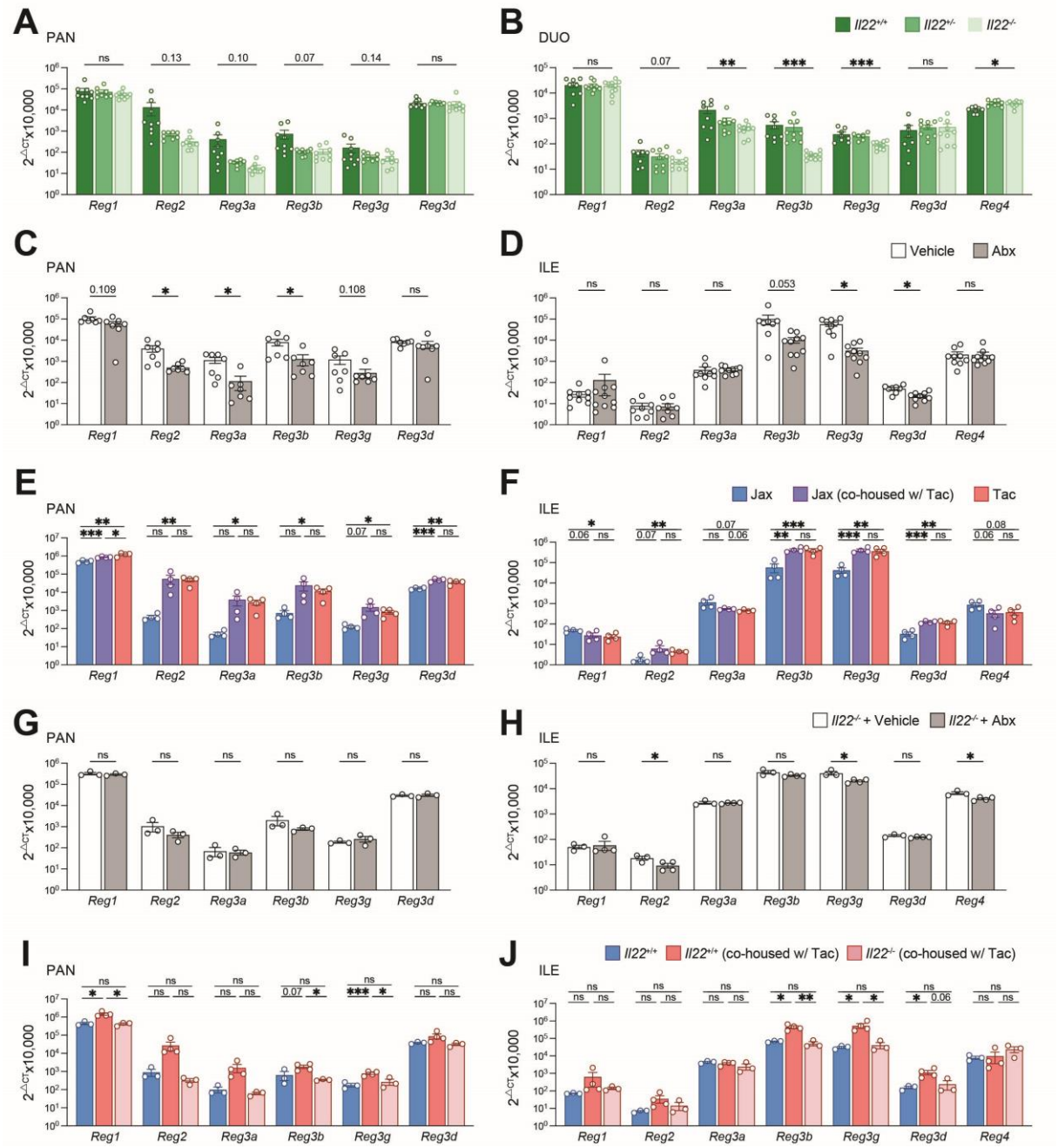


Figure 4.3 Pancreatic and intestinal *Reg* gene family transcripts correlate and are regulated by microbial colonization.
A-B. Expression levels of indicated *Reg* genes in pancreas (**A**) and duodenum (**B**) of *Il22*$^{+/+}$, *Il22*$^{+/-}$ and *Il22*$^{-/-}$ mice (n=9, 9 and 10, respectively) by Q-PCR. Data pooled from two independent experiments. **C-F**. Pancreatic and ileal expressions of indicated *Reg* genes in broad-spectrum antibiotics (Abx)- treated mice or its vehicle control (**C**, **D**)(pancreas *n*=7, vehicle ileum *n*=9, Abx ileum *n*=10), or in B6 mice from JAX, Taconic (Tac), or JAX-mice co-housed with Taconic mice (**E**, **F**) (*n*=4) for 4 weeks. **G-J**. Expression levels of indicated *Reg* genes in pancreas and ileum of *Il22*$^{-/-}$ mice treated with antibiotics or vehicle (**G**, **H**) (*n*=3), or *Il22*$^{+/+}$ (*n*=4) versus *Il22*$^{-/-}$ (*n*=3) littermate mice co-housed with Taconic mice and non-co-housed *Il22*$^{+/+}$ littermate controls (*n*=4) (**I**, **J**). Data on graphs C-J represent samples run on the same Q-PCR plate to permit direct comparison of expression levels between the two experiments. * p<0.05, ** p<0.01, *** p<0.001 by 2-tailed t-test.

Figure 4

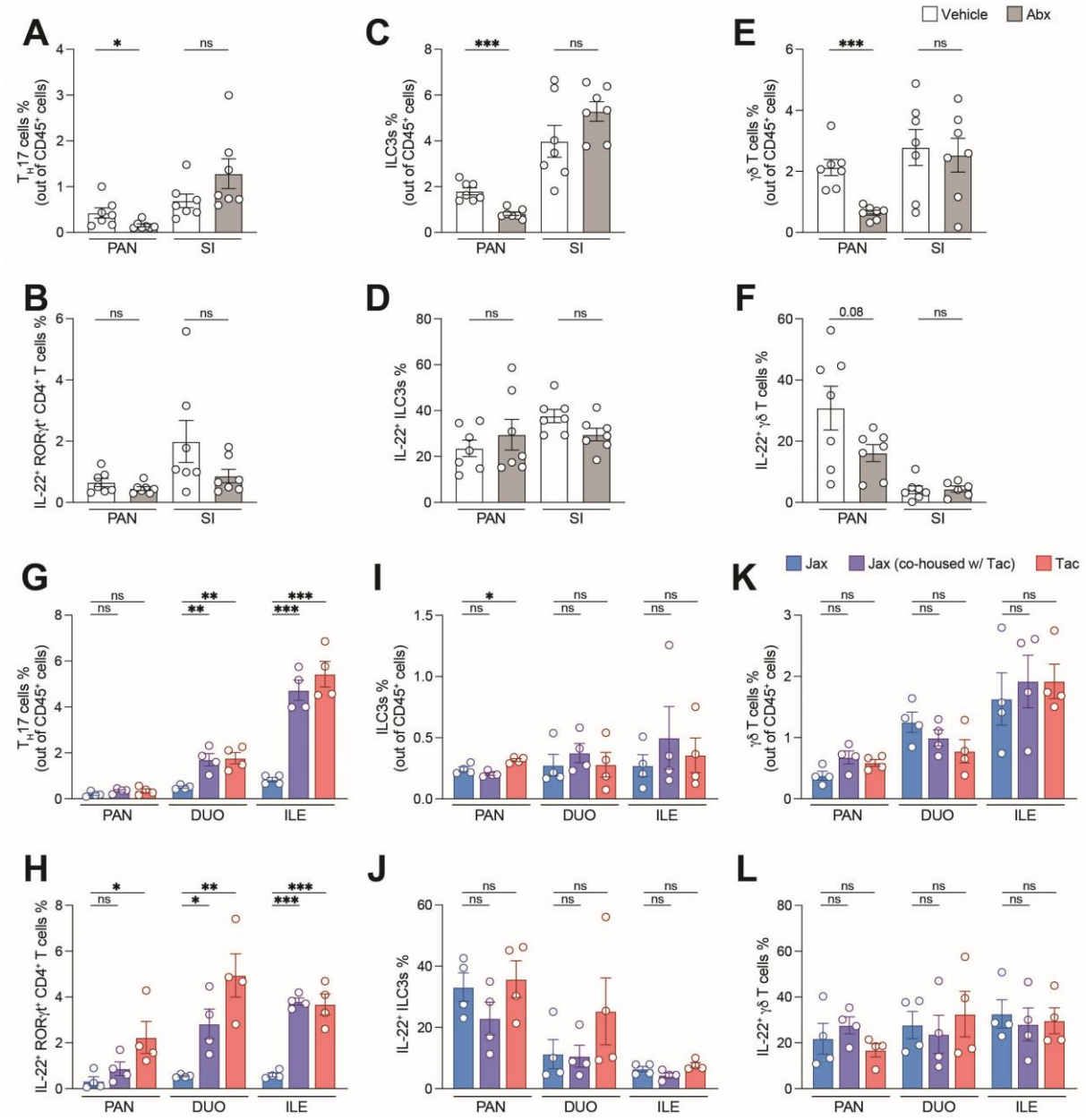


Figure 4.4 Differential IL-22 producers in the pancreas and gut upon antibiotics and SFB-colonization suggests context-dependent production.

A-F. Frequencies of T_H17 cells, IL-22$^+$RORγt$^+$ CD4$^+$ T cells, ILC3s, IL-22$^+$ ILC3s, γδ T cells, IL-22$^+$ γδ T cells in pancreas (PAN) or small intestine lamina propria (SI) of B6 mice after 4 weeks of broad spectrum antibiotics (Abx) or vehicle treatment. (n=7, pooled from two cohorts). **G-L**. Frequencies of T_H17 cells, IL-22$^+$RORγt$^+$ CD4$^+$ T cells, ILC3s, IL-22$^+$ ILC3s, γδ T cells, IL-22$^+$ γδ T cells in pancreas (PAN) or lamina propria of the duodenum (DUO) or ileum (ILE) of B6 mice from Jax, co-housed Jax B6 mice or B6 mice from Taconic (*n*=4). * p<0.05, ** p<0.01, *** p<0.001 by 2-tailed t-test.

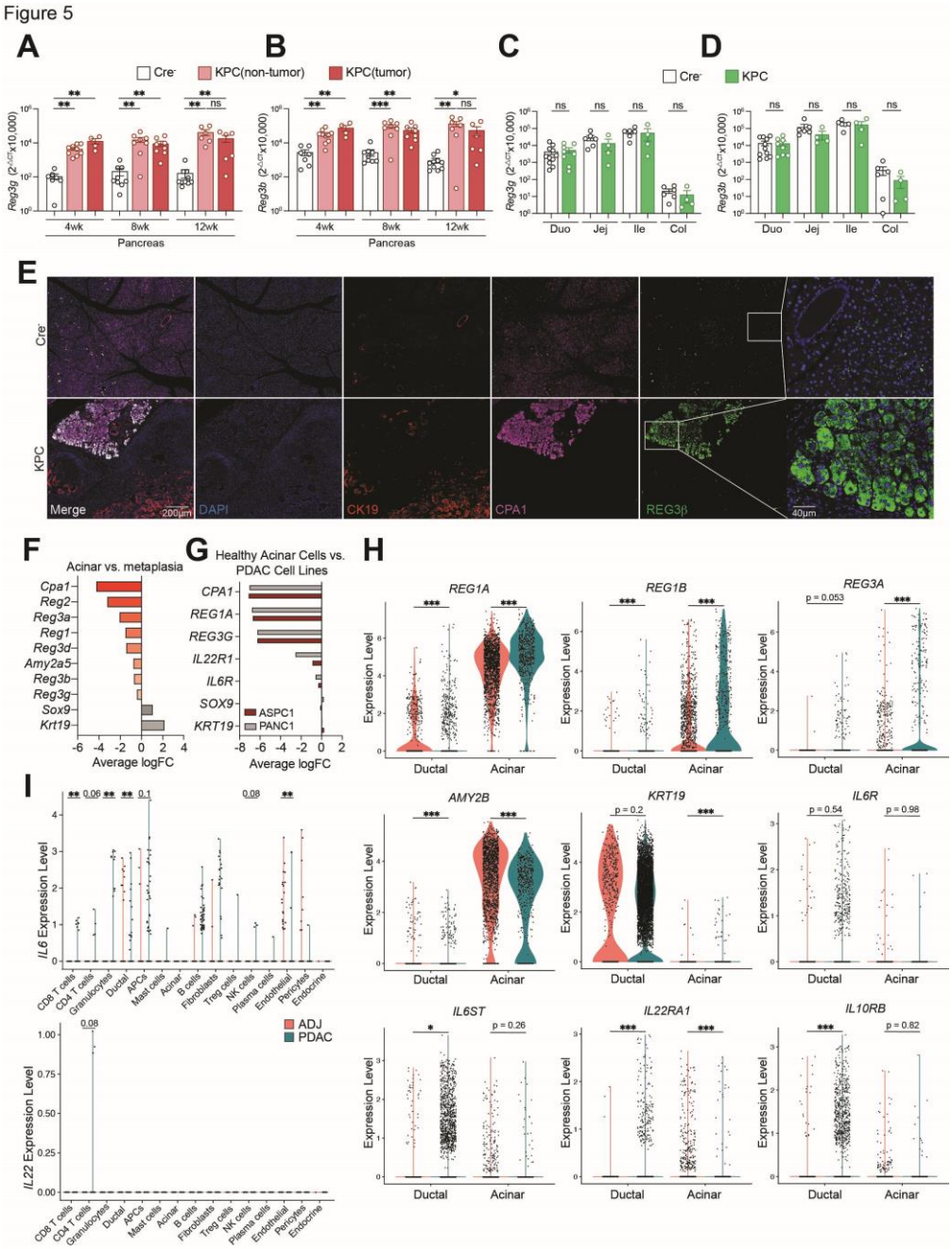


Figure 4.5 A mouse model of primary pancreatic ductal adenocarcinoma triggers *Reg* upregulation in pancreas but not gut.
A, B. Pancreatic expressions of *Reg3g* (**A**) and *Reg3b* (**B**) in KPC mice or their Cre$^-$ littermates at 4, 8 or 12 weeks post tamoxifen-induced PDAC onset measured by Q-PCR (WT n=7, 9,10, PDAC n=9, 8, 6 for 4, 8, 12 weeks, respectively). Data pooled from 3 cohorts per time point. **C, D.** Intestinal expressions of *Reg3g* (**C**) and *Reg3b* (**D**) in different gut segments of KPC mice or their Cre$^-$ littermates at 12 weeks post tamoxifen-induced PDAC onset measured by Q-PCR (WT n=6 (Jej, Ile, Col) or 11 (Duo), PDAC n=4 (Jej, Ile, Col) or 8(Duo)). Data pooled from 2-3 independent cohorts. **E**. Pancreatic sections from KPC mice at 12 weeks post tamoxifen treatment or Cre$^-$ littermates stained for ductal marker CK19, acinar marker CPA1, REG3β and DAPI (nuclei). Bar=200 μm, inset bar=40 μm. **F.** Bar graph of Log2 fold change of indicated genes in acinar versus metaplastic pancreatic cells in mouse *scRNAseq*. **G.** Bar graph of Log2 fold change of indicated genes in PDAC cell lines *versus* isolated healthy human acinar cells analyzed by Q-PCR. **H**. Violin plots of *REG1A, REG1B, REG3A, AMY2B, KRT19, IL6R, IL6ST, IL22RA1* and *IL10RB* expressions in human acinar versus ductal cells in PDAC or adjacent tissues based on *scRNAseq.* **I.** Violin plots of *Il6* and *Il22* in all cell types recovered from human PDAC or healthy adjacent tissues analyzed by *scRNAseq*. * p<0.05, ** p<0.01, *** p<0.001 2-tailed t-test.

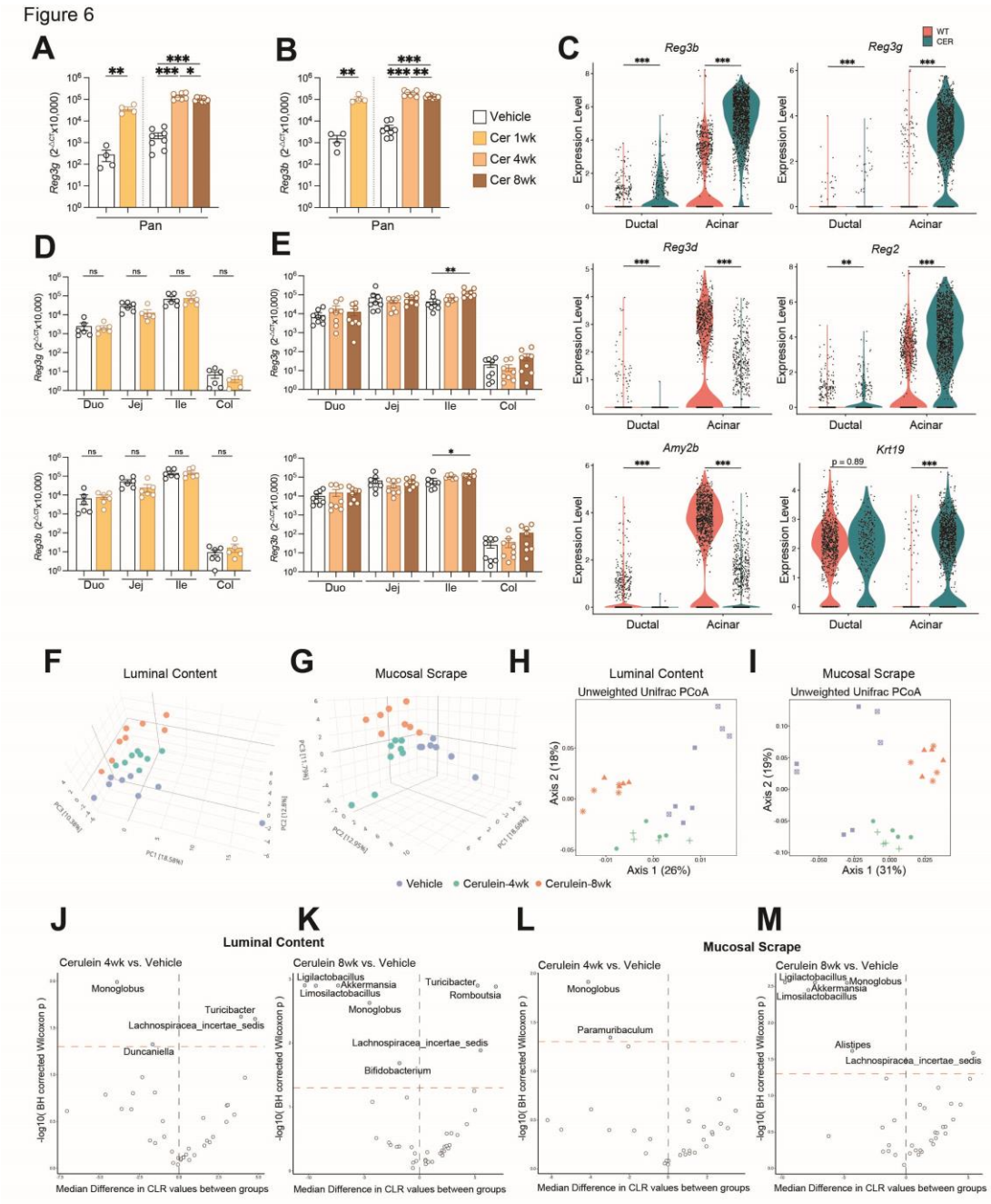


Figure 4.6 Cerulein induced pancreatitis triggers upregulation of *Reg* genes in pancreas and modifies the gut microbiome.
A, B. Pancreatic expression of *Reg3g* (**A**) and *Reg3b* (**B**) in mice treated with Cerulein for 1, 4 or 8 weeks and age-matched vehicle control mice housed in parallel (*n*=4 (1 week) or 8 (4 and 8 week treatment)). Data representative of one experiment per time point. **C**. Violin plots of *Reg3b, Reg3g, Reg3d, Reg2, Amy2b* and *Krt19* expressions in mouse acinar versus ductal cells from vehicle or Cerulein treated mice based on *scRNAseq.* **D, E**. Intestinal expressions of *Reg3g* and *Reg3b* in all gut segments from mice treated with Cerulein or vehicle for one week (**D**) or 4 and 8 weeks (**E**) measured by Q-PCR (*n*=6 (1 week) or 8(4 and 8 weeks)). Data representative of one experiment per time point. **F-I**. PCA of duodenal luminal bacteria (**F**) and mucosa-associated bacteria (**G**) or beta-diversity of duodenal luminal bacteria (**H**) and mucosa-associated bacteria (**I**) of mice with indicated treatments (*n*=7-8). **J-M.** Volcano plots of bacteria enriched or de-enriched in the mucosa of mice treated with Cerulein for 4 (**J**) or 8 (**K**) weeks versus vehicle control mice, or in the lumen of mice treated with Cerulein for 4 (**L**) or 8 (**M**) weeks versus control mice (*n*=8). * p<0.05, ** p<0.01, *** p<0.001 by 2-tailed t-test.

Figure S1

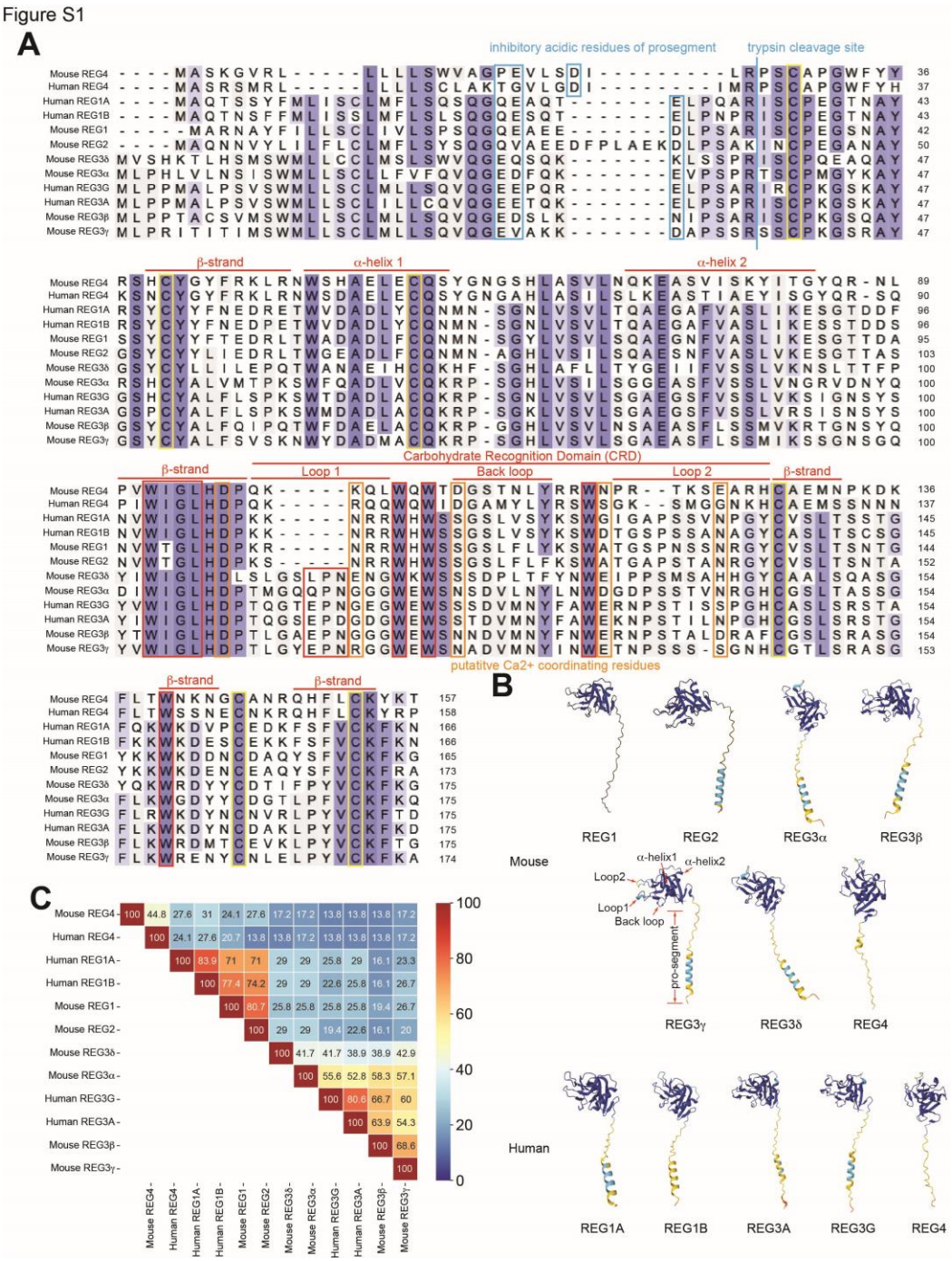


Figure 4.7 Mouse *Reg* and human *REG* gene family members are structurally conserved.
A. Amino acid sequence alignment of all mouse and human *Reg* gene family isoforms with the following characteristics annotated: position of acidic amino acid residues critical for inhibitory action of prosegment (one acidic residue sufficient for this property), and prosegment trypsin cleavage site (blue boxes and line), six cysteine residues for protein stabilization via disulfide bridges (yellow boxes), putative D/N/E residues used for coordinating Ca^{2+} ions for canonical ligand binding (orange boxes), features of the C-type lectin fold, notably two predicted alpha helices, five beta strands, a carbohydrate recognition domain (CRD) enriched in tryptophan (W) residues and forming a two-outward (Loop1 and Loop 2) one back-loop structure preceded by the WIGL motif, and the mannose binding EPN motif (red). **B**. Predicted structures of all mouse and human REG proteins (Alphafold), with key features of all REG proteins pointed out on REG3g. **C**. Sequence similarity between the carbohydrate recognition domains of all mouse and human REG proteins.

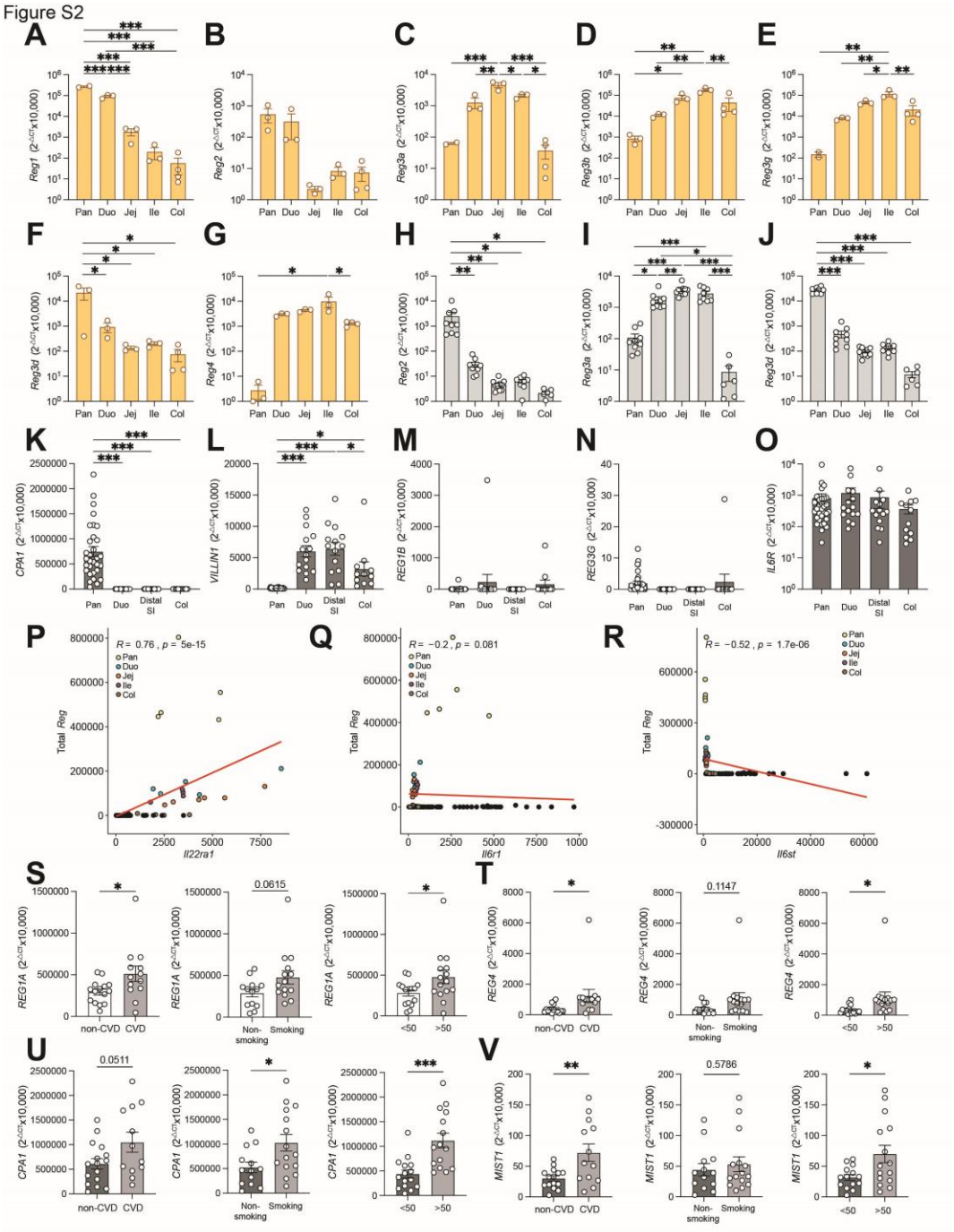


Figure 4.8 Mouse *Reg* and human *REG* gene family members differ in their expression patterns between pancreas and gut. **A-G**. Expression levels of indicated *Reg* genes in pancreas (pan), duodenum (duo), jejunum (jej), ileum (ile) and colon (col) of NOD mice by Q-PCR (*n*=3 except col, *n*=4). **H-J**. Expression levels of indicated *Reg* genes in pancreas (pan), duodenum (duo), jejunum (jej), ileum (ile) and colon (col) of C57Bl6 mice by Q-PCR (*n*=9 except col, *n*=6). **K-O**. Expression of *CPA1* (**K**), *VILLIN1* (**L**), *REG1B* (**M**), *REG3G* (**N**) and *IL6R*(O) in human pancreas (pan, n=31), duodenum (duo, *n*=15), distal small intestine (distal SI, *n*=14), and colon (col, *n*=11) by Q-PCR. **P-R**. Spearman correlations between total *Reg* expression and *Il22r1*, *Il6r1* or *Il6st*. **S-V**. Expression of *REG1A* (**S**)*, REG4* (**T**)*, CPA1* (**U**) *and MIST1*(**V**) in pancreas of donors with cardiovascular disease (CVD) or not, smoking history or not, and below vs above age of 50 at age of death. * p<0.05, ** p<0.01, *** p<0.001 by ANOVA for multivariant plots (A-N), * p<0.05, ** p<0.01, *** p<0.001 by 2-tailed t-test for two-way comparisons (O-Q).

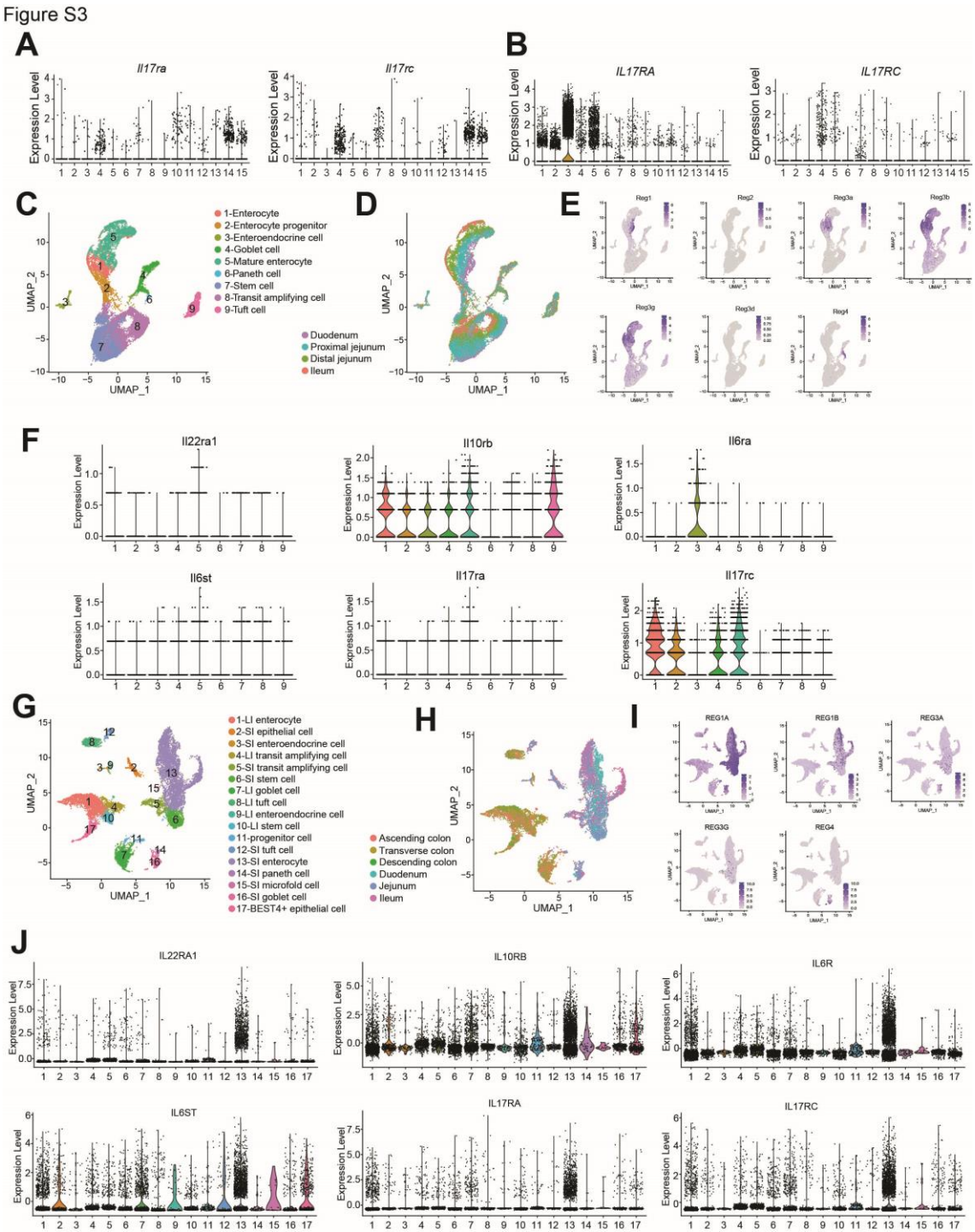


Figure 4.9 Gut and pancreas are enriched for *Reg* transcripts and the upstream signaling receptors.
A, B. Violin plots of IL-17 receptor genes across mouse pancreatic cell types (**A**) and human pancreatic cell types (**B**) based on *scRNAseq*. **C, D**. Annotated *scRNAseq* feature plots of mouse small intestine color coded by cell type (**C**) or gut segment of origin (**D**). **E**. Feature plots of mouse *Reg1, Reg2, Reg3a, Reg3b, Reg3g, Reg3d* and *Reg4.* **F**. Violin plots of IL-6, IL-22 or IL-17 receptor subunit genes across mouse small intestinal cell types. **G, H**. Annotated *scRNAseq* feature plots of human intestine color coded by cell type (**G**) or gut segment of origin (**H**). **I**. Feature plots of human *REG1A, REG1B, REG3A, REG3B* and *REG4.* **J**. Violin plots of IL-6, IL-22 or IL-17 receptor subunit genes across human intestinal cell types.

Figure S4

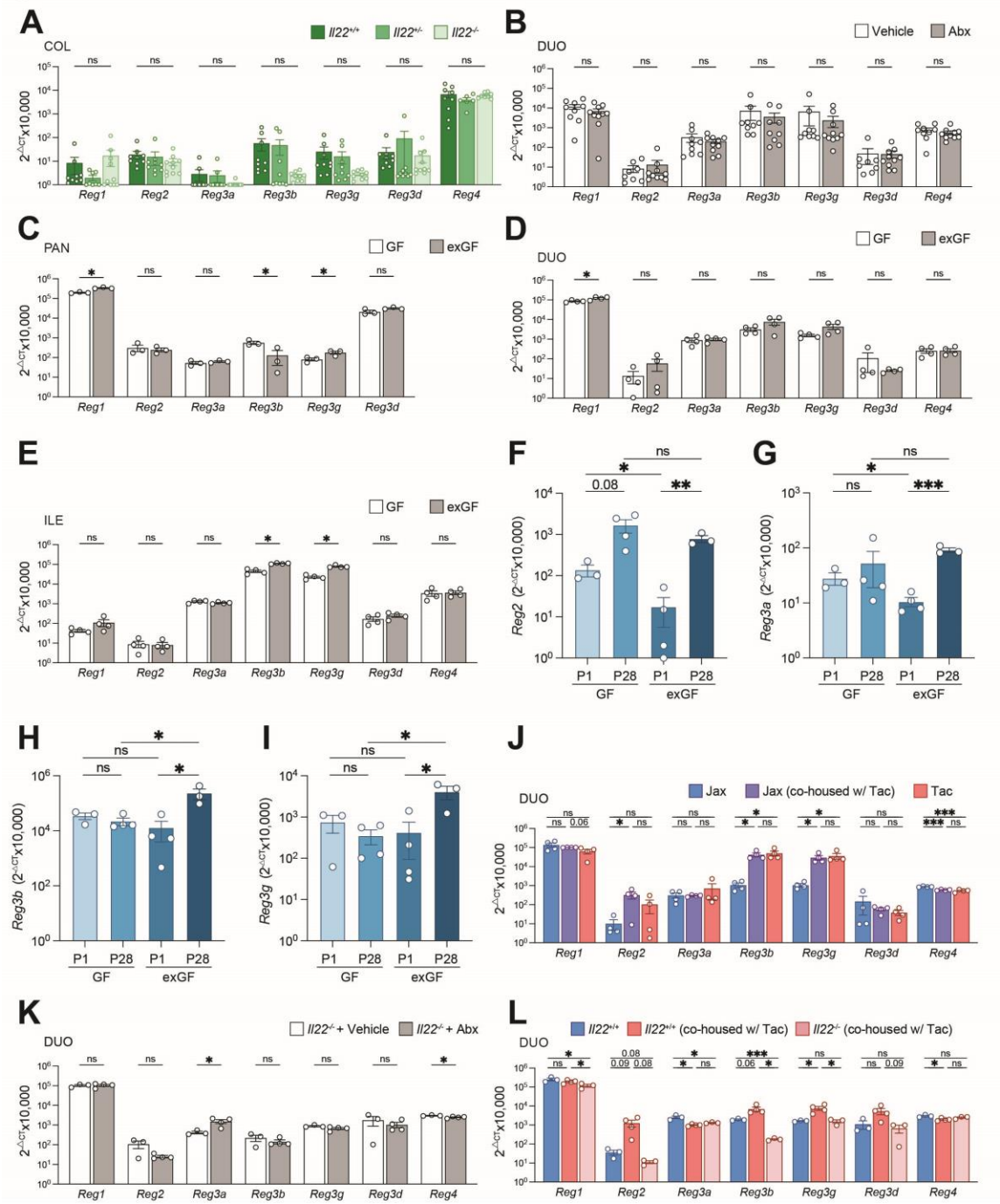


Figure 4.10 Dependence of baseline pancreatic and intestinal *Reg* expression on IL-22 and postnatal environmental exposure.
A. Colonic expression levels of indicated *Reg* genes in *Il22*$^{+/+}$, *Il22*$^{+/-}$ and *Il22*$^{-/-}$ mice (n=9, 9 and 10, respectively) by Q-PCR. Data pooled from two independent experiments. **B.** Duodenal expression levels of indicated *Reg* genes in antibiotics-treated mice and its vehicle controls (vehicle n=9, Abx n=10). **C-E.** Expression levels of indicated *Reg* genes in pancreas, duodenum and ileum of GF and ex-GF mice (n=3). **F-I**. Pancreatic expressions of indicated antimicrobial genes in GF or exGF mice harvested at P1 or P28 by Q-PCR (n=3-4). **J**. Duodenal expressions of indicated *Reg* genes in B6 mice from JAX, or Taconic (Tac), or JAX-mice co-housed with Taconic mice (n=4) for 4 weeks. **K**. Duodenal expression levels of indicated *Reg* genes of *Il22*$^{-/-}$ mice treated with antibiotics or vehicle (n=3), as well as **L**. *Il22*$^{+/+}$ (n=4) or *Il22*$^{-/-}$ (n=4) littermate mice co-housed with Taconic mice and non-co-housed *Il22*$^{+/+}$ controls (n=3). * p<0.05, ** p<0.01, *** p<0.001 by 2-tailed t-test.

Figure S5

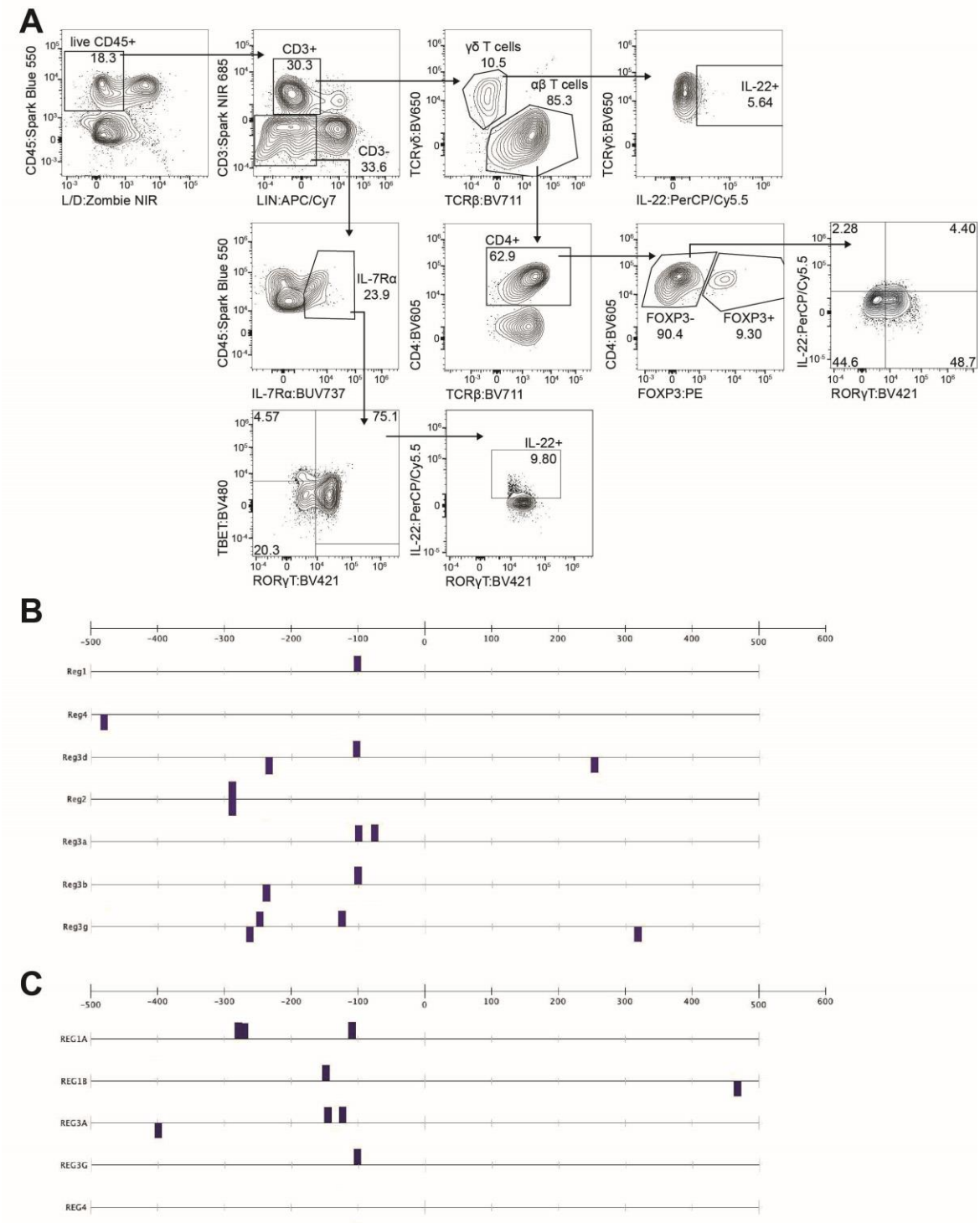


Figure 4.11 Transcription binding site analysis of *REG/Reg* family members.
A. Gating strategy to identify (IL-22^{+}) RORγt^{+} CD4^{+} T cells, (IL-22^{+}) ILC3s and (IL-22^{+}) γδ T cells for Fig. 4. LIN gate includes B220, NK1.1and CD11c. ILC3 are defined as LIN^{-}IL-7Rα^{+}RORγt^{+}. **B-C.** Binding site analysis of STAT3 at the promoter region of indicated mouse *Reg* (**B**) and human *REG* (**C**) genes.

Figure S6

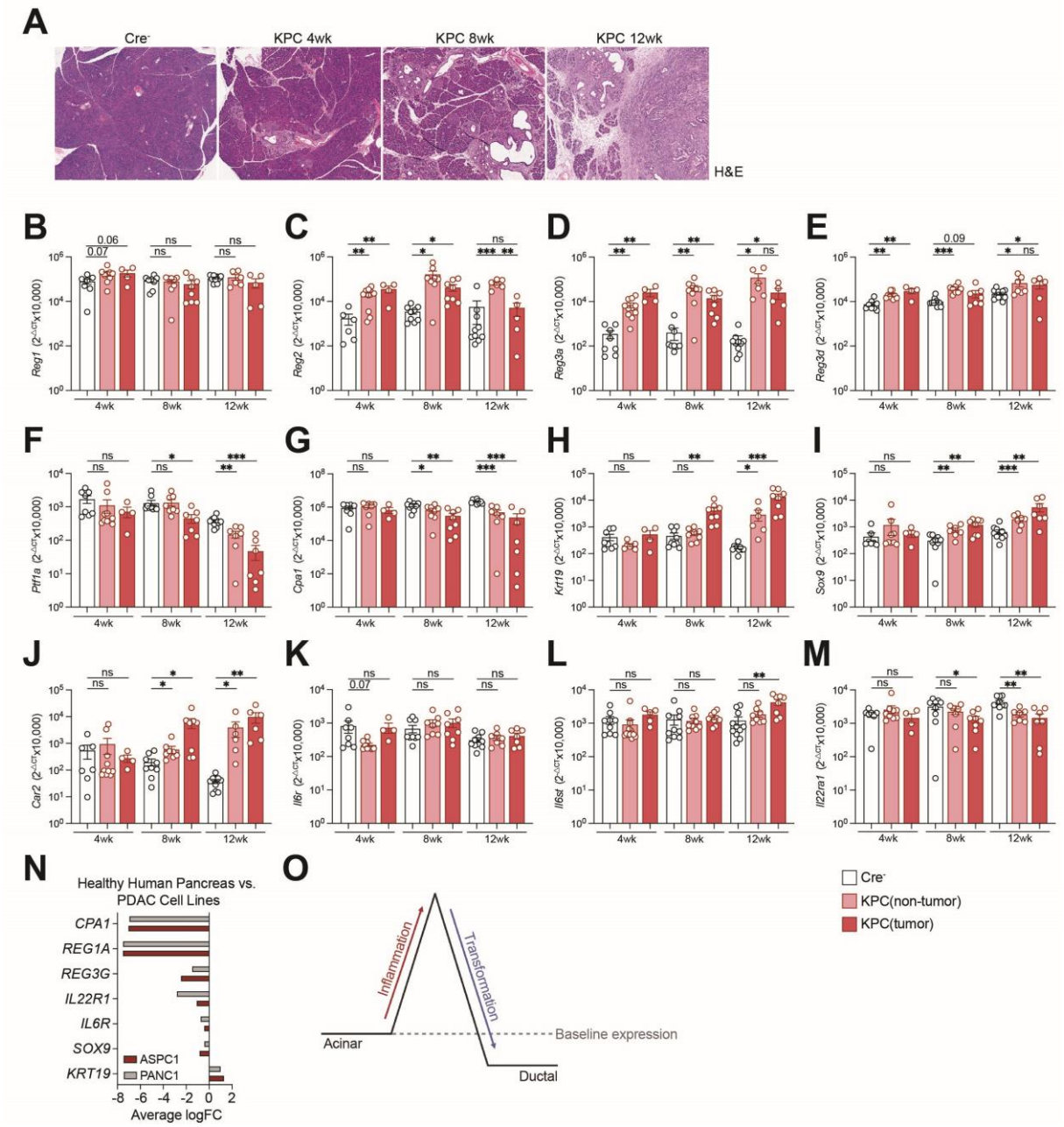


Figure 4.12 A mouse model of primary pancreatic ductal adenocarcinoma triggers *Reg* upregulation in pancreas but not gut.
A. Representative H&E-stained paraffin sections of pancreas from KPC mice at 4-, 8- or 12-weeks post tamoxifen treatment and Cre- mice (littermate to 12-week KPC mice). **B-M.** Pancreatic expression of *Reg1*(**B**), *Reg2* (**C**), *Reg3a* (**D**), *Reg3d* (**E**), *Ptf1a* (**F**), *Cpa1*(**G**), *Krt19* (**H**), *Sox9* (**I**), *Car2*(**J**), *Il6r* (**K**), *Il6st* (**L**) and *Il22r1a* (**M**) in KPC mice or Cre- littermates at 4-, 8- or 12-weeks post tamoxifen-induced PDAC onset, measured by Q-PCR (WT *n*=7, 9, 10, PDAC *n*=9, 8, 6 at 4, 8, 12 weeks, respectively). Data pooled from 3 cohorts per time point. **N.** Bar graph of Log2 fold change of indicated genes in healthy human pancreas versus human PDAC cell lines analyzed by Q-PCR. **O**. Proposed *REG/Reg* expression during the course of PDAC progression. * p<0.05, ** p<0.01, *** p<0.001 by student t-test.

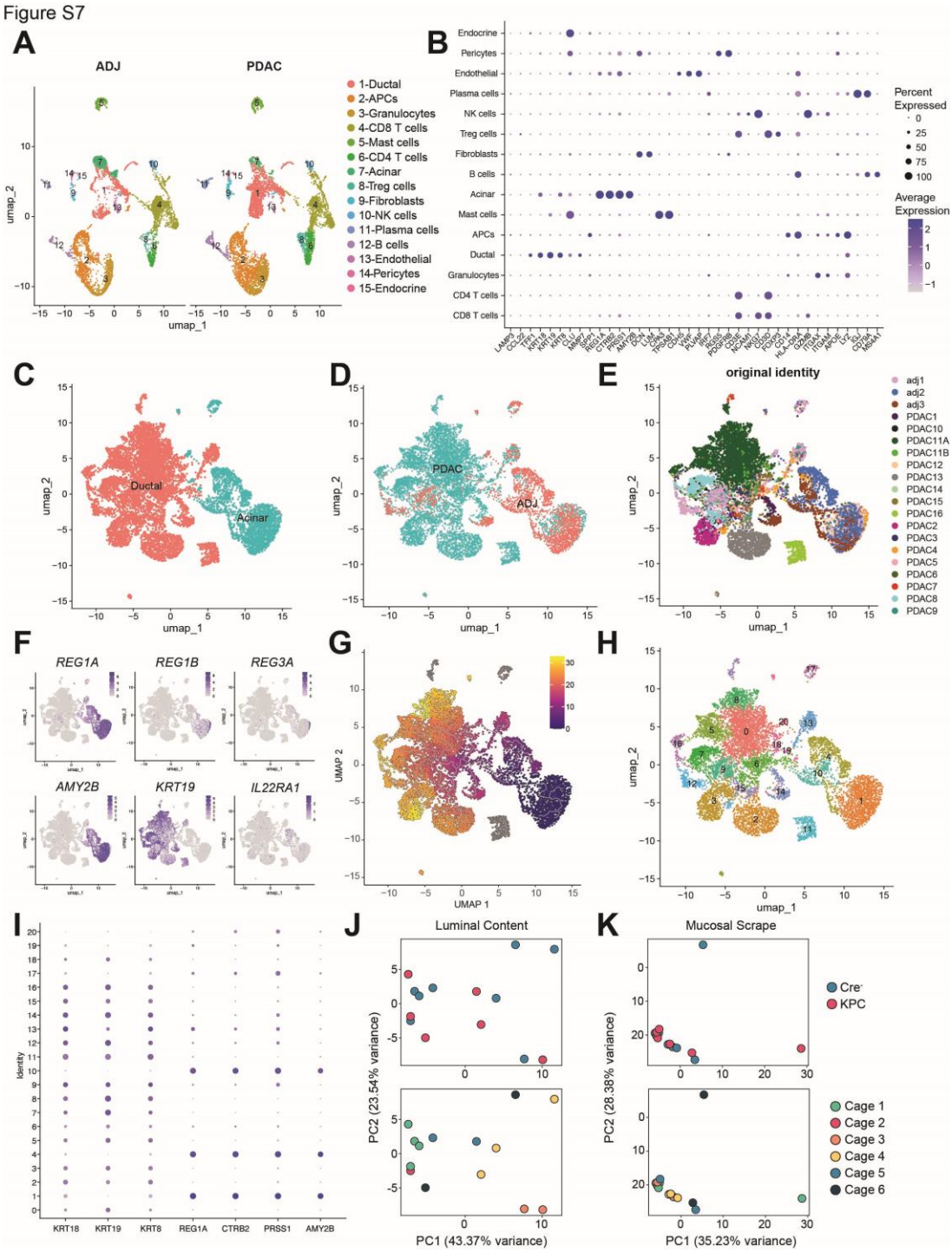


Figure 4.13 Human PDAC scRNAseq analysis for *REG* genes and murine duodenal microbiome upon PDAC induction.
A, B. Downsampled UMAPs of cell type clusters (**A**) and dot plot of cluster defining genes (**B**) from pancreatic cells isolated from human PDAC or adjacent tissues analyzed by *scRNAseq*. **C-I.** UMAPs of only acinar and ductal cells coded by cell type (**C**), sample type (**D**), donor sample (**E**), indicated genes (**F**), pseudotime analysis (**G**) and cluster number (**H**) of cells from PDAC and adjacent tissues. **I**. Dot plot of *REG* genes and acinar/ductal marker gene expressions in each cluster identified in **H**. **J**, **K**. PCA of CLR (centered log-ratio transformation) of relative abundance duodenal Luminal Content (**J**) and Mucosal Scrape (**K**) from KPC (n=6) or Cre$^-$ littermates (n=8) taken 12 weeks post tumor induction. Each PCA is coded once by genotype (top) and once by cage identity (bottom).

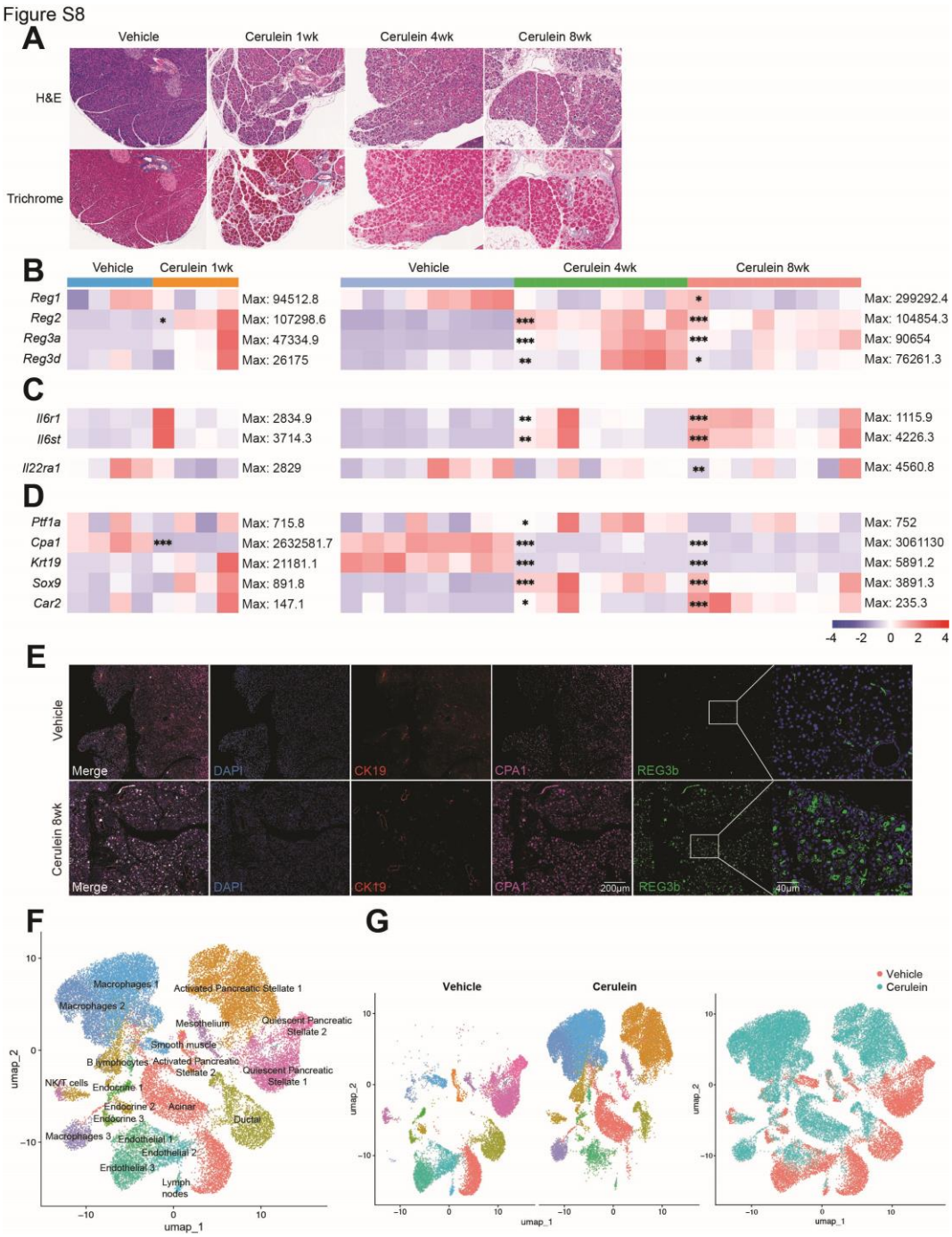


Figure 4.14 Cerulein induced pancreatitis triggers upregulation of *Reg* genes in pancreas but not gut.
A. Representative H+E- (top) and trichome- (bottom) stained paraffin sections of pancreata from mice with indicated treatments. **B-D.** Heatmap of expressions of indicated *Reg* genes (**B**), interleukin receptor genes (**C**) and acinar/ductal marker genes (**D**) in pancreata from mice treated with cerulein for 1, 4 or 8 weeks and age-matched vehicle treated mice measured by Q-PCR (n=4 (1 week) or 8 (4 and 8 weeks)). Data representative of one experiment per time point. Maximal expression level per row indicated at the right of each row. **E.** Pancreatic sections from mice treated with cerulein or vehicle for 8 weeks stained for ductal marker CK19, acinar marker CPA1, REG3β and DAPI (nuclei). Bar=200 μm, inset bar=40 μm. **F**, **G.** UMAPs of cell type clusters (**F**) and downsampled (left) and color coded by contribution by cells (right) (**G**) from pancreata of vehicle- or cerulein-treated mice based on *scRNAseq*. * p<0.05, ** p<0.01, *** p<0.001 by ANOVA (4 and 8 weeks cerulein comparisons) or two tailed t-test (1 week cerulein comparisons).

Figure S9

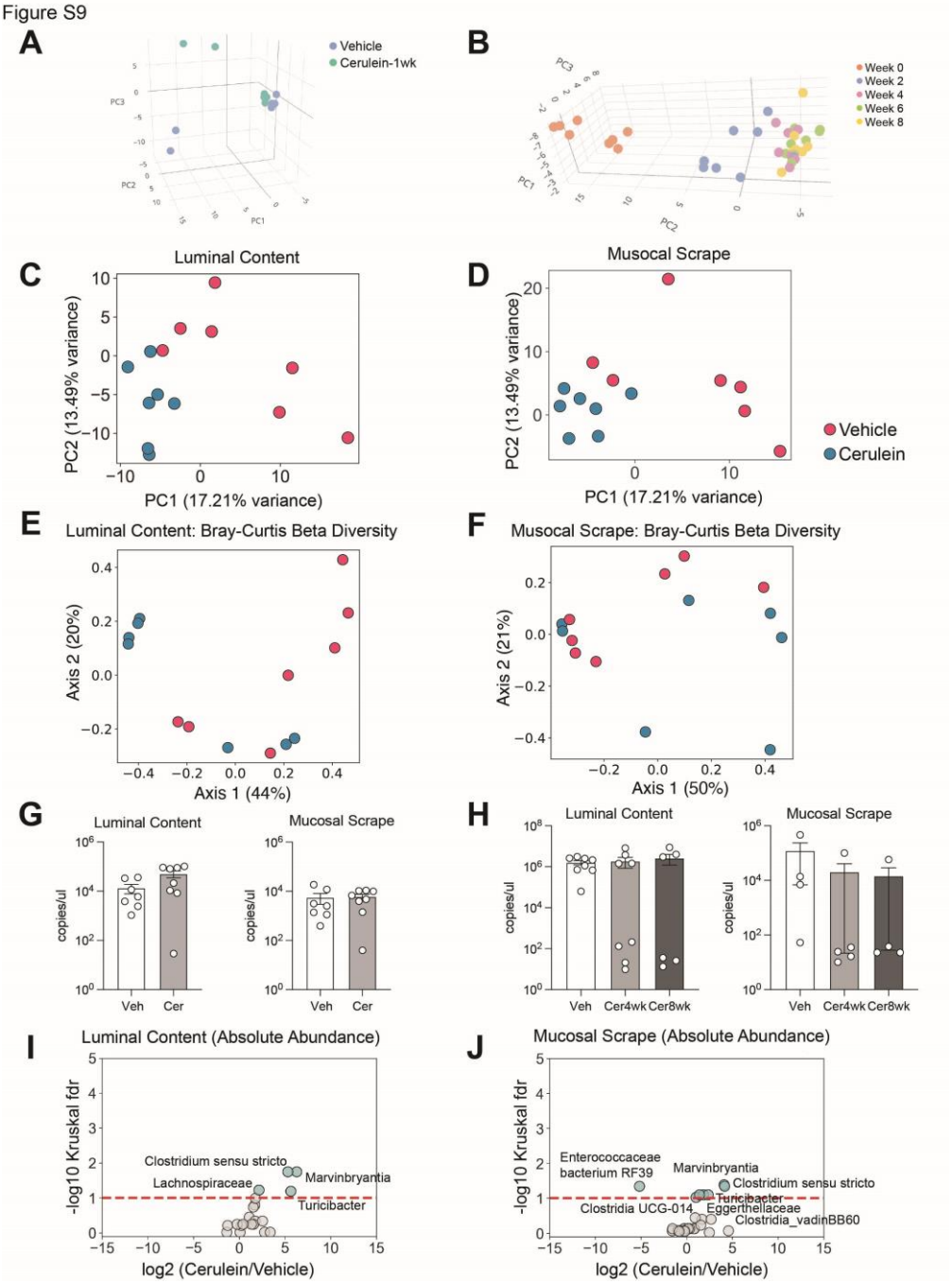


Figure 4.15 Cerulein induced pancreatitis modifies the gut microbiome.
A, B. PCA analysis of fecal microbiome of mice treated with cerulein or vehicle for 1 week (**A**) or 4 or 8 weeks (**B**) (*n*=8 per group). **C, D**. PCA of CLR (centered log-ratio transformation) of duodenal luminal bacteria (**C**) and mucosa-associated bacteria (**D**) of mice treated with cerulein or vehicle for 1 week (absolute abundance) (*n*=8). **E, F.** Bray-Curtis beta-diversity analysis of duodenal luminal bacteria (absolute abundance) (**E**) and mucosa-associated bacteria (**F**) of mice treated with cerulein or vehicle for 1 week (*n*=8). **G, H.** Total microbial load in duodenal mucosa or lumen of mice treated with cerulein for 1 week (**G**) or 4 or 8 weeks (**H**) or vehicle control measured by quantitative 16S Q-PCR (*n*=8, samples with amount below detection threshold were excluded). **I, J.** Volcano plots of bacteria enriched or de-enriched in the duodenal lumen (**I**) or mucosa (**J**) of mice treated with cerulein or vehicle for 1 week (*n*=8).

4.7 Material and methods

Reagents

The following reagents were used: Trizol (Thermo Fisher Scientific), Qubit RNA IQ Assay Kit (Thermo Fisher Scientific), Superscript IV (Thermo Fisher Scientific), Cerulein (Bachem), Trichome (Sigma), Sheep anti-mouse REG3B (R&D, AF5110), Rat anti-mouse CK19 (DHSB, AB2133570), Goat anti-mouse CPA1 (R&D, AF2765), AF488 donkey anti-sheep (Jackson Immunoresearch, 713-545-003), Cy3 donkey anti-rat (Jackson Immunoresearch, 712-165-153), AF647 donkey anti-goat (Jackson Immunoresearch, 705-605-147), DAPI Fluoromount G Clear Mounting Media (SouthernBiotech). Flow cytometry antibodies used were: Spark Blue™ 550 anti-mouse CD45 Antibody (BioLegend, 103166), Spark NIR™ 685 anti-mouse CD3 Antibody (BioLegend, 100262), BV711 hamster-anti-mouse γδ T-cell receptor (BD Biosciences, 563994), PerCP/Cy5.5 goat-anti-mouse IL-22 (BioLegend, 516411), BUV737 rat-anti-mouse IL-7α (BD Biosciences, 612841), BV605 rat-anti-mouse CD4 (BD Biosciences, 563151), PE rat-anti-mouse FOXP3 (eBiosciences, 50-112-9663), BV421 mouse-anti-mouse RORγt (BD Biosciences, 562894), BV480 mouse-anti-mouse T-BET (BD Biosciences, 568111).

Human specimens

Human pancreas samples were obtained through the Gift of Hope organ donor program (Dr. Piotr Witkowski). Human gut samples were obtained through the Gift of Hope organ donor program (Drs. Jonathan Kent and Lucia Madariaga). The studies were deemed exempted from further IRB review by the University of Chicago BSD IRB on the basis of them being secondary research on material from deceased and de-identified subjects (IRB19-1942 and IRB19-1085) .

Mice

All experiments were performed in accordance with the University of Chicago ACUP. C57BL/6J, NOD/ShiLtJ, Ptf1a$^{CreERT2/w}$, *Trp53*$^{fl/fl}$, and Kras$^{LSL-G12D}$, *Il22*$^{tm1.1(icre)Stck}$/J (*IL22*^{Cre}) were purchased from The Jackson Laboratory and crossed and maintained at the University of Chicago animal facility adhering to the IACUC protocol under specific pathogen-free (SPF) conditions, with the additional stipulations of the mice being free of segmented filamentous bacteria (SFB), murine norovirus (MNV) and Hpp. Germ free (GF) mice were purchased from Taconic and maintained in isolators in the gnotobiotic facility at the University of Chicago. Ex-GF mice in our study describe the offspring of GF mice that had been taken out of our isolators, colonized with microbiota from Jax mice mated under our strict SPF conditions for at least two generations with the same bedding and food as provided in isolators.

Pancreatic cancer induction

Ptf1a$^{CreERT2/w}$*Trp53*$^{fl/fl}$Kras$^{LSL-G12D/w}$ (KPC) mice and their wildtype littermates (Ptf1a$^{w/w}$*Trp53*$^{fl/fl}$Kras$^{LSL-G12D/w}$ or Ptf1a$^{w/w}$*Trp53*$^{fl/fl}$Kras$^{w/w}$) were fed with tamoxifen-containing diet (Envigo # TD.130858) for 7 days at 3-4 weeks of age for cancer induction. Mice were sacrificed at indicated time points. Pancreas and different intestinal segments were taken for subsequent processing and analysis.

Model of acute and chronic cerulein-induced pancreatitis

The acute pancreatitis was induced by 6 hourly intraperitoneal injections of 50ug/kg of the CCK analogue cerulein on each injection day, 3 injection days per week for 1 week. The chronic pancreatitis was induced by 6 hourly intraperitoneal injections of 50ug/kg cerulein on each

injection day, 2 injection days per week for 4-8 weeks. Control mice were injected with the same amount of saline.

Broad-spectrum antibiotics treatment

B6 or *Il22*$^{-/-}$ mice were provided with drinking water containing 1g/L ampicillin, 1g/L neomycin, 0.5g/L Vancomycin, 0.5g/L Metronidazole and 2g/L Truvia for 4 weeks. The pancreas, duodenum and ileum were harvested for qPCR and flow cytometry analysis.

Naturally transmission of segmented filamentous bacteria (SFB) by co-housing

SFB-free mice (purchased from Jax) were co-housed with SFB-bearing mice (purchased from Taconic) for 4 weeks. The pancreas, duodenum and ileum were harvested for qPCR and flow cytometry analysis.

REG protein sequence alignment

Protein sequences of mouse and human REG family members were obtained from the UniProt database (uniprot.org). Multiple sequence alignment was performed using the built-in alignment tool in UniProt, with the number of iterations set to 3. Sequence similarity matrix was obtained from the alignment output.

REG protein structural prediction and RMSD calculation

Trypsin cleavage sites were identified in the amino acid sequences of each REG protein. The resulting truncated sequences were input into the “Monomer structure prediction with AlphaFold” module on Tamarind Bio (tamarind.bio/alphafold). To test for module accuracy, the predicted

structures were superimposed onto the predicted full-length structures extracted from AlphaFold database (alphafold.ebi.ac.uk). Root mean square deviation (RMSD) of atomic positions was calculated between each REG protein using PyMOL (Version 2.5.8).

Cell culture

Mammalian cells were all grown in a humidified incubator with 5% CO_2 at 37°C. PANC1 cells (ATCC) were grown in Dulbecco's Modified Eagle Media (DMEM, Gibco) supplemented with 10% FBS and 100 U/mL penicillin and streptomycin. ASPC1 cells (ATCC) were grown in RPMI-1640 media supplemented with 10% FBS and 100 U/mL penicillin and streptomycin.

Human Acinar Cell Culture

Human pancreata were subjected to tissue digest and acinar cell cluster versus islet separation as previously described.(Gołębiewska et al., 2019) The acinar fraction was further dissociated by incubating every 10 mL cell suspension or tissue sample with 2 mL of 0.05% trypsin at room temperature for 20 minutes with intermittent pipetting. The reaction was quenched with 10 mL of 1× CMRL 1066, centrifuged at 1500 rpm for 5 minutes, and the pellet was resuspended in 40 mL of 1× CMRL 1066 before culturing the isolated acinar cells in CMRL 1066 medium supplemented with 10 mL of Albumin Human USP, 25% Solution, and 0.5 mL of Heparin USP (10,000 IU/mL) at 37°C with 5% CO_2; cells were then plated at a density of approximately 1 million per well in a 6-well low-adhesion plate and harvested 24 hours post-plating in RNAlater and stored at -80 °C for downstream analysis.

Tissue procurement, RNA extraction and Real-time PCR

Mouse pancreatic and intestinal tissues were frozen in RNAlater and stored at -80 °C. Human pancreata were stored as entire organs at -20C for less than 12 months. Human intestinal pieces were frozen in RNAlater and stored at -80 °C, and only the mucosa processed for RNA extraction. Human PDAC cell lines were directly harvested into TRIzol. Total RNA from samples was extracted using TRIzol, RNA integrity was verified by Qubit RNA IQ Assay and cDNA generated by reverse transcription using SuperScript IV kit according to the manufacturer's protocol. Quantitative real-time PCR was performed using Power SYBR Green PCR Master Mix (Applied Biosystems) on Quanstudio 6 Flex machine (Thermo Fisher Scientific). The relative expression of target genes was normalized to *36B4* (mouse) or *B-ACTIN* (human) expression and calculated using the formula of $2^{-\Delta Ct}$ x10000. All data were averaged from at least 2 replicates. Newly designed primers were verified for single peak melting curves, single band products on an agarose gel and linearity within the range of measured CT values.

Table 4.1 Primer list

Gene Name	Species	Primer Sequence		Source
36B4	Mouse	Forward	5′-GCCGTGATGCCCAGGGAAGAC-3′	Designed in house
		Reverse	5′-CATCTGCTTGGAGCCCACGTT-3′	
Reg1	Mouse	Forward	5′-ATGGCTAGGAACGCCTACTTC-3′	Designed in house
		Reverse	5′-CCCAAGTTAAACGGTCTTCAGT-3′	
Reg2	Mouse	Forward	5′-CTGCCAACCGTGGTTATTG-3′	Designed in house
		Reverse	5′-GGCTCTGAACTTGCAGACAA-3′	
Reg3a	Mouse	Forward	5′-ATTGGGCTCCATGATCCA-3′	Designed in house
		Reverse	5′-AGATAATTCAGCACATCGGAGTT-3′	
Reg3b	Mouse	Forward	5′-ACTCCCTGAAGAATATACCCTCC-3′	Designed in house
		Reverse	5′-CGCTATTGAGCACAGATACGAG-3′	
Reg3g	Mouse	Forward	5′-TCCACCTCTGTTGGGTTCAT-3′	Designed in house
		Reverse	5′-AAGCTTCCTTCCTGTCCTCC-3′	
Reg3d	Mouse	Forward	5′-AGGGGAGTTTGCCCAATGAA-3′	Designed in house
		Reverse	5′-TGAGGCCTGAGACAAAGCTG-3′	

Gene Name	Species	Primer Sequence		Source
Reg4	Mouse	Forward	5′-GGCTCTGAGGGCCTTGAAAT-3′	Designed in house
		Reverse	5′-GCACAGCTGGGTCTCAAGAT-3′	
Il22	Mouse	Forward	5′-TCATCGGGGAGAAACTGTTC-3′	Designed in house
		Reverse	5′-CATGTAGGGCTGGAACCTGT-3′	
Il6	Mouse	Forward	5′-CTGCAAGAGACTTCCATCCAG-3′	Designed in house
		Reverse	5′-AGTGGTATAGACAGGTCTGTTGG-3′	
Il22r1	Mouse	Forward	5′-TTGACTCCGATATTGTCCAAGG-3′	Designed in house
		Reverse	5′-GTAGCCCAGATAACAGAGCAAG-3′	
Il10rb	Mouse	Forward	5′-GTGTTCAAGTTCGAGGGTTTC-3′	Designed in house
		Reverse	5′-GCAGACCATGAAGACCGAG-3′	
Il6r1	Mouse	Forward	5′-GCCACCGTTACCCTGATTTG-3′	Designed in house
		Reverse	5′-TCCTGTGGTAGTCCATTCTCTG-3′	
Il6st	Mouse	Forward	5′-TTACTACGTGAATGCCAGCTACA-3′	Designed in house
		Reverse	5′-GACGTGGTTCTGTTGATGACA-3′	
Krt19	Mouse	Forward	5′-GTTCTCAGACCTGCGTCC-3′	Designed in house
		Reverse	5′-TGACCCAATGCGTACTGAAC-3′	
Sox9	Mouse	Forward	5′-CAAGACTCTGGGCAAGCTC-3′	Designed in house
		Reverse	5′-GGGCTGGTACTTGTAATCGG-3′	
Cpa1	Mouse	Forward	5′-GTCTACACCCACAAAACGAATC-3′	Designed in house
		Reverse	5′-ACGGTAAGTTTCTGAGCAGG-3′	
Car2	Mouse	Forward	5′-GATGGATTGGCTGTTTTGGG-3′	Designed in house
		Reverse	5′-GGAGCAAGGGTCGAAGTTAG-3′	
Ptf1a	Mouse	Forward	5′-AGGACCCCAGAAAACTCAAC-3′	Designed in house
		Reverse	5′-CAATATGCACAAAGACGCGG-3′	
B-ACTIN	Human	Forward	5′-GCGAGAAGATGACCCAGA-3′	Adopted from *Tsuchida et. al, 2017*
		Reverse	5′-CAGAGGCGTACAGGGATA-3′	
REG1A	Human	Forward	5′-AGGAGAGTGGCACTGATGACTT-3′	Adopted from *Tsuchida et. al, 2017*
		Reverse	5′-TAGGAGACCAGGGACCCACTG-3′	
REG1B	Human	Forward	5′-ATTGGGCTCCATGATCCA-3′	Adopted from *Tsuchida et. al, 2017*
		Reverse	5′-AGATAATTCAGCACATCGGAGTT-3′	
REG3A	Human	Forward	5′- AGAGAATATTCGCTTAATTCC-3′	Adopted from *Tsuchida et. al, 2017*
		Reverse	5′- AATGAAGAGACTGAAATGACA-3′	

Gene Name	Species	Primer Sequence		Source
REG3G	Human	Forward	5′- GAATATTCTCCCCAAACTG-3′	Adopted from *Tsuchida et. al, 2017*
		Reverse	5′- GAGAAAAGCCTGAAATGAAG-3′	
REG4	Human	Forward	5′- ATCCTGGTCTGGCAAGTC -3′	Adopted from *Tsuchida et. al, 2017*
		Reverse	5′- CGTTGCTGCTCCAAGTTA -3′	
CPA1	Human	Forward	5′- TGGTGTTGAGTGTCCTGTTG-3′	Designed in house
		Reverse	5′- CTCCTTCACCTTCTGTACCTG-3′	
VILLIN1	Human	Forward	5′- CAGGATGACTTGGAAGAGGATG-3′	Designed in house
		Reverse	5′- GGGATGGGTCTTGAGGTATTC-3′	
IL22RA1	Human	Forward	5′- GGTCAACCGCACCTACCAAATG-3′	Designed in house
		Reverse	5′- TGATGGTGCCAAGGAACTCTGTG-3′	
IL10R2	Human	Forward	5′- GGAATGGAGTGAGCCTGTCTGT-3′	Designed in house
		Reverse	5′- AAACGCACCACAGCAAGGCGAA-3′	
IL6R	Human	Forward	5′- GACTGTGCACTTGCTGGTGGAT-3′	Designed in house
		Reverse	5′- ACTTCCTCACCAAGAGCACAGC-3′	
IL6ST	Human	Forward	5′- CACCCTGTATCACAGACTGGCA-3′	Designed in house
		Reverse	5′- TTCAGGGCTTCCTGGTCCATCA -3′	
IL22RA2	Human		Hs00364814_m1	Thermofisher Taqman
PTF1A	Human	Forward	5′- TCCGAACAGCCAAAGTCTG -3′	Designed in house
		Reverse	5′- ACATAATCAGATCTTCAGCCGAG -3′	
MIST1	Human	Forward	5′- AGGGCCTCACCTTCCTG -3′	Designed in house
		Reverse	5′- GCCTCTGTGTCCTGCAC -3′	
SOX9	Human	Forward	5′- GTACCCGCACTTGCACAAC -3′	Designed in house
		Reverse	5′- TCTCGCTCTCGTTCAGAAGTC -3′	
KRT19	Human	Forward	5′- TAGAGGTGAAGATCCGCGAC -3′	Designed in house
		Reverse	5′- CCGTCTCAAACTTGGTTCGG -3′	

Histological imaging and assessment

Specimens were immediately collected from mice and fixed in 4% paraformaldehyde for 1 hour at room temperature and rinsed in 70% ethanol. All the samples were graded-ethanol dehydrated, embedded in paraffin, cut into 5-µm–thick sections using microtome and then stained with hematoxylin and eosin (H&E) or special Masson trichrome for histomorphometric assessment at

University of Chicago Medicine Human Tissue Resource Center. The stained sections were sent to University of Chicago Microscopy Core for whole slide scanning using Olympus VS200 slideview research slide scanner at 20x resolution.

Immunofluorescent staining

5-µm-thick paraffin-sections were heated to 65°C for 20min and rinse twice in xylene for 10min to de-paraffinize. Slides were re-hydrated using graded-ethanol and then blocked for 30 min at RT with blocking buffer (5% donkey serum, 2.5% BSA in 1X PBS). Slides were permeabilized with 0.1% Saponin if necessary, then incubated overnight in a humidified chamber at 4°C with antibodies (REG3β and CPA1 at 1:100, CK19 at 1:50 dilution). The next day, slides underwent three PBST (1X PBS with 0.05% Tween-20) washes, and were incubated with appropriate secondary antibodies (1:500 dilution) for 1hr at RT. After three more PBST washes, slides were mounted using DAPI Fluoromount G Clear Mounting Media. Stained slides were sent for whole slide scanning.

Flow Cytometry

Cells were first stained for viability using LIVE/DEAD™ Dead Cells Stain kits or Zombie NIR™ Fixable Viability kit. For surface epitopes, cells were resuspended in antibody cocktail and incubated for 20 min at 4°C. Cells were incubated in Fixation/permeabilization solution for 30 min, then stained for nuclear epitopes overnight. Intracellular and nuclear antibodies were diluted in 1x Permeabilization buffer. Flow cytometry was conducted on a 5-laser Aurora spectral flow cytometer and analyzed using FlowJo Software. The antibodies used are listed in the Reagents section.

Bioinformatic analysis of published scRNAseq datasets

scRNAseq data was obtained from the NCBI GEO database. Counts were used as input for the R package Seurat. Cells were initially filtered to remove doublets and poor-quality cells based on the unique molecular identifiers (UMIs), number of features, and percentage of mitochondrial genes (<0.25). To normalize gene counts, Seurat's LogNormalize function was used with default parameters (scale factor = 10,000). Variable genes were then identified using the Seurat function FindVariableFeatures with default parameters. The data was scaled using ScaleData and then subjected to dimensionality reduction by PCA using RunPCA. The cells were clustered using Seurat's FindNeighbors followed by FindClusters prior to visualization by RunUMAP. For mouse wildtype and cerulein-treated mouse pancreatic scRNAseq dataset GSE188819(Chondronasiou et al., 2022), clusters annotations were included in the counts file downloaded from GEO database. For mouse pancreatic cancer scRNAseq data GSE141017(Schlesinger et al., 2020), logFold changes of genes of interest between acinar and metaplastic cells were extracted and plotted. For human scRNAseq data from GSE155698(Steele et al., 2020), clusters were annotated based on the gene set presented in Figure 2b of Steele et al, 2020(Steele et al., 2020). For the plots shown in Figure S7A, data integration was performed using IntegrateLayers function in Seurat. Integrated data was then downsampled to visualize the relative contribution of each cell type. For intestinal epithelial cell scRNAseq data from GSE185224 (human)(Burclaff et al., 2022) and GSE201859 (mouse)(Zwick et al., 2024), processed Seurat objects were downloaded from https://cellxgene.cziscience.com/datasets. Specific expression was visualized using FeaturePlot and VlnPlot functions. Statistical analysis was performed using the ggpubr package in R by t-test.

Collection of duodenal content and mucosal scrape

The small intestine was removed and the duodenum segment (the first quarter) was identified. Luminal contents were collected by gently squeezing the duodenum. The duodenum was then opened longitudinally and the mucosal surface was scraped using a curled forcep. Both fractions were collected into sterile eppendorf tubes and weighed. The tools were cleaned after each collection.

Duodenal host depletion, extraction, library preparation, sequencing, and analysis

The host depletion method was adopted from *Wu-Woods et. al, 2023*(Wu-Woods et al., 2023). In summary, duodenal luminal contents and mucosal scrapes were placed into 2-ml 1.4-mm ceramic bead-beating tubes (Lysing Matrix D from MP Biomedical, catalog no. 1169130-CF) and 400 µL of sterile 0.9% saline was added into the bead-beating tube. Samples were homogenized for 30s at 4.5 m s^{-1} on Qiagen's TissueLyser II and then immediately placed on ice. 150 µL of homogenized tissue was placed into clean microfuge tubes containing 10 µL of buffer (100 mM Tris + 40 mM $MgCl_2$, pH 8.0 and 0.22 µm sterile filtered), 33 µL of saline (0.9% NaCl, autoclaved), 2 µL of Benzonase Nuclease HC (EMD Millipore catalog no. 71205) and 5 µL of Proteinase K (NEB catalog no. P8107S). Tubes were incubated for 15 min at 37 °C with shaking at 600 rpm, then pelleted at 10,000g for 2 min. The supernatant was discarded and pellets were resuspended in 150 µL of PrimeStore MTM (Longhorn) to inactivate residual enzymatic activity and stored at −80 °C until shipment to Caltech.

Nucleic-acid extraction was performed using Qiagen's AllPrep PowerViral DNA/RNA Kit (catalog no. 28000-50) using 3 rounds of bead beating for 1 min at 6.0 m s^{-1} per round on the

FastPrep-24 MP Bio Homogenizer. Reagent DX (0.5% v/v; Qiagen catalog no. 19088) was added to PM1 prior to bead beating to reduce foaming.

16S rRNA gene Quantitative Sequencing (Quant-Seq) was performed as previously described(Barlow et al., 2020). In summary, the V4 (515F-806R) region of the 16S rRNA gene was amplified in duplicate using 5µL template in a total reaction volume of 20µL. Libraries were amplified to ~15,000 RFU before removal and duplicate reactions were pooled. Sequencing was performed by Fulgent Genetics using the Illumina MiSeq, v2 Standard, 2x250bp.

For microbial abundance measurements, qPCR and ddPCR were performed using the same V4 (515F-806R) primer set. For ddPCR, as previously described(Barlow et al., 2020), the QX200 droplet dPCR system (Bio-Rad catalog no. 1864001, 1864002) was utilized with 2.5µL of template in a total reaction volume of 25 µL. For qPCR, 1uL of template was added to the following components (final concentration reported): 1X SSOFast EvaGreen Supermix (Bio-Rad catalog no. 1725201), 500 nM forward and reverse primer (F: 5'- CAG CMG CCG CGG TAA -3', R: 5'- GGA CTA CHV GGG TWT CTA AT -3') for a total reaction volume of 10 µL. Amplification and quantification was performed on the CFX96 RT-PCR machine (Bio-Rad) under the following cycling conditions: 94 °C for 3 min, up to 40 cycles of 94 °C for 45 s, 52 °C for 30 s, and 68 °C for 30 s. Conversion from Cq to copies per µL was performed using a standard curve and validated with ddPCR.

Sequencing analysis was performed as previously described(Barlow et al., 2020). In brief, processing was performed with QIIME2 (v2022.8) and taxonomy assigned with SILVA 138 99% OTU 515F-806R reference database using unrarefied data. Dada2 trimming parameters were set to the base pair where average quality scores dropped below 30. Raw sequence data, ASV abundance and taxonomy tables, were generated. All downstream analysis was performed at the

genus-level. Taxa below LOD (limit of detection) were identified based on Poisson statistics, as previously described(Barlow et al., 2021), and set to zero in downstream analysis performed in Python (v3.9.12).

Fecal DNA extraction, 16S library preparation, sequencing and analysis

Fecal microbial DNA was extracted using the QIAamp PowerFecal Pro DNA kit (Qiagen). Prior to extraction, samples were subjected to mechanical disruption using a bead beating method using Qiagen's TissueLyser II. Samples were then centrifuged, and supernatant was resuspended in CD2, that effectively removes inhibitors by precipitating non-DNA organic and inorganic materials including polysaccharides, cell debris and proteins. DNA was purified routinely using a silica spin column filter membrane. By adding solution CD3, a high-concentration salt solution, DNA selectively binds to the membrane which is recovered using elution buffer. DNA is then quantified using Qubit. 16S Q-PCR was used to determine the total bacterial load in each sample.

The V4-V5 region of 16S rRNA gene was amplified using universal bacterial primers – 563F (5'-nnnnnnnn-NNNNNNNNNNNN-AYTGGGYDTAAA-GNG-3') and 926R (5'-nnnnnnnn-NNNNNNNNNNNN-CCGTCAATTYHT-TTRAGT-3'), where 'N' represents the barcodes, 'n' are additional nucleotides added to offset primer sequencing. The approximately ~360 bp amplicons were then purified using bead-based size selection, quantified, and pooled at equimolar concentrations. Illumina sequencing-compatible Combinatorial Dual Index (CDI) adapters were ligated onto the pools using the QIAseq 1-step amplicon library kit (Qiagen). Library QC was performed using Qubit and Tapestation and sequenced on Illumina MiSeq platform to generate 2x250bp paired-end reads.

Dada2 (v1.18.0) was used as the default pipeline for processing MiSeq 16S rRNA reads with minor modifications in R (v4.0.3). Specifically, reads were first trimmed at 190 bp for both forward and reverse reads to remove low-quality nucleotides. Chimeras were detected and removed using the default consensus method in the dada2 pipeline. Then, ASVs with lengths between 320 bp and 365 bp were kept and deemed as high quality ASVs. Taxonomy of the resultant ASVs was assigned to the genus level using the RDP classifier (v2.13) and trainset 18 (release 11.5) with a minimum bootstrap confidence score of 80. Raw sequence data, ASV abundance and Taxonomy tables, and bar plots, were generated. Samples below 1000 reads and features present in 2 or fewer samples were excluded from the analysis. The Kruskal-Wallis test was used to check significance. Volcano plots were generated using results from the R package ALDEx2. Alpha and beta diversities were estimated using Phyloseq on the repeatedly rarefied datasets (100 iterations) using the R package mirlyn.

Statistical analysis Q-PCR data

Statistical analyses were performed using *GraphPad Prism* software (version 10.0; GraphPad, La Jolla, Calif). Graphs were generated using *GraphPad Prism* or *Rstudio*. Data are displayed as mean (SD) for at least 3 replicates. Comparison between 2 groups was performed using Student *t* test, whereas comparison among multiple groups was performed using 1-way analysis of variance. A P value < 0.05 indicates statistical significance.

Chapter 5. Thesis Discussion

This thesis defines a conceptual shift in how immune responses are organized across the upper digestive system by identifying antigen origin, subcellular localization, and inter-organ regulation as additional determinants of immune outcome. Collectively, the work demonstrates that T cell fate is not dictated solely by antigen dose or inflammatory context, but also by antigen source, which governs access to specialized antigen-presenting cell (APC) subsets and bias the selection of tolerance mechanisms.

A central finding is that despite their shared similar anatomical environment, immune tolerance to dietary antigens and epithelial self-antigens is mediated by distinct APC subsets. Oral antigens rely predominantly on RORγt^{+}MHC-II^{+} APCs, whereas epithelial self-antigens engage BATF3^{+} cDC1s. Moreover, even within self-antigens, subcellular locations, further stratifies antigen access to different APC populations. This reveals an additional layer of immune regulation in which both "source" and "location" of an antigen determine the fate of its cognate T cells. Antigen source can gate access to specific APC subsets, thereby influencing downstream T cell differentiation, as distinct APCs possess specialized capabilities to direct lineage commitment. Consequently, these differences translate into functional consequences for susceptibility to inflammation, providing a mechanistic explanation for why certain antigens elicit pathological responses while others are maintained in a state of tolerance.

A second major insight is that tissue-specific tolerance of co-drained organs is preserved but not isolated. The liver, pancreas, and intestine employ distinct tolerance mechanisms, ranging from immune ignorance, clonal deletion to Treg induction, but these programs are partially by shared lymphatic environments. Lymph node co-drainage does not homogenize immune responses

but selectively influences specific outcomes, particularly Treg differentiation. Furthermore, inflammatory perturbations in one tissue can unmask pathogenic T cell responses in another, establishing a framework for understanding inter-organ immune coordination.

Finally, besides coordinated adaptive responses, this work identifies coordinated innate immunity as an additional layer of inter-organ communication, exemplified by the *REG/Reg* gene family. The differential regulation of inducible versus constitutive REG isoforms in the intestine and pancreas, and their responsiveness to microbiota-dependent signals, suggests that the gut and pancreas can engage in a shared innate defense program. This supports a model in which these tissues communicate not only through shared lymphatics system but also through inflammatory signals from the vasculature.

These findings have several important implications. First, they establish a refined framework for predicting T cell fate based on antigen source and tissue context, with direct relevance to autoimmune disease, food allergy, and cancer. Second, they highlight inter-organ communication as a potential therapeutic avenue. Modulating APC subset engagement or the lymph node milieu through a more accessible organ, such as the gut, may enable selective enhancement of tolerance or immunity in less accessible tissue, including the pancreas and liver.

Future directions should focus on defining the molecular mechanisms that govern APC access to distinct antigen source, as well as elucidating how innate and adaptive immune responses are coordinated across tissues. Therapeutically, strategies that manipulate antigen form or delivery, reprogram APC subsets, or modulate inter-organ signaling pathways may enable precise control of immune responses in complex, multi-organ diseases.

Bibliography

Abadie, V., Kim, S. M., Lejeune, T., Palanski, B. A., Ernest, J. D., Tastet, O., Voisine, J., Discepolo, V., Marietta, E. V., Hawash, M. B. F., Ciszewski, C., Bouziat, R., Panigrahi, K., Horwath, I., Zurenski, M. A., Lawrence, I., Dumaine, A., Yotova, V., Grenier, J. C., … Jabri, B. (2020). IL-15, gluten and HLA-DQ8 drive tissue destruction in coeliac disease. *Nature*, *578*(7796), 600–604. https://doi.org/10.1038/S41586-020-2003-8;TECHMETA

Abergel, C., Chenivesse, S., Stinnakre, M. G., Guasco, S., Bréchot, C., Claverie, J. M., Devinoy, E., & Christa, L. (1999). Crystallization and preliminary crystallographic study of HIP/PAP, a human C-lectin overexpressed in primary liver cancers. *Acta Crystallographica Section D: Biological Crystallography*, *55*(8). https://doi.org/10.1107/S0907444999007969

Abramson, J., Dobeš, J., Lyu, M., & Sonnenberg, G. F. (2023). The emerging family of RORγt+ antigen-presenting cells. *Nature Reviews. Immunology*, *24*(1), 64. https://doi.org/10.1038/S41577-023-00906-5

Akagbosu, B., Tayyebi, Z., Shibu, G., Paucar Iza, Y. A., Deep, D., Parisotto, Y. F., Fisher, L., Pasolli, H. A., Thevin, V., Elmentaite, R., Knott, M., Hemmers, S., Jahn, L., Friedrich, C., Verter, J., Wang, Z. M., van den Brink, M., Gasteiger, G., Grünewald, T. G. P., … Brown, C. C. (2022a). Novel antigen-presenting cell imparts Treg-dependent tolerance to gut microbiota. *Nature*, *610*, 752–760. https://doi.org/10.1038/s41586-022-05309-5

Álvarez-Aznar, A., Martínez-Corral, I., Daubel, N., Betsholtz, C., Mäkinen, T., & Gaengel, K. (2020). Tamoxifen-independent recombination of reporter genes limits lineage tracing and mosaic analysis using CreERT2 lines. *Transgenic Research*, *29*(1), 53–68. https://doi.org/10.1007/S11248-019-00177-8

Ansaldo, E., Slayden, L. C., Ching, K. L., Koch, M. A., Wolf, N. K., Plichta, D. R., Brown, E. M., Graham, D. B., Xavier, R. J., Moon, J. J., & Barton, G. M. (2019). Akkermansia muciniphila induces intestinal adaptive immune responses during homeostasis. *Science*, *364*(6446), 1179–1184. https://doi.org/10.1126/SCIENCE.AAW7479

Apiz Saab, J. J., Dzierozynski, L. N., Jonker, P. B., AminiTabrizi, R., Shah, H., Menjivar, R. E., Scott, A. J., Nwosu, Z. C., Zhu, Z., Chen, R. N., Oh, M., Sheehan, C., Wahl, D. R., Pasca di Magliano, M., Lyssiotis, C. A., Macleod, K. F., Weber, C. R., & Muir, A. (2023). Pancreatic tumors exhibit myeloid-driven amino acid stress and upregulate arginine biosynthesis. *ELife*, *12*. https://doi.org/10.7554/ELIFE.81289

Aykut, B., Pushalkar, S., Chen, R., Li, Q., Abengozar, R., Kim, J. I., Shadaloey, S. A., Wu, D., Preiss, P., Verma, N., Guo, Y., Saxena, A., Vardhan, M., Diskin, B., Wang, W., Leinwand, J., Kurz, E., Kochen Rossi, J. A., Hundeyin, M., … Miller, G. (2019). The fungal mycobiome promotes pancreatic oncogenesis via activation of MBL. *Nature*, *574*(7777). https://doi.org/10.1038/s41586-019-1608-2

Backx, E., Coolens, K., Van den Bossche, J. L., Houbracken, I., Espinet, E., & Rooman, I. (2022). On the Origin of Pancreatic Cancer: Molecular Tumor Subtypes in Perspective of Exocrine Cell Plasticity. *Cellular and Molecular Gastroenterology and Hepatology*, *13*(4), 1243–1253. https://doi.org/10.1016/J.JCMGH.2021.11.010

Backx, E., Wauters, E., Baldan, J., Van Bulck, M., Michiels, E., Heremans, Y., De Paep, D. L., Kurokawa, M., Goyama, S., Bouwens, L., Jacquemin, P., Houbracken, I., & Rooman, I. (2021). MECOM permits pancreatic acinar cell dedifferentiation avoiding cell death under stress conditions. *Cell Death and Differentiation*, *28*(9). https://doi.org/10.1038/s41418-021-00771-6

Baeza, N., Sanchez, D., Christa, L., Guy-Crotte, O., Vialettes, B., & Figarella, C. (2001). Pancreatitis-associated protein (HIP/PAP) gene expression is upregulated in NOD mice pancreas and localized in exocrine tissue during diabetes. *Digestion*, *64*(4). https://doi.org/10.1159/000048867

Bankhead, P., Loughrey, M. B., Fernández, J. A., Dombrowski, Y., McArt, D. G., Dunne, P. D., McQuaid, S., Gray, R. T., Murray, L. J., Coleman, H. G., James, J. A., Salto-Tellez, M., & Hamilton, P. W. (2017). QuPath: Open source software for digital pathology image analysis. *Scientific Reports*, *7*(1), 1–7. https://doi.org/10.1038/S41598-017-17204-5;TECHMETA

Barlow, J. T., Bogatyrev, S. R., & Ismagilov, R. F. (2020). A quantitative sequencing framework for absolute abundance measurements of mucosal and lumenal microbial communities. *Nature Communications*, *11*(1). https://doi.org/10.1038/s41467-020-16224-6

Barlow, J. T., Leite, G., Romano, A. E., Sedighi, R., Chang, C., Celly, S., Rezaie, A., Mathur, R., Pimentel, M., & Ismagilov, R. F. (2021). Quantitative sequencing clarifies the role of disruptor taxa, oral microbiota, and strict anaerobes in the human small-intestine microbiome. *Microbiome*, *9*(1). https://doi.org/10.1186/s40168-021-01162-2

Behnsen, J., Jellbauer, S., Wong, C. P., Edwards, R. A., George, M. D., Ouyang, W., & Raffatellu, M. (2014). The Cytokine IL-22 Promotes Pathogen Colonization by Suppressing Related Commensal Bacteria. *Immunity*, *40*(2). https://doi.org/10.1016/j.immuni.2014.01.003

Bexelius, T. S., Ljung, R., Mattsson, F., & Lagergren, J. (2013). Cardiovascular disease and risk of acute pancreatitis in a population-based study. *Pancreas*, *42*(6). https://doi.org/10.1097/MPA.0b013e318287cb62

Bogatyrev, S. R., Rolando, J. C., & Ismagilov, R. F. (2020a). Self-reinoculation with fecal flora changes microbiota density and composition leading to an altered bile-acid profile in the mouse small intestine. *Microbiome*, *8*(1). https://doi.org/10.1186/s40168-020-0785-4

Bohe, H., Bohe, M., Lundberg, E., Polling, Å., & Ohlsson, K. (1997). Production and secretion of pancreatic secretory trypsin inhibitor in normal human small intestine. *Journal of Gastroenterology*, *32*(5). https://doi.org/10.1007/BF02934111

Bouziat, R., Hinterleitner, R., Brown, J. J., Stencel-Baerenwald, J. E., Ikizler, M., Mayassi, T., Meisel, M., Kim, S. M., Discepolo, V., Pruijssers, A. J., Ernest, J. D., Iskarpatyoti, J. A., Costes, L. M. M., Lawrence, I., Palanski, B. A., Varma, M., Zurenski, M. A., Khomandiak, S., McAllister, N., … Jabri, B. (2017). Reovirus infection triggers inflammatory responses to dietary antigens and development of celiac disease. *Science*, *356*(6333), 44–50. https://doi.org/10.1126/SCIENCE.AAH5298

Brown, C. C., Gudjonson, H., Pritykin, Y., Deep, D., Lavallée, V. P., Mendoza, A., Fromme, R., Mazutis, L., Ariyan, C., Leslie, C., Pe'er, D., & Rudensky, A. Y. (2019). Transcriptional Basis of Mouse and Human Dendritic Cell Heterogeneity. *Cell*, *179*, 846-863.e24. https://doi.org/10.1016/j.cell.2019.09.035

Brown, H., Komnick, M. R., Brigleb, P. H., Dermody, T. S., & Esterházy, D. (2023a). Lymph node sharing between pancreas, gut, and liver leads to immune crosstalk and regulation of pancreatic autoimmunity. *Immunity*, *56*(9), 2070-2085.e11. https://doi.org/10.1016/j.immuni.2023.07.008

Brown, J. J., Short, S. P., Stencel-Baerenwald, J., Urbanek, K., Pruijssers, A. J., McAllister, N., Ikizler, M., Taylor, G., Aravamudhan, P., Khomandiak, S., Jabri, B., Williams, C. S., & Dermody, T. S. (2018). Reovirus-Induced Apoptosis in the Intestine Limits Establishment of Enteric Infection. *Journal of Virology*, *92*(10), e02062-17. https://doi.org/10.1128/JVI.02062-17

Burch, G. E., Tsui, C. Y., & Harb, J. M. (1973). Hepatitis in Mice Infected with Coxsackie Virus B1. *British Journal of Experimental Pathology*, *54*(3), 249. https://pmc.ncbi.nlm.nih.gov/articles/PMC2072594/

Burclaff, J., Bliton, R. J., Breau, K. A., Ok, M. T., Gomez-Martinez, I., Ranek, J. S., Bhatt, A. P., Purvis, J. E., Woosley, J. T., & Magness, S. T. (2022). A Proximal-to-Distal Survey of Healthy Adult Human Small Intestine and Colon Epithelium by Single-Cell Transcriptomics. *CMGH*, *13*(5). https://doi.org/10.1016/j.jcmgh.2022.02.007

Cabric, V., & Brown, C. C. (2025). Thetis cells: regulators of intestinal immune tolerance. In *Current Opinion in Immunology* (Vol. 95). Elsevier Ltd. https://doi.org/10.1016/j.coi.2025.102570

Cabric, V., Franco Parisotto, Y., Park, T., Akagbosu, B., Zhao, Z., Lo, Y., Shibu, G., Fisher, L., Paucar Iza, Y. A., Leslie, C., & Brown, C. C. (2025). A wave of Thetis cells imparts tolerance to food antigens early in life. *Science*. https://doi.org/10.1126/science.adp0535

Caio, G., Volta, U., Sapone, A., Leffler, D. A., De Giorgio, R., Catassi, C., & Fasano, A. (2019). Celiac disease: a comprehensive current review. *BMC Medicine*, *17*(1), 142. https://doi.org/10.1186/s12916-019-1380-z

Calne, R. Y., Sells, R. A., Pena, J. R., Davis, D. R., Millard, P. R., Herbertson, B. M., Binns, R. M., & Davies, D. A. L. (1969). Induction of Immunological Tolerance by Porcine Liver Allografts. *Nature 1969 223:5205*, *223*(5205), 472–476. https://doi.org/10.1038/223472a0

Canesso, M. C. C., de Castro, T. B. R., Nakandakari-Higa, S., Lockhart, A., Luehr, J., Bortolatto, J., Parsa, R., Esterházy, D., Lyu, M., Liu, T. T., Murphy, K. M., Sonnenberg, G. F., Reis, B. S., Victora, G. D., & Mucida, D. (2025). Identification of antigen-presenting cell–T cell interactions driving immune responses to food. *Science*, *387*(6739). https://doi.org/10.1126/science.ado5088

Cash, H. L., Whitham, C. V, Behrendt, C. L., & Hooper, L. V. (2006). Symbiotic bacteria direct expression of an intestinal bactericidal lectin. *Science (New York, N.Y.)*, *313*, 1126–1130. https://doi.org/10.1126/science.1127119

Cash, H. L., Whitham, C. V., & Hooper, L. V. (2006). Refolding, purification, and characterization of human and murine RegIII proteins expressed in Escherichia coli. *Protein Expression and Purification*, *48*(1), 151–159. https://doi.org/10.1016/j.pep.2006.01.014

Chandra, V., Li, L., Le Roux, O., Zhang, Y., Howell, R. M., Rupani, D. N., Baydogan, S., Miller, H. D., Riquelme, E., Petrosino, J., Kim, M. P., Bhat, K. P. L., White, J. R., Kolls, J. K., Pylayeva-Gupta, Y., & McAllister, F. (2024). Gut epithelial Interleukin-17 receptor A signaling can modulate distant tumors growth through microbial regulation. *Cancer Cell*, *42*(1). https://doi.org/10.1016/j.ccell.2023.12.006

Chen, R., Pan, S., Yi, E. C., Donohoe, S., Bronner, M. P., Potter, J. D., Goodlett, D. R., Aebersold, R., & Brentnall, T. A. (2006). Quantitative proteomic profiling of pancreatic cancer juice. *Proteomics*, *6*(13). https://doi.org/10.1002/pmic.200500702

Chen, W., Imasaka, M., Lee, M., Fukui, H., Nishiura, H., & Ohmuraya, M. (2023a). Reg family proteins contribute to inflammation and pancreatic stellate cells activation in chronic pancreatitis. *Scientific Reports 2023 13:1*, *13*(1), 12201-. https://doi.org/10.1038/s41598-023-39178-3

Chiffoleau, E. (2018). C-type lectin-like receptors as emerging orchestrators of sterile inflammation represent potential therapeutic targets. In *Frontiers in Immunology* (Vol. 9, Number FEB). https://doi.org/10.3389/fimmu.2018.00227

Choi, S. M., McAleer, J. P., Zheng, M., Pociask, D. A., Kaplan, M. H., Qin, S., Reinhart, T. A., & Kolls, J. K. (2013). Innate Stat3-mediated induction of the antimicrobial protein Reg3γ is required for host defense against MRSA pneumonia. *Journal of Experimental Medicine*, *210*(3). https://doi.org/10.1084/jem.20120260

Chondronasiou, D., Martínez de Villarreal, J., Melendez, E., Lynch, C. J., Pozo, N. del, Kovatcheva, M., Aguilera, M., Prats, N., Real, F. X., & Serrano, M. (2022). Deciphering the roadmap of in vivo reprogramming toward pluripotency. *Stem Cell Reports*, *17*(11). https://doi.org/10.1016/j.stemcr.2022.09.009

Chu, V. T., Weber, T., Graf, R., Sommermann, T., Petsch, K., Sack, U., Volchkov, P., Rajewsky, K., & Kühn, R. (2016). Efficient generation of Rosa26 knock-in mice using CRISPR/Cas9 in C57BL/6 zygotes. *BMC Biotechnology*, *16*(1), 1–15. https://doi.org/10.1186/S12896-016-0234-4/TABLES/3

Coombes, J. L., Siddiqui, K. R. R., Arancibia-Cárcamo, C. V., Hall, J., Sun, C. M., Belkaid, Y., & Powrie, F. (2007). A functionally specialized population of mucosal CD103+ DCs induces Foxp3+ regulatory T cells via a TGF-beta and retinoic acid-dependent mechanism. *The Journal of Experimental Medicine*, *204*(8), 1757–1764. https://doi.org/10.1084/JEM.20070590

Crispe, I. N. (2014). Immune tolerance in liver disease. *Hepatology*, *60*(6), 2109–2117. https://doi.org/10.1002/HEP.27254;WEBSITE:WEBSITE:PERICLES;JOURNAL:JOURNAL:15273350;WGROUP:STRING:PUBLICATION

Darnaud, M., Dos Santos, A., Gonzalez, P., Augui, S., Lacoste, C., Desterke, C., De Hertogh, G., Valentino, E., Braun, E., Zheng, J., Boisgard, R., Neut, C., Dubuquoy, L., Chiappini, F., Samuel, D., Lepage, P., Guerrieri, F., Doré, J., Bréchot, C., … Faivre, J. (2018). Enteric Delivery of Regenerating Family Member 3 alpha Alters the Intestinal Microbiota and Controls Inflammation in Mice With Colitis. *Gastroenterology*, *154*(4). https://doi.org/10.1053/j.gastro.2017.11.003

De Luca, A., Zelante, T., D'Angelo, C., Zagarella, S., Fallarino, F., Spreca, A., Iannitti, R. G., Bonifazi, P., Renauld, J. C., Bistoni, F., Puccetti, P., & Romani, L. (2010). IL-22 defines a novel immune pathway of antifungal resistance. *Mucosal Immunology*, *3*(4). https://doi.org/10.1038/mi.2010.22

Deki, H., & Sato, T. (1988). An anatomic study of the peripancreatic lymphatics. *Surgical and Radiologic Anatomy 1988 10:2*, *10*(2), 121–135. https://doi.org/10.1007/BF02307820

Dias, C., & Nylandsted, J. (2021). Plasma membrane integrity in health and disease: significance and therapeutic potential. In *Cell Discovery* (Vol. 7, Number 1). https://doi.org/10.1038/s41421-020-00233-2

Dorner, M., Horwitz, J. A., Robbins, J. B., Barry, W. T., Feng, Q., Mu, K., Jones, C. T., Schoggins, J. W., Catanese, M. T., Burton, D. R., Law, M., Rice, C. M., & Ploss, A. (2011). A genetically humanized mouse model for hepatitis C virus infection. *Nature*, *474*(7350), 208–212. https://doi.org/10.1038/NATURE10168

dos Santos, P. Q., Guedes, J. C., de Jesus, R. P., Santos, R. R. dos, & Fiaconne, R. L. (2017). Effects of using symbiotics in the clinical nutritional evolution of patients with chronic

pancreatitis: Study prospective, randomized, controlled, double blind. *Clinical Nutrition ESPEN*, *18*, 9–15. https://doi.org/10.1016/j.clnesp.2017.01.005

Doyle, C. J., Yancey, K., Pitt, H. A., Wang, M., Bemis, K., Yip-Schneider, M. T., Sherman, S. T., Lillemoe, K. D., Goggins, M. D., & Schmidt, C. M. (2012). The proteome of normal pancreatic juice. *Pancreas*, *41*(2). https://doi.org/10.1097/MPA.0b013e31822862f6

Durai, V., & Murphy, K. M. (2016). Functions of Murine Dendritic Cells. *Immunity*, *45*(4), 719–736. https://doi.org/10.1016/j.immuni.2016.10.010

Eble, J. A. (2019). Structurally robust and functionally highly versatile—C-type lectin (-related) proteins in snake venoms. In *Toxins* (Vol. 11, Number 3). https://doi.org/10.3390/toxins11030136

El Marjou, F., Janssen, K. P., Chang, B. H. J., Li, M., Hindie, V., Chan, L., Louvard, D., Chambon, P., Metzger, D., & Robine, S. (2004). Tissue-specific and inducible Cre-mediated recombination in the gut epithelium. *Genesis*, *39*(3), 186–193. https://doi.org/10.1002/GENE.20042

Esterházy, D., Canesso, M. C. C., Mesin, L., Muller, P. A., de Castro, T. B. R., Lockhart, A., ElJalby, M., Faria, A. M. C., & Mucida, D. (2019a). Compartmentalized gut lymph node drainage dictates adaptive immune responses. *Nature*, *569*(7754), 126–130. https://doi.org/10.1038/S41586-019-1125-3;TECHMETA

Esterházy, D., Loschko, J., London, M., Jove, V., Oliveira, T. Y., & Mucida, D. (2016a). Classical dendritic cells are required for dietary antigen-mediated induction of peripheral T reg cells and tolerance. *Nature Immunology*, *17*, 545–555. https://doi.org/10.1038/ni.3408

Fatkhullina, A. R., Kent, J., Brown, H., Christiansen, N., Lisicka, W., Madariaga, M. L., & Esterházy, D. (2025). Medullary stromal cells define small intestinal lymph node identity in humans and mice. *Cell Reports*, *44*(10), 116441. https://doi.org/10.1016/J.CELREP.2025.116441

Ferri, S., Longhi, M. S., De Molo, C., Lalanne, C., Muratori, P., Granito, A., Hussain, M. J., Ma, Y., Lenzi, M., Mieli-Vergani, G., Bianchi, F. B., Vergani, D., & Muratori, L. (2010). A multifaceted imbalance of T cells with regulatory function characterizes type 1 autoimmune hepatitis. *Hepatology (Baltimore, Md.)*, *52*(3), 999–1007. https://doi.org/10.1002/HEP.23792

Fiske, K. L., Brigleb, P. H., Sanchez, L. M., Hinterleitner, R., Taylor, G. M., & Dermody, T. S. (2024). Strain-specific differences in reovirus infection of murine macrophages segregate with polymorphisms in viral outer-capsid protein σ3. *Journal of Virology*, *98*(11). https://doi.org/10.1128/JVI.01147-24

Fonseca, D. M. Da, Hand, T. W., Han, S. J., Gerner, M. Y., Zaretsky, A. G., Byrd, A. L., Harrison, O. J., Ortiz, A. M., Quinones, M., Trinchieri, G., Brenchley, J. M., Brodsky, I. E.,

Germain, R. N., Randolph, G. J., & Belkaid, Y. (2015). Microbiota-Dependent Sequelae of Acute Infection Compromise Tissue-Specific Immunity. *Cell*, *163*(2), 354–366. https://doi.org/10.1016/j.cell.2015.08.030

Fu, L., Upadhyay, R., Pokrovskii, M., Chen, F. M., Romero-Meza, G., Griesemer, A., & Littman, D. R. (2025). PRDM16-dependent antigen-presenting cells induce tolerance to gut antigens. *Nature*, *642*(8068), 756–765. https://doi.org/10.1038/S41586-025-08982-4;TECHMETA

Fu, S., Zhang, N., Yopp, A. C., Chen, D., Mao, M., Chen, D., Zhang, H., Ding, Y., & Bromberg, J. S. (2004). TGF-β induces Foxp3 + T-regulatory cells from CD4 + CD25 - precursors. *American Journal of Transplantation*, *4*(10), 1614–1627. https://doi.org/10.1111/j.1600-6143.2004.00566.x

Fumagalli, V., & Iannacone, M. (2024). Unlocking CD8+ T cell potential in chronic hepatitis B virus infection. *Nature Reviews Gastroenterology & Hepatology 2024 22:2*, *22*(2), 92–93. https://doi.org/10.1038/s41575-024-01015-x

Gabba, A., Bogucka, A., Luz, J. G., Diniz, A., Coelho, H., Corzana, F., Cañada, F. J., Marcelo, F., Murphy, P. V., & Birrane, G. (2021). Crystal Structure of the Carbohydrate Recognition Domain of the Human Macrophage Galactose C-Type Lectin Bound to GalNAc and the Tumor-Associated Tn Antigen. *Biochemistry*, *60*(17). https://doi.org/10.1021/acs.biochem.1c00009

Gao, Y., Nish, S. A., Jiang, R., Hou, L., Licona-Limón, P., Weinstein, J. S., Zhao, H., & Medzhitov, R. (2013). Control of T helper 2 responses by transcription factor IRF4-dependent dendritic cells. *Immunity*, *39*(4), 722–732. https://doi.org/10.1016/j.immuni.2013.08.028

Glaubitz, J., Asgarbeik, S., Lange, R., Mazloum, H., Elsheikh, H., Weiss, F. U., & Sendler, M. (2023). Immune response mechanisms in acute and chronic pancreatitis: strategies for therapeutic intervention. *Frontiers in Immunology*, *14*, 1279539. https://doi.org/10.3389/FIMMU.2023.1279539/FULL

Gołębiewska, J. E., Bachul, P. J., Wang, L. J., Matosz, S., Basto, L., Kijek, M. R., Fillman, N., Gołąb, K., Tibudan, M., Dębska-Ślizień, A., Millis, J. M., Fung, J., & Witkowski, P. (2019). Validation of a New North American Islet Donor Score for Donor Pancreas Selection and Successful Islet Isolation in a Medium-Volume Islet Transplant Center. *Cell Transplantation*, *28*, 185–194. https://doi.org/10.1177/0963689718816989

Guerra, C., Schuhmacher, A. J., Cañamero, M., Grippo, P. J., Verdaguer, L., Pérez-Gallego, L., Dubus, P., Sandgren, E. P., & Barbacid, M. (2007). Chronic Pancreatitis Is Essential for Induction of Pancreatic Ductal Adenocarcinoma by K-Ras Oncogenes in Adult Mice. *Cancer Cell*. https://doi.org/10.1016/j.ccr.2007.01.012

Guo, X., Zhao, J., Hao, J., Chen, J., Lyu, M., Liu, H., Li, N., Song, P., Wang, W., Chu, C., & Sonnenberg, G. (2025). *RORγt+ APCs require a distinct cis-regulatory element to instruct tolerance to dietary antigens*. https://doi.org/10.21203/rs.3.rs-4865841/v1

Hepworth, M. R., Monticelli, L. A., Fung, T. C., Ziegler, C. G. K., Grunberg, S., Sinha, R., Mantegazza, A. R., Ma, H. L., Crawford, A., Angelosanto, J. M., John Wherry, E., Koni, P. A., Bushman, F. D., Elson, C. O., Eberl, G., Artis, D., & Sonnenberg, G. F. (2013). Innate lymphoid cells regulate CD4+ T-cell responses to intestinal commensal bacteria. *Nature*, *498*(7452), 113–117. https://doi.org/10.1038/NATURE12240

Hildebrand, F., Nguyen, T. L. A., Brinkman, B., Yunta, R. G., Cauwe, B., Vandenabeele, P., Liston, A., & Raes, J. (2013). Inflammation-associated enterotypes, host genotype, cage and inter-individual effects drive gut microbiota variation in common laboratory mice. *Genome Biology*, *14*(1). https://doi.org/10.1186/gb-2013-14-1-r4

Hildner, K., Edelson, B. T., Purtha, W. E., Diamond, M., Matsushita, H., Kohyama, M., Calderon, B., Schraml, B. U., Unanue, E. R., Diamond, M. S., Schreiber, R. D., Murphy, T. L., & Murphy, K. M. (2008a). Batf3 deficiency reveals a critical role for CD8α+ dendritic cells in cytotoxic T cell immunity. *Science*, *322*, 1097–1100. https://doi.org/10.1126/science.1164206

Hirota, M., Ohmuraya, M., & Baba, H. (2006). The role of trypsin, trypsin inhibitor, and trypsin receptor in the onset and aggravation of pancreatitis. In *Journal of Gastroenterology* (Vol. 41, Number 9). https://doi.org/10.1007/s00535-006-1874-2

Hu, W., & Pasare, C. (2013). Location, location, location: tissue-specific regulation of immune responses. *Journal of Leukocyte Biology*, *94*(3), 409–421. https://doi.org/10.1189/JLB.0413207;WGROUP:STRING:PUBLICATION

Huang, H., Wang, Z., Zhang, Y., Pradhan, R. N., Ganguly, D., Chandra, R., Murimwa, G., Wright, S., Gu, X., Maddipati, R., Müller, S., Turley, S. J., & Brekken, R. A. (2022). Mesothelial cell-derived antigen-presenting cancer-associated fibroblasts induce expansion of regulatory T cells in pancreatic cancer. *Cancer Cell*, *40*(6), 656-673.e7. https://doi.org/10.1016/J.CCELL.2022.04.011

Huber, S., Gagliani, N., Zenewicz, L. A., Huber, F. J., Bosurgi, L., Hu, B., Hedl, M., Zhang, W., O'Connor, W., Murphy, A. J., Valenzuela, D. M., Yancopoulos, G. D., Booth, C. J., Cho, J. H., Ouyang, W., Abraham, C., & Flavell, R. A. (2012). IL-22BP is regulated by the inflammasome and modulates tumorigenesis in the intestine. *Nature*, *491*(7423). https://doi.org/10.1038/nature11535

Iovanna, J., Orelle, B., Keim, V., & Dagorn, J. C. (1991). Messenger RNA sequence and expression of rat pancreatitis-associated protein, a lectin-related protein overexpressed during acute experimental pancreatitis. *Journal of Biological Chemistry*, *266*(36). https://doi.org/10.1016/s0021-9258(18)54281-2

Ivanov, I. I., Atarashi, K., Manel, N., Brodie, E. L., Shima, T., Karaoz, U., Wei, D., Goldfarb, K. C., Santee, C. A., Lynch, S. V., Tanoue, T., Imaoka, A., Itoh, K., Takeda, K., Umesaki, Y., Honda, K., & Littman, D. R. (2009a). Induction of Intestinal Th17 Cells by Segmented Filamentous Bacteria. *Cell*, *139*(3), 485–498. https://doi.org/10.1016/j.cell.2009.09.033

Jenne, C. N., & Kubes, P. (2013). Immune surveillance by the liver. *Nature Immunology 2013 14:10*, *14*(10), 996–1006. https://doi.org/10.1038/ni.2691

Joeris, T., Gomez-Casado, C., Holmkvist, P., Tavernier, S. J., Silva-Sanchez, A., Klotz, L., Randall, T. D., Mowat, A. M., Kotarsky, K., Malissen, B., & Agace, W. W. (2021). Intestinal cDC1 drive cross-tolerance to epithelial-derived antigen via induction of FoxP3+CD8+ Tregs. *Science Immunology*, *6*(60). https://doi.org/10.1126/SCIIMMUNOL.ABD3774/SUPPL_FILE/SCIIMMUNOL.ABD3774_DATA

Kabacaoglu, D., Ciecielski, K. J., Ruess, D. A., & Algül, H. (2018). Immune checkpoint inhibition for pancreatic ductal adenocarcinoma: Current limitations and future options. *Frontiers in Immunology*, *9*(AUG), 396649. https://doi.org/10.3389/FIMMU.2018.01878/FULL

Kartal, E., Schmidt, T. S. B., Molina-Montes, E., Rodríguez-Perales, S., Wirbel, J., Maistrenko, O. M., Akanni, W. A., Alhamwe, B. A., Alves, R. J., Carrato, A., Erasmus, H. P., Estudillo, L., Finkelmeier, F., Fullam, A., Glazek, A. M., Gómez-Rubio, P., Hercog, R., Jung, F., Kandels, S., … Bork, P. (2022). A faecal microbiota signature with high specificity for pancreatic cancer. *Gut*, *71*(7). https://doi.org/10.1136/gutjnl-2021-324755

Kaup, M., Dassler, K., Weise, C., & Fuchs, H. (2002). Shedding of the transferrin receptor is mediated constitutively by an integral membrane metalloprotease sensitive to tumor necrosis factor α protease inhibitor-2. *Journal of Biological Chemistry*, *277*(41), 38494–38502. https://doi.org/10.1074/jbc.M203461200

Kawashima, K., Andreata, F., Beccaria, C. G., & Iannacone, M. (2024). Priming and Maintenance of Adaptive Immunity in the Liver. *Annual Review of Immunology*, *42*(1), 375–399. https://doi.org/10.1146/ANNUREV-IMMUNOL-090122-041354

Kedmi, R., & Littman, D. R. (2024). Antigen-presenting cells as specialized drivers of intestinal T cell functions. *Immunity*, *57*(10), 2269–2279. https://doi.org/10.1016/j.immuni.2024.09.011

Keir, M. E., Yi, T., Lu, T. T., & Ghilardi, N. (2020). The role of IL-22 in intestinal health and disease. *Journal of Experimental Medicine*, *217*(3). https://doi.org/10.1084/jem.20192195

Kinnebrew, M. A., Buffie, C. G., Diehl, G. E., Zenewicz, L. A., Leiner, I., Hohl, T. M., Flavell, R. A., Littman, D. R., & Pamer, E. G. (2012). Interleukin 23 Production by Intestinal CD103 +CD11b + Dendritic Cells in Response to Bacterial Flagellin Enhances Mucosal Innate Immune Defense. *Immunity*, *36*(2). https://doi.org/10.1016/j.immuni.2011.12.011

Kitamoto, Y., Yuan, X., Wu, Q., McCourt, D. W., & Sadler, J. E. (1994). Enterokinase, the initiator of intestinal digestion, is a mosaic protease composed of a distinctive assortment of domains. *Proceedings of the National Academy of Sciences of the United States of America*, *91*(16). https://doi.org/10.1073/pnas.91.16.7588

Kobayashi, T., Antar, A. A. R., Boehme, K. W., Danthi, P., Eby, E. A., Guglielmi, K. M., Holm, G. H., Johnson, E. M., Maginnis, M. S., Naik, S., Skelton, W. B., Wetzel, J. D., Wilson, G. J., Chappell, J. D., & Dermody, T. S. (2007). A Plasmid-Based Reverse Genetics System for Animal Double-Stranded RNA Viruses. *Cell Host & Microbe*, *1*(2), 147. https://doi.org/10.1016/J.CHOM.2007.03.003

Kubisch, C. H., & Logsdon, C. D. (2008). Endoplasmic reticulum stress and the pancreatic acinar cell. *Expert Review of Gastroenterology and Hepatology*, *2*(2), 249–260. https://doi.org/10.1586/17474124.2.2.249;JOURNAL:JOURNAL:IERH20

Kurashima, Y., Kigoshi, T., Murasaki, S., Arai, F., Shimada, K., Seki, N., Kim, Y. G., Hase, K., Ohno, H., Kawano, K., Ashida, H., Suzuki, T., Morimoto, M., Saito, Y., Sasou, A., Goda, Y., Yuki, Y., Inagaki, Y., Iijima, H., … Kiyono, H. (2021). Pancreatic glycoprotein 2 is a first line of defense for mucosal protection in intestinal inflammation. *Nature Communications*, *12*(1). https://doi.org/10.1038/s41467-021-21277-2

Kurts, C., Heath, W. R., Carbone, F. R., Allison, J., Miller, J. F. A. F., Kosaka, H., & Victoria. (1996). Constitutive class I-restricted exogenous presentation of self antigens in vivo. *The Journal of Experimental Medicine*, *184*(3), 923. https://doi.org/10.1084/JEM.184.3.923

Kuwada, T., Shiokawa, M., Kodama, Y., Ota, S., Kakiuchi, N., Nannya, Y., Yamazaki, H., Yoshida, H., Nakamura, T., Matsumoto, S., Muramoto, Y., Yamamoto, S., Honzawa, Y., Kuriyama, K., Okamoto, K., Hirano, T., Okada, H., Marui, S., Sogabe, Y., … Seno, H. (2021). Identification of an Anti–Integrin αvβ6 Autoantibody in Patients With Ulcerative Colitis. *Gastroenterology*, *160*(7), 2383-2394.e21. https://doi.org/10.1053/j.gastro.2021.02.019

Lanford, R. E., Feng, Z., Chavez, D., Guerra, B., Brasky, K. M., Zhou, Y., Yamane, D., Perelson, A. S., Walker, C. M., & Lemon, S. M. (2011). Acute hepatitis A virus infection is associated with a limited type I interferon response and persistence of intrahepatic viral RNA. *Proceedings of the National Academy of Sciences of the United States of America*, *108*(27), 11223–11228. https://doi.org/10.1073/PNAS.1101939108

Li, Q., Wang, H., Zogopoulos, G., Shao, Q., Dong, K., Lv, F., Nwilati, K., Gui, X. Y., Cuggia, A., Liu, J. L., & Gao, Z. H. (2016). Reg proteins promote acinar-to-ductal metaplasia and act as novel diagnostic and prognostic markers in pancreatic ductal adenocarcinoma. *Oncotarget*, *7*(47). https://doi.org/10.18632/oncotarget.12834

Li, Y., Watanabe, E., Kawashima, Y., Plichta, D. R., Wang, Z., Ujike, M., Ang, Q. Y., Wu, R., Furuichi, M., Takeshita, K., Yoshida, K., Nishiyama, K., Kearney, S. M., Suda, W., Hattori,

M., Sasajima, S., Matsunaga, T., Zhang, X., Watanabe, K., … Honda, K. (2022). Identification of trypsin-degrading commensals in the large intestine. *Nature*, *609*(7927). https://doi.org/10.1038/s41586-022-05181-3

Li, Z. W., & Shaw, G. S. (2023). Role of calcium-sensor proteins in cell membrane repair. In *Bioscience Reports* (Vol. 43, Number 2). https://doi.org/10.1042/BSR20220765

Liu, T. T., Kim, S., Desai, P., Kim, D. H., Huang, X., Ferris, S. T., Wu, R., Ou, F., Egawa, T., Van Dyken, S. J., Diamond, M. S., Johnson, P. F., Kubo, M., Murphy, T. L., & Murphy, K. M. (2022). Ablation of cDC2 development by triple mutations within the Zeb2 enhancer. *Nature*, *607*(7917), 142–148. https://doi.org/10.1038/S41586-022-04866-Z

Liu, X., Wang, J., Wang, H., Yin, G., Liu, Y., Lei, X., & Xiang, M. (2015). REG3A accelerates pancreatic cancer cell growth under IL-6-associated inflammatory condition: Involvement of a REG3A-JAK2/STAT3 positive feedback loop. *Cancer Letters*, *362*(1). https://doi.org/10.1016/j.canlet.2015.03.014

Liu, X., Zhou, Z., Cheng, Q., Wang, H., Cao, H., Xu, Q., Tuo, Y., Jiang, L., Zou, Y., Ren, H., & Xiang, M. (2017). Acceleration of pancreatic tumorigenesis under immunosuppressive microenvironment induced by reg3g overexpression. *Cell Death and Disease*, *8*(9). https://doi.org/10.1038/cddis.2017.424

Luberto, C., Hassler, D. F., Signorelli, P., Okamoto, Y., Sawai, H., Boros, E., Hazen-Martin, D. J., Obeid, L. M., Hannun, Y. A., & Smith, G. K. (2002). Inhibition of Tumor Necrosis Factor-induced Cell Death in MCF7 by a Novel Inhibitor of Neutral Sphingomyelinase. *Journal of Biological Chemistry*, *277*(43), 41128–41139. https://doi.org/10.1074/JBC.M206747200

Malherbe, L., Hausl, C., Teyton, L., & McHeyzer-Williams, M. G. (2004). Clonal selection of helper T cells is determined by an affinity threshold with no further skewing of TCR binding properties. *Immunity*, *21*(5), 669–679. https://doi.org/10.1016/j.immuni.2004.09.008

Marlies Ballegeer and Claude Libert. (2016). Different Cell Types Involved in Mediating Concanavalin A Induced Liver Injury: A Comprehensive Overview. *Gastroenterology & Hepatology Research*, *1*(1), 1–13. https://doi.org/10.24966/GHR-2566/100001

Mashayekhi, M., Sandau, M. M., Dunay, I. R., Frickel, E. M., Khan, A., Goldszmid, R. S., Sher, A., Ploegh, H. L., Murphy, T. L., Sibley, L. D., & Murphy, K. M. (2011). CD8α+ Dendritic Cells Are the Critical Source of Interleukin-12 that Controls Acute Infection by Toxoplasma gondii Tachyzoites. *Immunity*, *35*(2), 249–259. https://doi.org/10.1016/j.immuni.2011.08.008

McAllister, F., Bailey, J. M., Alsina, J., Nirschl, C. J., Sharma, R., Fan, H., Rattigan, Y., Roeser, J. C., Lankapalli, R. H., Zhang, H., Jaffee, E. M., Drake, C. G., Housseau, F., Maitra, A., Kolls, J. K., Sears, C. L., Pardoll, D. M., & Leach, S. D. (2014). Oncogenic kras activates a

hematopoietic-to-epithelial IL-17 signaling axis in preinvasive pancreatic neoplasia. *Cancer Cell*, *25*(5). https://doi.org/10.1016/j.ccr.2014.03.014

MCCUTCHEON, A. D. (1964). Reflux of duodenal contents in the pathogenesis of pancreatitis. *Gut*, *5*(3), 260. https://doi.org/10.1136/GUT.5.3.260

Medina Sanchez, L., Siller, M., Zeng, Y., Brigleb, P. H., Sangani, K. A., Soto, A. S., Engl, C., Laughlin, C. R., Rana, M., Van Der Kraak, L., Pandey, S. P., Bender, M. J., Fitzgerald, B., Hedden, L., Fiske, K., Taylor, G. M., Wright, A. P., Mehta, I. D., Rahman, S. A., … Hinterleitner, R. (2023). The gut protist Tritrichomonas arnold restrains virus-mediated loss of oral tolerance by modulating dietary antigen-presenting dendritic cells. *Immunity*, *56*(8), 1862-1875.e9. https://doi.org/10.1016/J.IMMUNI.2023.06.022

Minutti, C. M., Piot, C., Pereira da Costa, M., Chakravarty, P., Rogers, N., Huerga Encabo, H., Cardoso, A., Loong, J., Bessou, G., Mionnet, C., Langhorne, J., Bonnet, D., Dalod, M., Tomasello, E., & Reis e Sousa, C. (2024). Distinct ontogenetic lineages dictate cDC2 heterogeneity. *Nature Immunology*, *25*(3), 448–461. https://doi.org/10.1038/S41590-024-01745-9;SUBJMETA

Möller, K., Jenssen, C., Braden, B., Hocke, M., Hollerbach, S., Ignee, A., Faiss, S., Iglesias-Garcia, J., Sun, S., Dong, Y., Carrara, S., & Dietrich, C. F. (2023). Pancreatic changes with lifestyle and age: What is normal and what is concerning? In *Endoscopic Ultrasound* (Vol. 12, Number 2). https://doi.org/10.4103/EUS-D-22-00162

Mukherjee, S., Partch, C. L., Lehotzky, R. E., Whitham, C. V., Chu, H., Bevins, C. L., Gardner, K. H., & Hooper, L. V. (2009). Regulation of C-type lectin antimicrobial activity by a flexible N-terminal prosegment. *Journal of Biological Chemistry*, *284*(8). https://doi.org/10.1074/jbc.M808077200

Mukherjee, S., Zheng, H., Derebe, M. G., Callenberg, K. M., Partch, C. L., Rollins, D., Propheter, D. C., Rizo, J., Grabe, M., Jiang, Q. X., & Hooper, L. V. (2014). Antibacterial membrane attack by a pore-forming intestinal C-type lectin. *Nature*, *505*(7481). https://doi.org/10.1038/nature12729

Murphy, T. L., Grajales-Reyes, G. E., Wu, X., Tussiwand, R., Briseño, C. G., Iwata, A., Kretzer, N. M., Durai, V., & Murphy, K. M. (2016). Transcriptional Control of Dendritic Cell Development. *Annual Review of Immunology*, *34*, 93–119. https://doi.org/10.1146/ANNUREV-IMMUNOL-032713-120204

Nadatani, Y., Watanabe, T., Suda, W., Nakata, A., Matsumoto, Y., Kosaka, S., Higashimori, A., Otani, K., Hosomi, S., Tanaka, F., Nagami, Y., Kamata, N., Taira, K., Yamagami, H., Tanigawa, T., Hattori, M., & Fujiwara, Y. (2019). Gastric acid inhibitor aggravates indomethacin-induced small intestinal injury via reducing Lactobacillus johnsonii. *Scientific Reports*, *9*(1), 1–11. https://doi.org/10.1038/S41598-019-53559-7;TECHMETA

Nygaard, R. M., Lahti, L., Boehme, K. W., Ikizler, M., Doyle, J. D., Dermody, T. S., & Schiff, L. A. (2013). Genetic Determinants of Reovirus Pathogenesis in a Murine Model of Respiratory Infection. *Journal of Virology*, *87*(16), 9279–9289. https://doi.org/10.1128/JVI.00182-13;PAGEGROUP:STRING:PUBLICATION

Okamoto, H. (1999). The Reg gene family and Reg proteins: With special attention to the regeneration of pancreatic β-cells. *Journal of Hepato-Biliary-Pancreatic Surgery*, *6*(3). https://doi.org/10.1007/s005340050115

Pabst, O., & Mowat, A. M. (2012). Oral tolerance to food protein. *Mucosal Immunology*, *5*(3), 232–239. https://doi.org/10.1038/mi.2012.4

Pandol, S. J., Saluja, A. K., Imrie, C. W., & Banks, P. A. (2007). Acute Pancreatitis: Bench to the Bedside. *Gastroenterology*, *132*(3), 1127–1151. https://doi.org/10.1053/j.gastro.2007.01.055

Pao, W., Ooi, C. H., Birzele, F., Ruefli-Brasse, A., Cannarile, M. A., Reis, B., Scharf, S. H., Schubert, D. A., Hatje, K., Pelletier, N., Spleiss, O., & Reed, J. C. (2018). Tissue-specific immunoregulation: A call for better understanding of the "immunostat" in the context of cancer. *Cancer Discovery*, *8*(4), 395–402. https://doi.org/10.1158/2159-8290.CD-17-1320/333631/P/TISSUE-SPECIFIC-IMMUNOREGULATION-A-CALL-FOR-BETTER

Parikh, A., Stephan, A. F., & Tzanakakis, E. S. (2012). Regenerating proteins and their expression, regulation, and signaling. In *Biomolecular Concepts* (Vol. 3, Number 1). https://doi.org/10.1515/bmc.2011.055

Parisotto, Y. F., Cabric, V., Park, T., Akagbosu, B., Zhao, Z., Lo, Y., Fisher, L., Shibu, G., Paucar Iza, Y. A., Leslie, C., & Brown, C. C. (2024). *Thetis cells induce food-specific Treg cell differentiation and oral tolerance*. https://doi.org/10.1101/2024.05.08.592952

Perusina Lanfranca, M., Zhang, Y., Girgis, A., Kasselman, S., Lazarus, J., Kryczek, I., Delrosario, L., Rhim, A., Koneva, L., Sartor, M., Sun, L., Halbrook, C., Nathan, H., Shi, J., Crawford, H. C., Pasca di Magliano, M., Zou, W., & Frankel, T. L. (2020). Interleukin 22 Signaling Regulates Acinar Cell Plasticity to Promote Pancreatic Tumor Development in Mice. *Gastroenterology*, *158*(5). https://doi.org/10.1053/j.gastro.2019.12.010

Pushalkar, S., Hundeyin, M., Daley, D., Zambirinis, C. P., Kurz, E., Mishra, A., Mohan, N., Aykut, B., Usyk, M., Torres, L. E., Werba, G., Zhang, K., Guo, Y., Li, Q., Akkad, N., Lall, S., Wadowski, B., Gutierrez, J., Rossi, J. A. K., … Miller, G. (2018). The pancreatic cancer microbiome promotes oncogenesis by induction of innate and adaptive immune suppression. *Cancer Discovery*, *8*(4). https://doi.org/10.1158/2159-8290.CD-17-1134

Riquelme, E., Zhang, Y., Zhang, L., Montiel, M., Zoltan, M., Dong, W., Quesada, P., Sahin, I., Chandra, V., San Lucas, A., Scheet, P., Xu, H., Hanash, S. M., Feng, L., Burks, J. K., Do, K.-A., Peterson, C. B., Nejman, D., Tzeng, C.-W. D., … McAllister, F. (2019). Tumor

Microbiome Diversity and Composition Influence Pancreatic Cancer Outcomes. *Cell*. https://doi.org/10.1016/j.cell.2019.07.008

Rodrigues, P. F., Wu, S., Trsan, T., Panda, S. K., Fachi, J. L., Liu, Y., Du, S., de Oliveira, S., Antonova, A. U., Khantakova, D., Sudan, R., Desai, P., Diamond, M. S., Gilfillan, S., Anderson, S. K., Cella, M., & Colonna, M. (2025). Rorγt-positive dendritic cells are required for the induction of peripheral regulatory T cells in response to oral antigens. *Cell*, *188*(10), 2720-2737.e22. https://doi.org/10.1016/j.cell.2025.03.020

Rojas, M., Restrepo-Jiménez, P., Monsalve, D. M., Pacheco, Y., Acosta-Ampudia, Y., Ramírez-Santana, C., Leung, P. S. C., Ansari, A. A., Gershwin, M. E., & Anaya, J. M. (2018). Molecular mimicry and autoimmunity. *Journal of Autoimmunity*, *95*(4), 100–123. https://doi.org/10.1016/j.jaut.2018.10.012

Rooman, I., & Real, F. X. (2012). Pancreatic ductal adenocarcinoma and acinar cells: a matter of differentiation and development? *Gut*, *61*(3), 449–458. https://doi.org/10.1136/GUT.2010.235804

Rudnitsky, A., Oh, H., Margolin, M., Dassa, B., Shteinberg, I., Stoler-Barak, L., Shulman, Z., & Kedmi, R. (2025). A coordinated cellular network regulates tolerance to food. *Nature 2025 644:8075*, *644*(8075), 231–240. https://doi.org/10.1038/s41586-025-09173-x

Russell, A., Copio, J. N., Shi, Y., Kang, S., Franklin, C. L., & Ericsson, A. C. (2022). Reduced housing density improves statistical power of murine gut microbiota studies. *Cell Reports*, *39*(6). https://doi.org/10.1016/j.celrep.2022.110783

Sabat, R., Ouyang, W., & Wolk, K. (2014). Therapeutic opportunities of the IL-22-IL-22R1 system. In *Nature Reviews Drug Discovery* (Vol. 13, Number 1). https://doi.org/10.1038/nrd4176

Sabihi, M., Böttcher, M., Pelczar, P., & Huber, S. (2020). Microbiota-dependent effects of IL-22. In *Cells* (Vol. 9, Number 10). https://doi.org/10.3390/cells9102205

Sano, T., Huang, W., Hall, J. A., Yang, Y., Chen, A., Gavzy, S. J., Lee, J. Y., Ziel, J. W., Miraldi, E. R., Domingos, A. I., Bonneau, R., & Littman, D. R. (2015). An IL-23R/IL-22 Circuit Regulates Epithelial Serum Amyloid A to Promote Local Effector Th17 Responses. *Cell*, *163*(2), 381–393. https://doi.org/10.1016/j.cell.2015.08.061

Satpathy, A. T., Briseño, C. G., Lee, J. S., Ng, D., Manieri, N. A., Kc, W., Wu, X., Thomas, S. R., Lee, W. L., Turkoz, M., McDonald, K. G., Meredith, M. M., Song, C., Guidos, C. J., Newberry, R. D., Ouyang, W., Murphy, T. L., Stappenbeck, T. S., Gommerman, J. L., … Murphy, K. M. (2013). Notch2-dependent classical dendritic cells orchestrate intestinal immunity against attaching and effacing bacterial pathogens. *Nature Immunology*, *14*(9), 937. https://doi.org/10.1038/NI.2679

Schiering, C., Wincent, E., Metidji, A., Iseppon, A., Li, Y., Potocnik, A. J., Omenetti, S., Henderson, C. J., Wolf, C. R., Nebert, D. W., & Stockinger, B. (2017). Feedback control of AHR signalling regulates intestinal immunity. *Nature*, *542*(7640), 242–245.

Schlesinger, Y., Yosefov-Levi, O., Kolodkin-Gal, D., Granit, R. Z., Peters, L., Kalifa, R., Xia, L., Nasereddin, A., Shiff, I., Amran, O., Nevo, Y., Elgavish, S., Atlan, K., Zamir, G., & Parnas, O. (2020). Single-cell transcriptomes of pancreatic preinvasive lesions and cancer reveal acinar metaplastic cells' heterogeneity. *Nature Communications*, *11*(1). https://doi.org/10.1038/s41467-020-18207-z

Schnitger, A. K. D., Yassine, H., Kafatos, F. C., & Osta, M. A. (2009). Two C-type lectins cooperate to defend Anopheles gambiae against Gram-negative bacteria. *Journal of Biological Chemistry*, *284*(26). https://doi.org/10.1074/jbc.M808298200

Seki, N., Miyazaki, M., Suzuki, W., Hayashi, K., Arima, K., Myburgh, E., Izuhara, K., Brombacher, F., & Kubo, M. (2004). IL-4-induced GATA-3 expression is a time-restricted instruction switch for Th2 cell differentiation. *Journal of Immunology (Baltimore, Md. : 1950)*, *172*(10), 6158–6166. https://doi.org/10.4049/JIMMUNOL.172.10.6158

Sendler, M., & Lerch, M. M. (2020). The Complex Role of Trypsin in Pancreatitis. In *Gastroenterology* (Vol. 158, Number 4). https://doi.org/10.1053/j.gastro.2019.12.025

Shaw, M. H., Kamada, N., Kim, Y. G., & Núñez, G. (2012). Microbiota-induced IL-1β, but not IL-6, is critical for the development of steady-state T H17 cells in the intestine. *Journal of Experimental Medicine*, *209*(2). https://doi.org/10.1084/jem.20111703

Shin, J. H., Bozadjieva-Kramer, N., Shao, Y., Lyons-Abbott, S., Rupp, A. C., Sandoval, D. A., & Seeley, R. J. (2022). The gut peptide Reg3g links the small intestine microbiome to the regulation of energy balance, glucose levels, and gut function. *Cell Metabolism*, *34*(11). https://doi.org/10.1016/j.cmet.2022.09.024

Solà Tapias, N., Denadai-Souza, A., Rolland-Fourcade, C., Quaranta-Nicaise, M., Blanpied, C., Marcellin, M., Edir, A., Rolland, C., Cirillo, C., Dietrich, G., Alric, L., Portier, G., Kirzin, S., Bonnet, D., Mas, E., Burlet-Schiltz, O., Deraison, C., Bonnart, C., Vergnolle, N., & Barreau, F. (2021). Colitis Linked to Endoplasmic Reticulum Stress Induces Trypsin Activity Affecting Epithelial Functions. *Journal of Crohn's and Colitis*, *15*(9). https://doi.org/10.1093/ecco-jcc/jjab035

Steele, N. G., Carpenter, E. S., Kemp, S. B., Sirihorachai, V. R., The, S., Delrosario, L., Lazarus, J., Amir, E. ad D., Gunchick, V., Espinoza, C., Bell, S., Harris, L., Lima, F., Irizarry-Negron, V., Paglia, D., Macchia, J., Chu, A. K. Y., Schofield, H., Wamsteker, E. J., … Pasca di Magliano, M. (2020). Multimodal mapping of the tumor and peripheral blood immune landscape in human pancreatic cancer. *Nature Cancer*, *1*(11). https://doi.org/10.1038/s43018-020-00121-4

Stefka, A. T., Feehley, T., Tripathi, P., Qiu, J., McCoy, K., Mazmanian, S. K., Tjota, M. Y., Seo, G. Y., Cao, S., Theriault, B. R., Antonopoulos, D. A., Zhou, L., Chang, E. B., Fu, Y. X., & Nagler, C. R. (2014). Commensal bacteria protect against food allergen sensitization. *Proceedings of the National Academy of Sciences of the United States of America*, *111*(36). https://doi.org/10.1073/pnas.1412008111

Stelter, C., Käppeli, R., König, C., Krah, A., Hardt, W. D., Stecher, B., & Bumann, D. (2011). Salmonella-induced mucosal lectin RegIIIβ kills competing gut microbiota. *PLoS ONE*, *6*(6). https://doi.org/10.1371/journal.pone.0020749

Sun, C., Wang, X., Hui, Y., Fukui, H., Wang, B., & Miwa, H. (2021). The Potential Role of REG Family Proteins in Inflammatory and Inflammation-Associated Diseases of the Gastrointestinal Tract. *International Journal of Molecular Sciences*, *22*(13). https://doi.org/10.3390/IJMS22137196

Tan, C., Ling, Z., Huang, Y., Cao, Y., Liu, Q., Cai, T., Yuan, H., Liu, C., Li, Y., & Xu, K. (2015). Dysbiosis of intestinal microbiota associated with inflammation involved in the progression of acute pancreatitis. *Pancreas*, *44*, 868–875. https://doi.org/10.1097/MPA.0000000000000355

Taylor, T. V., & Rimmer, S. (1980). PANCREATIC-DUCT REFLUX IN PATIENTS WITH GALLSTONE PANCREATITIS? *The Lancet*, *315*(8173), 848–850. https://doi.org/10.1016/S0140-6736(80)91354-9

Thomas, R. M., Gharaibeh, R. Z., Gauthier, J., Beveridge, M., Pope, J. L., Guijarro, M. V., Yu, Q., He, Z., Ohland, C., Newsome, R., Trevino, J., Hughes, S. J., Reinhard, M., Winglee, K., Fodor, A. A., Zajac-Kaye, M., & Jobin, C. (2018). Intestinal microbiota enhances pancreatic carcinogenesis in preclinical models. *Carcinogenesis*, *39*(8). https://doi.org/10.1093/carcin/bgy073

Thomas, R. M., & Jobin, C. (2020). Microbiota in pancreatic health and disease: the next frontier in microbiome research. *Nature Reviews Gastroenterology and Hepatology*, *17*(1). https://doi.org/10.1038/s41575-019-0242-7

Thomson, A. W., & Knolle, P. A. (2010). Antigen-presenting cell function in the tolerogenic liver environment. *Nature Reviews. Immunology*, *10*(11), 753–766. https://doi.org/10.1038/NRI2858

Tomasiewicz, K., Modrzewska, R., Lyczak, A., & Krawczuk, G. (2005). TT virus infection and pancreatic cancer: Relationship or accidental coexistence. *World Journal of Gastroenterology : WJG*, *11*(18), 2847. https://doi.org/10.3748/WJG.V11.I18.2847

Tripathi, A., Debelius, J., Brenner, D. A., Karin, M., Loomba, R., Schnabl, B., & Knight, R. (2018). The gut-liver axis and the intersection with the microbiome. *Nature Reviews. Gastroenterology & Hepatology*, *15*(7), 397–411. https://doi.org/10.1038/S41575-018-0011-Z

Tsuchida, C., Sakuramoto-Tsuchida, S., Taked, M., Itaya-Hironaka, A., Yamauchi, A., Misu, M., Shobatake, R., Uchiyama, T., Makino, M., Pujol-Autonell, I., Vives-Pi, M., Ohbayashi, C., & Takasawa, S. (2017). Expression of REG family genes in human inflammatory bowel diseases and its regulation. *Biochemistry and Biophysics Reports*, *12*. https://doi.org/10.1016/j.bbrep.2017.10.003

Tussiwand, R., Everts, B., Grajales-Reyes, G. E., Kretzer, N. M., Iwata, A., Bagaitkar, J., Wu, X., Wong, R., Anderson, D. A., Murphy, T. L., Pearce, E. J., & Murphy, K. M. (2015). Klf4 expression in conventional dendritic cells is required for T helper 2 cell responses. *Immunity*, *42*(5), 916. https://doi.org/10.1016/J.IMMUNI.2015.04.017

Ullman, N. A., Burchard, P. R., Dunne, R. F., & Linehan, D. C. (2022). Immunologic Strategies in Pancreatic Cancer: Making Cold Tumors Hot. *Journal of Clinical Oncology*, *40*(24), 2789–2805. https://doi.org/10.1200/JCO.21.02616

Vaishnava, S., Yamamoto, M., Severson, K. M., Ruhn, K. A., Yu, X., Koren, O., Ley, R., Wakeland, E. K., & Hooper, L. V. (2011a). The antibacterial lectin RegIIIgamma promotes the spatial segregation of microbiota and host in the intestine. *Science (New York, N.Y.)*, *334*(6053), 255–258. https://doi.org/10.1126/SCIENCE.1209791

Vento, S., Bottazzo, G., Williams, R., Hegarty, J. E., Macchia, E., & Eddleston, A. L. W. F. (1984). ANTIGEN SPECIFIC SUPPRESSOR CELL FUNCTION IN AUTOIMMUNE CHRONIC ACTIVE HEPATITIS. *The Lancet*, *323*(8388), 1200–1204. https://doi.org/10.1016/S0140-6736(84)91691-X

Vezys, V., Olson, S., & Lefrançois, L. (2000). Expression of intestine-specific antigen reveals novel pathways of CD8 T cell tolerance induction. *Immunity*, *12*(5), 505–514. https://doi.org/10.1016/S1074-7613(00)80202-2

Wang, G.-P. (2010). Pancreatic secretory trypsin inhibitor: More than a trypsin inhibitor. *World Journal of Gastrointestinal Pathophysiology*, *1*(2). https://doi.org/10.4291/wjgp.v1.i2.85

Wang, J., Zhao, X., & Wan, Y. Y. (2023). Intricacies of TGF-β signaling in Treg and Th17 cell biology. *Cellular & Molecular Immunology 2023 20:9*, *20*(9), 1002–1022. https://doi.org/10.1038/s41423-023-01036-7

Wang, S., Liu, C., Yang, C., Jin, Y., Cui, Q., Wang, D., Ge, T., He, G., Li, W., Zhang, G., Liu, A., Xia, Y., Liu, Y., & Yu, J. (2024). PI3K/AKT/mTOR and PD-1/CTLA-4/CD28 pathways as key targets of cancer immunotherapy (Review). *Oncology Letters*, *28*(6), 1–8. https://doi.org/10.3892/OL.2024.14700/HTML

Wang, Y., Yin, Y., Chen, X., Zhao, Y., Wu, Y., Li, Y., Wang, X., Chen, H., & Xiang, C. (2019). Induction of Intestinal Th17 Cells by Flagellins From Segmented Filamentous Bacteria. *Frontiers in Immunology*, *10*. https://doi.org/10.3389/fimmu.2019.02750

Weis, W. I., & Drickamer, K. (1996). Structural basis of lectin-carbohydrate recognition. In *Annual Review of Biochemistry* (Vol. 65). https://doi.org/10.1146/annurev.bi.65.070196.002301

Weis, W. I., Kahn, R., Fourme, R., Drickamer, K., & Hendrickson, W. A. (1991). Structure of the calcium-dependent lectin domain from a rat mannose-binding protein determined by MAD phasing. *Science*, *254*(5038). https://doi.org/10.1126/science.1721241

Weisberg, S. P., Ural, B. B., & Farber, D. L. (2021). Tissue-specific immunity for a changing world. *Cell*, *184*(6), 1517–1529. https://doi.org/10.1016/J.CELL.2021.01.042

Winer, B. Y., Ding, Q., Gaska, J. M., & Ploss, A. (2016). In vivo models of hepatitis B and C virus infection. *FEBS Letters*, *590*(13), 1987–1999. https://doi.org/10.1002/1873-3468.12157

Wu, C., Li, M., & Chen, W. (2021). Characteristics of gut microbiota in cerulein-induced chronic pancreatitis. *Diabetes, Metabolic Syndrome and Obesity: Targets and Therapy*, *14*. https://doi.org/10.2147/DMSO.S291822

Wu-Woods, N. J., Barlow, J. T., Trigodet, F., Shaw, D. G., Romano, A. E., Jabri, B., Eren, A. M., & Ismagilov, R. F. (2023). Microbial-enrichment method enables high-throughput metagenomic characterization from host-rich samples. *Nature Methods*, *20*(11), 1672–1682. https://doi.org/10.1038/s41592-023-02025-4

Xiao, H., Ulmert, I., Bach, L., Huber, J., Narasimhan, H., Kurochkin, I., Chang, Y., Holst, S., Mörbe, U., Zhang, L., Schlitzer, A., Pereira, C. F., Schraml, B. U., Baumjohann, D., & Lahl, K. (2024). Genomic deletion of Bcl6 differentially affects conventional dendritic cell subsets and compromises Tfh/Tfr/Th17 cell responses. *Nature Communications 2024 15:1*, *15*(1), 3554-. https://doi.org/10.1038/s41467-024-46966-6

Xie, M. J., Motoo, Y., Iovanna, J. L., Su, S. B., Ohtsubo, K., Matsubara, F., & Sawabu, N. (2003). Overexpression of pancreatitis-associated protein (PAP) in human pancreatic ductal adenocarcinoma. *Digestive Diseases and Sciences*. https://doi.org/10.1023/A:1022520212447

Xing, Y., & Hogquist, K. A. (2012). T-Cell Tolerance: Central and Peripheral. *Cold Spring Harbor Perspectives in Biology*, *4*(6), a006957. https://doi.org/10.1101/CSHPERSPECT.A006957

Xu, M., Pokrovskii, M., Ding, Y., Yi, R., Au, C., Harrison, O. J., Galan, C., Belkaid, Y., Bonneau, R., & Littman, D. R. (2018). C-MAF-dependent regulatory T cells mediate immunological tolerance to a gut pathobiont. *Nature*, *554*(7692), 373–377. https://doi.org/10.1038/NATURE25500;TECHMETA

Yamashita, T., Iwakura, T., Matsui, K., Kawaguchi, H., Obana, M., Hayama, A., Maeda, M., Izumi, Y., Komuro, I., Ohsugi, Y., Fujimoto, M., Naka, T., Kishimoto, T., Nakayama, H., &

Fujio, Y. (2011). IL-6-mediated Th17 differentiation through RORγt is essential for the initiation of experimental autoimmune myocarditis. *Cardiovascular Research*, *91*(4), 640–648. https://doi.org/10.1093/CVR/CVR148

Yang, L., Qiao, S., Zhang, G., Lu, A., & Li, F. (2024). Inflammatory Processes: Key Mediators of Oncogenesis and Progression in Pancreatic Ductal Adenocarcinoma (PDAC). *International Journal of Molecular Sciences*, *25*(20), 10991. https://doi.org/10.3390/IJMS252010991

Yang, W., Yu, T., Huang, X., Bilotta, A. J., Xu, L., Lu, Y., Sun, J., Pan, F., Zhou, J., Zhang, W., Yao, S., Maynard, C. L., Singh, N., Dann, S. M., Liu, Z., & Cong, Y. (2020). Intestinal microbiota-derived short-chain fatty acids regulation of immune cell IL-22 production and gut immunity. *Nature Communications*, *11*(1). https://doi.org/10.1038/s41467-020-18262-6

Yang, Y., Torchinsky, M. B., Gobert, M., Xiong, H., Xu, M., Linehan, J. L., Alonzo, F., Ng, C., Chen, A., Lin, X., Sczesnak, A., Liao, J. J., Torres, V. J., Jenkins, M. K., Lafaille, J. J., & Littman, D. R. (2014). Focused specificity of intestinal TH17 cells towards commensal bacterial antigens. *Nature*, *510*(7503), 152–156. https://doi.org/10.1038/NATURE13279;TECHMETA

Yin, G., Du, J., Cao, H., Liu, X., Xu, Q., & Xiang, M. (2015). Reg3g Promotes Pancreatic Carcinogenesis in a Murine Model of Chronic Pancreatitis. *Digestive Diseases and Sciences*, *60*(12). https://doi.org/10.1007/s10620-015-3787-5

Zehn, D., Lee, S. Y., & Bevan, M. J. (2009). Complete but curtailed T-cell response to very low-affinity antigen. *Nature*, *458*(7235), 211–214. https://doi.org/10.1038/NATURE07657

Zelensky, A. N., & Gready, J. E. (2005). The C-type lectin-like domain superfamily. In *FEBS Journal* (Vol. 272, Number 24). https://doi.org/10.1111/j.1742-4658.2005.05031.x

Zenewicz, L. A. (2018). IL-22: There Is a Gap in Our Knowledge. *ImmunoHorizons*, *2*(6). https://doi.org/10.4049/immunohorizons.1800006

Zhang, H., Corredor, A. L. G., Messina-Pacheco, J., Li, Q., Zogopoulos, G., Kaddour, N., Wang, Y., Shi, B. yin, Gregorieff, A., Liu, J. li, & Gao, Z. hua. (2021). REG3A/REG3B promotes acinar to ductal metaplasia through binding to EXTL3 and activating the RAS-RAF-MEK-ERK signaling pathway. *Communications Biology*, *4*(1). https://doi.org/10.1038/s42003-021-02193-z

Zhang, J., Li, R., & Huang, S. (2022). The immunoregulation effect of tumor microenvironment in pancreatic ductal adenocarcinoma. *Frontiers in Oncology*, *12*, 951019. https://doi.org/10.3389/FONC.2022.951019

Zheng, H. C., Sugawara, A., Okamoto, H., Takasawa, S., Takahashi, H., Masuda, S., & Takano, Y. (2011). Expression profile of the REG gene family in colorectal carcinoma. *Journal of Histochemistry and Cytochemistry*, *59*(1). https://doi.org/10.1369/jhc.2010.956961

Zheng, Y., Valdez, P. A., Danilenko, D. M., Hu, Y., Sa, S. M., Gong, Q., Abbas, A. R., Modrusan, Z., Ghilardi, N., De Sauvage, F. J., & Ouyang, W. (2008a). Interleukin-22 mediates early host defense against attaching and effacing bacterial pathogens. *Nature Medicine*, *14*(3), 282–289. https://doi.org/10.1038/NM1720

Zhou, Y. D., Brown, H., Schaffer, E., Taylor, G. M., Fiske, K. L., Komnick, M. R., Lopez, S., Dermody, T. S., & Esterhazy, D. (2025). T cell fate is dictated by different antigen presenting cells in response to dietary versus gut epithelial self-antigen. *BioRxiv*, 2025.11.06.687030. https://doi.org/10.1101/2025.11.06.687030

Zhu, J., Jankovic, D., Oler, A. J., Wei, G., Sharma, S., Hu, G., Guo, L., Yagi, R., Yamane, H., Punkosdy, G., Feigenbaum, L., Zhao, K., & Paul, W. E. (2012). The Transcription Factor T-bet Is Induced by Multiple Pathways and Prevents an Endogenous Th2 Cell Program during Th1 Cell Responses. *Immunity*, *37*(4), 660–673. https://doi.org/10.1016/j.immuni.2012.09.007

Zhu, J., & Paul, W. E. (2010). Peripheral CD4+ T-cell differentiation regulated by networks of cytokines and transcription factors. *Immunological Reviews*, *238*(1), 247–262. https://doi.org/10.1111/J.1600-065X.2010.00951.X

Zhu, Y., He, C., Li, X., Cai, Y., Hu, J., Liao, Y., Zhao, J., Xia, L., He, W., Liu, L., Luo, C., Shu, X., Cai, Q., Chen, Y., & Lu, N. (2019). Gut microbiota dysbiosis worsens the severity of acute pancreatitis in patients and mice. *Journal of Gastroenterology*, *54*(4). https://doi.org/10.1007/s00535-018-1529-0

Zwick, R. K., Kasparek, P., Palikuqi, B., Viragova, S., Weichselbaum, L., McGinnis, C. S., McKinley, K. L., Rathnayake, A., Vaka, D., Nguyen, V., Trentesaux, C., Reyes, E., Gupta, A. R., Gartner, Z. J., Locksley, R. M., Gardner, J. M., Itzkovitz, S., Boffelli, D., & Klein, O. D. (2024). Epithelial zonation along the mouse and human small intestine defines five discrete metabolic domains. *Nature Cell Biology*, *26*(2). https://doi.org/10.1038/s41556-023-01337-z